Polymer Nanoparticles: A New Technological Platform for Emerging Applications

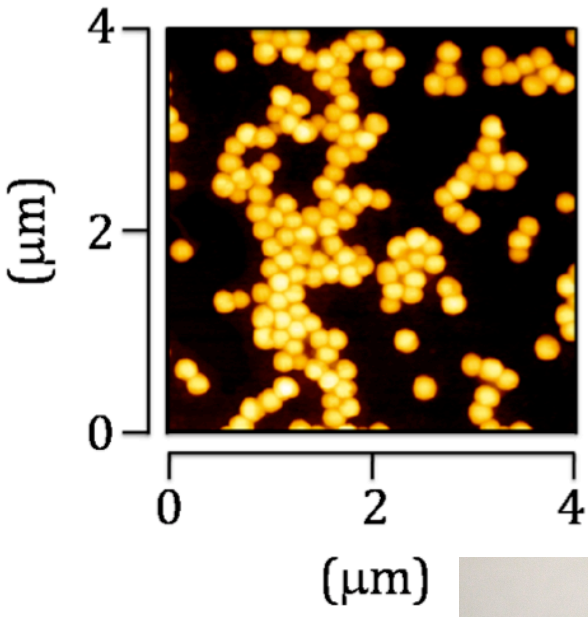

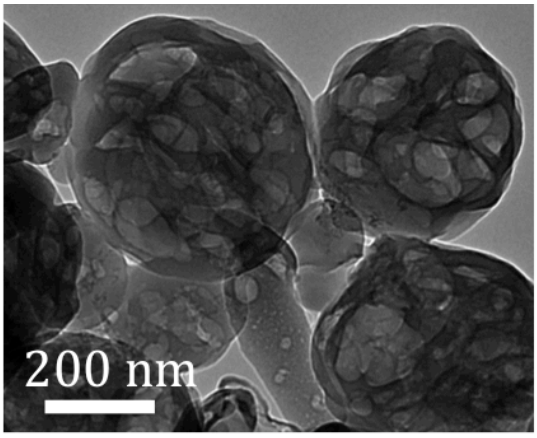

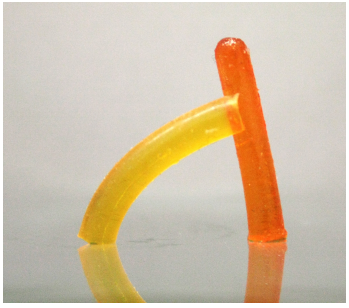

1 cm

PhD Thesis of
Simone Bonetti
Mat. Nr. 708679

Ph.D. Supervisor: Prof. Dr. Roberto Simonutti
Ph.D. Dean: Prof. Dr. Gianfranco Pacchioni

XXVIII Cycle
Ph.D. School in Nanostructures and Nanotechnology
Department of Materials Science

Polymer Nanoparticles:
A New Technological Platform
for
Emerging Applications

Ph.D. Thesis of

Simone Bonetti

Mat. Nr. 708679

Ph.D. Supervisor: Prof. Dr. Roberto Simonutti

Ph.D. Dean: Prof. Dr. Gianfranco Pacchioni

XXVIII Cycle

Ph.D. School in Nanostructures and Nanotechnology

Department of Materials Science

"*Courage is what it takes to stand up and speak;*

Courage is also what it takes to sit down and listen".

Winston Churchill

This work is dedicated to no one in particular. I owe everyone I met.

Copyright

Outline

Abstract

Polymer-based nanoparticles tackle many different fields, from extrinsic self-healing materials to cosmetics, from electronics to nanophotonics. The growing interest among this topic is mainly due to the wide range of application and market needs that polymers have been satisfying since their discovery. Moreover, polymer nanoparticles in the submicrometric dimensional range have been obtained by different methods. However, the scientific community is still debating whether bulk polymer properties are retained in this nanostructures or not.

In this work, a method for the in-situ monitoring of polymer chains aggregation state based on the time-resolved fluorescence of a tailored molecular rotor was developed. Differently from previous literature, this technique was calibrated and compared with standard differential scanning calorimetry, in order to have a replicable and robust standard reference. The results leaded to the conclusion that bulk polymer properties related to glass transition are conserved even in nanoparticles of some tens of nm in radius. This observation was used as an important paradigm towards the preparation and application of biphasic polymer-based nanoparticles. With this regard, an optimized semicontinuous emulsion polymerization protocol for the preparation of poly(*n*-butyl acrylate)@polystyrene (PBA@PS) core@shell nanoparticles was developed. These nanostructures were found to behave as force-responsive nano-objects, leading to the first example of baroplasticity detected on a single particle scale. Beyond the basic research interest on the nanomorphology evolution under non-equilibrium stress, this result can be interesting in manufacturing a new class of sealing nanoadditives in the field of extrinsic self-healing materials. We demonstrated that such PBA@PS nanoparticles can have even other applications. Namely, PBA@PS nanoparticles were used as nanocontainers for lipophilic derivatives of a biocompatible dye and as nanoemitters for sensitized up-conversion (SUC).

In order to overcome some limits of PBA@PS nanoparticles, liquid-core nanocapsules were prepared. These vascular systems are composed by a *n*-hexadecane (HD) core embedded in a plastomer poly(methyl methacrylate) (PMMA) shell. The preparation protocol of such nanocapsules was optimized in order to use them as nano-additives to be delivered within self-standing Proof-of-Concept polymer materials. Particularly, a poly(vinyl alcohol) bulk SUC film was prepared and found to be effective even in ambient conditions, demonstrating the potentialities of this system for everyday-applications.

Besides, HD@PMMA nanocontainers were used for encapsulating oxide nanocrystals for the preparation of hybrid polymer materials with enhanced refractive index. The nano-oxide loading within the HD core was so high that it inhibited either the crystallization of HD and the aggregation of the nanocrystals. Thanks to these capabilities, the oxide-loaded nanocapsules have been used during the bulk polymerization of PMMA, obtaining transparent bulk sample of PMMA with improved refractive index and naked eye transparency.

Concluding, with this work we devise examples about the applicability of polymer nanoparticles as smart additives within formulations for the preparation of hierarchical functional materials in the contest of a more sustainable chemistry for materials science applications.

1 Introduction

Meeting a wide range of applications and market needs can be addressed as the main features fuelling the huge interest growing around polymer nanoparticles[1]. Indeed several reports show their application in electronics[2], photonics[3], biotechnology[4] and environmental technology[5]. Polymer nanoparticles (PNPs) can be defined as solid, colloidal particles with dimensions in the range 10–10^4 nm[6]. The term PNPs can be also extended to nanospheres and nanocapsules. Particularly polymer nanospheres are matrix particles, where their entire mass is solid and molecules could eventually be adsorbed at the surface or embedded within the particle. Even though PNPs are generally spherical, non-spherical structures are also described in the literature[7]. On the other hand polymer nanocapsules are vesicular systems, where the entrapped payload is sequestrated to a cavity consisting of a liquid core surrounded by a solid polymer shell[8]. PNPs can be obtained either by polymerization of monomers or starting from a dispersion of preformed polymers. In this work we will focus on PNPs obtained with emulsion polymerization (section 2.2.1), but an insight on PNPs obtained from preformed polymer via solvent evaporation from emulsion droplets will be given in sections 2.2.2.

Emulsion polymerization (EP) firstly popped up in scientific publications after the Second World War, in 1946[9]. However, this almost 70 year old polymerization technique have been re-discovered in the last two decades on the wave of the need of a more sustainable and eco-friendly approach to chemistry. Emulsion polymerization can indeed be performed in green solvents (i.e. water), leading to final polymer nanostructures (i.e. nanoparticles, nanocapsules) with dimensions in the range of about 10^2 nm. Moreover, since the 1980s several sub micrometric microscopy techniques have been proposed, later in the 1990s-2000s they have been used as ubiquitous characterization tools in most of the academic laboratories. The technological capability of imaging with high spatial resolution the nanostructures obtained by emulsion techniques (Figure 1.1) has been fuelling new research lines[10] on this topic (Figure 1.2). Last but not least, emulsion polymerization has become a widely used synthetic tool even in several industrial scenarios (i.e. tyres, paintings, impact

modifiers, dermocosmesis, food industry etc.), with the nanotechnology world market forecast increasing exponentially[11].

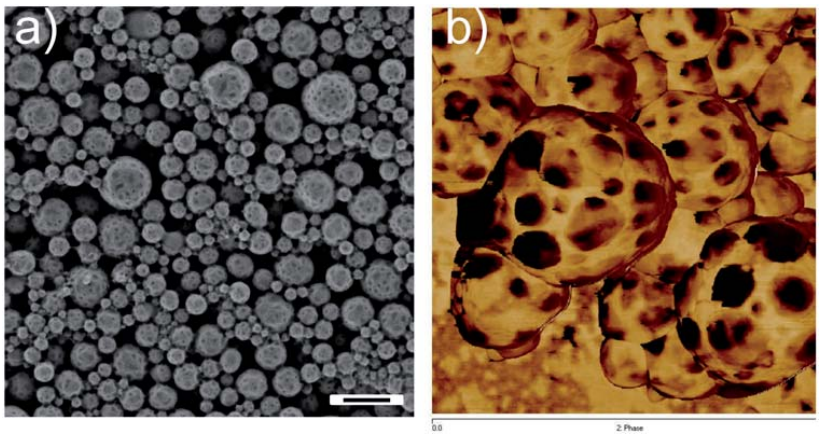

Figure 1.1: Representative SEM micrograph (a) and AFM phase contrast image 1 µm x 1µm (b) of patchy polymer particles obtained with miniemulsion polymerization technique. Scale bar represents 500 nm. After D. Crespy et al., *Polym. Chem.*, 2014, 5, 365-371. Copyright © Royal Society of Chemistry.

This PhD thesis takes birth in such a PNPs *renaissance* period. We strongly believe that PNPs can act as a new platform in order to prepare nanostructures and materials able to compensate, react and adapt to external stimuli. Moreover we strongly believe in Heraclitus of Ephesus words: "τὰ ὄντα ἰέναι τε πάντα καὶ μένειν οὐδέν (i.e. All entities move and nothing remains still)"[12]. Thus we decided to try to give new perspectives to PNPs, taking an explorative look in some proof-of-concept functional polymer nanostructures for potential technological applications.

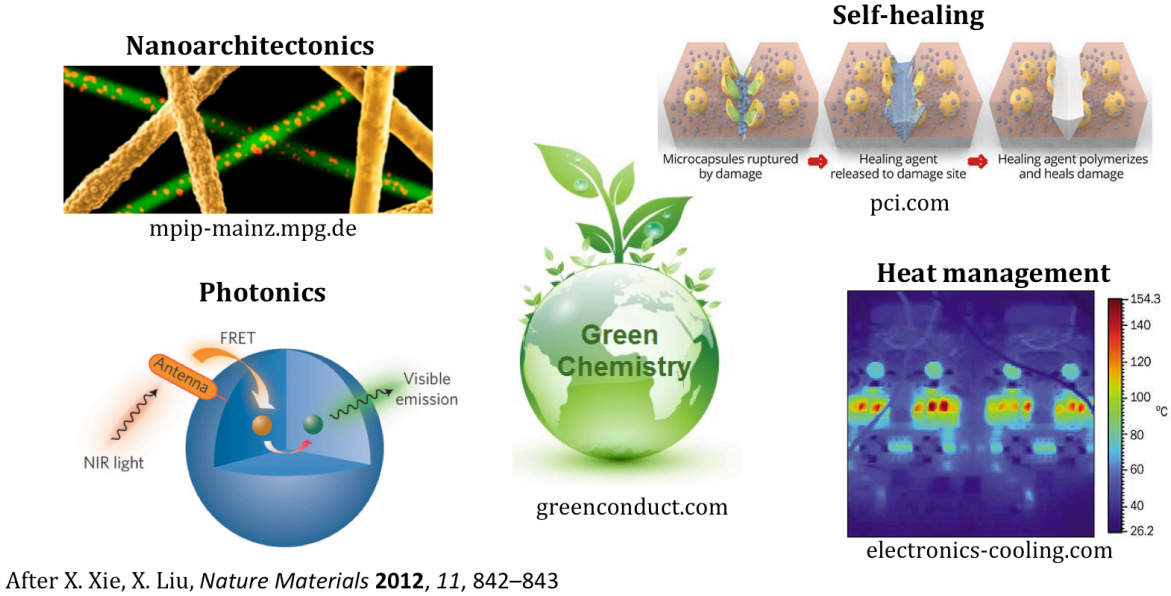

After X. Xie, X. Liu, *Nature Materials* **2012**, *11*, 842–843

Figure 1.2: Representative sketch of some of the potential application fields for PNPs fuelled by green chemistry trend.

Dealing with nanostructures and nanotechnology means facing the special properties of matter occurring below a given size threshold (i.e. <10^2 nm), when confinement effects arise. Since the target is to synthesize functional polymer nanostructure in the some 10^2 nm range, the first issue to face was the work of R.D. Priestley et al.[13] showing that the glass transition temperature (T_g, the temperature at which a polymer chain start reptating) of polystyrene (PS) confined to the nanoscale can deviate substantially from the bulk, due to T_g-confinement effect. Moving from the previous T_g-confinement works - focused on the thickness-dependence T_g in thin films - they shifted the attention to geometries beyond the two-dimensional freestanding films[14], namely PNPs and 3D-confinement. R.D. Priestley showed via modulated differential scanning calorimetry, that T_g decreases with size for PS NPs suspended in an aqueous solution (Figure 1.3), in agreement with the corresponding freestanding films. Furthermore, they were able to inhibit this confinement phenomenon by capping of polystyrene nanoparticles with a hard silica shell. Indeed such a hard shell leaded to a size invariant T_g of PS, embedded within the hybrid nanocapsules. It is clear that such results must be taken into account, since our long-term purpose is to prepare functional materials with either polymer nanoparticles or polymer nanocapsules as nanoadditives. Particularly, we need to know whether the T_g-related thermo-mechanical polymer properties (i.e. stiffness, vitrification and structural persistence) are stable at the nanoscale or not.

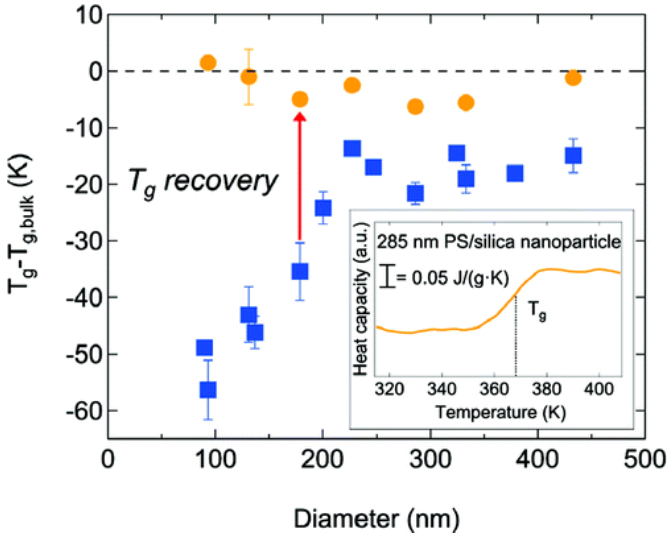

Figure 1.3: Change in T_g with respect to particle diameter for PS (blue ■) and PS/silica core–shell nanoparticles (yellow ●). Inset shows a MDSC thermogram for 285 nm PS/silica core–shell nanoparticles. After R.D. Priestley et al., *Macromolecules*, 2011, *44,* 10, 4001–4006. Copyright © American Chemical Society.

However, the scientific debate regarding the length scale of glassy dynamics in polymer-based nanomaterials is still dominated by contradictory results. For example, Tress et al.[15]

published in 2013 a paper studying the dynamics of condensed isolated poly(2-vinylpyridine) polymer chains, using broadband dielectric spectroscopy and a capacitor with nanostructured electrodes separated by 35 nanometres. They found that the dynamic glass transition (i.e. a cooperative process) can take place even in condensed isolated polymer chains because the length scale on which these fluctuations takes place — typically corresponding to two or three polymer segments — is much smaller than the extension of the coil as a whole. In Figure 1.4 dielectric loss spectra (recorded at 407 K) of bulk, semi-isolated chains, and isolated chains normalized by the respective maximum value are reported. In detail the latter two are broadened, especially on the low-frequency side, which corresponds to the occurrence of longer relaxation time modes. This demonstrated that the directly measured glass transition of condensed isolated polymer chains is bulk-like. Moreover, the observation of bulk-like dynamics proposed by Tress et al.[15] is in full agreement with the expected length scale proposed in 1992 from Fisher et al.[16] where dynamic glass transition is to be expected.

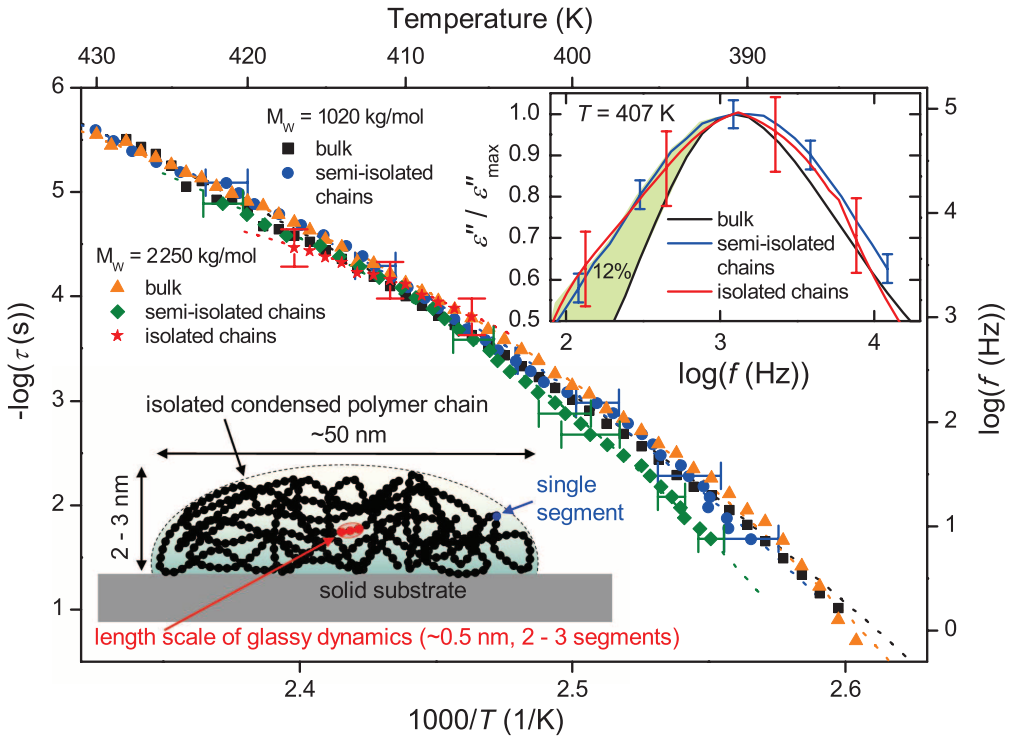

Figure 1.4: Activation plot of the α-relaxation of condensed semi-isolated and isolated P2VP polymer coils and the respective bulk dynamics for two molecular weights as indicated. Dielectric loss spectra (recorded at 407 K) of bulk, semi- isolated chains, and isolated chains normalized by the respective maximum value. The sketch at lower left illustrates the length scale intrinsic to glassy dynamics in comparison to the size of a single condensed polymer chain. From M. Tress, E.U. Mapesa, W. Kossack, W.K. Kipnusu, M. Reiche, F. Kremer, *Science* 2013, *341*, 1371. Copyright © American Association for the Advancement of Science.

Since the aim of this PhD thesis is the development of functional polymer nanoparticles and no common vision about the T_g-confinement phenomena have been proposed until now, the first step was to develop a characterization method investigating on what extent the properties of PNPs are changed. Then, in collaboration with Dr. Gianfranco Vaccaro, Prof. Dr. Luca Beverina and Prof. Francesco Meinardi, a method based on Time Resolved Fluorescence Spectroscopy (TRFS) of a tailored fluorescent probes was developed, giving a direct and fast access to the polymer aggregation states under various experimental conditions. Particularly, the detailed analysis of the time resolved photoluminescence (TRPL) of a specifically designed fluorescent molecular rotor (called AzeNaph1) enabling the direct monitoring of the onset reptation phenomena in different polymer samples is proposed in chapter 3. Molecular rotors are indeed donor-acceptor organic molecules with peculiar photophysics due to their high degree of intramolecular rotational freedom. Particularly, their lifetime strongly depends on the local viscosity of the environment and this effect can be used to monitor process such as block copolymer micelles formation [17] or bulk radical polymerization of methyl methacrylate[18]. We demonstrated that AzeNAph1 TRFS analysis can be of strategic interest in applied polymer science, because this approach is quantitative on real polymer samples (i.e. undiluted aqueous solution of scattering block copolymer micelles, commercial polymer chips and emulsions of polymer nanoparticles). We firstly demonstrate that the temperature dependence of the lifetime variation of AzeNaph1 can be used to detect the glass transition temperature of bulk polymer sample, by comparing the T_g values with the one obtained with standard DSC. Secondly, we used this method to measure the T_g of batches of PS NPs (60 nm and 156 nm in hydrodynamic diameter) directly in aqueous emulsion. Our data demonstrate the persistence of the polystyrene bulk T_g in both the NPs samples.

This demonstration of the permanence of the T_g - and of the thermo-mechanical properties related to - at the nanoscale drives to the next part of this work: the preparation of proof-of-concept functional PNPs. Particularly, the effort was focused on the synthesis and characterization of multiphasic (adhesive/plastomer, liquid core/plastomer shell) polymer based nanostructure. This kind of multiphase nanostructures obtained with aqueous emulsion polymerization protocols are gaining growing interest in field such as self-healing, photonics and heat-management, together with an interesting perspective in base research on nanoarchitectonics (Figure 1.3).

In detail, poly(*n*-butyl acrylate)@polystyrene (PBA@PS, adhesive/plastomer) nanoparticles (NPs) were synthesized (section 2.2.1.3) in order to combine the adhesive properties of PBA with the structural stability and low cost per unit weight of PS (chapter 4).

The aim was to verify the potential behaviour of these adhesive/plastomer PNPs as a capsule-based sealing nanoadditive potentially useful in the field of extrinsic self-healing materials (in which the healing agent must be pre-embedded in mesoscopic reservoirs)[19]. We thus developed an original semicontinuous EP protocol where the replacement of the commonly used linear surfactant (like sodium dodecyl sulfonate) with a branched surfactant (namely dioctyl sodium sulfosuccinate, AOT) plays a key role. Indeed AOT is generally more soluble in hydrophobic monomers than in water and, together with other branched sulfosuccinates, is extensively used due to the ability to form microemulsions without the presence of a short-chain alcohol as cosurfactant. AFM, SEM, ^{1}H-TD-NMR and solid state ^{13}C MAS NMR showed the biphasic nature of the sample with a strong phase separation between PBA and PS nanodomains. Particularly AFM force spectroscopy allowed to monitor in situ the breakdown dynamics of the nanoparticle, showing behaviour according to a pressure-induced partial intermixing of the different nanophases associated with baroplasticity. Representative force vs distance curves shows that this baroplastic mixture still has adhesive properties. The results can be potentially interesting in manufacturing a new class of polymer nanoparticles acting as capsule-based sealing additives to be delivered as smart aqueous inks or dry powder.

Other application we tested for such PBA@PS nanoparticles were based on the good optical properties and the PBA permeability to molecules in the 4 to 8 nm range. This gives the PBA@PS NP the possibility to act as nanocontainers, where PBA acts as the payload tank and PS as the structural external shell. In detail, we loaded the PBA core with lipophilic derivatives of carminic acid (see section 4.5.2) and with a sensitized up-conversion mixture of dyes (see section 4.5.1).

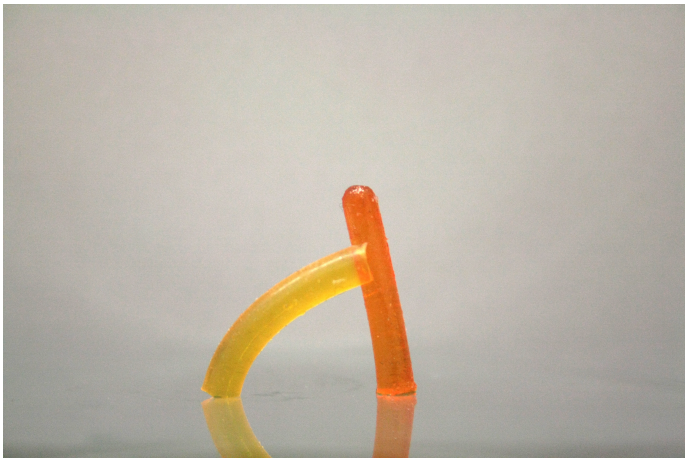

Figure 1.5: Photograph of PBA:EGDMA (4.5% v/V EGDMA content) self-standing bulk-samples. On the left the yellow sample loaded with the pivaloyl-derivative; on the right the orange sample loaded with the acetylated-derivative.

The lipophilic derivatives of carminic acid can be very interesting since few carminic acid derivatives are known. The main drawback of Carminic Acid (widely used in food industry thanks to its biocompatibility) stands in its insolubility in polymer matrix, strongly limiting its application in the polymer-industry. In section 4.5.2 we demonstrated that the derivatives synthesized by our partner group (UniMIB – Prof. Dr. Laura Cipolla) are soluble in cross-linked poly(*n*-butyl acrylate) bulk self-standing samples (see Figure 1.3 and section 4.5.2.1) and in PBA@PS core@shell NPs (section 4.5.2.2), thus proposing an effective way to introduce lipophilic derivatives of biocompatible dyes in everyday-life applications.

Moving to sensitized up-conversion (SUC) nanoemitters in section 4.5.1, the interest around this topic is triggered by the fact that SUC is widely considered among the most promising approach for photon energy managing processes, being efficient also at the solar irradiance. However, applications of SUC on real devices have not been yet fully accomplished because its conversion yield usually drops dramatically in the solid state, where the low dye mobility inhibits the diffusion-controlled mechanisms ruling SUC photophysics. In 2013 A. Monguzzi et al.[153] demonstrated that a single-phase elastomer like poly(*n*-butyl acrylate) (PBA) doped with proper dyes (platinum (II) octaetyl-porphyrin and 9,10-diphenylanthracene) can be used to fabricate an efficient photon up-converting material. Thanks to the residual molecular diffusion provided by the soft PBA host matrix, they obtained a record SUC yield of 17% at the solid state.

On the basis of these results, in collaboration with Dr. Angelo Monguzzi and Prof. Franco Meinardi, we decided to use the PBA@PS core@shell PNPs as aqueous SUC nanoemitters, with potential applications in imaging and proof-of-concept systems for SUC mechanism study under spatial confinement. Even if we successfully obtained an energy transfer yield of more than 50% in PBA@PS in aqueous emulsion, we were not able to reach the same efficiency measured in bulk-PBA probably because of i) columbic attractions between the donor dye and the surfactant, ii) detrimental effect of free-propagating radicals on conjugated acceptor dye and iii) migration of the acceptor dye into the shell.

In order to overcome this problem, we decided to widen our core@shell sample composition by the preparation of liquid-core nanocapsules (sections 2.2.1.4.1, 2.2.1.4.2, 2.2.1.4.3 and chapter 5). The core-forming medium is *n*-hexadecane (HD), while the shell-forming monomer is methyl methacrylate (MMA). In fact MMA and HD are completely miscible, but phase separation occurs during the emulsion polymerization process, due to the immiscibility of HD and poly-MMA. Lastly PMMA has a glass transition temperature (~118° C), compatible with the structural demand of a plastomer shell sequestrating a liquid. The

synthesis protocol was further optimized in order either to embed TiO_2 (anatase) nanocrystals capped with oleic acid within the HD and to have a liquid-core deliverable SUC nanoemitters (section 2.2.1.4.2).

The main motivation of embedding TiO_2 (anatase) nanocrystals within the liquid-core nanocapsules stands in the fact that specific applications - such as high refractive index devices, biomedical contrast enhanced imaging, colloidal crystals delivery - often require to exploit inorganic particles with peculiar properties and integrate them into deliverable, bio-friendly and easy-to-handle nanocontainers. With this regard, a single step emulsion polymerization for the in situ encapsulation of inorganic nanocrystals into polymeric nanocapsules preserving their intrinsic properties is proposed in section 5.1.2. As a case study, we nanoencapsulate colloidal-synthesized oleic acid capped anatase TiO_2 nanocrystals into a biphasic (liquid-solid) HD@PMMA nanocapsule. The presence of nanocrystals was confirmed by optical measurements, TEM micrographics and TGA analysis. Both DSC and ^{1}H-TD-NMR show that HD crystallization takes place only in TiO2-free nanocapsules (synthesized as blank reference in section 5.1.1), leading to potential applications in the field of latent thermal energy systems. In TiO_2-loaded NPs HD crystallization is inhibited probably because of crowding phenomena. Only with cryo-TEM was possible to collect the damage image related to the presence of HD in the TiO_2-loaded sample. Lastly, TiO_2-loaded nanocapsules were precipitated, dried and used as additives for the formulation of a tuneable refractive index bulk PMMA (section 5.2), with an increase in the refractive index of 1.35% respect to pure PMMA and maintaining a naked-eye transparency.

The synthesis protocol was further adapted for the preparation of a liquid-core SUC nanoemitters (section 2.2.1.4.3 and chapter 5.3). In order either not to generate O_2-rich radicals - passivizing the dyes involved in the sensitized up-conversion process - nor to activate propagating radicals within the oil phase, the water soluble 2,2'-Azobis(2-methylpropionamidine) dihydrochloride (AMPDC) radical initiator was used. In this way we minimize the probability that a free radical detrimentally interacts with the dyes. In fact the dyes are dissolved in the HD (i.e. paraffin unreactive in presence of radicals) core. In this way we obtained liquid-core nanocapsules acting as sensitized up-conversion nanoemitters of characteristic dimension around 40 nm, according to DLS measurements and SEM micrographics. The freshly prepared nanoemitters emulsion was then used as a solvent for poly(vinyl alcohol), PVA. The obtained solution (2.5% w/W PVA content) was deposited on a glass substrate and let dry in order to obtain a self-standing PVA film (section 5.3.2). The bulk PVA film was then observed with confocal optical microscope: all the images present a signal

associated with sensitized up-conversion. It is worth noticing that all the images were recorded in air, namely in presence of oxygen. The fact that the up-conversion signal is detectable in presence of oxygen demonstrates that the dyes are effectively sequestrated and protected within the nanocapsule.

The last part of this work is related on a pioneering study of solvent evaporation from emulsion droplets mechanism (section 2.2.2) involving a combined approach of Fluorescence Correlation Spectroscopy (FCS, section 2.3.5) and TRFS of molecular rotors (section 2.2.1.2.1 and chapter 6), developed in collaboration with Dr. Kaloian Koynov and Dr. Daniel Crespy at the Max-Planck Institut für Polymerforschung in Mainz. The preparation of polymer nanoparticles with solvent evaporation from emulsion droplets is one of the most common approaches for nanoparticles preparation starting from preformed polymer chains based on liquid-solid nucleation in confined environment. A polymer organic solution is mixed in an aqueous solution of surfactant, thus forming an emulsion. The emulsion is further stabilized by ultrasonication and stirring. At this stage a droplet emulsion of polymer, organic solvent, surfactant and water is formed. The droplet emulsion is then mildly heated, in order to drive the evaporation of the organic solvent and obtain dry PNPs. It offers indeed many possibilities such as control over nanoparticle size, encapsulation of various compounds, or fabrication of complex morphologies. This procedure is having a relevant success in fields such organic electronics and bioapplications, where the absence of impurities (i.e. unreacted monomer) is a must. However, little is known for the details of particle formation, i.e. for the transition from the initial liquid droplet emulsion to the final particle dispersion, especially in the case of particles with complex morphologies. A major reason is the lack of experimental techniques providing information on the internal morphology of very small nanodroplets and nanoparticles moving fast in a continuous liquid phase. In this respect, the very sensitive and selective technique of FCS (section 2.3.5.1) offers an interesting alternative and was already successfully used to quantify the evolution of nanodroplet/nanoparticle size, the process of droplet coalescence, or the amount of encapsulated compounds[20]. In this contribution, we will consider the use of tailored molecular rotors as fluorescent tracers within nanodroplets/nanoparticles in a FCS experiment as a way to obtain unique information on the kinetics of the particle formation. We demonstrated that the combining of FCS with molecular rotors opens the possibility to monitor simultaneously the overall droplet/particle dynamics (in terms of diffusivity and size) and the inner morphology of the droplets/particles (i.e. remaining solvent content or eventual phase separation), thus widening the range of parameters accessible in a single FCS experiment.

2 Experimental

2.1 Materials

n-butyl acrylate (BA, ≥99% containing 10-60 ppm monomethyl ether hydroquinone as inhibitor) and Styrene (STY, ≥99% *ReagentPlus*® 4-*tert*-butylcatechol as stabilizer) monomers were purified through distillation on aluminium oxide (activated, basic, Brockmann I) column. 2,2'-Azobis(2-methylpropionitrile) (AIBN, Sigma Aldrich, purum ≥98%) was recrystallized from methanol before usage. Dioctyl sulfosuccinate sodium salt (AOT, Sigma Aldrich, 98%), Chromasolv Water, 2,2'-Azobis(2-methylpropionamidine) dihydrochloride (AMPDC, Sigma Aldrich, purum ≥98%), sodium dodecyl sulphate (SDS, Sigma Aldrich, 99%), toluene (Sigma Aldrich, 99.7%), divinylbenzene (DVB, Sigma Aldrich, technical grade 80% containing 1000 ppm *p*-*tert*-butylcatechol as inhibitor) and hexadecane (HD, Sigma Aldrich, 99%) were used as received without further purification.

2.2 Synthetic Methods

Polymer nanoparticles (PNPs) are spreading in several areas (i.e. electronics, photonics, medicine, environmental technology, etc.) thanks to their unique properties, able to meet a wide range of applications and market needs[1]. Generally, PNPs can be obtained from the dispersion of preformed polymers (solvent evaporation [21], salting-out [22], dialysis [23], supercritical fluid technology[24]) or the polymerization of monomers (emulsion[25], mini-emulsion[26], micro-emulsion[27], surfactant-free emulsion[28], and interfacial polymerization[29]). The choice of method depends on factors such as particle size and distribution, area of application, tolerance to residual solvents or radicals, etc. In the next sections the emulsion polymerization protocols developed for PNPs preparation are presented (sections 2.2.1, 2.2.1.2, 2.2.1.3 and 2.2.1.4), together with an overview of solvent evaporation from emulsion droplets (section 2.2.2).

2.2.1 Emulsion Polymerization

Emulsion polymerization is a chemical process for producing waterborne PNPs and PNCs with various colloidal and physicochemical properties.[30] According to IUPAC definition, emulsion polymerization (EP) is a heterophase radical "*polymerization whereby monomer(s), initiator, dispersion medium, and possibly colloid stabilizer constitute initially an inhomogeneous system resulting in particles of colloidal dimensions containing the formed*

polymer". This heterogeneous free radical polymerization process involves emulsification of relatively hydrophobic monomers (such as butadiene, styrene, acrylonitrile, acrylate ester and methacrylate ester monomers, vinyl acetate, and vinyl chloride) in water by an oil-in-water emulsifier, followed by the initiation reaction with either a water- insoluble initiator (e.g. sodium persulfate) or an oil-soluble initiator (e.g. 2-2-azobisisobutyronitrile (AIBN))[31]. EP is among the most common methods used for the production of several specialty polymers. The use of water as the dispersion medium is environmentally friendly and also allows excellent heat dissipation during the polymerization. Depending on the utilization of surfactant, it can be classified as conventional and surfactant-free emulsion polymerization[32]. In this PhD thesis only conventional (i.e. involving the presence of surfactant) emulsion polymerization was used, therefore the description of the fundamental mechanism of surfactant-free emulsion will be skipped.

2.2.1.1 Conventional emulsion polymerization

The majority of the world's production by emulsion polymerization is obtained with conventional EP. A typical conventional EP formulation is comprised of water, a monomer of low water solubility, water-soluble or oil-soluble radical initiator and a surfactant. At the end of the reaction, PNPs are typically $\sim 10^2$ nm in size. Initiation occurs when a monomer molecule collides with an initiator molecule that may be either an ion or a free radical, depending on the nature of the initiator involved in the reaction. Alternatively, the monomer molecule can be transformed into an initiating radical by high-energy radiation (i.e. ultraviolet or strong visible light). Phase separation triggering the formation of stable solid particles can take place before or after the termination of the polymerization reaction.

2.2.1.1.1 Emulsion Polymerization general mechanism features

The reaction system during EP is characterized by the emulsified monomer droplets (ca. 10^{12}–10^{14} dm^{-3} in volume) dispersed in a continuous phase aqueous solution of an oil-in-water surfactant. Monomer-swollen micelles (ca. 5–10nm in diameter and 10^{19}– 10^{21} dm^{-3} in volume) may also exist in the reaction system, once the concentration of surfactant in the aqueous phase is higher than its critical micelle concentration (CMC). The hydrophobic monomer is present either in some of the surfactant micelles or even dissolved in traces in the aqueous phase (depending on its water solubility). Most of the monomer molecules dwell in the giant monomer reservoirs (i.e. monomer droplets). The polymerization is initiated by the addition of initiator. According to the micelle nucleation model - proposed by Harkins[33], Smith and Ewart[34] and later modified by Gardon[35] - submicron latex particles are generated via the capture of free radicals by micelles, having extremely large oil–water interfacial area. A very clear description of this process was proposed by Y. Luo and F.J. Schork in 2002[36] for the case of a water-soluble initiator. According to their description, "*free radicals originate in the aqueous phase by decomposition of the initiator. Monomer dissolved in the aqueous phase is polymerized by these radicals, forming oligomers. When the oligomers contain only a few monomer units, they are captured by micelles or existing polymer particles, and propagation continues in the oil phase*", driving to PNPs nucleation (Interval I in Figure 2.1). As a consequence, monomer-swollen micelles are successfully transformed into primary particles. In 1978, F.K. Hansen and J. Ugelstad[37] proposed that the nucleation of a primary particle occurs when the chain length of an oligomer radical reaches a critical value (n^*) and the number of primary particles per unit volume of water originating from homogeneous nucleation (N_1) can be calculated as

$$N_1(t) = 1/k_1\{[k_1\rho_i n^* t(k_2+1)^{n^*}]^{1/n^*} - (k_2+1)\}$$

$$k_1 = k_c/(k_p[\mathrm{M}]_w)$$

$$k_2 = (k_{tw}\rho_i)^{1/2}/(k_p[\mathrm{M}]_w)$$

where ρ_i is the rate of generation of free radicals in the aqueous phase, k_c is the average rate constant for the capture of free radicals by the particles, k_p is the propagation rate constant, k_{tw} the termination rate constant in water and $[\mathrm{M}]_w$ the concentration of monomer in water.

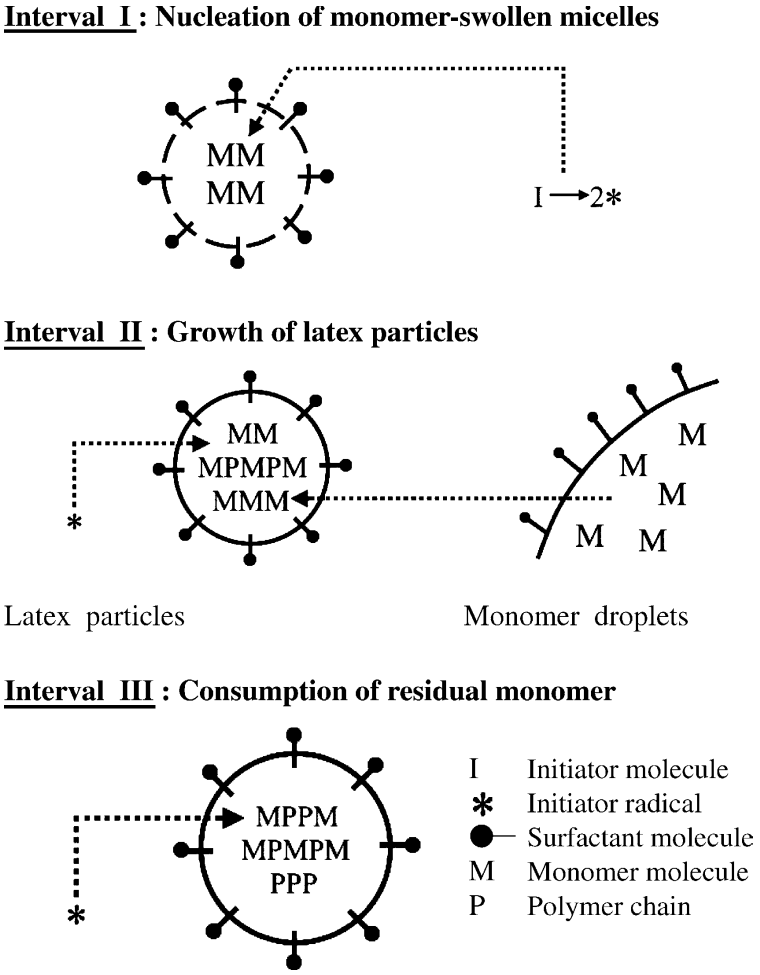

Figure 2.1: Schematic representation of the PNPs formation mechanism in an emulsion polymerization with water-soluble initiator. After C.S. Chern / Prog. Polym. Sci. 31 (2006) 443–486. Copyright © Elsevier B.V.

These early-stage particles keep growing by acquiring the reactant species from monomer droplets and monomer-swollen micelles (Interval II in Figure 2.1). In order to maintain adequate colloidal stability of the growing particle nuclei, micelles that do not contribute to particle nucleation disband to supply the increasing demand for surfactant. In addition, the surfactant molecules adsorbed on monomer droplets may also desorbs out of the droplet surface, diffuse across the continuous aqueous phase and then adsorb on the expanding particle surface. When all the monomer droplets disappear, the consumption of the residual monomer within the same particle takes place (Interval III in Figure 2.1) and latex particles become monomer-starved, triggering the continuous decrease in the concentration of monomer in the reaction loci toward the end of polymerization.

This description of the EP mechanism (reported more extensively in C.S. Chern, *Prog. Polym. Sci.* **2006**, *31*, 443-486, where the images and the main ideas were taken) gathers the

fundamental polymerizations steps when a water-soluble initiator is implied (i.e. when the initiating radicals are mostly generated in the aqueous phase).

However, still in the early 2000s, the scientific community was not able to draw a common picture of the EP mechanism when an oil-soluble initiator is used, fuelling a long lasting debate about the origin of the free radicals initiating polymerization in case of oil-soluble initiators. Two main different interpretations were proposed.

On one hand some researchers speculate that, since micelles and particles are quite small, once the oil-soluble initiator decomposes in a micelle or particle, the two newly born free radicals will terminate with each other before any other events (i.e. monomer propagation or free-radical exit) can occur. It is believed that the free radicals initiating the polymerization actually originate in the aqueous phase, from the small fraction of the total initiator that is dissolved in the aqueous phase.[38]

On the other hand researchers assume that one of the two newly born free radicals in a micelle or particle can desorb from the micelle or particle before mutual termination takes place.[39] The remaining free radical is then free to propagate within the embryo particle.

Their own mathematical models and experimental data support both hypotheses. Only in 2002 Y. Luo and F.J. Schork - in their study of butyl acrylate conventional emulsion (macroemulsion) and miniemulsion polymerizations carried out with an oil-soluble initiator (2-2' azobisisobutyronitrile) in the presence or absence of an aqueous-phase radical scavenger - concluded that for macroemulsion polymerization, the contribution from free radicals originating in the aqueous phase is predominant in the micellar nucleation of particles. On the other hand, free radicals originating in the particle phase contribute to the rate of polymerization, and the contribution increases with an increase in particle size. Lastly, for polymer particles with diameters of up to approximately 100 nm, polymerization is initiated from free radicals originating in the aqueous phase.

Notwithstanding such a fundamental debate, some general features can be drawn to get a sketch of the general mechanism of a radical emulsion polymerization. Once the initiator I_2 is activated either in the aqueous or oil-phase, it will form a couple of free radicals ($2I\bullet$) able to react with a monomer molecule (M) and to start a radical polymerization. The activation of the initiator can be triggered via thermal energy, light or catalyst.

$$I_2 \rightarrow 2I\bullet$$

Since the radical I• can be extremely reactive, it can drive to the formation of a primary radical (P_1•):

$$I\bullet + M \rightarrow P_1\bullet$$

The primary radical can further react with other monomer molecules (nM), increasing the molecular weight of the growing chain:

$$P_1\bullet + nM \rightarrow P_n\bullet$$

where n is the number of monomer molecules added to the growing chain and P_n• represents the growing polymer chain composed by n monomer units.

During the chain growth a second event could occur: chain transfer. Chain transfer is a polymerization reaction by which the activity of a growing polymer chain is transferred to another molecule[40]. Chain transfer can be either introduced deliberately into a polymerization (by use of a *chain transfer agent*) or it may be an unavoidable side-reaction with various components of the polymerization, such as monomer, polymer or solvent (generally labelled as X in the following). Chain transfer most likely lowers the molecular weight of the final polymer.

$$RM_n^{\bullet} + X \longrightarrow RM_n + X^{\bullet}$$

$$M + X^{\bullet} \longrightarrow XM^{\bullet}$$

Lastly, the termination of the radical is to be expected. The termination can occur either by disproportionation reaction or radical coupling. When disproportionation takes place, two growing polymer chains will react via a redox reaction in which two chains are reduced and oxidised to form two different products. In polymers it will mostly lead to two inactive polymer chains: one with a saturated terminal and the other with a not saturated terminal.

$$R\text{-}CH_2\text{-}CH_2\bullet + R'\text{-}CH_2\text{-}CH_2\bullet \rightarrow R\text{-}CH_2\text{-}CH_3 + R'\text{-}CH{=}CH_2$$

On the other hand, radical coupling termination occurs when two growing chains, P_n• with n monomers and P_m• with m monomers react and lead to an inactive polymer chain P composed of m+n monomers with higher molecular weight.

$$P_n\bullet + P_m\bullet \rightarrow P$$

Radical polymerization is quite attractive in application-oriented research since it is easy to trigger and a wide variety of monomers can be polymerized with this procedure. Some drawbacks must be mentioned: i) latent heat of reaction (easily dissipated when radical polymerization is performed in emulsion) and ii) relatively broad mass polydispersity mainly due to intrachain reaction (i.e. backbiting) or interchain reaction (ramifications).

It is worth pointing out that the definition of the actual reaction EP mechanism in presence of an oil-soluble initiator is not the main aim of this PhD thesis. On the other hand, the main aim is to give the reader some general guidelines for the preparation of EP formulations leading to the formation of interesting multiphase polymer nanostructures.

2.2.1.2 Protocol for the preparation of polystyrene nanoparticles loaded with the molecular rotor AzeNaph1

For the preparation of the 156 nm polystyrene NPs 40 ml of aqueous solution of sodium dodecylbenzene sulfate 0.1 g/L was prepared and degassed at 35°C bubbling N_2 for 60 minutes under magnetic stirring. 360 ppm of AzeNaph1 were dissolved in 3 ml of styrene, together with 10 mg of AIBN as radical initiator. The organic solution was then put in the aqueous phase drop wise. After 30 minutes of homogenization the emulsion was found to be stable and the temperature of the system was raised from 35°C to 80°C, so to start the polymerization. After 11 hours the reaction was quenched at 0°C. DLS and TRFS experiment were performed without further purification. DSC was performed on dry NP powder obtained by a precipitation of the aqueous emulsion in methanol. The precipitated was then dried in vacuum at room temperature overnight in order to avoid NPs syntherization. The powder was then characterized by Gel Permeation Chromatography: Mn = 112 kDa, Mw = 213 kDa and PDI =1.90.

For the preparation of the 60 nm in diameter NPs the concentration of sodium dodecylbenzene sulphate was increased to 15 g/L. All the other reactants, reaction and purification steps remained the same. Mn = 265 kDa, Mw = 394 kDa and PDI = 1.49.

2.2.1.2.1 Protocol for the preparation of reference bulk polymeric samples loaded with the molecular rotor AzeNaph1

Beside of the two PS nanoparticles batches, several bulk polymers loaded with AzeNaph1 were prepared in order to calibrate the measurement of T_g with TRPL. The bulk polymer sample used for AzeNaph1 TRFS calibration (see Figure 3.5 and 3.6) were synthesized following two different procedures:

i) by bulk polymerization (in the case of poly(*n*-butyl acrylate) and poly(ethyl acrylate));
ii) by solvent swelling of polymer chips (in the case of the sample prepared from commercial bulk polystyrene, Paraloid B72® and polypropylene).

For all bulk polymerization, 3 ml of monomer purified on activated alumina were used for the preparation of a 10^{-4} M solution of AzeNaph1 and 67 ppm of AIBN. The solution was

polymerized and annealed for three days at 80°C. The samples were bubble-free, transparent and with good optical quality.

(545±40) mg of industrial polymer chips were swelled with 1 ml of a $CHCl_3$ solution of AzeNaph1 10^{-4} M. The sample were put for two days at room temperature under the fume hood so to mildly remove the excess of $CHCl_3$. Lastly the sample were annealed at 80°C overnight.

2.2.1.3 Protocol for the preparation of poly(n-butyl acrylate)@polystyrene nanoparticles

The experimental procedure for the preparation of poly(*n*-butyl acrylate)@polystyrene nanoparticles is reported in reference 19, S. Bonetti et al. *Macromol. Rapid Commun.* **2016**, DOI: 10.1002/marc.201500625. All the related contents must be handled according to © 2016 WILEY-VCH Verlag GmbH & Co. KGaA, Weinheim.

2.2.1.3.1 Synthesis of poly(n-butyl acrylate) core

60 mL of Chromasolv water were put in a four necks flask and degassed with bubbling N2 at 35°C for an hour, under stirring.

Meanwhile, in a second flask, 3 ml (21 mmol) of BA were added to AOT and AIBN (quantities reported in Table 1). The feeding solution was degassed with freeze, pump and thaw (FPT) and added to the water with a flux of 3ml/h. The dripping was stopped after one hour and temperature was set at 70°C for three hours.

Table 1. Sample nomenclature and core synthesis conditions. Error AOT = $\pm$ 2.2•10^{-3} mmol, Error AIBN = $\pm$ 6.1 •10^{-3} mmol. After S. Bonetti et al. *Macromol. Rapid Commun.* **2016**, DOI: 10.1002/marc.201500625. © 2016 WILEY-VCH Verlag GmbH & Co. KGaA, Weinheim.

Core **Hyd. Diameter [nm]**	**PdI** [b]	**Initiator [mmol]**	**Surfactant [mmol]**
115.2	0.04	$4.23 \cdot 10^{-2}$	$1.24 \cdot 10^{-1}$

[a] DLS core size distribution is reported in Figure 2.2 dotted line.

[b] The polydispersity index measures the width of the particle size distribution and is defined as PdI=$(\sigma/\langle D \rangle)^2$, where σ is the standard deviation and <D> is the mean value of the hydrodynamic diameter.

2.2.1.3.2 Polystyrene cross-linked shell growth

During the polymerization of BA, a third flask was prepared with a solution of 9 ml (78 mmol) of STY, added with AIBN, AOT and DVB in the amounts reported in tab.2. The solution

was degassed via FPT and dripped into the pristine O/W emulsion at 3 ml/h. The reaction was allowed to proceed for 8 hours, then cooled to room temperature and homogenized for the next 8 hours.

Table 2. Hydrodynamic diameter and shell synthesis conditions. Error AOT = $\pm$ 2,2•10^{-3} mmol, Error AIBN = $\pm$ 6,1•10^{-3} mmol and Error DVB = $\pm$ 5,00•10^{-2} mmol. After S. Bonetti et al. *Macromol. Rapid Commun.* 2016, DOI: 10.1002/marc.201500625. © 2016 WILEY-VCH Verlag GmbH & Co. KGaA, Weinheim.

Core@shell Hyd. Diameter [nm] [a]	**PdI** [b]	**Initiator [mmol]**	**Surfactant [mmol]**	**Cross-linker [mmol]**
184.6	0.01	$1.79 \cdot 10^{-1}$	$5.46 \cdot 10^{-2}$	$8.30 \cdot 10^{-1}$

[a] DLS core@shell size distribution reported in Figure 2.2 continuous line.

[b] The polydispersity index measures the width of the particle size distribution and is defined as $PdI=(\sigma/\langle D\rangle)^2$, where σ is the standard deviation and $\langle D\rangle$ is the mean value of the hydrodynamic diameter.

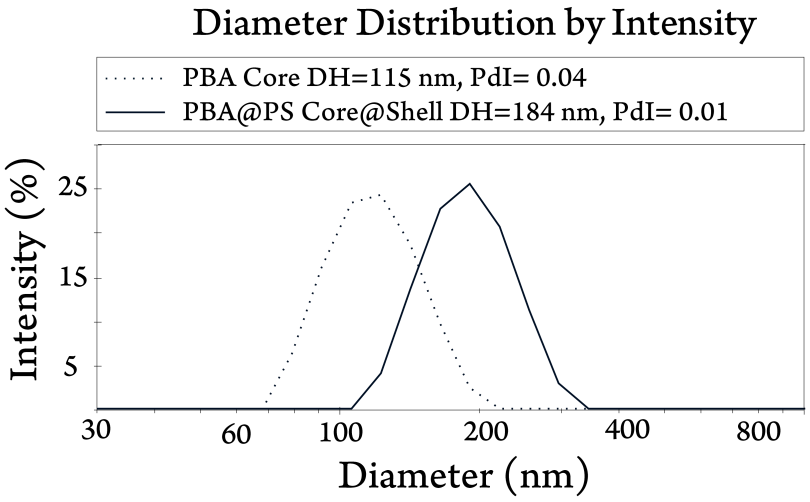

Figure 2.2: DLS diameter distributions by intensity for the PBA core (dotted line) and PBA@PS core@shell final nanoparticle (continuous line). After S. Bonetti et al. *Macromol. Rapid Commun.* 2016, DOI: 10.1002/marc.201500625. © 2016 WILEY-VCH Verlag GmbH & Co. KGaA, Weinheim.

Molecular weights and molecular weight distribution were determined using a WATERS 1515 equipped with a HPLC isocratic pump, WATERS 2414 refractive index detector and four Styragel columns (HR2, HR3, HR4 and HR5). GPC system has been calibrated with Polystyrene Sigma-Aldrich Standards. All measurements has been recorded in THF at 1.0 mL/min, 35°C.

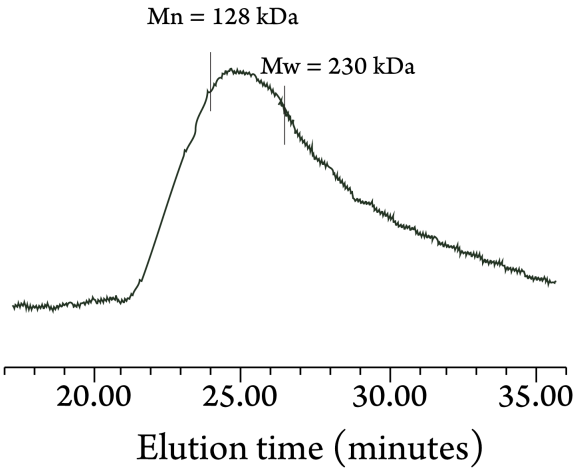

Figure 2.3: GPC chromatogram of PBA@PS core@shell nanoparticles. After S. Bonetti et al. *Macromol. Rapid Commun.* 2016, DOI: 10.1002/marc.201500625. © 2016 WILEY-VCH Verlag GmbH & Co. KGaA, Weinheim.

Typical molecular weights (polystyrene equivalent) of Mn=128 kDa, Mw=230 kDa and a polydispersity of 1.58 were calculated for core-shell NPs (Figure 2.3).

2.2.1.4 Protocols for the preparation liquid-core Nanocapsules

Liquid-core nanocapsules were prepared starting from *n*-hexadecane (HD) and methyl methacrylate (MMA) monomer in order to synthesize three different batches of nanocontainers: i) reference blank nanocapsules sample, ii) liquid-core nanocapsules loaded with TiO_2 nanocrystals and iii) sensitized photon up-conversion liquid-core nanoemitters. In the following sections the synthesis procedures are described in detail.

2.2.1.4.1 Hexadecane@poly(methyl methacrylate) Nanocapsules

This protocol is taken from the work of S. Khoee et al.[41] and further adapted modifying the purification steps to our purpose. 20 mmol MMA and 26 mmol of HD were mixed with 0.2 mmol of benzoyl peroxide as a radical initiator. This formulation was added to a solution of surfactants (150 mg of TWEEN 20 and 135 mg of sodium dodecyl sulphate) in 32 g of DI water. After being pre-emulsified under magnetic stirring at a rate of 1000 rpm for 30 min. Miniemulsification and homogenization were continued by ultrasonicating the mixture for 10 min at 30% amplitude. To avoid prepolymerization, the mixture was cooled in a water/ice bath during sonication. The obtained miniemulsion was poured into a single-necked reactor equipped with a magnetic stirrer, condenser, and inlet for nitrogen gas. Before starting the reaction, the reactor was purged with nitrogen for 40 min to remove oxygen. The reaction was carried out for 72 hours under a nitrogen atmosphere at 80°C and stirred at 700 rpm. The final latex was cooled down to room temperature for purification. Latex purification was firstly performed via a centrifugation in methanol for 60 minutes at 6000 rpm, in order to precipitate the polymerized nanocapsules. Secondly, for the removal of the superficially adsorbed HD, the latex has been centrifuged three times with a fresh hexane solution for 30 minutes at 6000 rpm. The final precipitated was then dried in vacuum (10^{-2}Torr) for further analysis. Typical molecular weight of Mn = 126 kDa, Mw = 218 kDa and polydispersity value of 1.70 were calculated for this synthesis by GPC.

2.2.1.4.2 Hexadecane@poly(methyl methacrylate) nanocapsules filled with TiO_2 Anatase nanocrystals

For the synthesis of the nanocapsules loaded with anatase TiO_2 nanocrystals 2ml of MMA and a dispersion of TiO_2 in 6 ml of HD were mixed with 51 mg of AIBN as a radical initiator. Synthesis procedure and purification steps follow from section 2.2.1.4.1.

2.2.1.4.3 Hexadecane@poly(methyl methacrylate) nanocapsules as sensitized up-conversion nanoemitters

In order to prepare Hexadecane@poly(methyl methacrylate) nanocapsules as sensitized up-conversion (SUC) nanoemitters, the synthesis protocol was changed in order to use a water-soluble radical initiator. In fact, as specified in section 4.5.1, it seems that the presence of an oil-soluble initiator within the droplets can be somehow detrimental regarding the ultimate efficiency of the energy transfer process involved in the SUC. Moreover, an azo water-soluble initiator was needed in order not to evolve oxygen during the initiator activation. Traces of oxygen (in the order of some %) can indeed inhibit the SUC process. In this regard we decided to use the water-soluble azo initiator 2,2'-Azobis(2-methylpropionamidine)dihydrochloride (Figure 2.4). All the solutions used in this reaction were degased via freeze-pump-thaw and stored under inert atmosphere (N_2 with O_2 concentration<0.1 ppm). The reaction was driven under nitrogen as well inside a glove box (O_2 concentration<0.1 ppm).

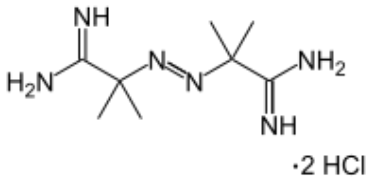

Figure 2.4: Structural formula of the water-soluble azo initiator 2,2'-Azobis(2-methylpropionamidine) dihydrochloride.

The formulation used for the synthesis of the nanoparticles is reported in table 3. The organic solution was made of 1.2 ml (4.08 mmol) of hexadecane solution containing the two dyes involved in the SUC process, namely Platinum octaethylporphyrin (10^{-4} M PtOEP) and 9,10-Diphenylanthracene (10^{-3} M DPA).

Table 3. Shell synthesis conditions for liquid-core HD@PMMA SUC nanoemitters.

Hexadecane [mmol]	**MMA [mmol]**	**Initiator [mmol]**	**Surfactant [mmol]**
4.08	3.10	$2.89 \cdot 10^{-2}$	$6.50 \cdot 10^{-2}$

The organic solution was added in 5 ml of an aqueous solution of water-soluble initiator (2,2'-Azobis(2-methylpropionamidine)dihydrochloride, $6.50 \cdot 10^{-2}$ mmol) and surfactant (3.75 g/L) under magnetic stirring at 700 rpm. The obtained emulsion was then homogenized for 1 hour under stirring (1500 rpm) at room temperature. After the homogenization the temperature was set at 80°C and let run for 24 hours under magnetic stirring at 700 rpm. The reaction was done under inert atmosphere (N_2, oxygen concentration < 0.1 ppm) in glove box. The pristine polymer nanocapsules dispersion was then characterized in terms of photophysics (lifetime and SUC parameters) and Dynamic Light Scattering. A small amount of emulsion was then diluted for SEM micrographics. Moreover, the emulsion was then precipitated and for further solid-state characterization. Firstly, 1 ml of emulsion was added in 1.2 ml of MeOH and centrifuged at 6000 rpm for 15 minutes. After this step a white precipitate appeared on the bottom of the vial. The precipitate was then rinsed with 2 ml of hexane and centrifuged at 6000 rpm for 15 minutes. The hexadecane rinse and centrifugation must be repeated twice (i.e. three hexadecane-stage overall). The final precipitate was then dried at room temperature in vacuum (10^{-2} Torr). The obtained dried powder was then characterized with DSC.

2.2.2 Solvent Evaporation from Emulsion Droplets

Polymer nanoparticles and nanocapsules are playing a pivotal role in different fields, ranging from basic research[42] to therapeutics[43], from energy conversion and storage[44] to organic electronics[45]. For applications in pharmacy and electronics the absence of impurities (i.e. toxic monomer, unreacted transfer agents, catalyst) in the final colloids is a severe request. Polymer nanoparticles obtained by solvent evaporation from emulsion droplets (SEED) – developed by G.W. Burton and C.P. O'Farrel in 1977[46] – have been found to fulfil this demand. SEED is indeed based on liquid-solid nucleation under confinement: preformed and purified polymers are dissolved in a good organic solvent and emulsified in an aqueous solution of stabilizer, thus forming a droplet emulsion. The organic solvent is then evaporated through the continuous aqueous phase, driving the polymer precipitation within the nanoparticles. Thanks to the absence of contaminants, SEED process is used for the preparation of biodegradable particles[47] and redox-responsive nanocapsules[48]. SEED main drawback lies in the fact that the colloidal stability of the emulsion is still the main issue when using emulsion droplets as templates for polymer nanoparticles preparation. The dimensional nonuniformity of the final SEED nanoparticles has been historically ascribed to coalescence between droplets and/or Ostwald ripening[49]. Dynamic light scattering (DLS) is regularly used at different stage of the SEED process to monitor the size of the scatterer. Unfortunately, the coalescence measured by DLS is questionable because phenomena with opposite effects on droplet/particle size cannot be easily decoupled. Particularly, the solvent evaporation in the SEED process leads indeed to a decrease in droplet/particle dimension whereas dimension can increase at the same time due to coalescence between droplets. Only in 2012 D. Schäffel et al.[50] developed a method for the in situ quantitative monitoring of coalescence based on Dual Colour Fluorescence Cross Correlation Spectroscopy (DC-FCCS), providing direct information about the extent of coalescence during the preparation of nanoparticles. They unambiguously show that coalescence does not play an important role in the preparation of polystyrene nanoparticles by SEED process and MiEP as well.

2.2.2.1 SEED protocol for the preparation of polystyrene nanoparticles loaded with ASB-158 molecular rotor to be analysed by Fluorescence Correlation Spectroscopy

For the preparation of the SEED formulation and FCS analysis, the procedure developed in Max Planck Institut für Polymerforschung was used[50] (see sketch in Figure 2.5). Particularly, 100 mg of Polystyrene were dissolved in 2.5 g toluene (4% w/W of solid content and 10^{-9}M of ASB158 molecular rotor) and added to 20 g of an aqueous solution of SDS (1 g/L). A macroemulsion was obtained by stirring the mixture at 1250 rpm for 1 h. The macroemulsion was sonicated using a Branson W450-D sonicator with a 1/2''-tip at 70% amplitude in a pulsed regime (30 s sonication, 10 s pause) under ice cooling. The obtained emulsions were then either directly analysed via FCS or transferred in a 50 mL reaction flask and stirred at 500 rpm and 40 °C for 12 h.

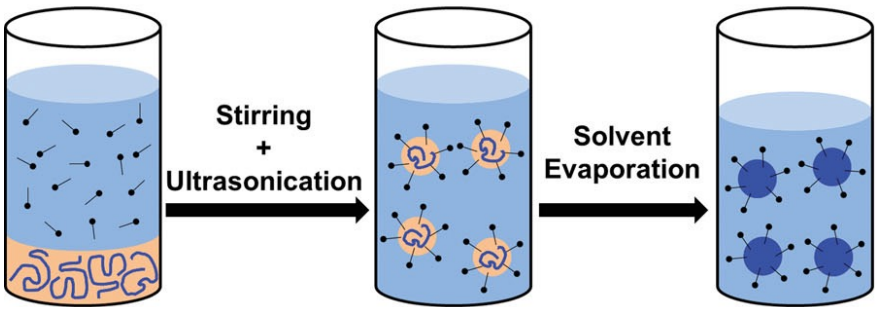

Figure 2.5: Sketch of the polystyrene nanoparticles preparation from solvent evaporation from emulsion droplets. Readapted from R.H. Staff et al. *Small* 2013, *9*, 3514-3522.

Fluorescence Correlation Spectroscopy measurements (see section 2.4.5 for detailed description) were conducted with a commercially available inverted microscope Olympus IX70 putting the sample into Attofluor chambers (see instrument details in section 2.3.5.3).

2.3 Characterization Methods

2.3.1 Time-Resolved Fluorescence Spectroscopy of molecular rotors, TRFS

Time-resolved measurements are widely used in fluorescence spectroscopy (also named time resolved fluorescence spectroscopy, TRFS), since they contain more information than the ones available from steady state data. Focusing the interest in polymer and colloid science, TRFS of suitable fluorescent probes gives a direct and fast access to the polymer aggregation states under various experimental conditions[51]. In 1980 K.Y. Law[52] showed that polymer aggregation state can be monitored – without need for chemical functionalization and

covalent bonding - by using molecular rotors. Molecular rotors are a class of donor-acceptor organic fluorophores, where the electron rich fraction is connected by a sigma C-C bond to the electron poor fraction. The rotation and banding of the two fractions around the sigma bond gives the molecule a high degree intramolecular rotational freedom. This feature strongly affects the emission intensity and lifetime of molecular rotor, strongly depending on local viscosity[53]. For this reason molecular rotors were found a good local probe for the local aggregation state in different experimental conditions[54]. For instance rotors are used to monitor bulk polymerization dynamics [55] as well as aggregation of amyloid fibres in biomedical assays[56].

In this manuscript the use of TRFS of specifically designed molecular rotors as a fast and versatile method for monitoring bulk and nanoscale polymer processes is reported. Particularly, the fluorescence lifetime of the rotors is a sensitive gauge for detecting T_g in bulk polymers as well as in EP nanoparticles (sections 3.2 and 3.3) and monitoring SEED process when coupled with Fluorescence Correlation Spectroscopy (section 2.4.6 and Chapter 6).

2.3.1.1 General meaning of the Lifetime

Prior to further discussion on lifetime measurements, understanding of the meaning of the lifetime τ is mandatory. When a sample containing a fluorophore is excited with an infinitely sharp (δ-function) laser light, an initial population (n_0) of fluorophores in the excited state is obtained.

The excited-state population decays with a rate ($\Gamma + k_{nr}$) according to

$$\frac{dn(t)}{dt} = \left(\Gamma + k_{nr}\right)n(t) \qquad (1)$$

Where $n(t)$ is the number of excited molecules at time t following excitation. Γ is the emissive rate and k_{nr} is the non-radiative decay rate. Emission is a random event and each excited fluorophore has the same probability of emitting in a given period of time. This results in an exponential decay of the excited state population, $n(t) = n_0 \exp(-t/\tau)$.

The direct physical observable in a fluorescent experiment is not the number of molecules $n(t)$, but rather the fluorescent intensity. The fluorescent intensity is proportional to $n(t)$ and can thus be written in terms of the time dependent intensity $I(t)$. Integration of eq. (1), with the intensity substituting the numbers of molecules, yields to the expression for a single exponential decay:

$$I(t) = I_0 \exp(-t/\tau) \qquad (2)$$

where I_0 is the intesity at time 0. The lifetime τ is the inverse of the total decay rate, $\tau = (\Gamma + k_{nr})^{-1}$. The fluorescent lifetime can be determined from the slope of the plot $\mathrm{Log}I(t)$ versus t and fitting the data to assumed decay models (single exponential decay or multiexponential decay).

The lifetime is the average amount of time a fluorophore remains in the excited state following excitation. This can be seen by calculating the average time in the excited state $\langle t \rangle$. This value is obtained by averaging t over intensity decay of the fluorophore:

$$\tau = (\Gamma + k_{nr})^{-1} = \frac{\int_0^\infty tI(t)dt}{\int_0^\infty I(t)dt} = \frac{\int_0^\infty t\exp(-t/\tau)dt}{\int_0^\infty \exp(-t/\tau)dt} = \langle t \rangle \qquad (3)$$

Lifetime is thus a statistical average and fluorophore emit randomly throughout the decay.

2.3.1.2 Molecular rotors lifetime, Förster-Hoffmann model

Molecular rotors are fluorescent molecules able to form twisted states through the rotation of one segment of the structure with respect to the rest of the molecule. Intramolecular rotation is strongly dependent on the environment (polarity, hydrogen bond formation, isomerization and steric hindrance)[57].

Of highest importance for our aim is steric hindrance, because it links the solvent's microviscosity to the formation rate of twisted intramolecular charge transfer (TICT) states, which, in turn, determines the lifetime of the process[58]. For this reason, molecular rotors have found a wide range of applications as fluorescent sensors of microviscosity and solvent free volume[59], beyond the spatial and temporal resolution typical of mechanical devices[60].

Such a microviscosity-dependent lifetime is described by Förster-Hoffmann equation[61]:

$$\mathrm{Log}\tau = C + x\mathrm{Log}\eta \qquad (4)$$

Where τ is the lifetime, η is solvent viscosity, x is a dye-dependent constant and C is a concentration and temperature constant. An example is given in Fig. 2.6[62].

Together with G. Vaccaro et al.[17], we developed a FCS procedure for the use of TRFS of a specifically designed molecular rotor as a method for monitoring of the self-assembly of *block* copolymers in solution into core-corona micelles. Particularly the sensitivity to the molar fraction of disorganized *vs.* self-assembled copolymer chains of the molecular rotor was

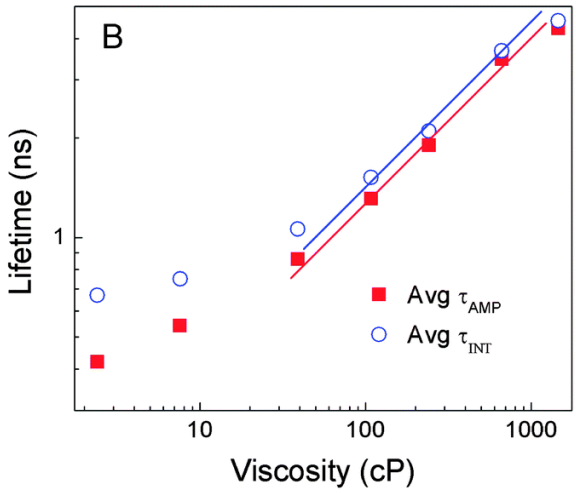

Figure 2.6: Lifetime behaviour of Bodipy homopolymer in an ethanol-glycerol mixture. Left extreme is pure ethanol ($\tau = 0.34$ ns, $\eta = 1.2$ cP), right extreme is pure glycerol ($\tau = 4.30$ ns, $\eta = 1457$ cP). After S. Rau et al. *Phys. Chem. Chem. Phys.* 2014, *16*, 27037. Copyright © Royal Society of Chemistry.

reported. On top we showed that the core of the core-corona micelles is below its T_g temperature, irrespective to its nanometric diameter.

Several independent works suggest the robustness of molecular rotors as local probes in polymer science. Indeed in Chapter 3 we describe their usage as a T_g probe for glass transition in bulk and nano polymer materials, while in Chapter 6 we performed e test experiment about the usage of molecular rotor as microviscosity-sensitive fluorescent tracers in Fluorescence Correlation Spectroscopy.

2.3.2 Dynamic Light Scattering

It is well known that when laser photons collide with colloid particles with solvodynamic dimension far less than incident wavelength undergoing Brownian motion, the scattering intensity fluctuates over time. Within this intensity fluctuation, information is contained about the time scale of movement of the scatterers[63]. Quantitative information about the scatterers size is gained through the analysis of the field autocorrelation function $g^1(q,\tau)$ and of the measured intensity autocorrelation function $g^2(q,\tau)$. q is the scattered wave vector and τ is the delay time.

$$g^2(q,\tau) = 1 + \beta[g^1(q,\tau)]^2$$

$g^2(q,\tau)$ is measured through the electronic hardware and software analysis of the photon statistics by Cumulants fit. Then, $g^1(q,\tau)$ can be calculated from through Siegert's equation[64]:

$$g^1(q,\tau) = e^{-\partial q^2 \tau}$$

where β is an experimental coherence correction factor depending on alignment and geometry of the Malvern Instrument Nano Series Zetasizer optical unit (section 2.3.2.2).
For each particle size population, $g^1(q,\tau)$ can be expressed as a single exponential decay:
where ∂ is the diffusion coefficient of the colloid, which is related to the solvodynamic diameter D of the particles and to the dispersant viscosity n via Stokes-Einstein equation.

$$\partial = \frac{k_B T}{3\pi n D}$$

2.3.2.1 DLS Data Analysis

Dynamic Light Scattering solvodynamic diameters are fitted with a lognormal distribution: a continuous probability distribution of a random variable whose logarithm is normally distributed. It can be expressed as:

$$f(D,\langle D\rangle,\sigma) = \frac{1}{\sqrt{2\pi}D\sigma} e^{\left[-\left(\frac{LogD - Log\langle D\rangle}{\sigma}\right)^2\right]}, \qquad \mathrm{D} > 0$$

where 〈D〉 is the mean value of the variable and s is the standard deviation (i.e. in this case is the solvodynamic diameter). PDI (or PdI) is the polydispersity index, which measures the width of the particle size distribution. Polydispersity can be expressed as:

$$PDI = \left(\frac{\sigma}{\langle D\rangle}\right)^2$$

where σ is the standard deviation and <D> is the mean value of the variable D.

2.3.2.2 DLS Instrument

Dynamic Light Scattering measurements were performed at 25°C on a Malvern Instruments Nano Series Zetasizer optical unit (Continuous Wave 4 mW He-Ne class 1 internal laser operating at 632.8 nm, measurement angles at 13° and 175° and Avalanche photodiode detector with Q.E.>50% at 633 nm).

2.3.3 ^{1}H-TD-NMR

Time-Domain NMR (TD-NMR) is an alternative to classical NMR, widely used for the structural characterization of chemical compounds. Since TD-NMR works at low magnetic fields (typically ~0.5 T) with permanent magnets, the system is far less expensive but much simpler and easier-to-cooled (i.e. without cryogenic gasses) in comparison to traditional ones. On the other hand, the low magnetic field leads to a resolution insufficient for obtaining Fourier-Transform spectra.

TD-NMR obtains information from the analysis of the dependence of signal intensity on time (i.e. from the raw free induction decay of the induced magnetization).

2.3.3.1 Magic Sandwich Echo sequence, MSE

In 2006 K. Saalwächter and co-workers proposed an improved proton NMR method for the real-time measurement of the hard/soft ratio, the crystallinity and the mobile-fraction dynamics in polymers[65]. Their MSE-refocused FID traces with CPMG-detected long-time decay (Fig.2.2) allows the simultaneous measurement of both the NMR crystallinity and the relaxation function for the mobile fraction, together with solving the receiver dead time problem. A significant part of the rigid fraction signal, usually decaying within 20 ms, vanishes during the receiver dead time (~ 30 ms). The overall decay of the mobile signal, far less demanding from a technical point of view, is monitored by a Carr-Purcell-Meiboom-Gills pulse train (Fig.2.2).

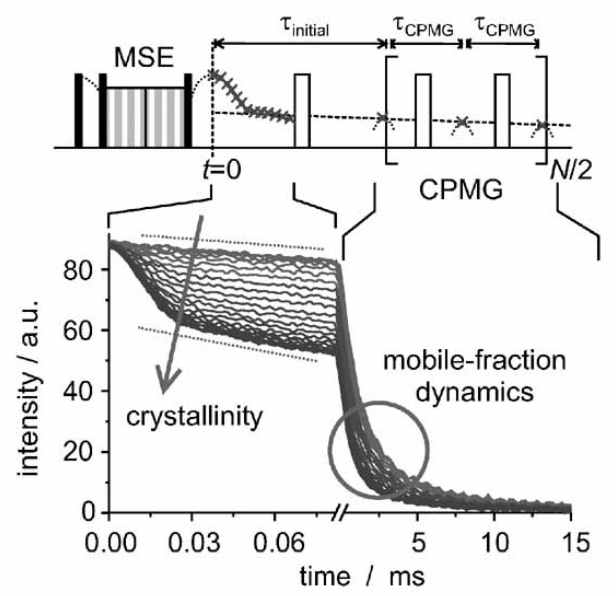

Figure 2.7: MSE-CPMG pulsed sequence (up) monitoring of the Isothermal crystallization (down) of syndiotactic Polypropylene. After A. Maus, C. Hertlein, K. Saalwächter, *Macromol. Chem. Phys.* 2006, *207*, 1150-1158. Copyright © John Wiley & Sons, Inc.

Experimentally, the FID is recorded as function of time (Fig.2.6) and fitted with the function below.

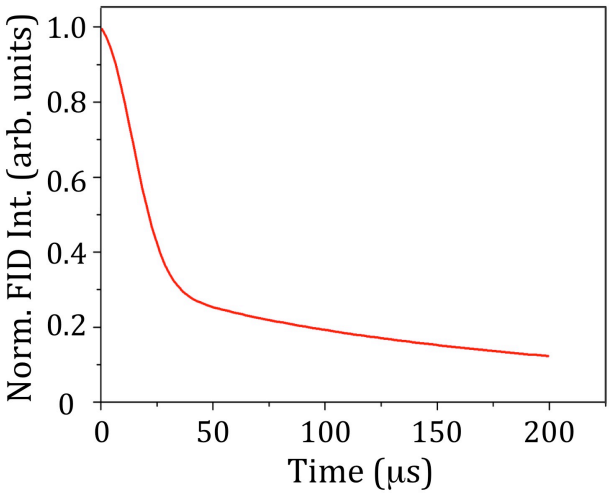

Figure 2.8: Representative normalized FID curve recorded with MSE-CPMG sequence.

$$f(t) = Rexp\left[-\left(\frac{t}{T_{2R}}\right)^2\right] + (1-R)exp\left[-\left(\frac{t}{T_{2M}}\right)^{na}\right]$$

The function *f(t)* is a linear combination of a Gaussian decay fitting the proton decay associated with nuclei embedded in a low mobility domain and of a stretched exponential decay associated to the behaviour of protons in a high mobility domain.

2.3.3.2 ^{1}H-TD-NMR Instrument

TD-^{1}H-NMR measurements were performed on a 0.5 T Bruker Minispec, a low resolution NMR spectrometer with proton Larmor frequency of 19.9 MHz, equipped with a static probe and a BVT3000 heater temperature control unit working with nitrogen gas. The temperature was calibrated using an external thermometer with an accuracy of 1 K. The precision is 0.1 K and the temperature is stable within that range during the measurement. The samples were left around ten minutes in the magnet to ensure thermal equilibration before starting the experiments.

2.3.4 Atomic Force Microscopy, AFM

AFM allows the imaging of the topography of conducting and insulating (i.e. not suitable for scanning tunnelling microscope) surfaces, in some cases with atomic resolution[66]. In the pioneering work of G. Binning, C.F. Quate and C. Gerber published in 1986 the main outcome was the possibility of imaging insulators surface *in air* with a lateral resolution of 30 Å and a vertical resolution less than 1 Å. Such an ability of AFM to generate image contrast, thanks to its unique contact probe methodology, and to work even in liquid environment[67] has been driving its popularity as an established method in cell biology[68], drug deliver[69], food science[70] and polymer science[71].

In the next chapter we would like to point out that AFM is not only a tool to image the topography of solid surfaces at high resolution but it can also be used to measure force-versus-distance curves, providing information on local material properties (i.e. elasticity, hardness, Hamaker constant, adhesion and surface charge densities). For this reason the measurement of force curves has become essential in the over mentioned different fields of research, form surface science to materials engineering and biology.

2.3.4.1 Force spectroscopy

This chapter was inspired from the extensive review of H.-J. Butt, D. Cappella and M. Kappl in *Surf. Sci. Rep.* **2005**, *59*, 1-152.

During an AFM topography experiment (Fig. 1) the sample is scanned in the plane (i.e. x, y directions) by a tip, mounted to a cantilever spring. The force between the tip and the sample is measured by monitoring the deflection of the cantilever during the scanning. The topography of the sample is obtained by plotting the deflection of the cantilever versus its (x, y) position on the sample. Alternatively, it is possible to plot the height position (i.e. z direction) of the translation stage. This height is controlled by the feedback loop, which maintains a constant force between tip and sample.

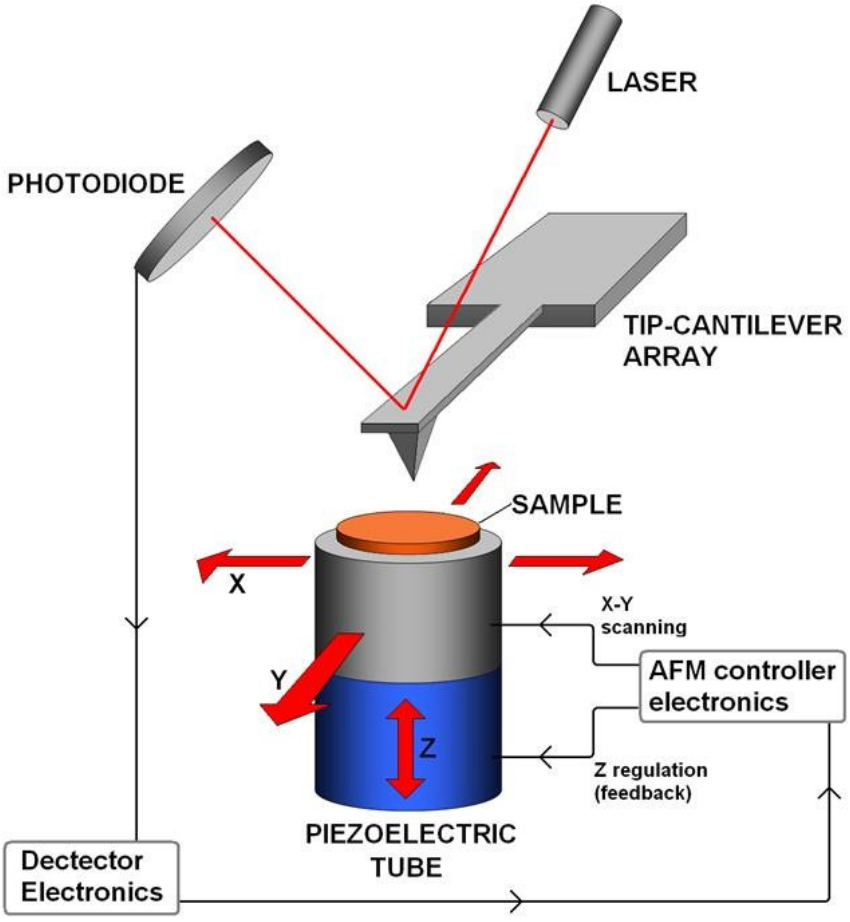

Figure 2.9: Schematic of an Atomic Force Microscope. After pharm.virginia.edu. Copyright © Rector and Board of Visitors.

Image contrast arises because the force between the tip and sample is a function of both tip–sample separation and of the of tip and sample composition (i.e. the materials they are

made of). To date, H.-J. Butt et al.[66a] reported that image contrast is mostly obtained from the so-called Born repulsion triggered by the very short range repulsion, which occurs when the electron orbitals of tip and sample overlap. However, further interactions between tip and sample can be used to characterize the properties of the sample, of the tip, or of the medium in between. These measurements are usually known as ''force measurements''. In an AFM force measurement the tip attached to a cantilever spring is moved towards the sample in normal direction (Figure 2.10). Vertical position of the tip and deflection of the cantilever are recorded and converted to force-versus-distance curves, briefly called ''force curves''.

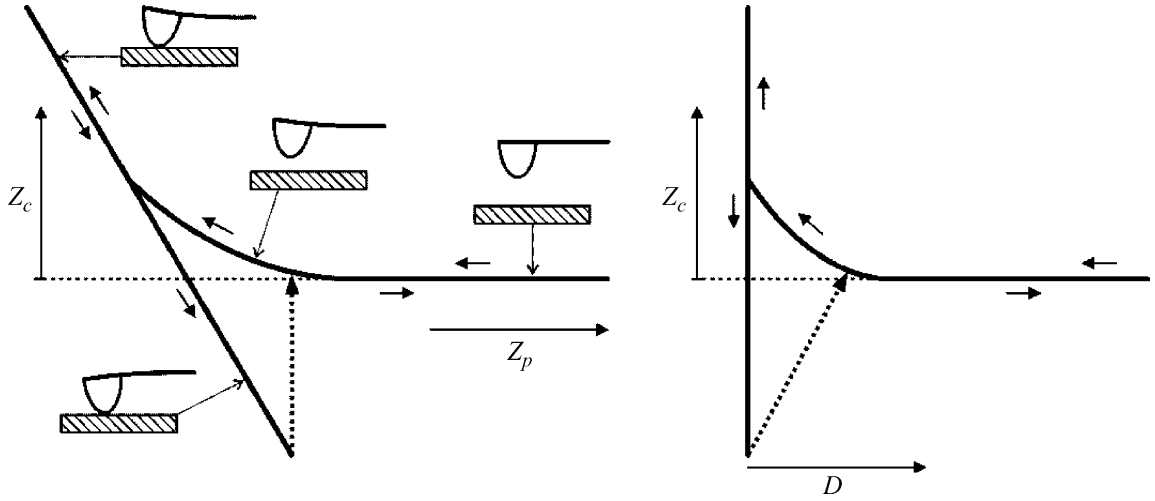

Figure 2.10: Schematic of a typical cantilever deflection-vs.-piezo height (Zc-vs.-Zp) curve (left) and corresponding Zc-vs.-D plot, with D = Zc + Zp during a force measurement. After H.-J. Butt et al. / Surface Science Reports 59 (2005) 1–152. Copyright © Elsevier B.V.

In a force measurement the sample is moved up and down by applying a voltage to the piezoelectric translator, onto which the sample is mounted, while measuring the cantilever deflection (Figure 2.10). The sample is one of the two interacting solid surfaces. The other solid surface is usually a microfabricated tip.

The result of a force measurement is a measure of the cantilever deflection, *Zc*, versus position of the piezo, *Zp*, normal to the surface. To obtain a force-versus-distance curve, *Zc* and *Zp* have to be converted into force and distance. The force F is obtained by multiplying the deflection of the cantilever with its spring constant *kc*: $F = kcZc$. The tip–sample separation D is calculated by adding the deflection to the position: $D = Zp + Zc$. *D* is now called tip–sample separation ''distance''.

The deflection of the cantilever is usually measured using the optical lever technique[72]. A laser diode beam is focused onto the end of the cantilever and the position of the reflected

beam is monitored by a position sensitive detector (PSD). To enhance the reflectivity of the cantilever, its backside is often covered with a thin gold layer. When a force is applied to the probe, the cantilever bends and the reflected light-beam moves through an angle equal to twice the change of the end slope *dZc/dX*.

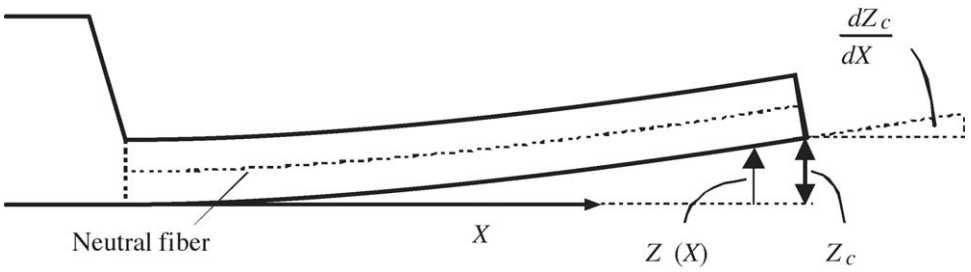

Figure 2.11: Schematic side view of a cantilever with a force at its end. X is the horizontal coordinate originating at the basis of the cantilever, Z(X) is the cantilever deflection at a the position X, Zc being the cantilever deflection at its end. After H.-J. Butt et al. / Surface Science Reports 59 (2005) 1–152. Copyright © Elsevier B.V.

For a cantilever with a rectangular cross-section of width w, length L, and thickness t_c, the change *dZc/dX* (Figure 2.11) is given by

$$\frac{\mathrm{d}Zc}{\mathrm{d}X} = 6\frac{FL^2}{Ewt_c^3}$$

Here, E is the Young's modulus of the cantilever material and F is the force applied to the end of the cantilever in normal direction. The signal detected with the optical lever technique is proportional to the end slope (*dZc/dX*) of the cantilever. The deflection of the cantilever is given by

$$Z_c = 4\frac{FL^3}{Ewt_c^3} = \frac{2}{3}L\frac{\mathrm{d}Z_c}{\mathrm{d}X}$$

Hence, the deflection is proportional to the signal. Anyway, it is worth noticing that that these relations only hold under equilibrium condition.

The direct physical observables measured during a force measurement are the photodiode current IPSD versus height position of the piezoelectric translator *Zp*. To obtain a force-versus-distance curve, IPSD and *Zp* have to be converted into force and distance[73]. Therefore sensitivity and zero distance need to be known. Both parameters must be inferred from the force curve itself and not through an independent method. The linear part of the ''contact regime'' in Figure 2.10 is assumed to be zero distance and its slope is the sensitivity. The

method is usually valid and reliable. However, in the case of highly deformable surfaces or layered structures, where strong repulsive forces may lead to false interpretations[74].

The force measurement AFM procedure has reached a state of maturity, since the basic mathematics describing the cantilever-tip-sample interaction has been developed.

2.3.4.2 AFM Instrument

AFM imaging and force spectroscopy were carried out with a JPK NanoWizard (JPK Instruments, Berlin, Germany) with closed loop scanner using silicon cantilevers (Olympus, Tokyo, Japan). Spring constants of cantilevers were determined using the thermal noise method.

2.3.5 Fluorescence Correlation Spectroscopy, FCS

In the early 1970s Fluorescence correlation spectroscopy was developed by D. Madge, E.L. Elson and W.W. Webb[75] together with M. Ehrenberg and R. Rigler[76], with the aim of drawing information about kinetic coefficients from the way a molecular system relaxes back to equilibrium after a perturbation[77]. As nicely described in Petra Schwille's 2001 review[81], in FCS the perturbation is not induced by the experimentalist (as in other relaxation techniques), but is taken of minute spontaneous temporal fluorescence intensity fluctuations due to diffusive dynamics of fluorescent species (small molecules, macromolecules, nanoparticles)[78], always occurring on a microscopic scale at room temperature.

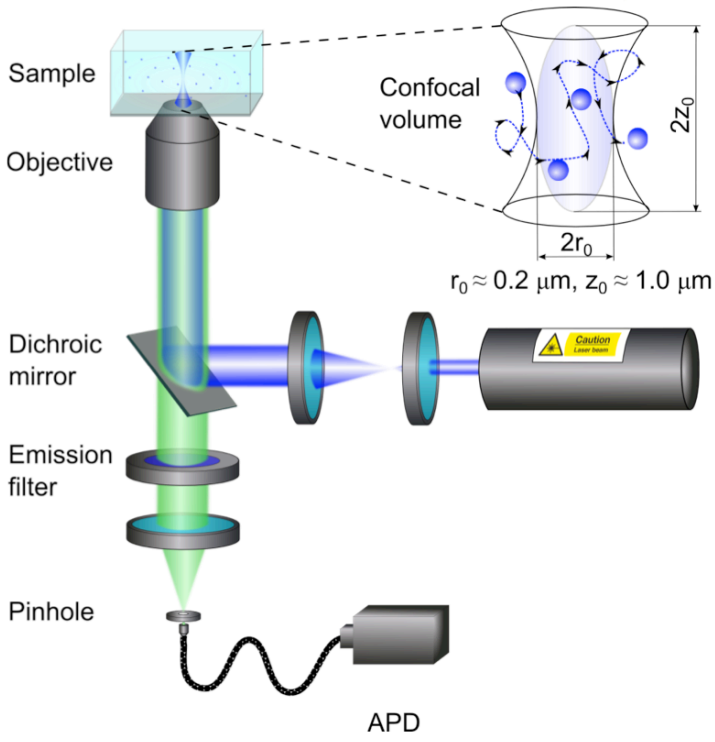

Figure 2.12: Fluorescence Correlation Spectroscopy confocal setup. Courtesy of Dr. Kaloian Koynov, Max Planck Institut für Polymerforschung.

Such intensity fluctuations can be better resolved the smaller the system under observation is, ideally on the level of single molecule. Using laser sources and ultrasensitive avalanche photodiode detectors (APD), fluorescence based detection and analysis on single molecule scale has been accomplished[79]. The first setup allowing the spatial restriction of the system under investigation to very small molecular numbers scale (i.e. close to the single molecule regime) was developed by R. Riegler et al.[80] and is based on a confocal scheme (in Figure 2.12). A small probing volume (an ellipsoid in the *f*L range, named confocal volume) is achieved by focusing the laser beam down to the resolution limit with an objective with high numerical aperture (usually N.A.>0.9). Fluorescence is thus excited only within the confocal volume, because only the molecules dwelling in this focal spot contribute to the measured signal. Only photons coming from the confocal volume are collected onto the photodiode via a pinhole positioned in the image plane, allowing the axial resolution modulation.

2.3.5.1 Theoretical framework of fluctuation analysis

An up-to-date comprehensive review about FCS was given by K. Koynov and H.-J Butt in 2013[81]. The temporal fluctuations in the detected fluorescence intensity $\delta I(t)$ (Figure 2.13-a), caused by the diffusion of fluorescent species through the confocal volume, are recorded and analysed by an autocorrelation function:

$$G(\tau) = 1 + \frac{\langle \delta I(t) I(t+\tau) \rangle}{\langle \delta I(t) \rangle^2} \quad (1)$$

In case of fluorescence fluctuations caused only by 3D diffusion of identical fluorescent species in and out the confocal volume, the autocorrelation function has the form (Figure 2.13-b):

$$G(\tau) = 1 + \frac{1}{N}\left(1 + \frac{\tau}{\tau_D}\right)\left(1 + \frac{\tau}{S\tau_D}\right)^{-\frac{1}{2}} \quad (2)$$

Here, N is the average number of fluorescent species in the observation volume and $S = z_0/r_0$ is the axial to radial dimensions of the confocal volume. The diffusion time τ_D of the species is related to their diffusion coefficient D, $\tau_D = {r_0}^2/4D$.

In a typical experiment the measured auto-correlation function (eqn. 1) is fitted with the analytical expression (eqn. 2), thus obtaining the diffusion time, the diffusion coefficient and the concentration of the fluorescent species. On top, if the measurement are performed in a diluted system, the hydrodynamic radius of the species is related to their diffusion coefficient through the Stokes-Einstein relation: $R_H = k_B T/6\pi\eta D$ (k_B is Boltzmann's constant, T the temperature and η the solution viscosity).

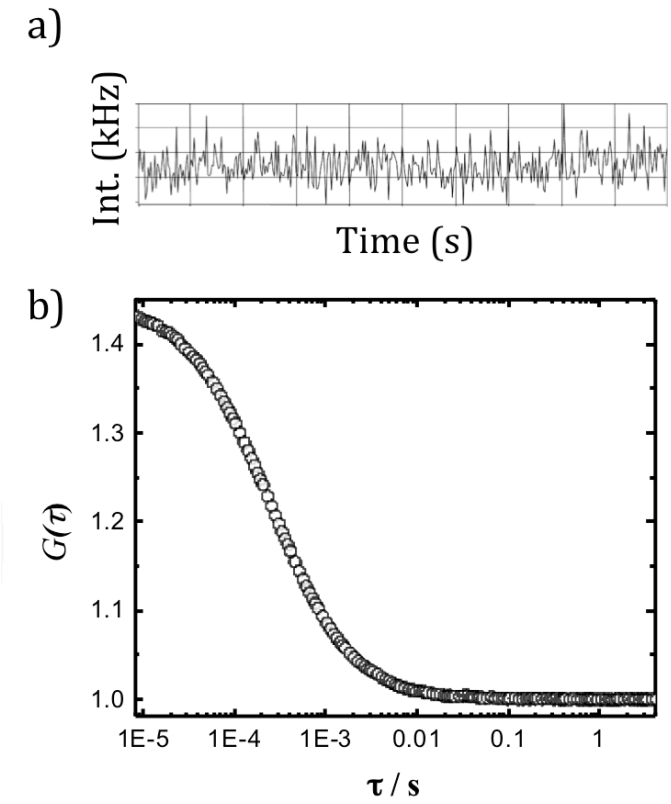

Figure 2.13: a) Temporal fluorescence intensity fluctuations due to scatterers Brownian diffusion in the confocal volume. b) Autocorrelation curve obtained from the correlation analysis of I(t).

Since r_0 depends strongly on the geometrical characterisics of the optical setup and the refractive index of the sampe media, a suitable calibration is performed by measuring the diffusion time of a tracer with known diffusion coefficient, in solution with refractive index similar to that of the sample media.

2.3.5.2 Coupling FCS with TRFS of a tailored molecular rotor

In the recent years, FCS has emerged as a powerful method for investigating the diffusion of fluorescent small molecules, macromolecules or nanoparticles in various environments[82]. If the application field of FCS started from biology[83], nowadays it is a well-established tool in polymer[84] and colloid science[85] as well. Particularly FCS allows the study of surface diffusion of adsorbed polymers[86], of tracer diffusion in in undiluted polymer solutions[87], cross-linked networks[88] and polymer melts[89]. Moreover the formation of amphiphilic block copolymer micelles and vesicles and their interaction with small molecules or nanoparticles was investigated[90]. FCS is then a powerful tool for the quantitative characterization of molecular transport at different length scales, as well as for the analysis of effective viscosity of the medium with micrometre resolution.

Notwithstanding, particularly in the field of submicrometric colloids, FCS still lacks of the ability of "looking inside" the particle, giving thus direct feedback of the polymer chains aggregation within the particle (i.e. solvent residuals in SEED process, local viscosity kinetic in MiEP, hardness of lipophilic core in amphphilic block copolymer micelles etc.). In order to shed new light on this topic, the direct coupling of FCS and time-resolved fluorescence spectroscopy of a tailored rotor, developed in collaboration with Dr. Kaloian Koynov at the Department of physics at interfaces at Max Planck Institute for Polymer Research in Mainz (Germany), is here described.

The so-called time-resolved FCS (i.e. the combination of time-resolved fluorescence detection with FCS) has been already described in literature. D.C. Lamb et al.[91] reported the time-gating of the fluorescent signal in the nanosecond range for suppressing the light scattering or the fluorescence of a fast fluorescence decay dye respect to a second dye with longer fluorescence decay. Indeed all photons arriving outside the time-gate were ignored and not included in the analysis. This idea of setting a time-gate for the selective suppression of unwanted signal in ultrasensitive fluorescence and luminescence detection is reported in literature by several authors[92]. This is the time-resolved equivalent of the use of spectral filters for blocking unwanted signals outside the spectral window of interest.

Böhmer et al.[93] reported a strategy based on the use of lifetime information of the measured fluorescence signal for extracting two independent FCS traces from the measured signal, without discarding any of the detected photons. In this way the complete time resolved spectrum is recorded and deconvoluted into the different contributions from the various emitting species.

The ASB158 molecular rotor in Figure 2.14 was used either as a microviscosity-sensitive or as a fluorescent tracer within the FCS experiment. We already demonstrated TRFS of molecular rotors is a suitable method to probe the relevant features of the self-assembly of amphiphilic block copolymers in aqueous solution[17] (i.e. minimum amount of water required to obtain complete self-assembly, minimum equilibration time of the dispersion after changing the composition, aggregation state of the nanoparticle core).

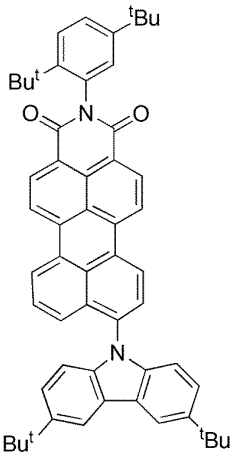

Figure 2.14: ASB158 Molecular Rotor used as FCS tracer in this work. Courtesy of Prof. Dr. Luca Beverina, UniMIB.

On top this kind of analysis is simple, quantitative and non-destructive.

The aim is now coupling in situ the FCS ability in monitoring nanostructure dimensions with the TRFS of a rotor, enabling the characterization of the local mobility within the nanostructure. Finally these quantity can be measured in the same sample, at the same time and in the same *f*L focal volume.

2.3.5.3 FCS Instrument

In this work, Fluorescence Correlation Spectroscopy measurements were conducted with a commercially available inverted microscope Olympus IX70, combined with a FluoView300 confocal laser scanning setup (Olympus) and a PicoQuant FCS upgrade with single photon counting avalanche photodiode τ-SPAD (PicoQuant). A water immersion objective (Olympus UPLSAPO 60XW 60x/1.2) was used. The molecular rotor was excited with a pulsed diode laser (λ = 470 nm, Power ≈ 0.3 mW and pulse length < 90 ps). Size and shape of the observation volumes were calculated by reference measurements conducted using Alexa Fluor 488® dye. This dye is appropriately excitable with the laser used and it has a well-known diffusion coefficients[94]. Throughout all measurements, an Attofluor chamber (25 mm round coverslip holder with fluorinated O-ring seal design and standard 35 mm diameter stage holder with 0.5 mm base dimension allowing clearance for the objective when focusing) was used as sample cell. Typical penetration depths used during the experiments were 5 μm from the coverslip/emulsion interphase, in order to minimize focal volume shape distortions.

3 Retention of Bulk Glass-Transition Temperature in Polystyrene nanoparticles

3.1 Introduction

"*The origins of the glass transition, despite its ubiquity in technology and everyday life, still remain mysterious*". Shin Kawana and Richard A.L. Jones chose this opening sentence for their 2001 article on Phys. Rev. E.[95]

It has been cited more than 240 times.

Large shifts in the glass transition temperature respect to bulk values were firstly observed in small systems, such as thin films, either supported on substrates[96] or freely standing[97], or glass-forming liquids confined in nanoscopic pores[98] in the 1990s. When polymer chains are confined in geometries with size in the order of tens of nanometres (i.e. very close to the bulk radius of gyration of polymer chains), the fraction of chains in contact with the surface increases, leading to a grater contribution of size and interfacial effects. Size effects are expected to occur when the length scale of the confining dimension (i.e. thickness in thin films) and the length scale governing T_g (i.e. a cooperatively rearranging region) coincide[99]. Interfacial effects dominate when the ratio of interfacial surface area to volume is increased[100]. This interplay between size and interfacial effects drives to controversial observations including either substantial increases[101] or decreases[102] in T_g.

Measurement of glass transition temperature (T_g) with differential scanning calorimetry (DSC) is well established in bulk materials but becomes elusive in nanostructured systems. DSC - patent by E.S. Watson and M.J. O'Neill in 1962[103] - is a thermo analytical technique where the difference in the amount of heat required to increase/decrease the temperature of a sample and reference is measured as a function of temperature. Both the sample and reference are maintained at the same temperature throughout the experiment[104]. Since then DSC has been widely used for the determination of thermal transitions (i.e. melting point, glass transition temperature, degradation temperature etc.) in polymeric materials[105].

In 2011 R.D. Priestley et al.[13] decided to move from two-dimensional spatial confinement in polymer thin films to three-dimensional confinement on polystyrene nanoparticles. They investigated the T_g of polymer nanoparticles under soft and hard confinement directly in aqueous emulsion via modulated differential scanning calorimetry (M-DSC). Conventional DSC becomes elusive in nanostructured systems, since it measures "only" the sum or average value of the heat flow from overlapping processes. The two overlapping processes in this case are the polystyrene glass transition ($T_{g,bulk}$∼90÷110°C) and water evaporation (T_{evap}∼100°C) where the NPs are dispersed. This makes simultaneous, quantitative and separate analysis of the individual reversible nanoparticle softening due to T_g and the irreversible water evaporation thermal processes impossible to detect and decouple with conventional DSC. On the other hand M-DSC uses two simultaneous heating rates: i) a linear heating rate providing information similar to standard DSC and ii) a sinusoidal or modulated heating rate that permits the simultaneous measurement of the sample's heat capacity. Among the pioneers in this field, in 1993 P.S. Gill, S.R. Sauerbrunn and M. Reading from TA instruments defined M-DSC as an "*extension to conventional DSC which provides information about the reversing and nonreversing characteristic of thermal events, as well as the ability to directly measure heat capacity"*[106].

It must be noticed that TA Instruments (producer of the instrument used by R.D. Priestley et al. in reference 13) stresses that "*M-DSC measures* neither *reversibility* nor *non-reversibility of transitions. The term "*reversing*" was chosen because true heat capacity (heat associated with increasing or decreasing a materials temperature) is* reversible*. However, a heat capacity change during a transition is almost never reversible. While a transition in the reversing signal is associated with a heat capacity change, it* may *or* may not *be reversible*"[107]. In our opinion this considerations could open some reliability issues about the general meaning on the study proposed by Priestley et al[13].

Moreover, Martin Tress et al.[15] showed in 2013 that glassy dynamics can be detected even in condensed isolated poly(2-vinylpiridine) (P2VP) polymer chains. This message collides with the picture proposed by Priestley et al.[13], giving an idea of how contradictory can be the results in this field of T_g at the nanoscale. The procedure proposed by Tress et al.[15] is based on the use of Broadband Dielectric Spectroscopy (BDS) combined with a nanostructured electrode arrangement enabling the measurement of samples without a continuous surface coverage. Hence, for the first time, the dynamic glass transition (i.e. the glass transition measured in terms of α-relaxation with BSD[108]) of condensed isolated polymer chains was directly measured and found to be bulk-like. Measurements show that this relaxation process

is still present in samples containing only isolated condensed polymer chains and similar semi-isolated agglomerates consisting of ~5 to 10 chains (estimation based on AFM measurements of condensed coil, on the molecular weight and bulk density).

In addition, these results and considerations completely agree with the length scale on which the dynamic glass transition was to be expected according to E. Fischer et al. in 1992[16].

Standing on this state of the art overview, the main issue is clear: even if results are contradictory, the scientific community is still thinking on how and to what extent the properties of polymer are changed at the nanoscale?

In order to give an original answer to this question, a method based on the TRFS of a tailored molecular rotor for the measurement of glass transition temperature is proposed. We decided to calibrate this method with standard DSC, in order to have an easy-to-replicate and robust calibration standard. Moreover the responsiveness of molecular rotor lifetime due to local viscosity variations is known since the early 1970s for the Förster-Hoffmann model[61]. In our opinion this could give our message a good degree of generality and reliability within the scientific community.

3.2 TRFS of AzeNaph1 for glass transition detection in bulk polymers

Since, to the best of our knowledge, the literature in the field of glass transition in polymer nanoparticles is still controversial, in this section we propose a method based on the TRFS of a tailored molecular rotor for the measurement of glass transition temperature in polymer samples and polymer nanoparticles (section 2.2.1.2 and 2.2.1.2.1). The fluorescent probe of choice is the donor–acceptor derivative AzeNaph1 (Figure 3.1) whose fluorescence lifetime strongly depends on the rotation of its electron donating and rigid dibenzoazepine residue with respect to the electron deficient naphthalene imide residue[17].

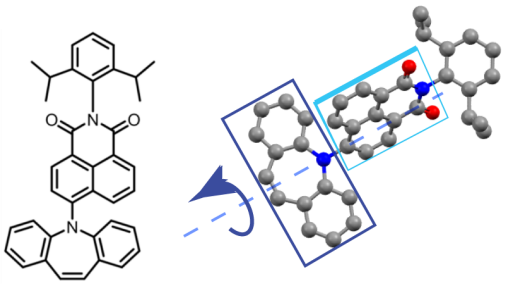

Figure 3.1: AzeNaph1 structure formula (LEFT) and 3D structure (RIGHT). After G. Vaccaro et al. *Chem. Commun.* 2013, *49*, 8474. Copyright © Royal Society of Chemistry.

Its fluorescence lifetime is extremely sensitive to the environment, ranging from hundred ps for liquids and polymers above T_g to 6–8 ns for glassy polymers, with a lifetime characteristic of the employed polymer.

Just by recording the rotor luminescence lifetime as a function of the polymerization time, it is possible to easily follow the bulk polymerization kinetics of styrene into polystyrene Figure 3.2.

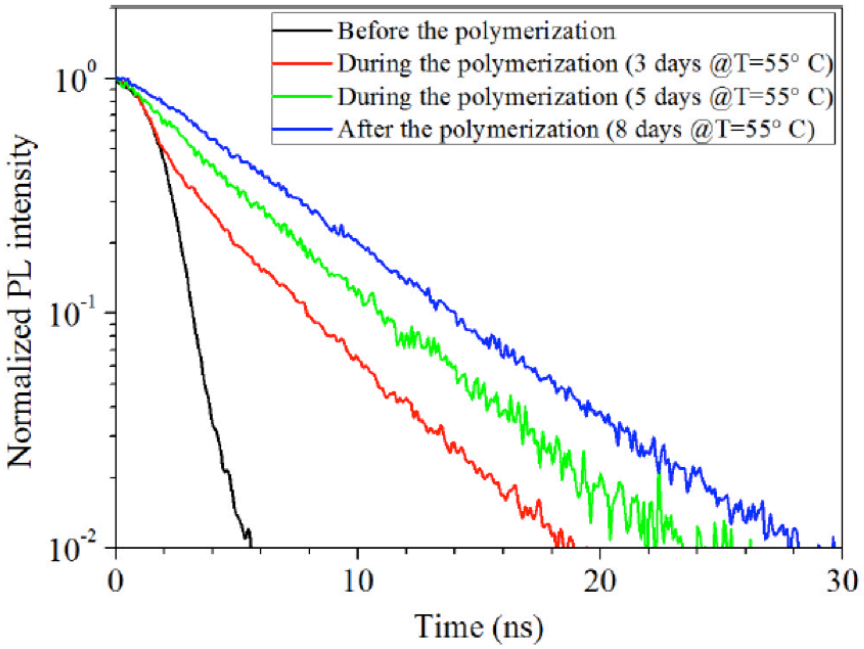

Figure 3.2: Time decay profile of AzeNaph1 acquired before, during and after the polymerization a T=55°C in a styrene solution containing 100 ppm of lauryl peroxide as radical initiator. After G. Vaccaro et al. *Chem. Commun.* 2013, *49*, 8474. Copyright © Royal Society of Chemistry.

The emission decay of AzeNaph1 behaves as a perfect single exponential in homogeneous samples. The decay is fast in liquid samples, slow in solid ones but always well fitting a monoexponential law. This is not a common characteristic of standard molecular rotors. This is the reason why in all previous studies of polymerization kinetics based on the luminescence of a probe, authors mainly focused on the luminescence intensity instead of lifetime[109, 110]. The process of the fluorescence decay for a AzeNaph1 involves radiative and non-radiative decay channels, in which the radiative decay is reasonably assumed to be unrelated with the relaxation process of the host matrix and independent of temperature, while the non-radiative decay is strongly affected by the surrounding solvent or host matrix molecules[111]. Then molecular rotors TRPL lifetime can be interpreted with Förster-Hoffmann model[61], linking the measured lifetime τ with the local viscosity of the host matrix.

$$\mathrm{Log}\tau = C + x\mathrm{Log}\eta$$

Where C and x are host/rotor dependent constants ($0 \leq x \leq 1$).

In principle, TRPL of molecular rotors can be very sensitive to the variation in the local viscosity due to the onset of polymer chains reptation (i.e. the occurrence of glass transition).

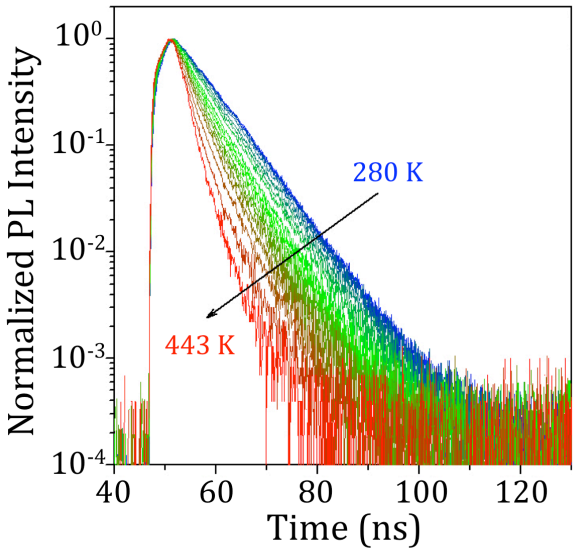

Figure 3.3: Representative series of time decay profile of AzeNaph1 embedded in a commercial polystyrene bulk sample at different temperature. From 280 K ($T<<T_g$) to 443 K ($T>T_g$) a monotonic decrease in lifetime is detected, coherent with the Förster-Hoffmann model.

In fact in Figure 3.3 a series of representative time decay profile of AzeNaph1 embedded in a commercial polystyrene bulk sample as function of temperature. From 280 K ($T<<T_g$) to 443 K ($T>T_g$) a monotonic decrease in lifetime is detected, coherent with the Förster-Hoffmann model[61]. The slope of the decay curve is the inverse of the lifetime. Therefore it is possible to normalize the measured lifetime (polymer matrix dependent in absolute value) respect to the low temperature plateau value and plotting this lifetime variation as a function of temperature, obtaining the master curve in Figure 3.4 where AzeNaph1 lifetime variation as function of temperature in various polymers with different T_g is reported.

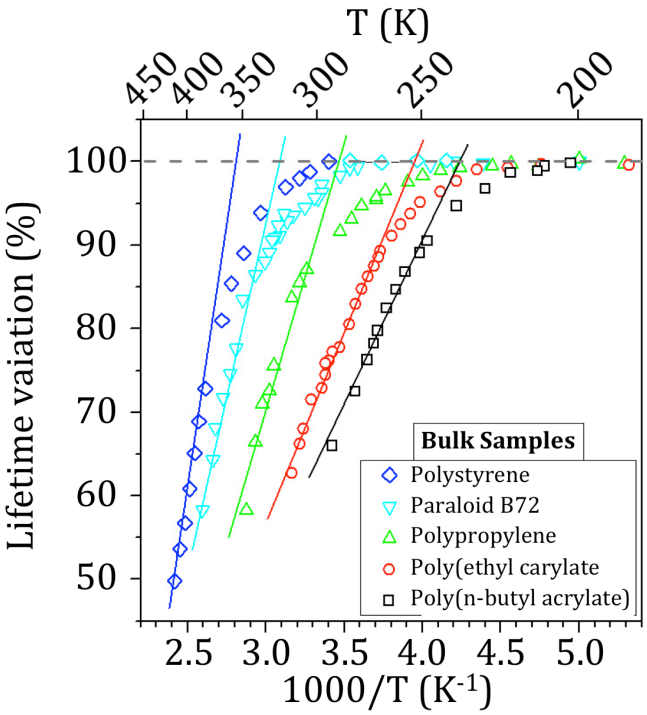

Figure 3.4: Lifetime variation of the molecular rotor AzeNaph1 embedded in different bulk polymer matrix as a function of temperature variation. A variation in slope is detected at temperature close to the T_g measured with DSC.

It is worth noticing that the change in slope in the rotor lifetime variation can be interpreted as the point where reptation starts. In fact the extrapolated T_g values with TRFS are in good agreement with T_g values measured by Differential Scanning calorimetry shown in Figure 3.5.

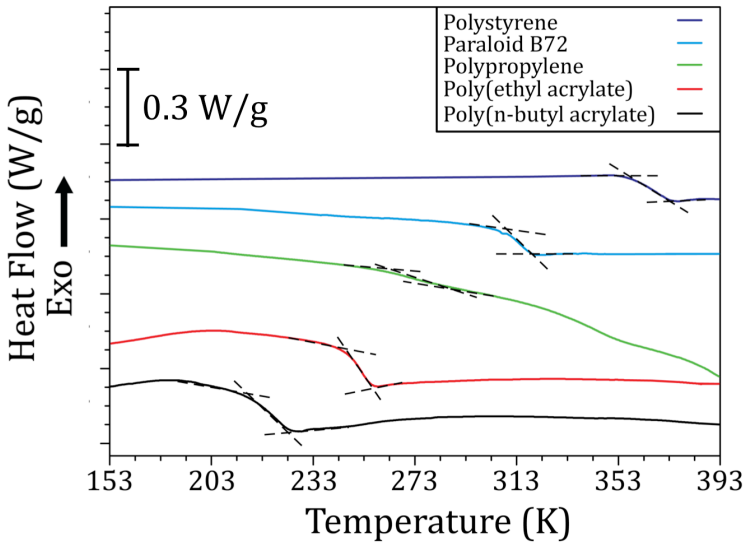

Figure 3.5: DSC traces (first scan only) for the bulk polymers sample where the molecular rotor AzeNaph1 was embedded. Note the DSC trace of polypropylene (green line): the endothermic phenomena occurring at T>313K are due to the melting of low molecular weight fractions always present in commercial chips, like the one used in this study.

In Figure 3.6 T_g values measured with TRFS with the ones measured with standard DSC are compared. The dashed line with slope one is meant to show the limiting case where TRFS values perfectly coincides with the values measured with standard DSC. All the experimental values shows a good correlation with DSC-measured ones, underlying the potentialities of such the TRFS method.

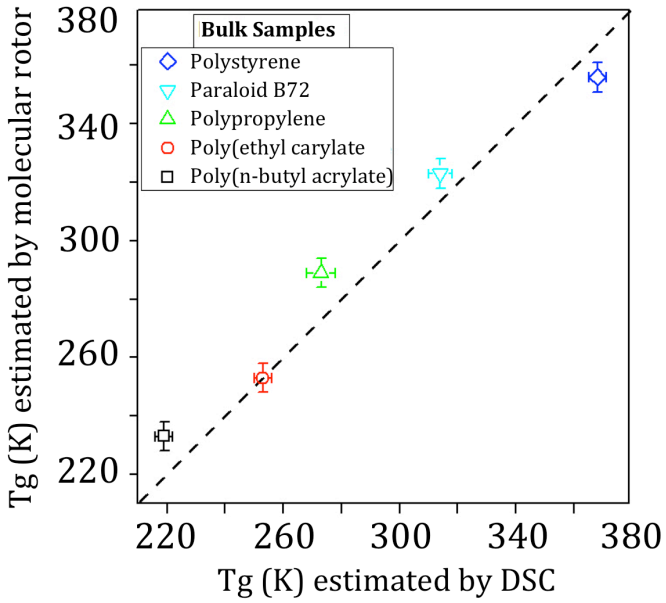

Figure 3.6: Tg values measured with TRFS are compared with the ones measured with standard DSC. The dashed line with slope one is meant to show the limiting case where TRFS values correlates with the one measured with standard DSC.

In the next section we will show how AzeNAph1 TRL analysis can be of strategic interest in the study of glass transition in polymer emulsions. Particularly, the measurement of the T_g of polystyrene NPs in aqueous emulsion is commented.

3.3 TRFS of the molecular rotor AzeNaph1 embedded in PS NPs

In Figure 3.7 the DLS size distribution by intensity for the freshly prepared PS NPs emulsions of 60 nm and 156 nm in average diameter are proposed. Both samples show a monodisperse size distribution with PdI values of 0.074 and 0.098 respectively. After DLS measurement the aqueous emulsion were both precipitated in excess of methanol, obtaining a white precipitate. The white precipitate was then filtered and dried overnight in vacuum (10^{-2}

Torr) at room temperature. The dry powder was characterized with DSC (heating from 273 K to 473 K, cooling to 273 K and back to 473 K at 20 K/min) in order to detect T_g (cycles performed under inert N_2 atmosphere, 80 ml/min flow).

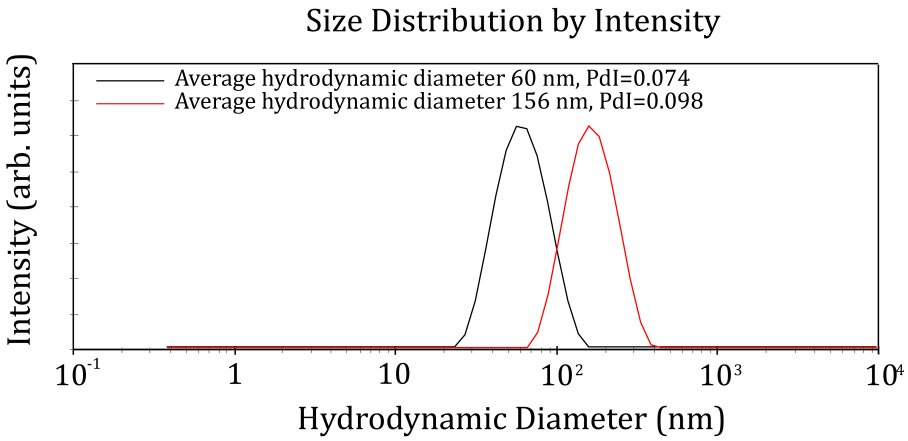

Figure 3.7: DLS hydrodynamic diameter distributions by intensity for the 60 nm PS NPs (black line) and 156 nm PS NPs (red line) loaded with AzeNaph1. Both the distribution are monodisperse and monomodal.

In Figure 3.8 the first and second scan of both emulsion samples are shown. Either in the 156 nm sample and in the 60 nm one during the first scan a T_g of (375±5) K is detected. This value is compatible with the bulk T_g value of PS. In the first scan, after the T_g detection, an exothermic peak is detected due to NPs syntherization. This is confirmed from the fact that, after DSC measurement, the sample is no more a white powder but as a single piece of polymer (see representative photograph in Figure 3.9).

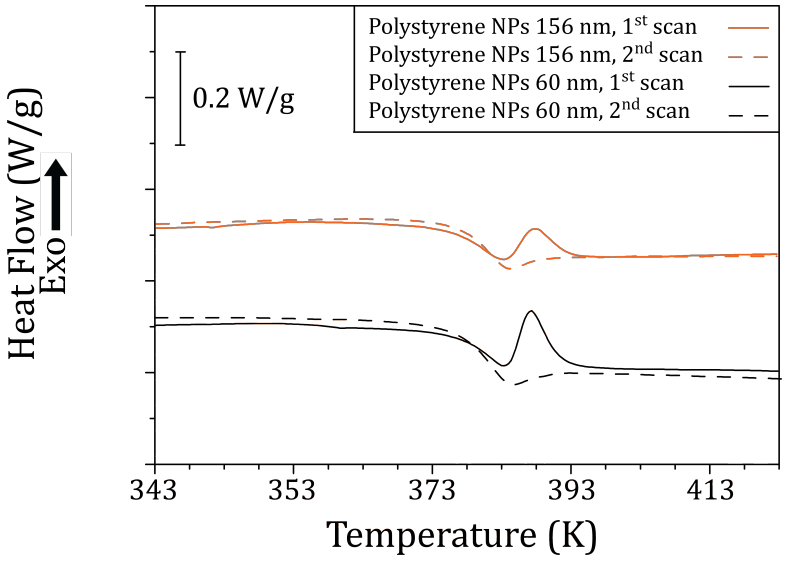

Figure 3.8: DSC traces of the first (continuous line) and second (dotted line) scan for the 60 nm in diameter (black line) and 156 nm in diameter (orange line) PS NPs. Prior to measurements all the sample were precipitated in methanol and dried in vacuum.

It is worth noticing that the exothermic peak is more intense in the 60 nm PS NPs batch. This is coherent with the higher surface/volume ratio in the 60 nm sample with respect to the 156 nm PS NPs one.

Even after NPs syntherization the T_g value does not vary, thus confirming that the PS bulk T_g value is representative to the one measured in both the precipitated NPs samples.

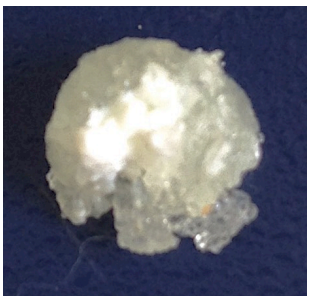

Figure 3.9: Representative photograph of the 156 nm NPs samples after the first DSC cycle from 273 K to 473K confirming that the exothermic peak in figure 3.7 is due to NPs syntherization. Signs of melting and powder syntherization are clearly visible particularly at the borders.

The key point is now using the TRFS method in order to measure the PS NPs T_g directly in the emulsion state. In our opinion this measurement will report the actual T_g value due to the aggregation state of PS chains within the emulsion of nanoparticles (i.e. in their "native" state).

All the time-resolved PL measurements were performed with excitation at 405 nm (3.06 eV), using a pulsed diode laser with a repetition rate of 2 MHz (Edinburgh EPL405), and

detection in photon-counting mode, using a Hamamatsu R943-02 photomultiplier connected to an Ortec 9353 multichannel scaler. Overall, the time resolution was about 1 ns. Each measurement was done on a freshly prepared PS NPs aqueous emulsion sealed in a glass vial, in order to prevent water evaporation along the measurement. For the TRFS measurement reported in Figure 3.10, the abrupt change in slope occurs at 380 K and 374 K for the 160 nm and 60 nm PS NPs, respectively.

The values in Figure 3.10 (measured directly in emulsion) are in agreement with the ones measured on dry PS NPs powder with DSC in Figure 3.8. In our opinion, this is a strong evidence of the fact that PS NPs either directly in emulsion and in the dry powder state retain a T_g value comparable with the one of bulk PS.

The retention of the PS bulk T_g value even in nanoparticles with dimension from 60 nm to 160 nm can offer a general design paradigm for the preparation of more complex polymer nanostructures. In the following chapters (4 and 5) examples of multiphase polymer nanostructures to be used as proof-of-concept application test field are proposed.

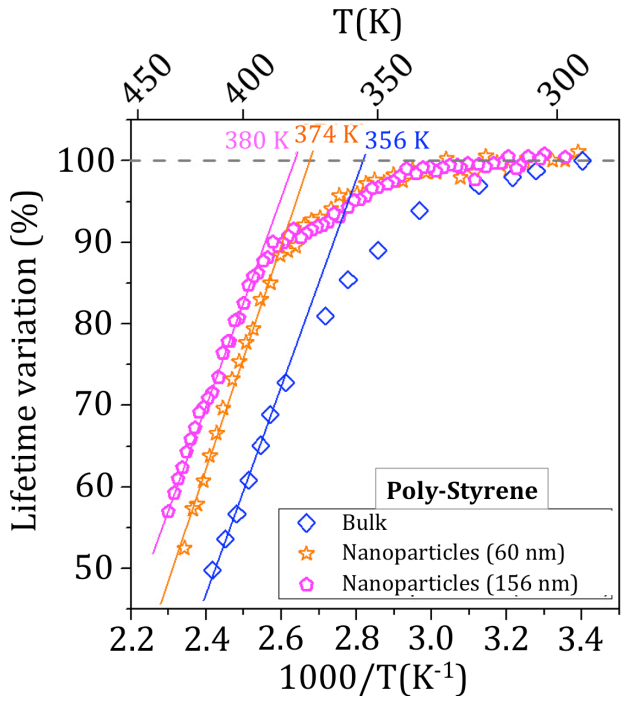

Figure 3.10: Lifetime variation of the molecular rotor AzeNaph1 embedded in different bulk polymer PS NPs (60nm and 160 nm) as a function of temperature variation measured DIRECTLY IN EMULSION. A variation in slope is detected at temperature close to the T_g measured with DSC. PS commercial bulk sample loaded with AzeNaph1 showing is reported as reference.

4 Poly(n-butyl acrylate)@Polystyrene NPs: morphology and collateral applications

4.1 Introduction

Advances in the field of nanotechnologies have fuelled the need for design and synthesis of multicomponent nanoparticles with defined internal structures[112]. The idea is to tailor the composition, structure and functionalities with nanometric control, leading to new properties and applications[113]. Particularly, the combination of two polymers with contrasted characteristics (soft/hard, hydrophilicity/hydrophobicity, etc.) at the nanoscale makes the design of materials with unique combinations of antagonistic properties possible[114]. Emulsion Polymerization (EP) has been found to be a strategic tool for preparation of multiphase latex[115]. Compared to polymerization processes in organic solvents, EP can be performed in green and biologically friendly solvents such as water[116]. Hence EP has been playing an important role as suitable tool for the synthesis of multiphase nanoparticles for selective encapsulation of active molecules for bioimaging and drug-delivery[117]. Mostly, for the preparation of such biphasic nanoparticles a two-stage process is applied[118]: core-forming monomer is firstly emulsified in a continuous phase, then the polymerization of the nanodroplets is initiated. Then the enthalpy driven seeded EP of the shell-forming monomer is performed. Depending on monomers/water ratio and post-polymerization treatments, emulsion particles with different core@shell morphologies can be achieved[119].

An idealized core@shell structure shows a complete phase separation between the two chemically distinct components. A situation widely reported in literature shows the presence of an interphase[120], sometimes strengthening the connection between the core and the shell[121]. About the actual morphology and the extent of such an interphase there is not a unique interpretation. The debate around the PBA@PS nanoparticles morphology is still very vivid: examples of phase inversion[122], occluded[123] and not-ideal[124] structures are widely report in literature in the case of PBA@PS nanoparticles.

Our method for obtaining nanoparticles poly(*n*-butyl acrylate)@polystyrene (PBA@PS) with ideal core@shell structure[19] is based on a semicontinuous EP protocol (section 2.2.1.3). A two stage process is applied, in order to emulsify and polymerize the core-forming monomer and to force the enthalpy-driven shell growth. A key improvement is the replacement of the commonly used surfactant, linear sodium dodecyl sulfonate (SDS) with

dioctyl sodium sulfosuccinate (AOT), a branched surfactant, generally more soluble in hydrophobic monomers than in water[125]. AOT and other branched sulfosuccinates are extensively used in the formation of microemulsions[126] and in medical formulations[127], due to their ability to form microemulsions without the presence of a short-chain alcohol as cosurfactant[128].

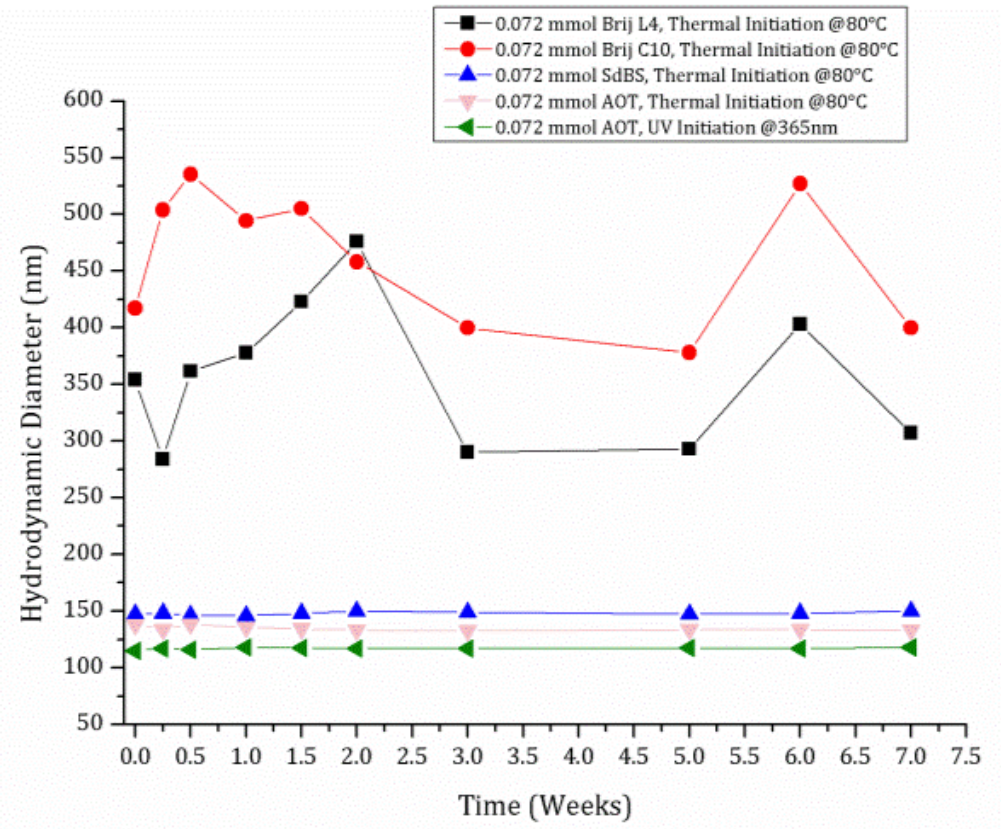

Figure 4.1: Average DLS hydrodynamic diameter of five batches of PBA nanoparticles synthesized with different surfactants as function of the final emulsion shelf-life (line is meant to guide the eye). Time 0 weeks stands for measurement performed on fresh emulsion.

About the effectiveness of AOT, we performed a shelf-life experiment on five control samples of a PBA emulsion prepared with the same amount of five different surfactant (see Figure 4.1). Namely we used 0.072 mmol of non-ionic surfactants (Brij L4, Brij C10) and anionic surfactants (SDS and AOT). The emulsion were prepared by dropping 3 ml (21 mmol) of a BA monomer solution containing the surfactant and the AIBN initiator (0.042 mmol) into 160 ml of water under mechanical stirring. Four of the five reactions were thermally initiated at 70°C (3 hours reaction time) and one was initiated with UV radiation (24 hours reaction time). In between the different DLS measurements, the samples were stored in the dark at room temperature. As you can see from Figure 4.1, the average particle DLS diameter of the polymer nanoparticles obtained using non-ionic surfactants fluctuates over a some weeks

time scale. On the other hand, the average particle DLS diameter of the polymer nanoparticles obtained using anionic surfactants remains constant for seven weeks even with a low T_g polymer like PBA. Particularly, when AOT and SDS are used in the same concentration, our set of data suggests that AOT allows to reach slightly smaller final size of the nanoparticles. On the basis of the effectiveness of AOT in tuning the final PNPs dimensions without co-surfactant (simplifying thus the emulsion formulation) and on its usage in medical formulation as well, we decided to use it in our synthesis protocol. In this way we aim to propose a more sustainable emulsion synthesis protocol for the preparation of biphasic polymer nanoparticles.

However, to the best of our knowledge, there are only two reports about the use of AOT in EP, no one of them reporting core@shell structures[129].

Here the study of PBA@PS NPs, a potentially interesting sealing system merging the adhesive PBA properties with the renowned PS shape stability, is proposed. Previous literature underlines that the effective sequestration of PBA within a PS shell is a critical issue due to the higher PBA hydrophilicity respect to PS, leading to phase inversion phenomena[122]. Our DLS, AFM and SEM measurements clearly show that the outer shell of the nanoparticles we obtained is compatible with the presence of glassy PS. Moreover, the DSC thermograms and solid state (TD-^{1}H-NMR, CP-MAS and SPE ^{13}C-NMR) NMR spectra we recorded shows that there is no intermixing between the two phases. The peculiar mobility of each phases is indeed preserved. AFM, SEM, ^{1}H-TD-NMR and solid state ^{13}C-MAS-NMR showed the biphasic nature of the sample either with Cross Polarization and Single Pulse Experiment. Particularly AFM force spectroscopy allowed to monitor in situ the breakdown dynamics of the nanoparticle, showing a behaviour according to a pressure-induced partial intermixing of the different nanophases associated with baroplasticity. The results can be potentially interesting in manufacturing a new class of polymer nanoparticles acting as capsule-based sealing nanoadditives to be delivered as smart aqueous inks. Moreover we propose two alternatives application of these core@shell nanoparticles for the encapsulation of lipophilic derivatives of carminic acid (a biocompatible dye) and for the encapsulation of sensitized up-conversion dyes.

4.2 Compositional characterization

Dried latex powder of PBA@PS has been characterized with ATR-FTIR (Figure 4.2), providing chemical information averaged over a depth from approximately 500 nm to 2000 nm in the 3000 cm^{-1} to 600 cm^{-1} wavenumber region[130] of the diamond probe used in this work. Since our core@shell nanostructures has 184 nm in average DLS diameter range, ATR-FTIR is able to scan either the PS cross-linked shell and the *n*-PBA core, thus giving an overall compositional characterization of the nanoparticles (Figure 7). The ATR-FTIR spectra interpretation is given in table 3.[131]

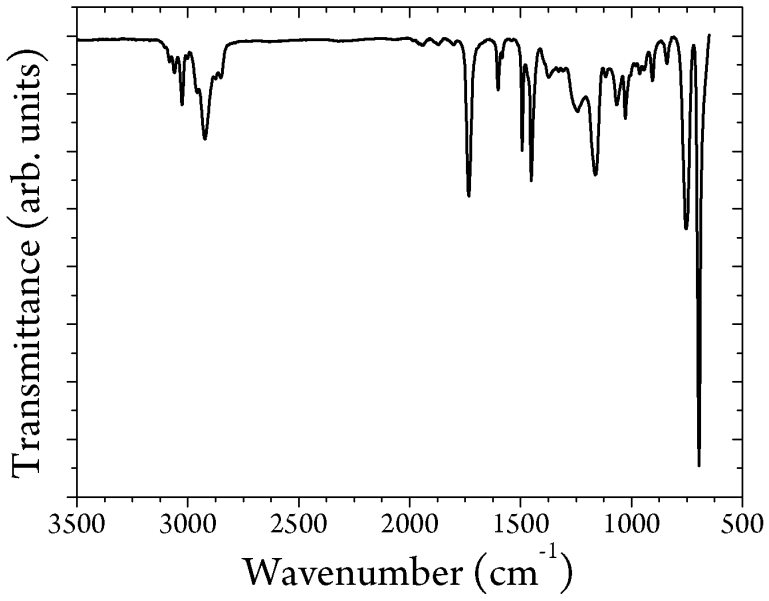

Figure 4.2: ATR-FTIR transmitted spectra of PBA@PS nanoparticles.

Table 3. ATR-FTIR peak labelling based on Reference [131].

Wavenumber (cm^{-1})	**Vibrational mode**
3100-3000	Aromatic ring stretching
3000-2850	Aliphatic chain stretching
1735	C=O Stretch
1600-1585 and 1500-1400	Aromatic C-C in ring stretch
1300-1100	Asymmetrical C-CO-O stretching
860-680	Aromatic C-H bending

Thermal characterization of the whole nanoparticle was performed with DSC (Figure 4.3), revealing the presence of two distinct glass transitions at temperatures expected for PBA and PS respectively (220 K and 380K). This confirm that phase separation is strong enough to allow at least part of the PS and PBA to evolve independently as the homopolymer, but does not exclude the presence of an interphase with peculiar behaviour.

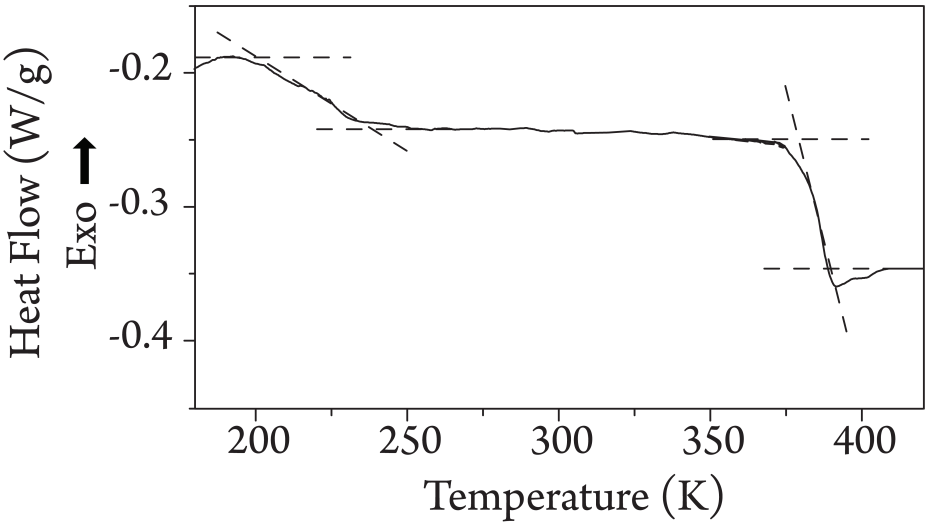

Figure 4.3: DSC trace of the sample (first scan + exo up). Two distinct glass transitions at temperatures expected for PBA and PS respectively (220 K and 380K) are detected. After S.Bonetti, M. Farina, M. Mauri, K. Koynov, H.-J. Butt, M. Kappl, R. Simonutti, Macromol. Rapid Commun. 2016, DOI: 10.1002/marc.201500625. © 2016 WILEY-VCH Verlag GmbH & Co. KGaA, Weinheim.

DSC measurements were performed on a Mettler Toledo DSC 1 Star^e System. The samples were characterized with the following method: 1) 30 min isotherm 123K ; 2) from 123K to 423K @ 20K/min; 3) 5 min isotherm 423K; 4) from 423K to 123K @ -20K/min; 5) 5 min isotherm 123K; 6) from 123K to 473K @ 20K/min. All segments were driven under 80ml/min N_2 flux.

Since DSC characterization does not exclude the presence of an interphase with peculiar behaviour, a more detailed analysis of polymer dynamics over a wide range of temperature (from 203 K to 443 K) was provided by studying proton relaxation through ^{1}H-TD-NMR (Figure 4.4). Compared to other ^{1}H-NMR techniques concentrating on the analysis of proton relaxations in terms of chemical shift, this technique involves a time resolved analysis of the free induction decay (FID) after a $\pi/2$ pulse (see section 2.3.3), where contributions with different relaxation times are associated to populations of polymer chains with different mobility. Even if glassy and crystalline fractions display such a short relaxation time that their

signal decays completely during instrumental dead time, by implementing a Magic Sandwich Echo (MSE, section 2.3.3.1) refocusing block it is possible to ensure quantitative detection[132] of all protons in the sample.

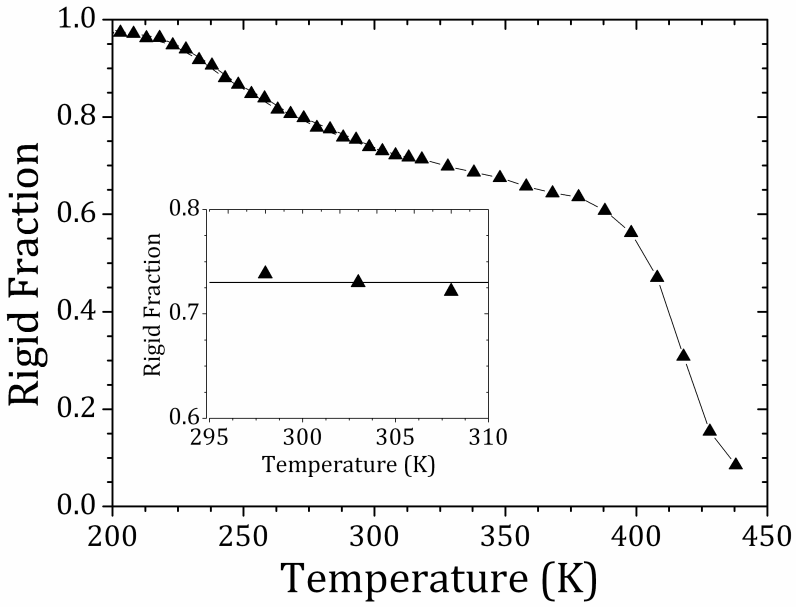

Figure 4.4: Temperature trend of PBA@PS core@shell nanoparticles rigid fraction (line is meant to guide the eye). Error bars (±0.02) are smaller than the point size. The inset shows the region close to room temperature: the line represents the expected composition for ideal core-shell structure. After S.Bonetti, M. Farina, M. Mauri, K. Koynov, H.-J. Butt, M. Kappl, R. Simonutti, Macromol. Rapid Commun. 2016, DOI: 10.1002/marc.201500625. © 2016 WILEY-VCH Verlag GmbH & Co. KGaA, Weinheim.

In PBA@PS NPs, a fraction (R) of protons with very restricted mobility was isolated, with a temperature dependence shown in Figure 4.4. The fraction R, associated to glassy phases, approaches unity when temperature is below PBA T_g (~220 K). When $T<T_{g,PBA}$ the protons relaxation of all components is indicative of polymer chains without significant mobility in the NMR timescale. Conversely, R decreases to zero when $T>T_{g,PS}$ (~380 K): polymer chains are reptating[133] and the whole system is eventually mobilized.

In correspondence of DSC measured glass transition, R value can vary in a complex way, but if pristine NPs are measured in the region close to room temperature (see inset in Figure 4.4), which is far away from both transitions, R measured value is quantitatively dependent on the proton weighted fraction of each polymer[134]. In particular, the observed measured value corresponds to the theoretical (73±2)% value for ideal core@shell nanoparticles expected by the synthesis feed conditions (see section 2.2.1.3), suggesting full phase separation and very weak interphase contribution.

Further proof of the phase separation within PBA@PS nanoparticles and thus of coexistence in the same particle of a hard shell and soft core is provided by solid state ^{13}C-Magic Angle Spinning (MAS) NMR performed on precipitated NPs. Solid state Cross Polarization (CP) ^{13}C-MAS and Single Pulse Experiment (SPE) sequences were applied.

^{13}C-MAS-NMR experiments were recorded on a solid state magic angle spinning Bruker Avance 300 at 298K. Sample was heavily packed in a 4mm ZrO_2 rotor. Spinning rate was set to 9000 Hz for both experiments. SPE was recorded with 4096 scans using a recycle delay of 2s. For CP-MAS, 1024 scans were acquired and a contact time of 1.5 ms and a recycle delay of 4 s were used. The usage of short contact time (1.5 ms) in CP-MAS experiment[135] allows selecting the rigid components of the NPs. Indeed the ^{13}C CP-MAS NMR spectrum in Figure 4.5 is dominated by the characteristic PS peaks (40 ppm, 42ppm, 47 ppm, 130 ppm and 147 ppm)[137].

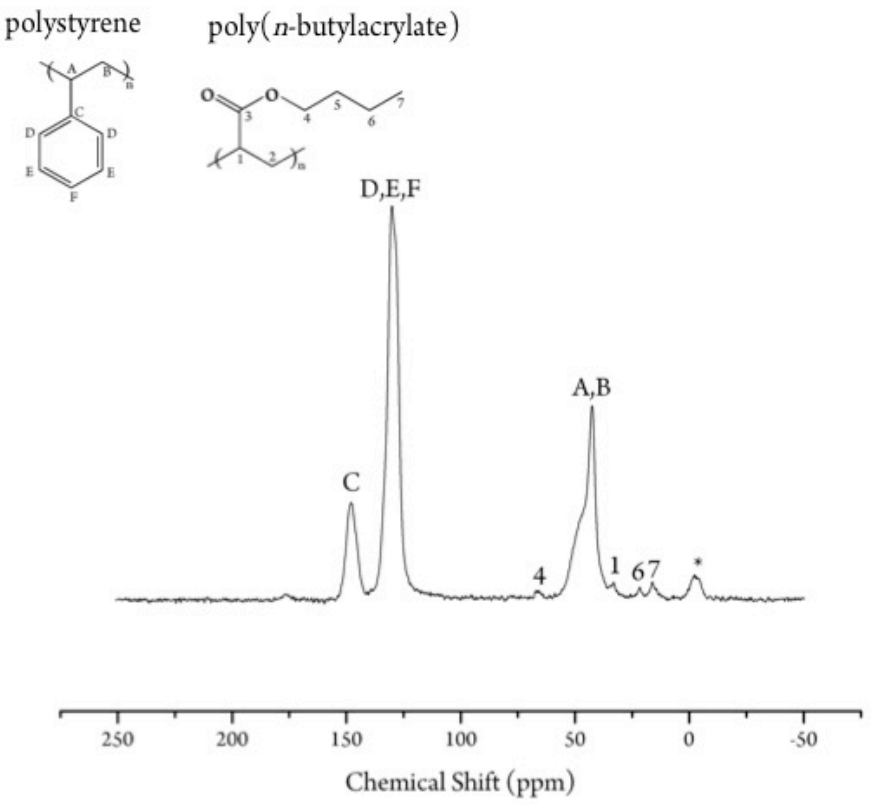

Figure 4.5: ^{13}C CP-MAS NMR spectrum of PBA@PS NPs dominated by the peaks of glassy PS (40 ppm, 42ppm, 47 ppm, 130 ppm and 147 ppm). (*) Indicates a spinning sideband. After S. Bonetti et al. *Macromol. Rapid Commun.* 2016, DOI: 10.1002/marc.201500625. © 2016 WILEY-VCH Verlag GmbH & Co. KGaA, Weinheim.

Conversely to ^{13}C CP-MAS NMR with short contact time mainly selecting the rigid components, SPE MAS ^{13}C NMR spectrum (Figure 4.6) acquired with 2 s recycle delay selects the mobile components endowed with fast ^{13}C relaxation times[136]. In this latter case, the characteristic PBA peaks (at 16 ppm, 21 ppm, 30 ppm, 33 ppm, 40 ppm, 66 ppm and 176 ppm) appear in addition to the PS peaks[137].

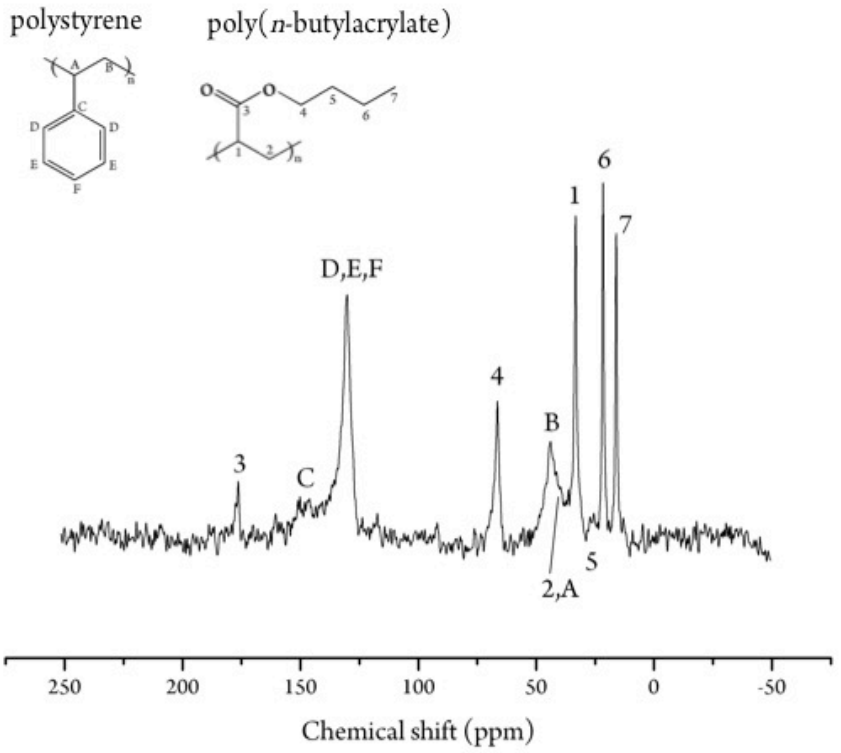

Figure 4.6: ^{13}C SPE-MAS NMR spectrum of PBA@PS NPs, where the characteristic PBA peaks (at 16 ppm, 21 ppm, 30 ppm, 33 ppm, 40 ppm, 66 ppm and 176 ppm) appear in addition to the PS peaks, suggesting a strong phase separation. After S. Bonetti et al. *Macromol. Rapid Commun.* 2016, DOI: 10.1002/marc.201500625. © 2016 WILEY-VCH Verlag GmbH & Co. KGaA, Weinheim.

The comparison of the two spectra provides the picture of a phase separated system where PBA shows an higher mobility compared to PS (Figure 4.7). This view is also confirmed by the line width (LWHM) of PBA resonances ranging from 130 Hz to 60 Hz, much narrower than the PS values of over 300 Hz. In fact ^{13}C resonances of amorphous polymers acquired at temperature $T>>T_g$ present quite narrow LWHM due to high frequency of local motions,

approaching the extreme narrowing regime. Instead in glassy polymers ($T<<T_g$), strong proton carbon dipolar couplings not reduced by molecular motions lead to wide resonances.

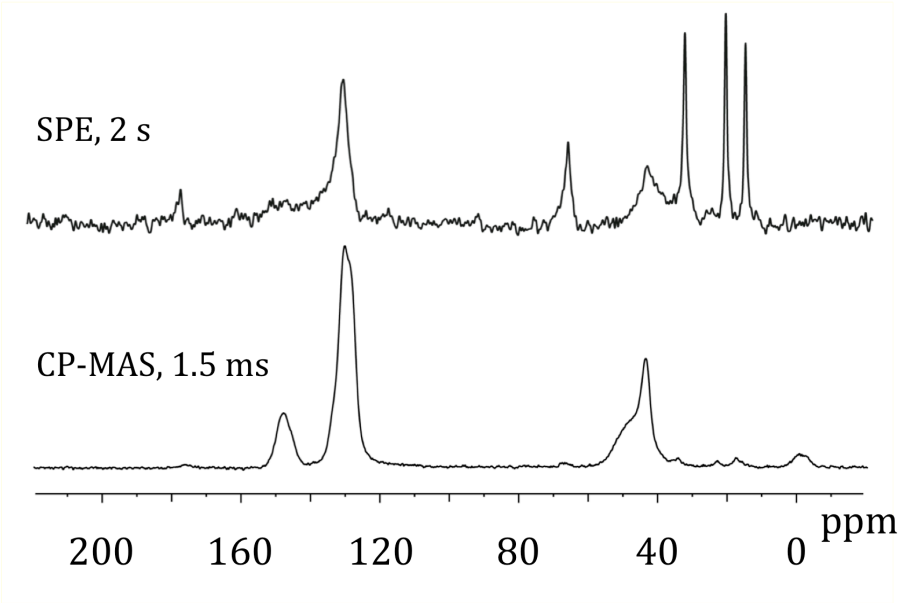

Figure 4.7: SPE and ^{13}C-MAS NMR spectra of PBA@PS NPs. After S.Bonetti, M. Farina, M. Mauri, K. Koynov, H.-J. Butt, M. Kappl, R. Simonutti, Macromol. Rapid Commun. 2016, DOI: 10.1002/marc.201500625. © 2016 WILEY-VCH Verlag GmbH & Co. KGaA, Weinheim.

Thus ^{13}C MAS NMR confirms an almost complete phase separation between PBA and PS and that the two polymers at room temperature present a mobility quite similar to that of the respective bulk phases.

4.3 Morphological Characterization

PBA@PS NPs dimensions were measured by AFM, DLS and SEM (Figure 4.8). The AFM image was collected at ambient condition in intermittent contact mode on a sample deposited on freshly cleaved mica and dried in a vacuum oven at 75°C for 16 hours before thermalization at room temperature (Figure 4.8-a).

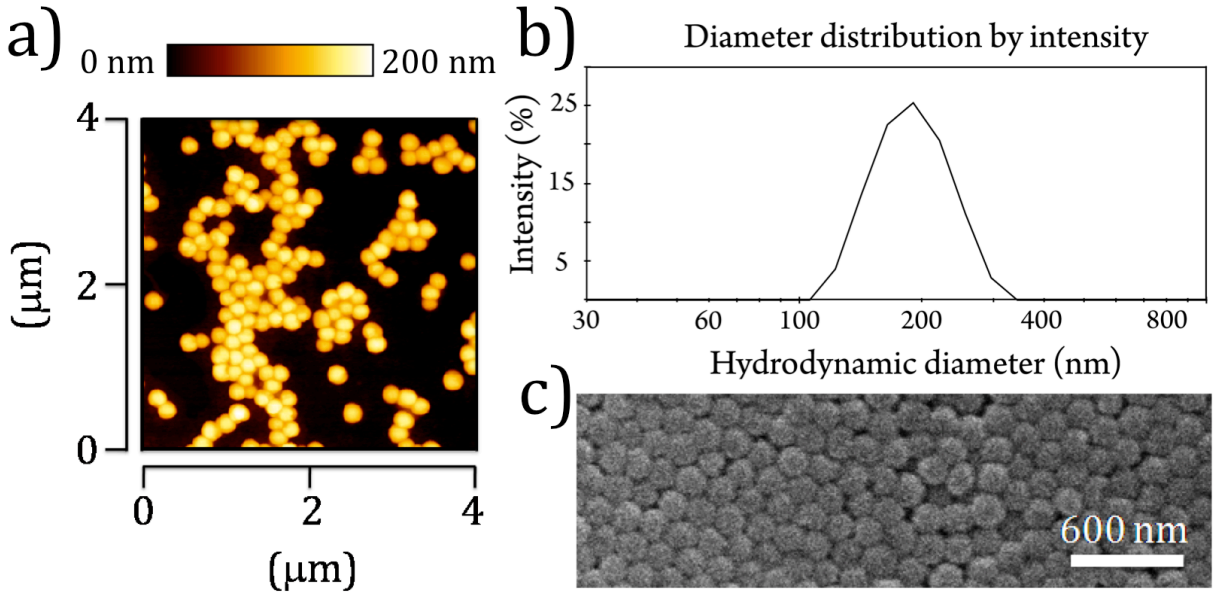

Figure 4.8: a) AFM image (4 µm x 4 µm x 200 nm), b) DLS hydrodynamic diameter distribution and c) SEM micrography of PBA@PS core-shell nanoparticles. After S.Bonetti, M. Farina, M. Mauri, K. Koynov, H.-J. Butt, M. Kappl, R. Simonutti, Macromol. Rapid Commun. 2016, DOI: 10.1002/marc.201500625. © 2016 WILEY-VCH Verlag GmbH & Co. KGaA, Weinheim.

The shape and height of particles extracted from the image indicate monodisperse spheres with diameters of 164±11 nm (calculated averaging N=100 NPs, Figure a.1 in Appendix). This result is in good agreement with both the SEM image (Figure 4.8-c, average diameter of 168±11 calculated over N=100 NPs in Figure a.2 in Appendix) recorded without thermal treatment and with DLS measurement (Figure 4.8-b, average diameter of 184 nm and PDI=0.01) performed on the freshly prepared emulsion. This remarkable shape persistence - even in presence of the strong capillary and surface forces associated to drying and adsorption on the mica substrate - suggests that the outer part of the nanostructure is purely PS, a polymer that can be shaped at the nanoscale into highly stable forms[138].

The mechanical characterization on single-particle scale can be of strategic interest in order to gather a deeper insight on the inner morphology of the nanostructure. Particularly, AFM force-versus-distances curves, so-called force spectroscopy measurements[139], can be

used to characterize the mechanical properties of polymer vesicles[140] and polymer granular nanoparticles[42]. During our experiments, in between of force curve recording (see Figure 4.9 and 4.10 for representative curves), AFM was switched back to intermittent contact mode in order to image the nanoparticle for detection of eventual damage or indentation and to reposition the tip over the centre of the particle.

In Figure 4.9 a representative force versus distance curve of an intact NP is presented. From either the approach and retraction curve it is clear that no adhesive force are experimented by the tip, suggesting an elastic glassy contact with the PS surface without indentation (as confirmed by the retraction curve). It is worth noticing that the distance where the PS surface properties are probed is zero in Figure 4.9, even if we are on the top of the PBA@PS nanoparticles and not on the mica substrate. This is due to the fact that the feedback loop of the AFM operating in Force Spectroscopy stops the cantilever at "zero" when it detects a force value according to the load set by the user. Among the series of experiment we performed, we set the applied force value in order to detect the surface properties of the intact PBA@PS NP. Namely a force value < 250 nN is needed.

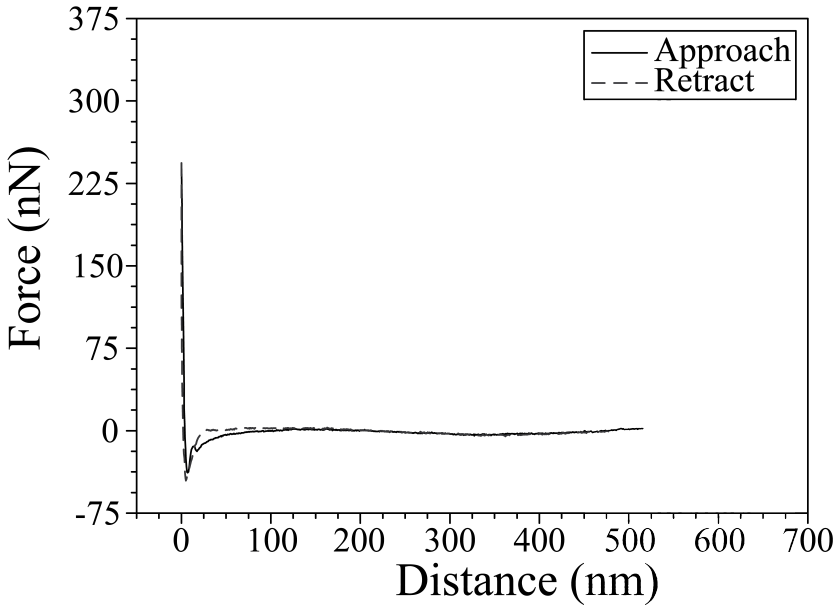

Figure 4.9: Representative force vs distance curve recorded on the top of the PBA@PS NP with increasing load up to 250 nN (cantilever with a nominal spring constant of 42 N/m). Up to this limit the NP is still intact. After S.Bonetti, M. Farina, M. Mauri, K. Koynov, H.-J. Butt, M. Kappl, R. Simonutti, Macromol. Rapid Commun. 2016, DOI: 10.1002/marc.201500625. © 2016 WILEY-VCH Verlag GmbH & Co. KGaA, Weinheim.

This set of data agrees with all the previous evidences underlying that the outer phase of the core@shell NPs is glassy-like.

In Figure 4.10 a representative force-distance curve recorded on the top of a collapsing PBA@PS NP is proposed. During the approach, a first abrupt increase in the measured force is detected, due to the contact between the tip and the PS glassy shell. In some tens of nm the indentation of the glassy shell occurs. Then the tip reaches a second contact regime. Adhesion force in the order of several tens of nN is observed upon retraction and the collapsed NP is stretched out by 130 nm before it detaches from the AFM tip. This is an evidence of the adhesive properties of the collapsed NP.

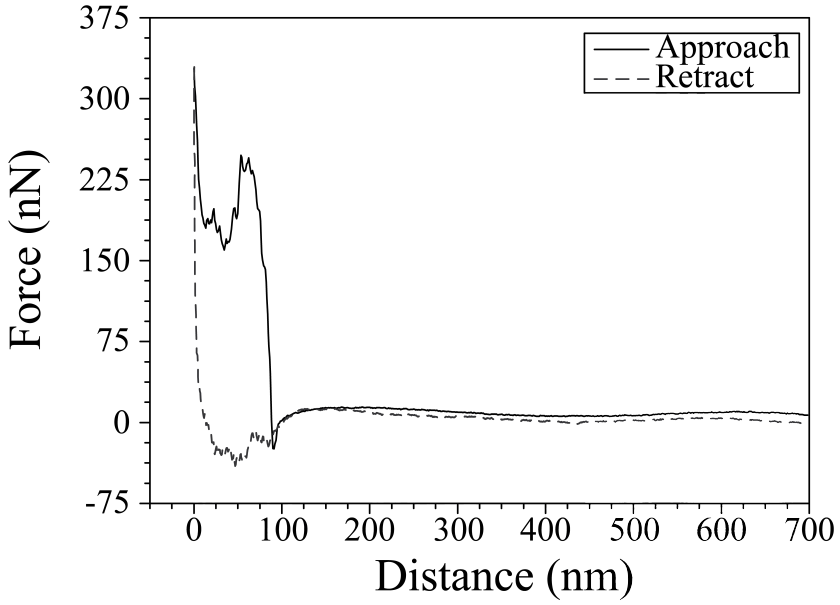

Figure 4.10: Representative force vs distance curve recorded on the top of the PBA@PS NP with load over the force threshold of 250 nN (cantilever with a nominal spring constant of 42 N/m), showing the NP collapse. After S.Bonetti, M. Farina, M. Mauri, K. Koynov, H.-J. Butt, M. Kappl, R. Simonutti, Macromol. Rapid Commun. 2016, DOI: 10.1002/marc.201500625. © 2016 WILEY-VCH Verlag GmbH & Co. KGaA, Weinheim.

AFM topography image in Figure 4.11 were performed using a cantilever with a spring constant of k = 1.38 N m^{-1}, applying loads in the range between 15 nN and 500 nN. The particle was not chemically fixed on the surface, not to vary its mechanical properties. In Figure 4.11-a the image of a typical isolated nanoparticle is acquired using intermittent contact mode. The 3D representation clearly defines a spherical shape, with dimension compatible with the average diameter obtained via SEM and the NPs DLS size distribution in solution. Similar images were recorded upon increasing the load up to 150 nN, when the plastic deformation of the external shell was detected (Figure 4.11-b).

A. Solmaz et al.[141] showed that in the case of a glassy polymer, such as PS, at sufficiently high loads a permanent indentation can be induced even on polymersomes. When the tip

radius is significantly smaller than the nanoparticle radius, the tip will penetrate into it generating an indentation. Since the radius of the tip used in this experiment is around 10 nm (according to manufacturer specification), thus significantly smaller than the PBA@PS nanoparticle, indentation is expected. The image in Figure 4.11-b supports this behaviour, showing a glassy external fracture on the surface of the particle compatible with a PS plastomer shell. Only when the external load is set to 500 nN the NPs collapses and flows (Figure 4.11-c and 4.11-d). Note that in Figure 4.11-c the scale bar is now 18 nm instead of 200 nm, underlying the NP exhibits an overall melt-like flow.

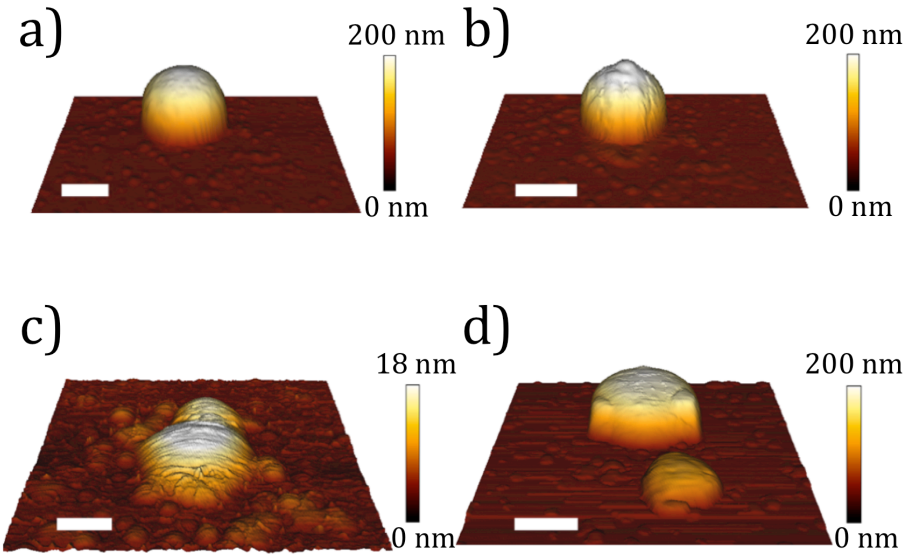

Figure 4.11: a) AFM image of a PBA@PS nanoparticle prior to load application. b) AFM image of a PBA@PS nanoparticle after an applied load of 150 nN. c) AFM image of a PBA@PS nanoparticle after an applied load of 500 nN. d) AFM image of another PBA@PS nanoparticle after an applied load of 150 nN. White bars are 100 nm (a, b, c images were recorded on the same particle using a Si cantilever of k=1.38 N m^{-1} while d image was recorded on a second particle using a Si cantilever of k=1.52 N m^{-1}). After S.Bonetti, M. Farina, M. Mauri, K. Koynov, H.-J. Butt, M. Kappl, R. Simonutti, Macromol. Rapid Commun. 2016, DOI: 10.1002/marc.201500625. © 2016 WILEY-VCH Verlag GmbH & Co. KGaA, Weinheim.

Polymeric systems comprising one glassy and one rubbery component able to flow at room temperature under external applied pressure are already known in literature as baroplastics[142]. Particularly A. Mayes et al. demonstrated that block copolymers[143] and core-shell NPs[144] consisting of low T_g core (poly(2-ethylhexyl acrylate) or PBA) and a high T_g (PS) shell can be compression moulded at 25°C under 34.5 MPa for 5 min. This unusual room temperature baroplastic processing (which normal wise occurs at T>200°C for plastomers like PS) is due to a partial mixing of the two components under pressure. A similar behaviour

was reported by K.H. Lee et al. on PBA-PS nanoblends[145]. In our opinion the NP breakdowns in Figure 4.11-c and Figure 4.11-d can be interpreted assuming a pressure-induced partial intermixing of dissimilar nanophase domains, resulting in a semi-solid state that facilitates flows.

In order to gather a deeper understanding on the PBA@PS breakdown, a control experiment probing the mechanical response of pure PBA NPs was performed (see Figure 4.12). A droplet of aqueous dispersion of pure PBA NPs (synthesized with the same procedure used for the synthesis of the PBA core of the PBA@PS NPs in section 2.2.1.3.1) was cast onto a freshly cleaved mica substrate. After water evaporation, imaging with tapping mode revealed that the PBA NPs had spread on the mica, with a consequent partial coverage of the substrate itself by a PBA film (thickness up to several hundred nanometres). In order to study the mechanical properties of PBA by Force Spectroscopy, a cantilever with 74.2 kHz resonance frequency and a spring constant value of 1.2 N/m was used and the representative measured force-curve is shown in Figure 4.12.

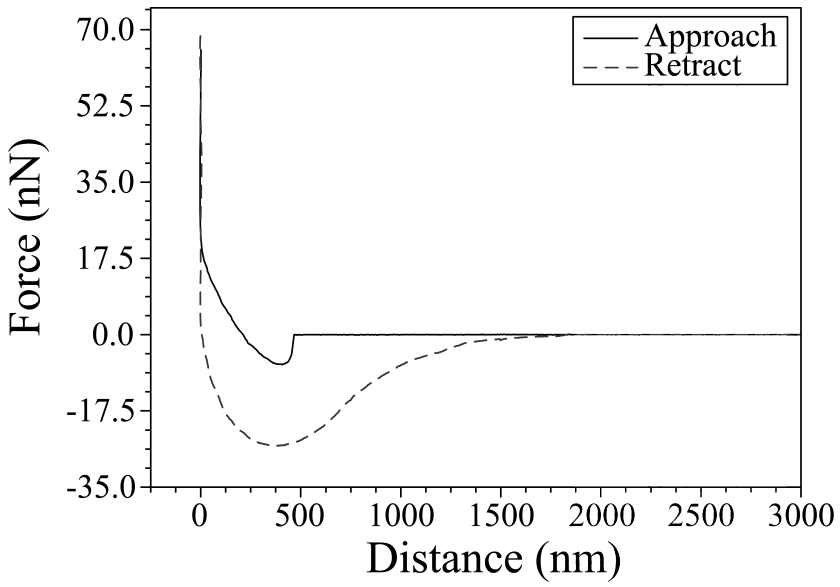

Figure 4.12: Representative force curve recorded on the top of a PBA film obtained from the deposition of an aqueous solution of PBA nanoparticles onto freshly cleaved mica substrate. **After S.Bonetti, M. Farina, M. Mauri, K. Koynov, H.-J. Butt, M. Kappl, R. Simonutti, Macromol. Rapid Commun. 2016, DOI: 10.1002/marc.201500625. © 2016 WILEY-VCH Verlag GmbH & Co. KGaA, Weinheim**.

In Figure 4.12 a representative force curve recorded on the top of the PBA film obtained by drop-casting of pure PBA NPs is presented. It is worth noticing that, during the approach, the tip is pulled into the PBA film as soon as the tip touches the film surface (~500nm). Only by applying a compressive force of some tens of nN it is possible to penetrate the PBA film.

The film thickness extracted from the distance between the onset of attraction and the transition to hard wall repulsion is 460 nm. Significant adhesion of several tens of nN is observed upon retraction and the PBA film is stretched out by more than 1.5 μm before it ruptures from the AFM tip. This confirms the adhesive nature of pure PBA but points out some difference between the force curve recorded on the collapsing NP (Figure 4.10). Even if both the force-curves shows an adhesive regime, the pure-adhesive behaviour of PBA film is not fully recall in PBA@PS NPs. In our opinion this is a further control evidence that the outer shell of the PBA@PS is glassy and that the PBA@PS collapse is associated with a "simple" shell plastic rupture, triggering PBA release.

Standing on the difference between the force curves of the damaged NP and of the pure PBA NPs film, the assumption of a baroplastic collapse of the PBA@PS NP can explain either the overall melt-like flow in Figure 4.11-c of the NP and the absence of sharp edges due to glassy fracture in Figure 4.11-d.

Concluding, an effective synthetic strategy for the preparation of PBA@PS core-shell NPs is presented together with a comprehensive characterization of the NPs. AFM, SEM, ^{1}H-TD-NMR and solid state ^{13}C MAS NMR showed the biphasic nature of the sample. Particularly, AFM force spectroscopy allowed to monitor in situ the breakdown characteristic of the nanoparticle, showing a behaviour compatible with a pressure-induced intermixing of the two different nanophase domains associated with baroplasticity. To the best of our knowledge, this is the first report of a baroplastic collapse on a single-particle scale. Together with the AFM imaging of baroplasticity, force spectroscopy allows the estimation of the forces involved in the process. Such evidences can be interested in self-healing application field as well, since the baroplastic NP collapse is a force-triggered release of a semi-solid flowing glue from a capsule-based nanocontainer. In our opinion our findings are likely to be of great interest to polymer scientists and researchers working on polymer nanoparticles as well as for material scientists working on sealing nanoadditives to be applied in extrinsic self-healing materials.

4.4 Perspective test: how small can we go preserving the PBA@PS strong phase separation?

The characterization of poly(*n*-butyl acrylate)@polystyrene (PBA@PS) nanoparticles (NPs) of different dimensions (184 nm, 127 nm, 90 nm and 45 nm in average DLS diameter) obtained via the semicontinuous emulsion polymerization protocol (section 2.2.1.3) is here presented.

In this section we want to understand whether the strong phase separation observed on the 184 nm sample is conserved shrinking the dimension of the final biphasic PBA@PS nanoparticle. In the following, the four different samples are labelled with their hydrodynamic diameters for the final core@shell structures obtained from DLS measurements (Figure 4.13).

The dimension was tuned varying the AOT surfactant content during the synthesis. Particularly, for the core synthesis $1.24 \cdot 10^{-1}$ mmol were used for the preparation of the 184 nm sample (115 nm hydrodynamic core diameter), $6.80 \cdot 10^{-1}$ mmol of AOT for the 127 nm sample (73 nm hydrodynamic core diameter), 3.49 mmol of AOT for the 90 nm sample (70 nm hydrodynamic core diameter) and 9.12 mmol of AOT for the 45 nm sample (DLS hydrodynamic core diameter not accessible with DLS).

For the shell-growth step the AOT content was tuned by adding $5.46 \cdot 10^{-2}$ mmol (184 nm), $4.61 \cdot 10^{-1}$ mmol (127 nm), 2.33 mmol (90 nm) and $5.11 \cdot 10^{-2}$ mmol (45 nm). In all cases either for the core step and for the final core@shell PdI calculated by DLS were far below 0.1 (real PdI index are in the range from 0.03 to 0.09 for all samples), indicating the sharp monodispersity of the particle size distribution in intensity.

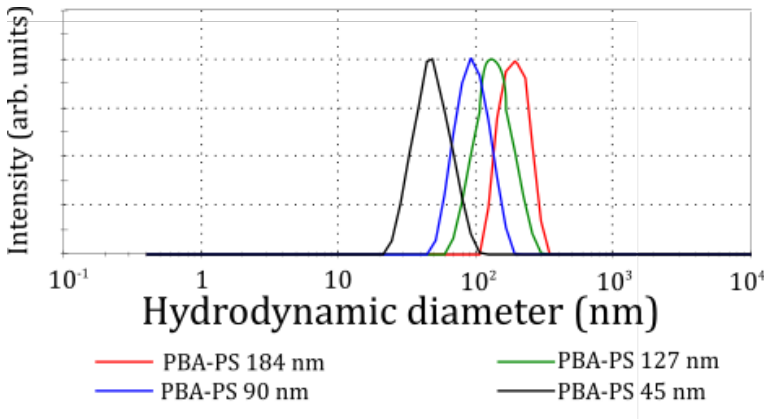

Figure 4.13: Particle size distribution by intensity obtained with DLS experiment for (red-line 184 nm, green line 127 nm, blue line 90 nm, black line 45 nm) PBA@PS core@shell samples. In the caption average hydrodynamic diameters are reported for all samples.

In Figure 4.14 DSC traces of all samples are reported. In all the measurements, PBA T_g (220±15) K and cross-linked PS T_g (375±10) K are visible. However, a third T_g value can be detected in the 90 nm and in the 45 nm samples. The measured T_g values were respectively of (290±3) K and of (285±2) K. According to Mellinger et al.[121], the detection of an additional T_g can be attributed to the presence of an interphase between the two homopolymer phases. Moreover, since in Figure 4.14 it is possible to have the experimental value of T_{gINT}, it is possible to elicit the interphase composition via Fox Equation[146] by knowing the T_g of the homopolymers participating at the interphase formation (i.e. T_{gPS} and T_{gPBA}). With this

formalism the interphase composition of the 90 nm sample is $PS_{Interphase}$=(52±1)% w/W, and $PS_{Interphase}$ =(60±3)% w/W in 45 nm sample. $PBA_{Interphase}$ = (100 - $PS_{Interphase}$)% w/W values follow automatically.

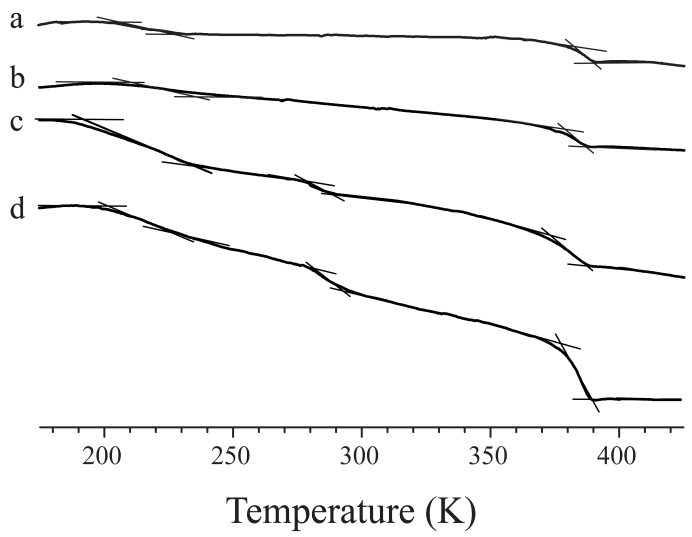

Figure 4.14: First scan DSC traces for (a.184 nm, b.127 nm, c.90 nm, d.45 nm) PBA@PS core@shell samples. Exo-Up.

Dried latex powder has been further characterized with ATR-FTIR, providing chemical information averaged over a depth from approximately 500 nm to 2000 nm in the 3000 cm^{-1} to 600 cm^{-1} wavenumber region of the diamond probe used in this work[130]. Since our biphasic NPs are in the 45 nm to 184 nm diameter range, ATR-FTIR is able to scan either the PS cross-linked shell and the *n*-PBA core, thus probing the whole compositional characterization of the nanoparticles. In Figure 4.15 the region between 1100 cm^{-1} and 1300 cm^{-1} (region of the asymmetrical C-CO-O stretching) is shown. As one can see, moving from the biggest NPs to the smallest ones, a distortion in the peak shape is detected. Recent papers[147] ascribe similar peaks distortion to Mie scattering when the NPs radius is between 242 nm and 2310 nm. However, since the NPs shown here are far smaller than the resonant Mie size, the deformation in the region of the asymmetrical C-CO-O stretching with dimension must be induced by other factors, such as a change in the inner morphology of the nanoparticles for instance.

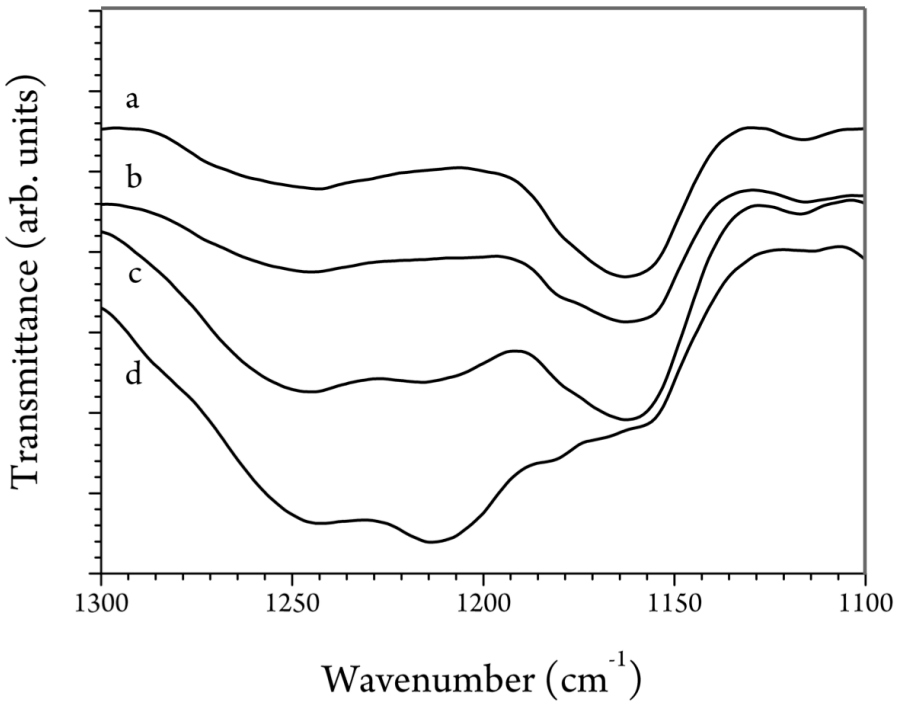

Figure 4.15: ATR-FTIR transmittance spectra of PBA@PS core@shell nanoparticles (a.184nm, b.127 nm, c.90 nm, d.45 nm).

Characterization of chain mobility, to further validate the presence of an interphase, is performed through ^{1}H-TD-NMR Magic Sandwich Echo (MSE) experiments, as before. Total proton rigid fraction temperature dependence is shown in Figure 4.16: the proton rigid fraction R is strictly dependent on the nanoparticles sizes. Particularly, for each sample, it approaches to one when temperature is below PBA T_g: the protons decay of all component describe the situation of frozen polymer chains. R sharply decreases to zero when the temperature is above PS T_g: polymer chains are fully mobilized. In the temperature range between PBA and PS T_g, R decreases when the temperature is raised. Particularly, in 127 nm and 184 nm NPs proton rigid fraction decreases smoothly, while it shows a change in behaviour in 45 nm and 90 nm ones. In our opinion this matches with ATR-FTIR peak distortion and DSC traces, suggesting the presence of an interphase with peculiar mobility.

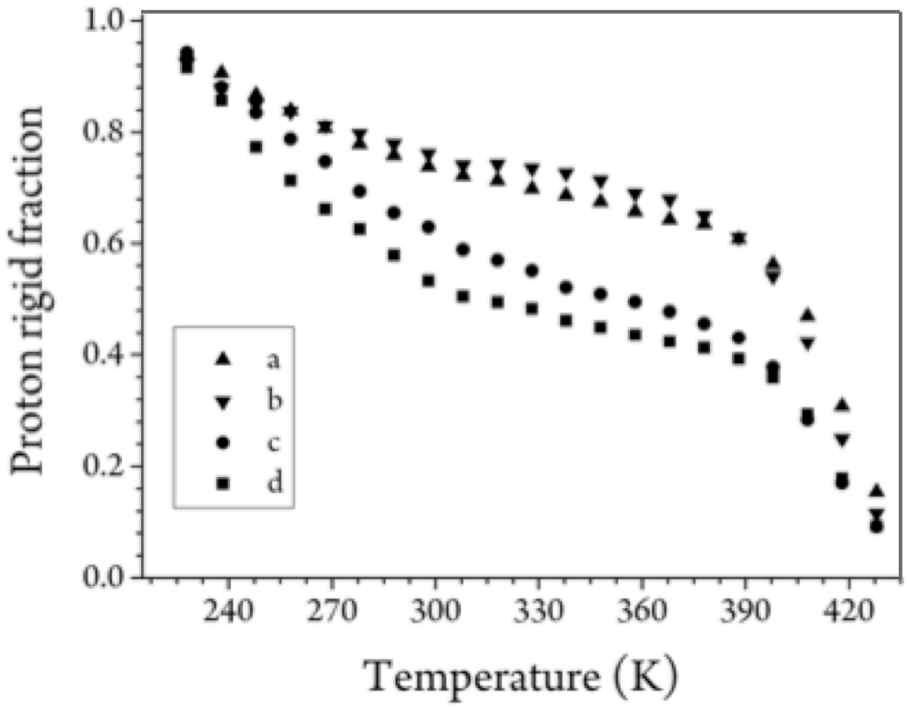

Figure 4.16: Temperature trend of PBA@PS core@shell nanoparticles rigid fraction (a.184 nm, b.127 nm, c.90 nm, d.45 nm).

TGA experiments on all samples showed that the former evidences are not due to an intermixing between the two homopolymers, PBA and PS. In fact, most probably due the increased AOT content in the emulsion formulation is also playing a pivotal role. Indeed in Figure 4.17 the TGA of all samples are shown and two significant weight losses are detected in 127 nm, 90 nm and 45 nm sample. By comparison with the TGA of pure AOT, in 127 nm sample the peak can be due to small traces of superficial AOT. Anyway such a weight loss in the order of ~ 4% w/W does not affect neither the DSC scan nor ATR-FTIR and TD-^{1}H-NMR spectra, suggesting no perturbation in the core@shell phase-separated morphology.

Far more detrimental in terms of morphology is the weight loss recorded in the temperature range between 276 °C and 286°C in the smallest samples of 90 nm and 45 nm. Taking into account that AOT degrades at 285°C, this weight loss can be ascribed to AOT presence within the sample. Moreover the measured weight loss for the 90 nm sample is 14.7% w/W and 31.2 % w/W for the 45 nm sample. This values is coherent with the amount of surfactant used during the synthesis.

In order to validate our vision, a check experiment was performed: the 45 nm sample was rinsed in MeOH at room temperature overnight under constant magnetic stirring, so to

extract the free AOT within the sample. After this step a white precipitate was still present. This white precipitate was then analysed with TGA (Figure 4.18).

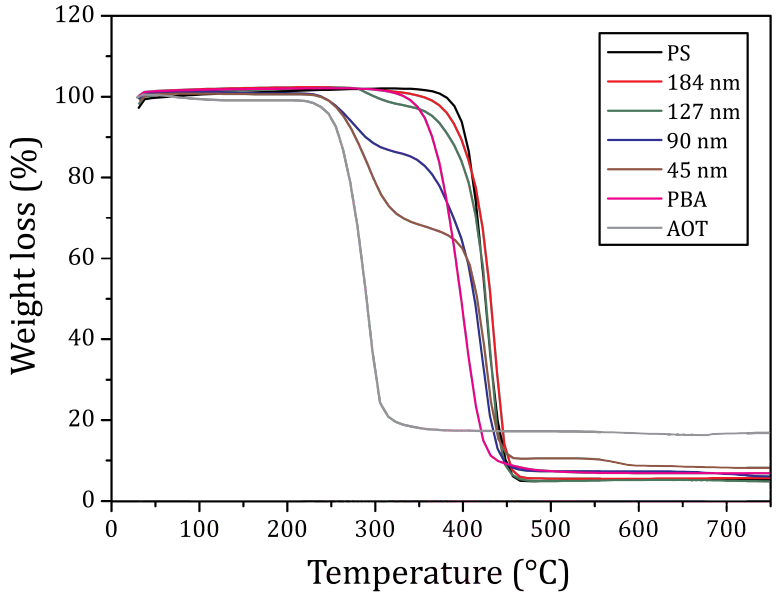

Figure 4.17: TGA curves on PBA@PS samples recorded in air. TGA of pure PS, pure PBA and AOT are reported for comparison. In the 90 nm and 45 nm samples a significant weight loss of 14.7% and 31.2% due to the presence of AOT is recorded.

In Figure 4.18 TGA traces of the pristine 45 nm PBA@PS sample (black line) and of the rinsed 45 nm PBA@PS (red line) are reported. The weight loss recorded in the temperature range between 276 °C and 286°C (i.e. the same range of the thermal decomposition of AOT) in the pristine sample decreases dramatically in the rinsed one.

Standing on these evidences, we can speculate that the surfactant is playing a crucial active role during the synthesis of the 90 nm and 45 nm sample. The over mentioned interphase effect are most probably due to phenomena connected to the high quantity of surfactant necessary to shrink the dimensions of the final nanoparticles.

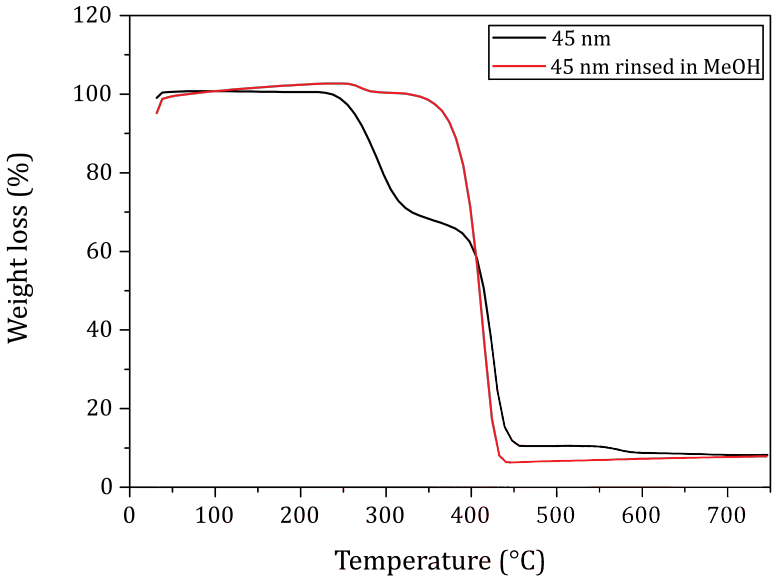

Figure 4.18: TGA curves of the PBA@PS sample of 45 nm pristine (black line) and on after rinsing in MeoH (red line) recorded in air. The AOT weight loss drops from 31.2% to traces in the order some percent.

Moreover, according to the AOT IR spectrum in Figure 4.19, the distortion of the peak in the region between 1100 cm^{-1} and 1300 cm^{-1} (i.e. region of the asymmetrical C-CO-O stretching) is not induced by a change in the inner morphology of the nanoparticles, but probably from the presence of AOT surfactant-rich interphase.

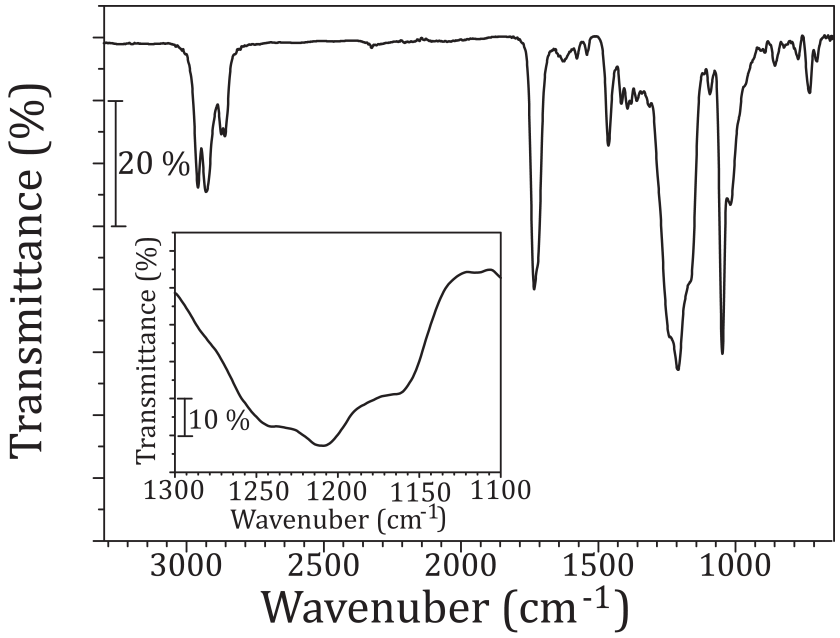

Figure 4.19: AOT IR spectra. The peak shape in the region between 1100 cm^{-1} and 1300 cm^{-1} (i.e. region of the asymmetrical C-CO-O stretching) mimics the distortion detected in Figure 4.15.

Lastly the third T_g detected with DSC and the drop in the proton rigid fraction detected with TD-^{1}H-NMR cannot be univocally ascribed to an intermixing between the PBA and PS domains to be described with Flory Equation. Indeed the results strongly suggest that AOT is not playing as a passive template agent, but contributes to form a not-defined mesophase in the 90 nm and 45 nm sample. Even if this can be really fascinating for the study of fundamental properties, this could dramatically limit the application of such nanostructures as well-defined, structured nanocontainers.

Concluding, standing on the evidence and control experiments we collected, the emulsion polymerization protocol here proposed is replicable and effective for the preparation of core@shell PBA@PS nanoparticles with a well-defined compartmentalized internal structure only for hydrodynamic diameter of the PBA core higher than 70 nm and for hydrodynamic diameter of the final core@shell nanoparticle higher than 90 nm. All the features have been taken into account in the following sections in order to give some proof-of-concept examples of potential application fields of such PBA@PS NPs.

4.5 *Poly(n-butyl acrylate)@Polystyrene nanoparticles acting as functional nanocontainers*

Selective loading of active molecule in nanocontainers has been gaining a growing interest recently[148]. Polymer nanoparticles obtained via Emulsion Polymerization (EP) are playing a pivotal role in the field of selective encapsulation of guest molecules [149]. Polymer nanoparticles and nanocapsules have indeed the capability of either protecting the environment from their content and the content from the environment (i.e. oxidation of guest molecule, aggregation for nanocrystals).

In our opinion PBA@PS core@shell Nanoparticles can act as a model for different nanocontainers preparation. Ideal core@shell PBA@PS nanoparticles offer a well defined and compartmentalized internal organization, with two regions defined either by the different chemical composition and the spatial position (Figure 4.20).

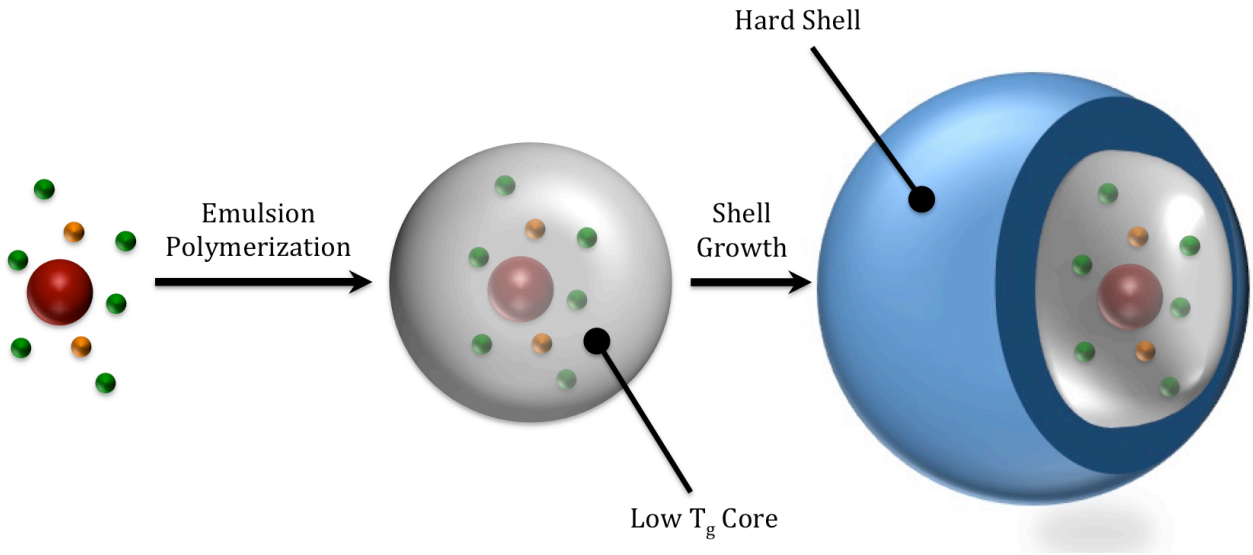

Figure 4.20: Graphical sketch of the stages involved in the formation of the core@shell nanocontainers.

Particularly PBA core is acting as the inner tank for the guest molecule, since it has flexibility, shape stability and sufficient permeability to molecules in the 4-8 nm diameter range[150]. Moreover PBA is a low-cost and easy-to-handle apolar elastomer with a T_g~-50°C belonging to polyacrylates. Together with the widespread application of polyacrylates in many commercial products[151], they are gaining growing interest in the most recent photonic research in the field of luminescent solar concentrators[152] and in sensitized up-conversion single phase bulk systems[153], because of their high optical quality.

Since we want to confine functional dyes inside deliverable nanocontainers with PBA core, a shell of a structural (i.e. with high T_g) and transparent polymer is needed. In this regard, PS

is a thermoplastic polymer with a $T_g \sim 100°C$ which can be made transparent. On top its chain mesh properties can be easily tuned via the copolymerization with divinylbenzene, allowing the modulation of the T_g values together with the final bulk properties. Thanks to its hydrophobicity it can be either easily polymerized in emulsion and it can effectively cover the PBA core in semicontinuous two-step EP (section 2.2.1.3).

In the following sections, two possible applications of the PBA@PS core@shell nanoparticles are proposed (Functional nanocontainers for Sensitized Up-Conversion-SUC, section 4.5.1, and for the encapsulation of modified carbohydrate-based dyes, section 4.5.2).

4.5.1 Sensitized Up-Conversion polymer-based nanocontainers

Sensitized Up-Conversion (SUC) is a recent photon managing strategy particularly promising in the field of solar energy [154] and photocatalytic water splitting [155]. SUC phenomenon is obtained with non-coherent low-intensity sources and it is based (Figure 4.21) on the annihilation of metastable triplet states (TTA) of proper organic dyes (acceptors) indirectly populated via resonant energy transfer (ET) from selected sensitizers (donors)[156].

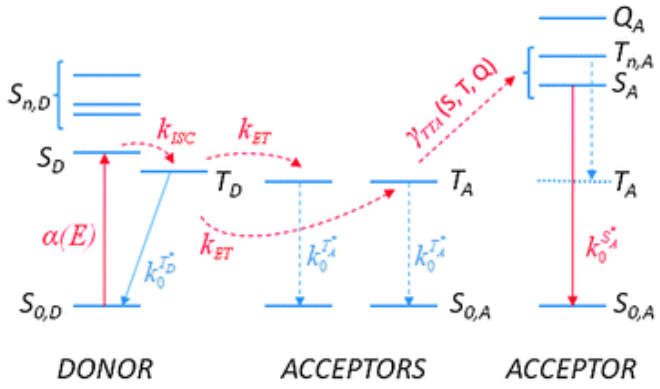

Figure 4.21: Outline of the energy levels involved in the SUC process for a model donor/acceptor pair. Solid arrows indicate transitions in which a photon is involved while dashed arrows indicate radiation less transitions. After A. Monguzzi *et al Phys. Chem. Chem. Phys.* 2012, *14*, 4322. Copyright © Royal Society of Chemistry.

The involved photophysics is to date well assessed and summarized in the contribution of A. Monguzzi *et al*[157]. SUC has been obtained in various spectral windows (from NIR to UV) in solution with non-coherent excitation powers density around 0.1 mW/cm^2 and overall quantum yield as high as 25-30% [158]. Even thought J.P. Spindler *et al.* [159] indirectly demonstrate that the ultimate overall quantum yield can reach 50%, the use of high volatile organic solvents poses significant issues for industrialization, particularly regarding the environmental sustainability of the technology.

There is indeed a strong effort in building up a solid state SUC material. It is worth noticing that SUC performances obtained in solution have been only partially replicated at solid state, where SUC lacks of efficiency[160]. This is mainly due to the fact that SUC is ruled by short range interaction such as Dexter Energy Transfer and TTA. The latters are both bimolecular interactions determined by the triplet diffusion length, which can be expressed as L_D:

$$L_D = \sqrt{D\tau_T}$$

where τ_T is the triplet lifetime and D is the triplet diffusion coefficient. D can be expressed as a function of the parameters of the matrix and of the diffusing species:

$$D = \frac{kT}{6\pi\eta R}$$

T is the temperature, k is the Boltzmann constant, η is the viscosity of the matrix and R is the radius of the diffusing species in spherical approximation.

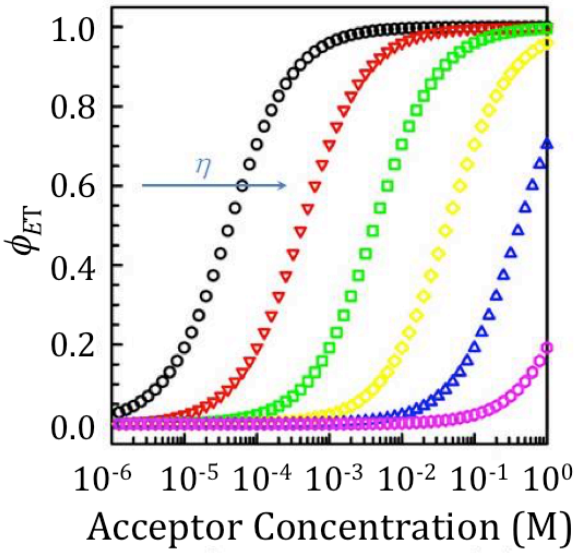

Figure 4.22: Calculated energy transfer efficiency (ϕ_{ET}) as a function of acceptor concentration in matrices with different viscosity (η). Courtesy of Dr. Angelo Monguzzi.

Standing on this considerations, the short-range interactions involved in both ET and TTA steps impose severe requirements on the excitation mobility[161], not fulfilled at solid state. Indeed in Figure 4.22 one can see that - by keeping constant Donor and Acceptor concentrations - the higher the viscosity of the matrix, the lower is the energy transfer. This is a semi-quantitative demonstration of the fact that SUC in solid matrix is difficult to achieve since the molecular diffusion of the dyes is limited. However, A. Monguzzi *et al.*[153] recently overcame this limit and obtained for the first time a SUC yield in solid comparable with that of

the corresponding solution under excitation of few times the solar irradiance, by employing a single phase elastomeric material (PBA). They showed that the performance of these systems are strictly comparable with those in liquid phase since the low molecular mobility is compensated by a lengthening of the triplet lifetimes which still allows for the required large diffusion length of excitation energy.

Following this evidences in this section we present the results about the engineering of a nanocontainer PBA@PS core@shell nanoparticle, with the PBA core loaded with SUC acceptor donor pair, in order to obtain deliverable SUC nanoemitters. This work is in collaboration with Prof. Dr. Franco Meinardi's group.

4.5.1.1 Inclusion of Pd- Tetrabenzotetraphenyl porphyrin, SUC Donor

In order to incorporate effectively the SUC Donor (Pd-Tetrabenzotetraphenyl porphyrin/ $PdPh_4TPB$, Figure 4.23) in the PBA core via the over mentioned EP protocol, a surfactant acting as monomer droplet template is needed.

Porphyrins are receiving particular attention thanks to their well-understood rigid and planar molecular geometry, together with their tailorable spectroscopic and photochemical properties, as well as their renowned multifuncionality and eventual biocompatibility. All these issues are boosting the research on porphyrin-based supramolecular nanoarchitectures, which are supposed to be very promising candidates for the development of advanced supramolecular nanomaterials[162].

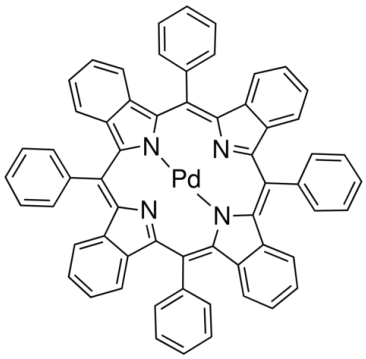

Figure 4.23: SUC donor, Pd-Tetrabenzotetraphenyl porphyrin ($PdPh_4TPB$).

Moreover porphyrins are renowned for their ability of form such supramolecular aggregates in presence of surfactant such as sodium dodecyl benzene sulphonate, with the so-called Surfactant Assisted Self-assembly (SAS)[163]. In the SAS process organic molecules,

which are dissolved in a guest solvent, are organized with the assistance of surfactants dispersed in a host solvent. The structure of porphyrins[164], concentration of porphyrins[165] and concentration of surfactants[166] are responsible for SAS.

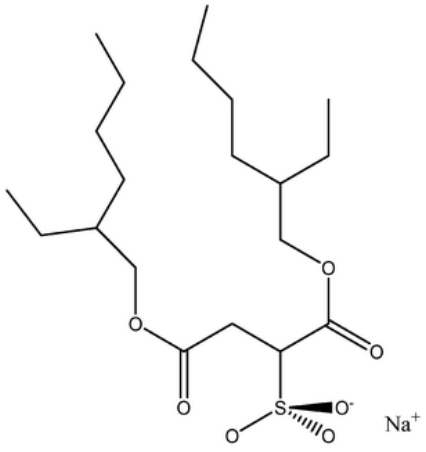

Figure 4.24: Dioctyl sulfosuccinated sodium salt molecular structure.

Since in the present study we are interested in exploiting $PdPh_4TPB$ as a SUC donor in a single-phase core@shell nanoparticle core, porphyrin SAS ability is a tremendous issue to solve in order to maintain the dynamics of SUC process and not spoil or inhibit the SUC interaction between $PdPh_4TPB$ and its acceptor 9,10-Bis-phenelethyinil-antracene (BPEA, Figure 4.27). Since porphyrin SAS is most likely happening with surfactant having a single aliphatic chain (i.e. cetyltrimethylammonium bromide[167] or sodium dodecyl sulphate[168]), we decided to keep using dioctyl sulfosuccinate sodium salt (AOT, Figure 4.24) as a branched surfactant with higher steric hindrance and less prone to SAS aggregations. In order to validate our picture and verify the incorporation of Pd-TBTPP in a PBA@PS core@shell nanoparticles, a solution 0.1 mM of Pd-TBTPP in 21 mmol of BA was polymerized via the over mentioned EP protocol (0.04 mmol of AIBN, 0.69 mmol of AOT) in N_2 atmosphere. Prior to polymerization the feeding solution was purified and degased with three cycles of Freeze/Pump/Thaw (FPT). After three hours of reaction at 70°C, a solution of 78.3 mmol of STY, 89 μl of divinylbenzene (DVB), 0.174 mmol of AIBN and 0.464 mmol of AOT was added to the PBA emulsion to grow the shell. All the steps of the reaction were driven under N_2 atmosphere. The final core@shell nanoparticles show a diameter of 110 nm with PdI=0.039. It was not possible to measure the core dimensions, since the $PdPh_4TPB$ is adsorbing at λ=633 nm of the DLS system, spoiling thus the correlation data. The spherical shape and the monodispersity of the nanocontainers are confirmed by SEM micrograph in Figure 4.25.

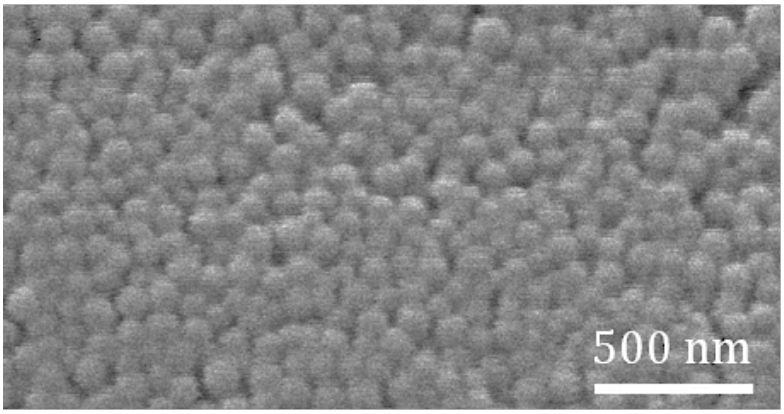

Figure 4.25: Representative SEM micrograph of SUC PBA@PS nanocontainers.

In order to check the incorporation of $PdPh_4TPB$ in the core@shell structures, absorption spectra were recorded (Figure 4.26).

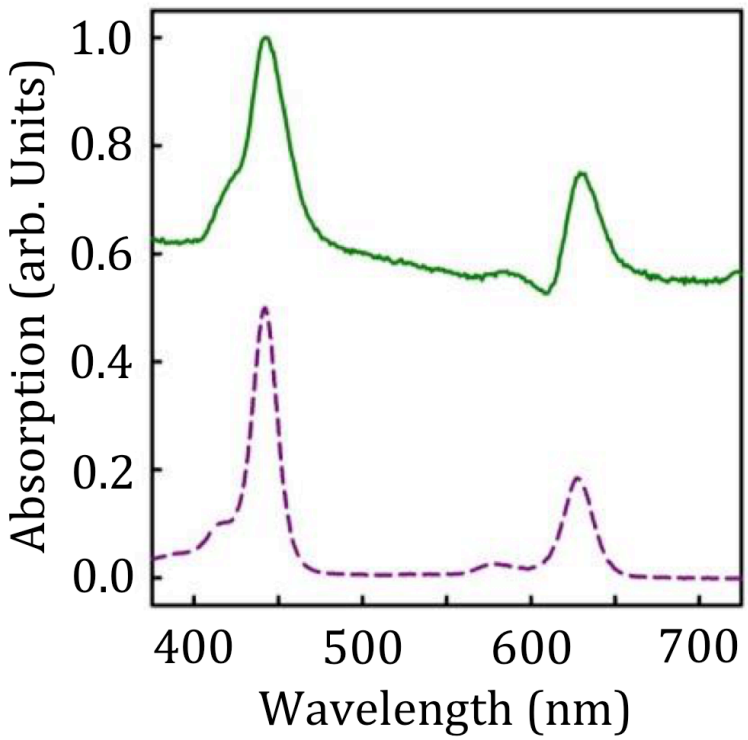

Figure 4.26: Comparison between absorption spectrum of $PdPh_4TPB$ in PBA@PS Nanoparticles (green line) and in bulk PBA sample (violet dashed line) under 632 nm laser excitation.

In Figure 4.26 a comparison between the spectrum of a bulk PBA sample loaded with 0.1 mM of $PdPh_4TPB$ (violet dashed line) and the spectrum of $PdPh_4TPB$ inside the nanoparticles (green line) is reported. Standing on the spectral shape and on the spare solubility of $PdPh_4TPB$ in STY, it is possible to say that the $PdPh_4TPB$ is confined in the PBA core.

For recording a SUC signal, the absence of oxygen is needed (namely oxygen concentration below 0.1 ppm). The absence of oxygen can be checked by TR-photoluminescence experiments in Figure 4.27.

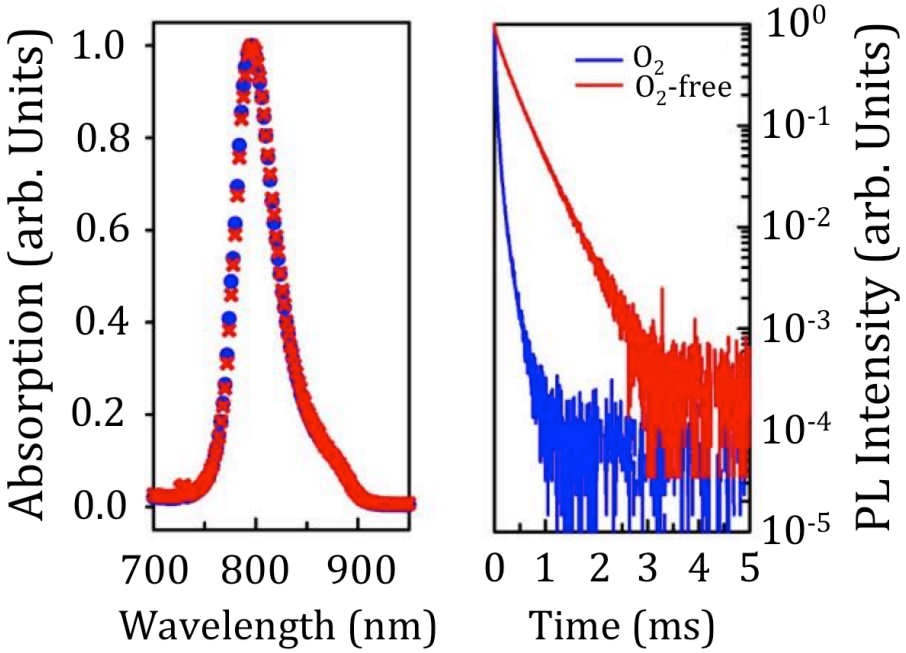

Figure 4.26: LEFT- Absorption spectra (zoom in the 700 to 900 nm region) of an oxygen free (red line) and an in-oxygen (blue line) PBA@PS $PdPh_4TPB$ batches under 632 nm laser excitation. RIGHT- TR-Photoluminescence of an oxygen-free (red line) and an in oxygen (blue line) sample under 632 nm modulated excitation .

In Figure 4.27-RIGHT photoluminescence (PL) and Time resolved photoluminescence (TR-PL) data from a PBA@PS core@shell nanoparticles synthesized under N2 atmosphere (Red circles, red line – labelled O_2-free) and in presence of oxygen (Blue circles, blue line – labelled O_2) are reported. Static PL (Figure 4.27-LEFT) is not sensitive to the synthesis atmosphere, since the spectra is not changing between the two samples. On the other hand TR-PL spectra (Figure 4.37-RIGHT) shows that only in the oxygen-free sample the $PdPh_4TPB$ has a lifetime long enough to lead to SUC.

4.5.1.2 Energy transfer efficiency study

In order to study the energy transfer efficiency of the process, five samples with different concentration of 9,10-Bis-phenilethynil-antracene, BPEA, acceptor (Figure 4.28) in the PBA core were synthesized. A scale down of the reaction was performed by reducing the overall amount of water to 53 ml. All the other quantities were reduced accordingly.

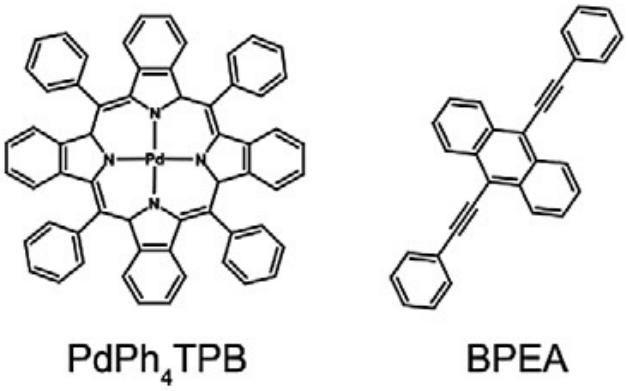

Figure 4.27: Molecular structure of the dyes used as SUC couple. Pd-TetraBenzoPhenilPorphyrin ($PdPh_4TPB$, left) is the donor while 9,10-Bis-phenilethynil-antracene (BPEA, right) act as acceptor.

Typically for the core emulsion polymerization 7 mmol of BA were mixed with $(2.6\pm0.1)\cdot10^{-2}$ mmol of AIBN and $2.5\cdot10^{-1}$ mmol of AOT. The $PdPh_4TPB$ was added in order to obtain a $1\cdot10^{-4}$ M solution. The shell growth was performed by adding a second feed solution containing 26 mmol of STY, 29.5 ml of DVB, $(5.8\pm0.2)\cdot10^{-2}$ mmol of AIBN and $1.5\cdot10^{-1}$ mmol of AOT. All the remaining reaction parameters (dropping, reaction times and temperature) were kept from the synthesis in section. The five different batches of PBA@PS nanoparticles synthesized had an average hydrodynamic diameter of (112 ± 20)nm calculated within the series. All the single average diameters are monomodal and monodisperse (PDI<0.1). In Figure 4.29 the PL intensity upon excitation at 635 nm in the wavelength region from 400 nm to 600 nm associated to SUC signal is reported. Sample 30 and 33 shows the best relative SUC intensities among the series.

Reaction Labelling	BPEA-Acceptor Concentration
30	$5\cdot10^{-4}$ M
31	$2.5\cdot10^{-4}$ M
32	$1\cdot10^{-3}$ M
33	$2.5\cdot10^{-3}$ M
34	$5\cdot10^{-3}$ M

Table 4. Reaction labelling and BPEA-acceptor concentrations used in the PBA@PS samples series synthesized for the study of the SUC process.

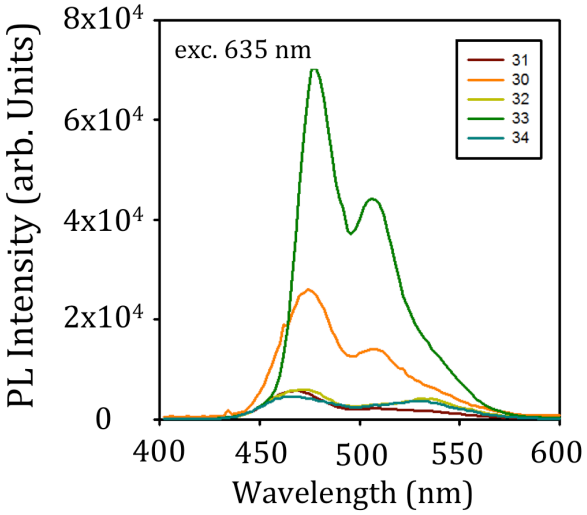

Figure 4.28: PL intensity in the wavelength region from 400 nm to 600 nm associated to SUC signal (excitation wavelength of 635 nm).

However, in Figure 4.30 the residual $PdPh_4TPB$ PL intensity upon excitation at 635 nm is reported. The residual PL intensity of the donor means that there is a fraction of donors ($PdPh_4TPB$) not transferring energy to the acceptor molecule. This can be due to several reasons: deactivation of acceptor molecules due to the confined environment (i.e. droplet) where the polymerization takes places, migration to some of either the donor dyes to the interface defined by the anionic surfactant or of the acceptor molecule to the PS shell due to π–π interactions.

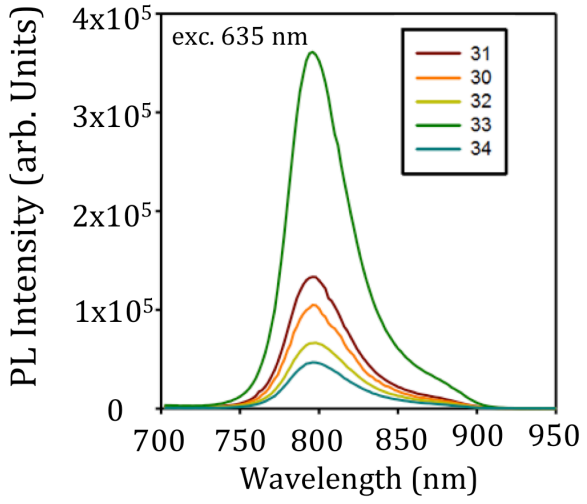

Figure 4.29: PL intensity of the residual $PdPh_4TPB$ (donor) upon excitation at 635 nm in the wavelength region between 700 nm and 950 nm in PBA@PS samples.

In order to speculate the motivation of the residual $PdPh_4TPB$, five PBA bulk samples loaded with the SUC dyes were synthetized and characterized. BPEA and $PdPh_4TPB$ have been added to 2 mL of *n*-butyl acrylate containing 10^{-3} M AIBN, changing the BPEA concentration from 10^{-6}M to $5 \cdot 10^{-3}$ M. $PdPh_4TPB$ concentration was kept constant at $1 \cdot 10^{-4}$ M. Free radical bulk polymerization has been carried out at RT until the liquid converted to self standing rubber (barely 1 week).

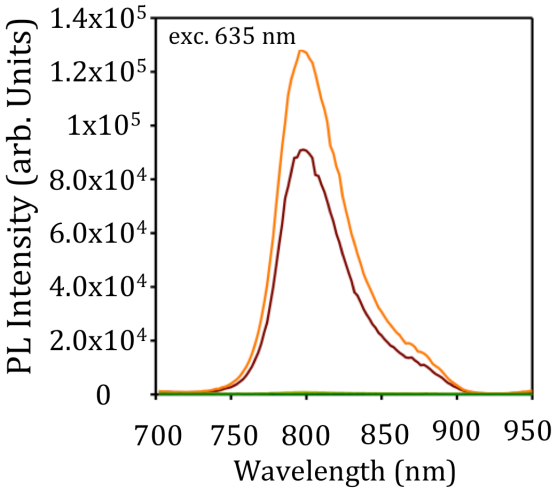

Figure 4.30: PL intensity of the residual $PdPh_4TPB$ (donor) upon excitation at 635 nm in the wavelength region between 700 nm and 950 nm in bulk PBA samples.

In Figure 4.31 the PL intensity of the residual $PdPh_4TPB$ (donor) upon excitation at 635 nm in the wavelength region between 700 nm and 950 nm in bulk PBA samples. Differently from PBA@PS sample, the residual PL intensity of the porphyrin drops to zero (i.e. complete energy transfer) for BPEA concentration around 2.5 10^{-3} M.

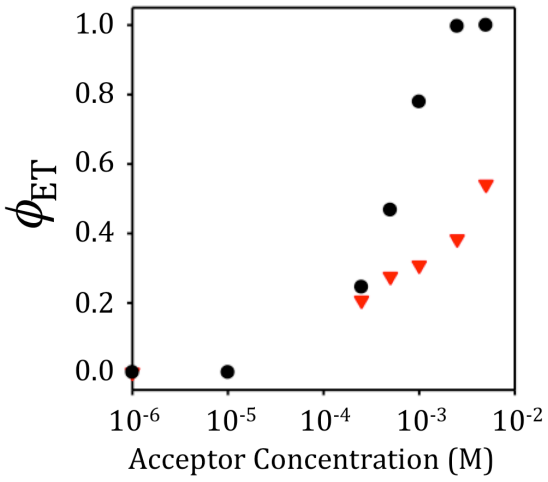

Figure 4.31: Comparison of ET yields in PBA@PS core@shell nanoparticles (red triangles, 58% record value) and PBA bulk samples (black circles, 100% record value) as a function of acceptor concentration C_A.

By calculating the ET yield as Φ_{ET} = 1- (τ_{ET}/τ_0), where τ_0 is the $PdPh_4TBP$ lifetime in PBA@PS particles without BPEA and τ_{ET} is the $PdPh_4TPB$ lifetime in PBA@PS particles in presence of a given amount of BPEA, one can estimate the energy transfer efficiency as a function of BPEA acceptor concentration (Figure 4.32). From the ET yield versus acceptor concentration in Figure 4.32, it is possible to see that PBA@PS samples are not able to reach the 100% yield (record value around 58%). On the other hand in PBA bulk samples 100% ET yield is reached either in the 2.5 10^{-3} M and 5 10^{-3} M BPEA samples.

In our opinion the reason for this inefficiency are manifold. First of all emulsion polymerization occurs in a confined locus, namely the 10^2 nm droplet. Within the polymerizing droplets phenomena such as radical formation, propagation and desorption are occurring and could be potentially detrimental for a coniugate molecule like BPEA. Moreover the stability and the dimension of the droplets are defined from the presence of AOT, an anionic surfactant. Besides, AOT could thus attract the $PdPh_4TPB$ (porphyrin enclosing a metal cation), sequestrating part of the Donor at the interface. The donor trapped at the interface is no more able either to diffuse nor interact with the acceptor and drive the SUC process. The last option can be the migration of the conjugated acceptor BPEA in the PS shell, because of $\pi-\pi$ interactions.

Moreover, the scattering is playing an important role in the drop of the ET yield. PBA@PS in aqueous solution act as scatterers, meaning that a considerable fraction of the incident photons is just scattered away.

However we have been able to produce different batches of PBA@PS nanoparticles acting as SUC nanoemitters. The ET yield of the PBA@PS nanoemitters reached the 58% in water, opening potential application in terms of bioimaging and photodynamic therapies but also triggering new idea to solve the over mentioned problems. In fact a possible solution is proposed in section 5.3.

4.5.2 Inclusion of hydrophobic carminic acid derivatives in polymer matrices and nanoparticles

Among all different classes of natural pigments, carminic acid belongs to the so-called Hydroxyanthraquinoids (HAQN, Figure 4.33). HAQN are widely used in cosmetic manufacturing[169], textile dying[170], food biocolorants[171] and only recently in other fields such as coordination applications[172] and dye-sensitized solar cells[173].

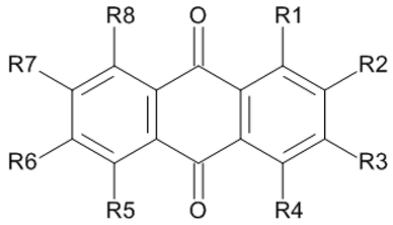

Figure 4.32: Scaffold of Hydroxyanthraquinoids.

All HAQN dyes are polar molecules with extended hydrogen bonding responsible for their spare solubility in water and for their complete insolubility in apolar (lipophilic) systems, such as synthetic monomers.

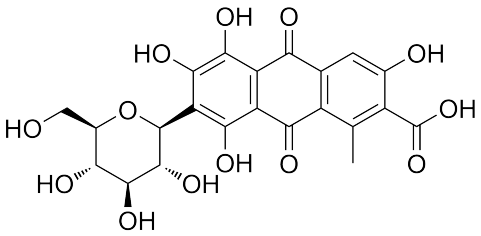

Figure 4.33: Structure formula of carminic acid.

Namely, carminic acid (Figure 4.34) is a red dye extracted from cochineal insects (dactylopius coccus)[174] with a peculiar resistance to light, heat and chemical oxidation, making it even more stable then synthetic food colorants. Nevertheless it is unstable at low pH. To date, very few carminic acid derivatisation have been proposed in order to tune its hydrophilicity and solubility in organic phases.

Together with Prof. Dr. Laura Cipolla we have included – for the first time to our knowledge – hydrophobic carminic acid derivatives in organic polymer matrices and biphasic polymer nanoparticles. The proposed derivatisations, modifying the hydroxyl groups present

in the molecule, make the dye more hydrophobic by ester bonds entering and allowing industrial applications.

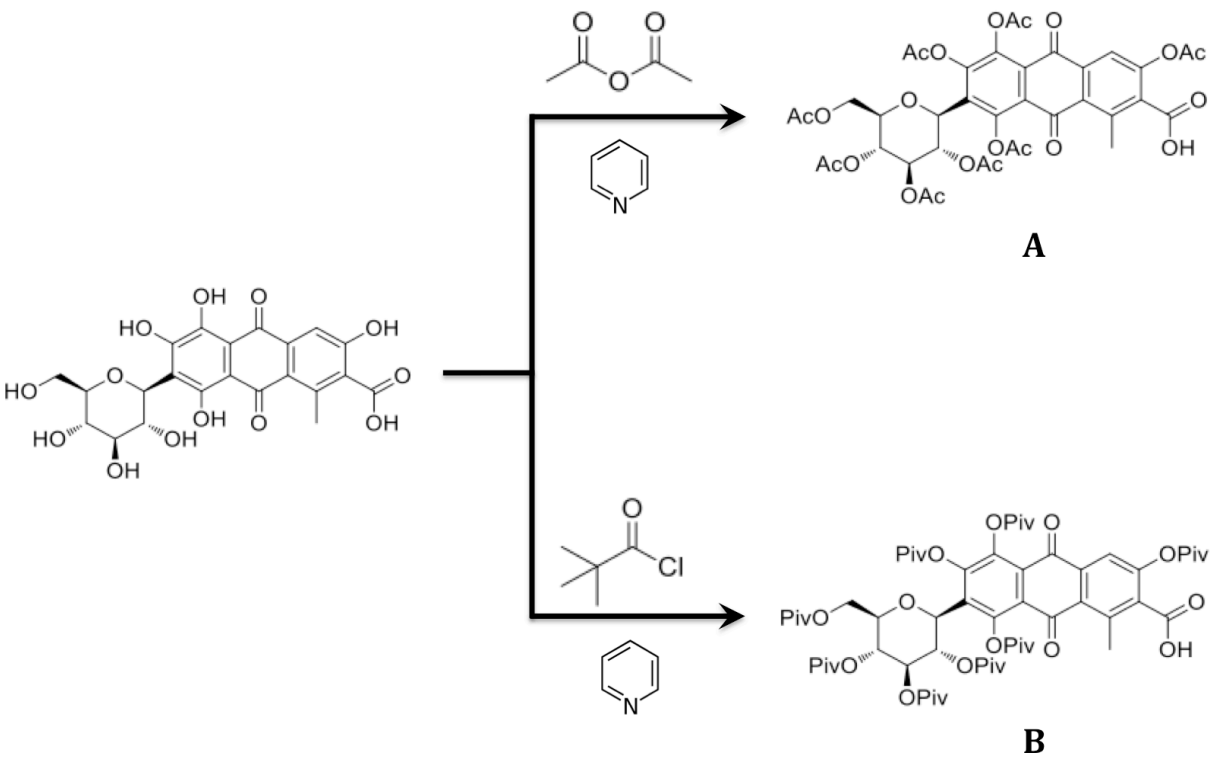

Figure 4.34: Modification of carminic acid with acetic anhydride and pyridine (A), pivaloyl chloride and pyridine. Courtesy of Davide Origgi, M.Sc. synthesizing the derivatives.

The acetylation of carminic acid with acetic anhydride in pyridine as reaction solvent is proposed (Figure 4.35-A). Usually, carbohydrates request 4-dimethylaminopyridine (DMAP) as catalyst promoting the attack of the anhydride. The nucleophilic character of the endocyclic nitrogen within the aromatic ring of DMAP makes the attack in position 4 of the anthraquinone portion possible. The reaction requires an excess of anhydride to promote the attack on the hydroxyls present in the molecular structure of the pristine dye. The particular reactivity of the hydroxyanthrapurin portion of the dye does not allow a stoichiometric reaction. The reaction is quenched in ethanol to carry out an extraction with ethyl acetate and HCl (5 %) to recover the hydrophobic product obtained from the reaction. Finally, a mixture of compounds with a brilliant orange colour (Figure 4.36-center) is obtained. We will refer to this mixture as to first derivative, called **5** in the following.

The second reaction proposed is the functionalization of the hydroxyl groups of carminic acid with pivaloyl chloride in pyridine solvent. This reaction requires an excess of the acyl chloride to counteract the reactivity of anthraquinone dye (Figure 4.35-B). The resulting product consists almost entirely of the fully esterified compound, showing a bright

yellow colour (Figure 4.36-RIGHT). This pivaloyl derivative will be labelled as **6** in the following.

Figure 4.35: LEFT: Photograph of the dry powders of carminic acid (red, labelled 2). CENTRE: acetylated derivative (orange, labelled 5). RIGHT: pivaloyl-derivative (yellow, labelled 6).

In Figure 4.36, the photograph of the dry powders of the pristine carminic acid (**2**), of the acetylate-derivative mixture (**5**) and of the pivaloyl-derivative (**6**) is reported. A colour shift from red (**2**) to orange (**5**) and yellow (**6**) is observed by naked eye. In order to investigate quantitatively the optical properties of **2**, **5** and **6**, absorption and steady-state photoluminescence (PL) analysis were performed.

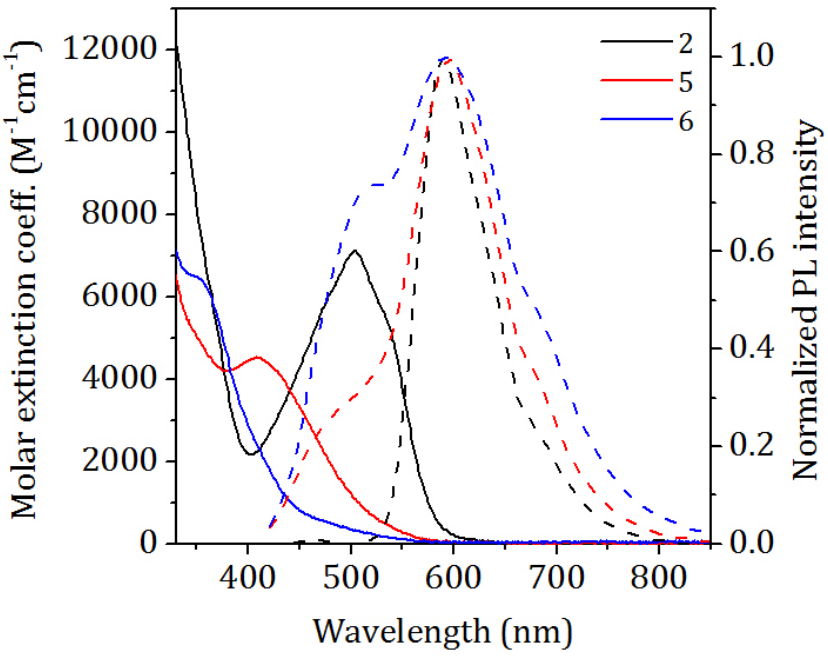

Figure 4.36: Molar extinction coefficient (solid-lines) and PL (dashed lines) spectra (dashed-lines) acquired for compounds 2, 5 and 6 in dimethyl sulfoxide.

Since dimethyl sulfoxide (DMSO) was indeed found to be a good solvent for all the dyes, the molar extinction coefficients estimated for compounds **2**, **5** and **6** in DMSO solution are shown in Figure 4.37 (solid lines). Carminic acid absorption spectrum is dominated by a band peaked at about 500 nm, conferring its characteristic red colour. It is worth noticing that derivatives **5** and **6** show a hypsochromic shift (i.e. blue shift) of the main peak. Indeed, molecule **5** has a band peaked at about 410 nm, whereas only a shoulder at 360 nm can be detected for compound **6**. A hypsochromic effect is usually observed when derivatisation is performed with substituents causing a reduction in conjugation of the chromophore.[175]

Moreover, in the same Figure 4.37 (dashed lines), the steady-state PL spectra of all the three compounds in DMSO solution are presented. PL spectrum of carminic acid (**2**) is peaked at 610 nm, while the PL spectra of the derivatives **5** and **6** are dominated by the same emission with the superimposition of a band peaked at about 500 nm. This latter band is more intense for the molecule **6** than for **5**, in qualitative agreement with the more blue-shift observed in the absorption spectra (continuous line in Figure 4.37).

4.5.2.1 Bulk Polymer matrices

Once obtained the carminic acid lipophilic derivatives, the incorporation into a PBA matrices was performed. The PBA samples were obtained by bulk polymerization (Figure 4.38) at 80°C for 24 hours of a BA solution with 60 ppm of an oil-soluble radical initiator (2,2'-Azobisisobutyronitrile, AIBN) and a dye concentration of 10^{-3} M. Bulk free radical polymerization was used because it is know to be the only synthetic method allowing the production on an industrial scale of thick and large polyacrylates plates having excellent optical properties[176]. Moreover, it can be performed without the need of organic solvents.[177]

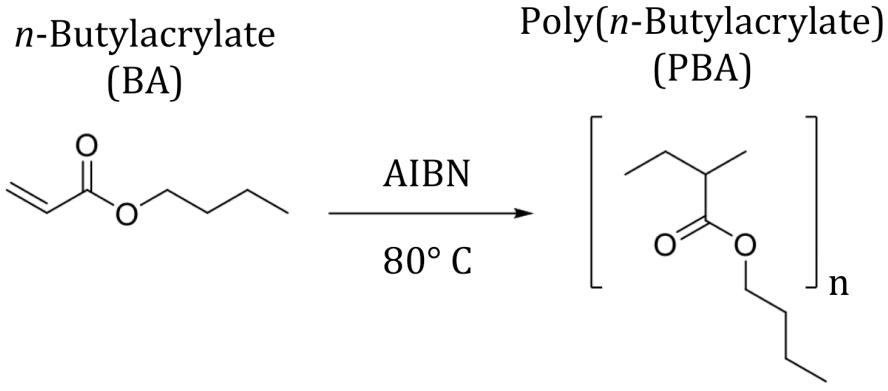

Figure 4.37: Bulk polymerization reaction of *n*-butyl acrylate monomer to poly(*n*-butyl acrylate).

BA was previously purified through distillation on aluminium oxide (activated, basic, Brockmann I) column and AIBN was re-crystallized twice from methanol before usage. As one can see from Figure 4.39-LEFT, pure carminic acid cannot be dissolved in BA leading to phase separation. On the other hand, the synthesized derivatives **5** (Figure 4.39-CENTER) and **6** (Figure 4.39-RIGHT) dissolve very well in the organic BA monomer and the polymerization could proceed until conversion without phase separation.

Figure 4.38: LEFT: Photograph of a 10^{-3}M solution of carminic acid in a BA solution. Phase separation is clearly visible. CENTER: Photograph of a 10^{-3}M solution of the carminic acid acetyl-derivative (5) in a BA solution. RIGHT: Photograph of a 10^{-3}M solution of the carminic acid pivaloyl-derivative (6) in a BA solution.

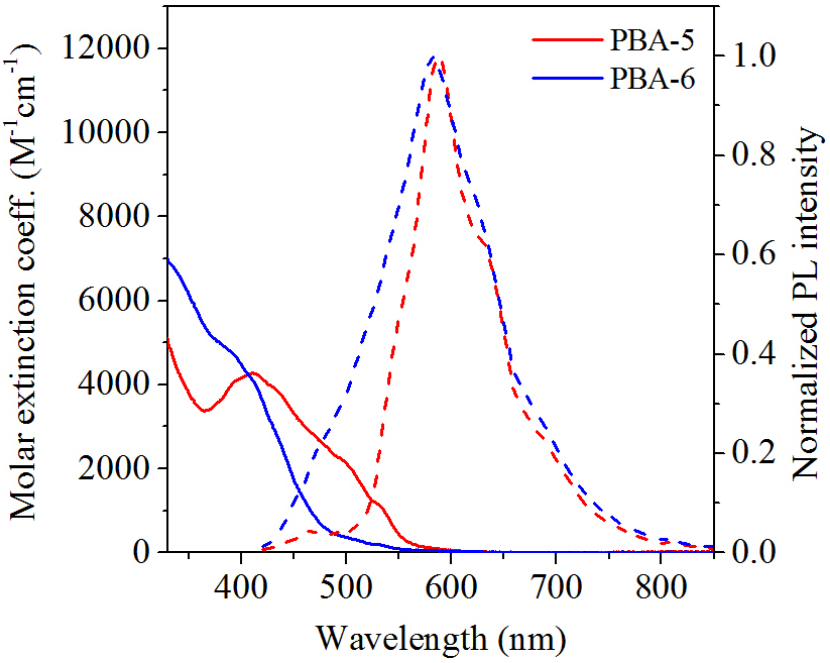

Figure 4.39: Molar extinction coefficient (solid-lines) and PL spectra (dashed-lines) acquired for PBA-5 and PBA-6 samples.

The absorption and steady-state spectra acquired for PBA samples doped with derivative **5** and **6**, named respectively **PBA-5** and **PBA-6,** are shown in Figure 4.40. Both samples exhibit almost the same absorption spectra, in terms of shape and molar extinction coefficient, with respect to the behaviour of molecule **5** and **6** in DMSO. This suggests that the PBA matrix

does not affect their absorption properties. Similar observations were found by comparing their PL spectra in DMSO solution and in bulk polymer matrix. Moreover the presence of dyes **5** and **6** does not alter the T_g-value expected for PBA. Indeed the measured T_g (continuous line in Figure 4.41) remains ~ -50°C (midpoint) in both **PBA-5** and **PBA-6** sample.

Additionally the derivatives **5** and **6** are soluble in PBA and Ethylene glycol dimethacrylate (PBA:EGDMA) solutions. In detail, 6.0 mg of dye, 2.5 mg of AIBN were added in 4.3 ml solution with the 4.5% in volume of EGDMA. The formulation was then put in a sealed mould at 80°C till complete conversion. By adding EGDMA as crosslinking agent, it is possible to obtain elastomeric sample suitable for the preparation of self-standing polymer goods. A representative photograph of the samples is reported in Figure 4.41.

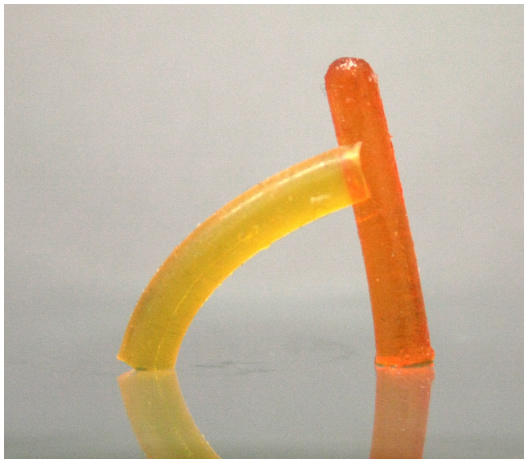

Figure 4.40: Photograph of PBA:EGDMA (4.5% v/V EGDMA content) self-standing bulk-samples. LEFT: yellow sample loaded with the 6 derivative. RIGHT: the orange sample loaded with the 5 derivative.

DSC traces for PBA and PBA:EGDMA samples doped with molecules **5** and **6** are reported in Figure 4.42. The cross-linked sample (dashed line) shows an increase in the measured T_g value in the order of some degrees (typically from -50°C to -46°C for midpoint values) due to the presence of EGDMA. Similarly to the case pure PBA dye-doped samples, even PBA:EGDMA thermal properties (in terms of T_g-value) seems to be unaffected by the presence of both dye **5** and **6**.

All these findings suggest that the two synthetic molecules characterized by a more hydrophobic nature than carminic acid, can be used such as dye for polymer matrices, preserving the absorption properties observed in DMSO solution and their colour. PL investigation reveals that the well-known emission band at 610 nm of the carminic acid is also found in molecules **5** and **6**. However, these latters show in solution another emission band at 500 nm (missing in the molecule **2**), due to the hypsochromic shift triggered by derivatisation.

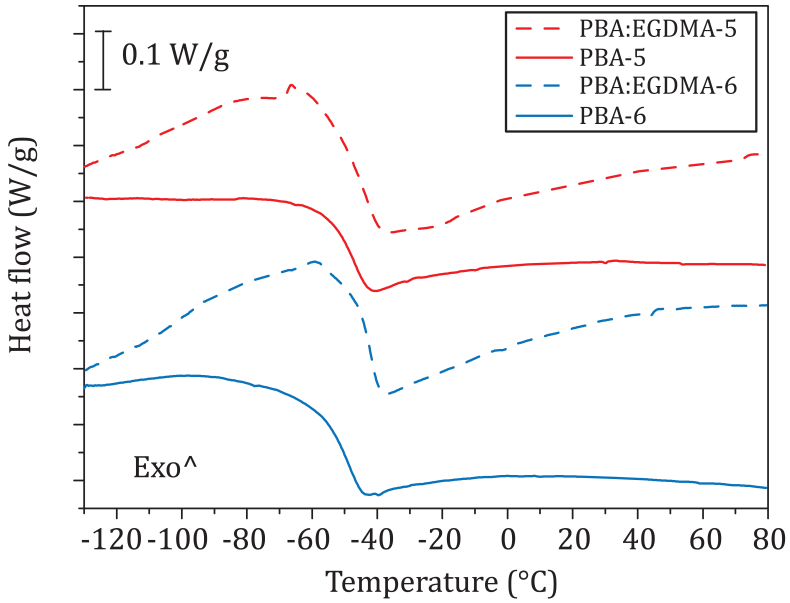

Figure 4.41: DSC traces (first scan, exo up) of the PBA (continuous lines) and PBA:EGDMA (dashed lines) samples doped with derivatives 5 (red lines) and 6 (blue lines).

Moreover we demonstrated (Figure 4.41) that derivatives **5** and **6** can be successfully used to homogeneously dope self-standing bulk polymeric samples, thus opening potential routes towards bio-inspired dyes in polymer industry.

4.5.2.2 PBA@PS Nanoparticles

In the previous section, the incorporation of lipophilic derivatives of carminic acid was proposed. Here the encapsulation of the acetylated-derivative into PBA@PS polymer nanocapsules is showed. This dye was chosen because its chromic properties are the closest to the pure carminic acid ones.

An organic solution composed by 7.4 mg of AIBN and 3 ml of BA monomer was used as solvent for dissolving the acetylated-derivative of carminic acid (final dye concentration ~ 10^{-3}M). The organic solution was dissolved into a degassed aqueous phase of 50 ml of water containing 27.3 mg of AOT surfactant. After homogenization, the temperature was set at 70°C. After three hours of reaction, the core dimensions were checked by DLS (124 nm and PdI<0.1) and the shell forming formulation (6 ml of STY, 16.1 mg of AIBN and 59 μl of DVB) was added drop wise in the reaction flask. Final core@shell PBA@PS size distribution measured by DLS resulted in a monodisperse peak of 183 nm average diameter. After water evaporation and drying, a pink precipitate was obtained (Figure 4.43)

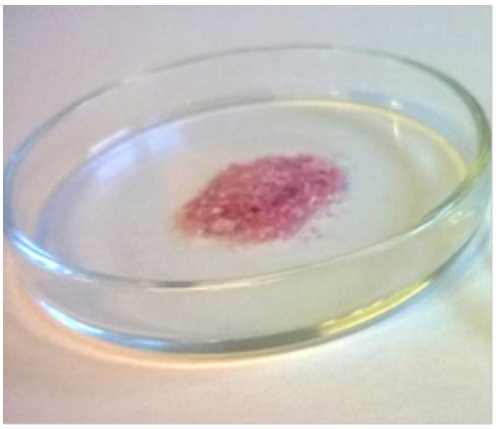

Figure 4.42: Photograph of the PBA@PS core@shell particles loaded with the acetylated derivatives of carminic acid. Neither dye leakage nor fading were observed from the powder even after several months.

The powder was stored in air at ambient condition for several months, without showing any dye leakage or fading.

5 *Liquid-core n-hexadecane@poly(methyl methacrylate) Nanocapsules*

5.1 Introduction

The petroleum shortages during the 1970s energy crisis - affecting most of the western countries - triggered the efforts of the research and economic community towards alternative energy sources and energy management behaviour, potentially fulfilling the world energy demand. Some seventy years before, in 1901 Kyle filed a patent[178] on using palmitic acid and stearic acid to maintain the required temperature during the manufacturing of tin sheets. Palmitic acid and stearic acid are fatty acid known to belong to the so-called Phase Change Materials PCMs[179].

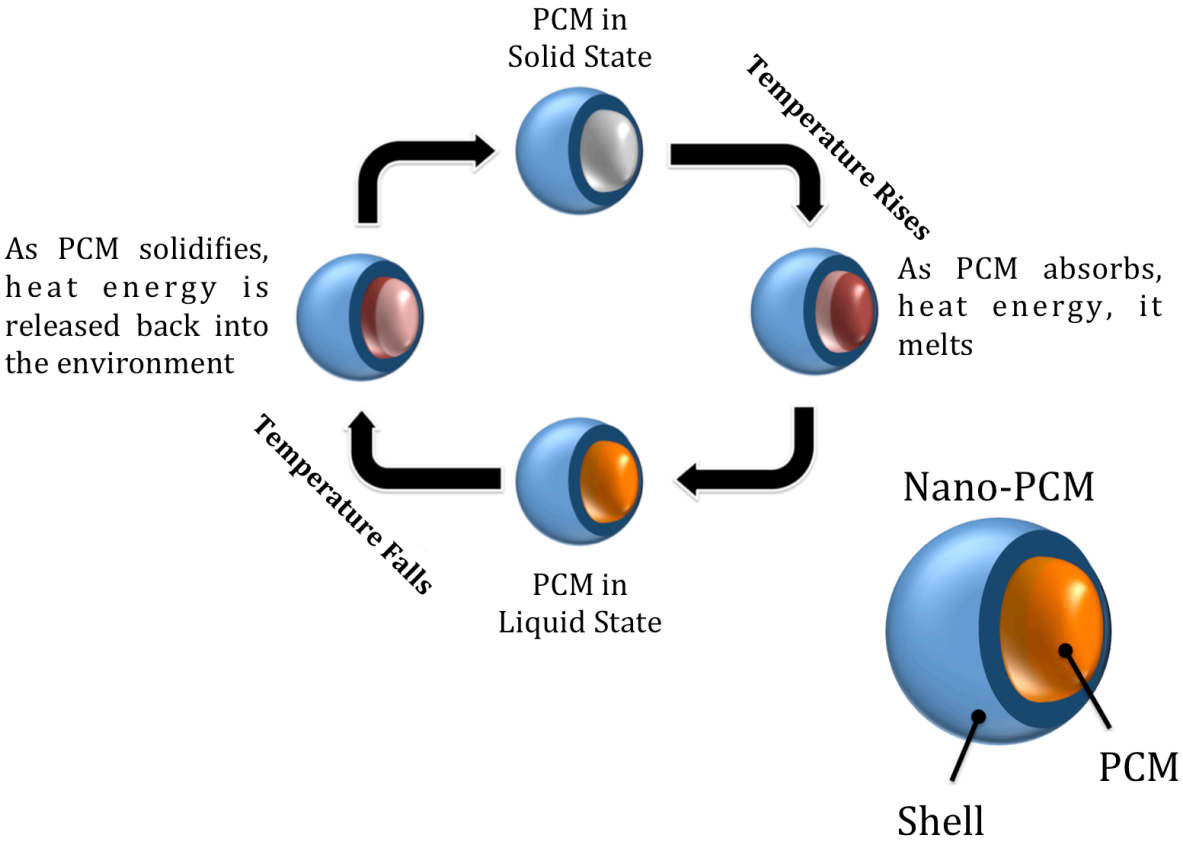

Figure 5.1: Representative sketch of the working principle of an encapsulated PCMs as latent thermal energy storage system.

The term PCMs in this contest refers to materials having large latent heat of fusion with regards to melting and solidifying at a nearly constant temperature, thus having the ability of

storing and releasing large amounts of heat energy in response to a small temperature change[180]. A representative sketch of PCMs working principle is shown in Figure 5.1.

Indeed PCMs have been studied for several decades and applied in solar energy moduli[181], thermal storage building materials[182], air conditioning[183], thermo-regulating intelligent textiles[184], temperature sensitive food packaging[185] and medical devices[186] thanks to their high-energy storage density and sharp transition temperature. In this work we are interested in PCMs microencapsulation, which involves the covering of the PCM core material with a coating or shell material. The dimension of the final capsule (called MicroPCM) defines the size of the PCM, which in turns plays an important role in determining its melting behaviour. When a PCM experiences a phase transition from solid to liquid and vice versa, the heat transfer flowing to and from the PCM is defined[187] as

$$Q = hA\Delta T$$

Where h is the heat transfer coefficient ($Wm^{-2}K^{-1}$), A is the heat transfer surface area (m^2) and ΔT is the difference in temperature between the PCM surface and its surroundings. It can be deduced from this formula that if the size of a PCM structure is reduced by a factor of 10, the time required for complete melting will be reduced by a factor of 100[188]. Concluding, the smallest the PCM structure, the most efficient use of the latent heat of fusion and the fastest is the melting process unrewarding the phase change material embedded.

In order to build such biphasic nanocapsules it is mandatory to find a synthetic approach able to embed the PCM within a capsule made of a coating shell material. Emulsion Polymerization (EP) can be a powerful tool when *n*-alkanes PCMs and acrylate shells are used (see the representative sketch in Figure 5.2). In fact, acrylic monomers and *n*-alkanes are miscible and can thus be sheared in order to obtain a homogeneous droplet emulsion in water. Once the polymerization of the monomer is started, by means of a radical initiator and temperature, phase separation occurs due to the immiscibility between *n*-alkanes and polyacrylates. Lastly, by using a proper surfactant and by tuning the PCM/monomer/surfactant ratio, it is possible to dominate the final microcapsule dimensions (from tens of nm up to μm).

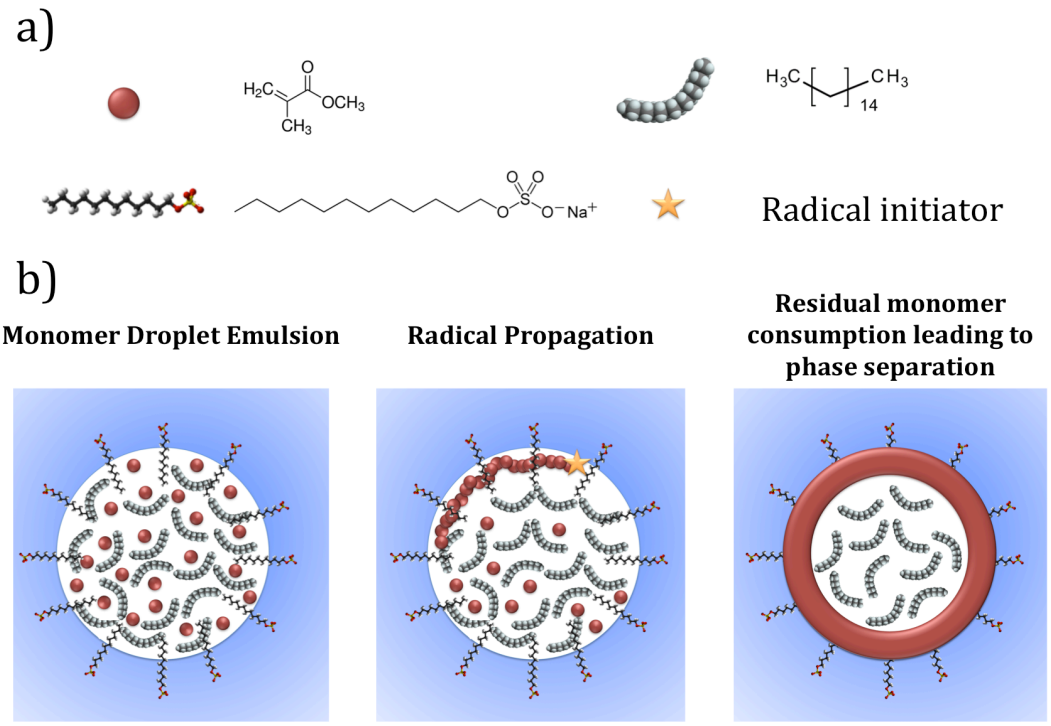

Figure 5.2: a) General formulation used for a nanocapsules synthesis: methyl methacrylate (monomer, MMA), *n*-hexadecane (HD), sodium dodecyl sulphate (surfactant, SDS) and a radical initiator. b) Representative sketch of the nanocapsules formation. Since HD and MMA are soluble, they can form a stable organic droplet when dispersed in an aqueous solution of SDS (typical concentration ~ g/L). Once the polymerization is activated from the radical initiator (either oil-soluble or water-soluble), the growth of PMMA chains takes place. PMMA and HD are no more soluble and phase separation occurs. When the polymerization reaches conversion, phase separation leads to stable nanocapsules with a PMMA shell embedding HD.

With this procedure it is possible to obtain easy-to-handle MicroPCMs, which can be moved from site to site as an aqueous solution to be casted on the desired surface. It is also possible to precipitate the MicroPCM as a stable powder, which can be later re-dispersed in organic solvents or turned into self-standing films by sintering, ink jet printing or extrusion at occurrence. The temperature response of the MicroPCMs can be tuned by choosing the right PCM (i.e. with the proper transition temperature and heat exchange properties) or by having a moisture of PCMs within the core.

In section 5.1.1, the characterization of *n*-hexadecane@poly(methyl methacrylate) nanocapsules is proposed. Moreover, a strategy for the encapsulation TiO_2 anatase nanocrystals within such nanoparticles is presented (section 5.1.2) together with the utilisation of *n*-hexadecane@poly(methyl methacrylate) nanocapsules as liquid-core sensitized up-conversion nanoemitters (5.3).

5.1.1 n-hexadecane@poly(methyl methacrylate) nanocapsules

The liquid core nanocapsules (NCs) are constituted from a *n*-hexadecane (HD) core embedded within a poly(methyl methacrylate) – PMMA – shell (HD@PMMA). The freshly prepared emulsion was firstly characterized with DLS for measuring the average hydrodynamic diameter distribution and polydispersity of the nanocapsules. In Figure 5.3 the particle size distribution in intensity is shown. The size distribution is monomodal and no aggregates nor secondary particles were detected. The measured average hydrodynamic diameter is 360 nm.

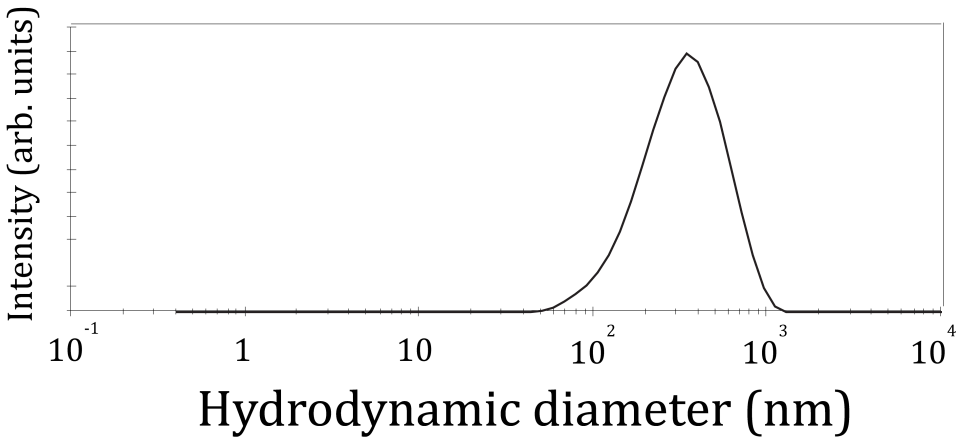

Figure 5.3: Representative particle size distribution of HD@pMMA nanocapsules in intensity, with average diameter of 360 nm. The distribution is monomodal (i.e. no aggregates nor secondary particles distribution).

After the purification (centrifugation in methanol and three centrifugation steps in *n*-hexane) of the pristine emulsion, a white precipitate was obtained. The precipitate was then dried in vacuum (10^{-2} Torr) at room temperature, in order to obtain an easy-to-handle white powder. The powder was then characterized by DSC for the quantification of the HD content. HD indeed has a crystallization peak at 17°C, with an experimental enthalpy of crystallization of ≈ 255 Jg^{-1} (Figure 5.4).

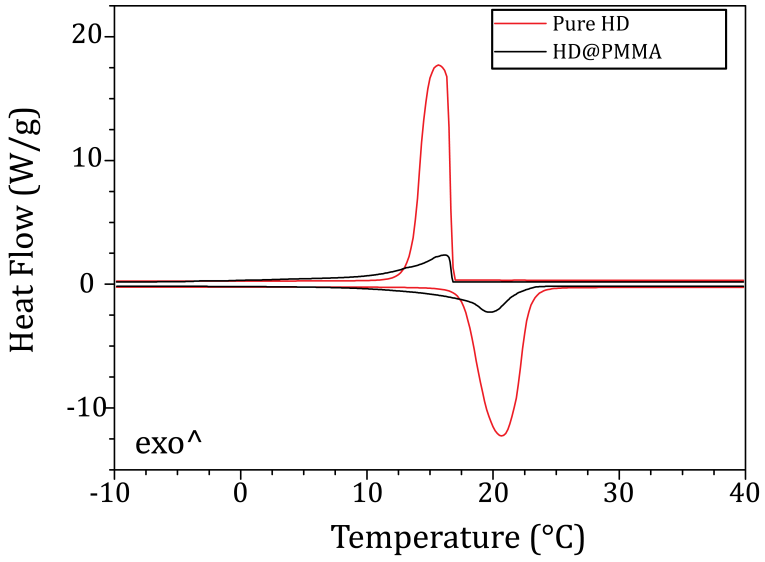

Figure 5.4: Comparison of representative DSC curves of HD@pMMA nanocapsules (black line) and pure HD (red line). Assuming the peaks in HD@pMMA NCs are due only to the presence of HD, from the ration between the crystallization integral measured in the HD@pMMA NCs and the one of pure HD, it is possible to estimate the content a ≈ 54% w/W content of HD within the nanocapsule.

In Figure 5.4 one can see that the sharp transition peaks in the pure HD get broader in the HD@pMMA NCs. This is coherent with the observation that transitions of *n*-alkanes in the bulk phase are commonly observed to have small magnitudes of supercooling, while for *n*-alkanes confined in small droplets within capsules wall supercooling is found to be much larger (≈10-16 °C)[189].

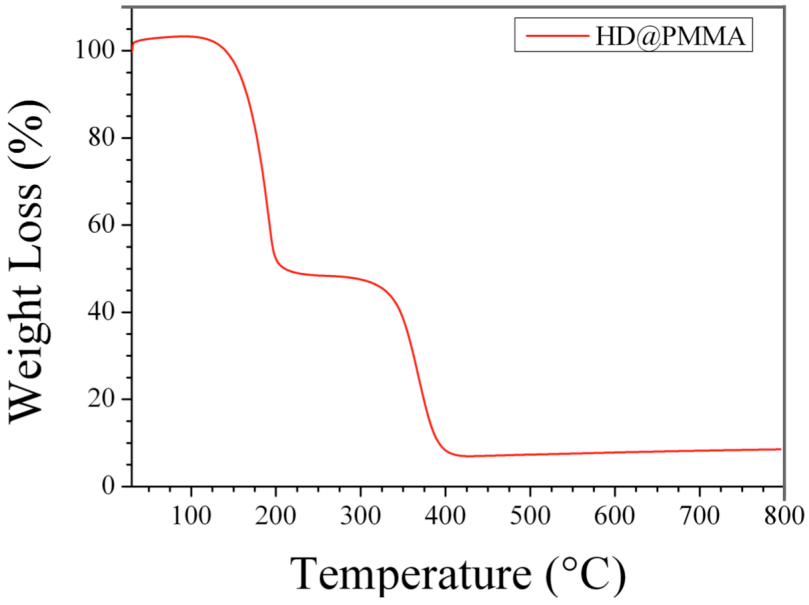

Figure 5.5: TGA curve of HD@pMMA nanocapsules recorded in air from 30°C to 800°C suggesting an HD content of about 53% w/W.

The broadening of the peak in Figure 5.4, together with the purification procedure reported in section 2.2.1.4.1, strongly suggest the effective encapsulation of HD. By applying the procedure proposed by S. Khoee et al.[41], an HD content of about 54 % w/W within the nanocapsules was calculated. A further evidence of the presence of embedded HD in the NCs is given from TGA in Figure 5.5, where two weight losses are detected and, according to previous literature[41], can be respectively ascribed to HD and PMMA.

Moreover, the presence of a liquid-like phase in the purified dry powder of HD@pMMA nanocapsules was verified also by ^{1}H-TD-NMR with MSE pulsed sequence (Figure 5.6). ^{1}H-TD-NMR allows the discrimination of protons in terms of difference in local mobility by means of MSE pulsed sequence (see section 2.3.3.1).

In HD@pMMA NCs a rigid fraction associated with protons of restricted mobility on a NMR time-scale was detected and its temperature trend is reported in Figure 5.6 in the range from -40°C and 160°C. An abrupt drop in rigid fraction is detected in the range from 0 °C to 17°C. As for DSC, this decrease in detected rigid fraction over more than ten degrees Celsius can be associated with HD supercooling phenomena under confinement. A second decrease in rigid fraction value is detected at about 120 °C, compatible with the T_g value of bulk pMMA.

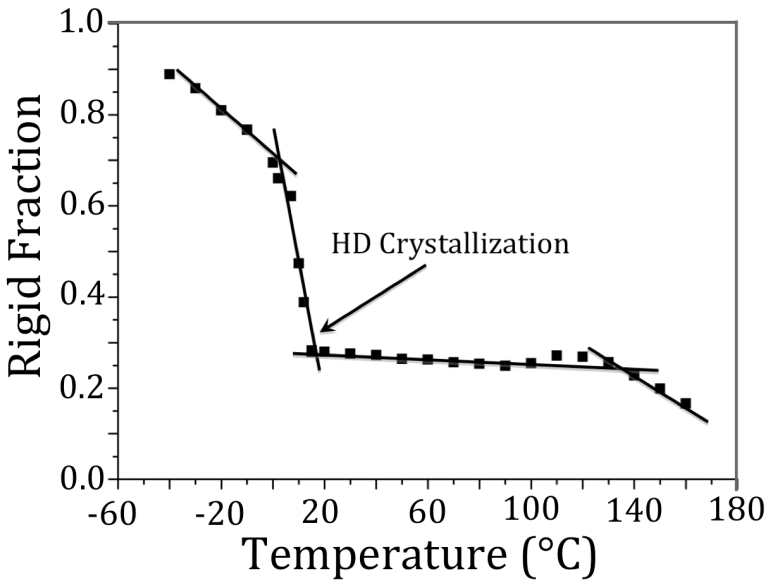

Figure 5.6: Rigid fraction temperature trend recorded by ^{1}H-TD-NMR of the purified HD@pMMA dry powder. An abrupt drop in rigid fraction is detected in the range from 0 °C to 17°C associate with HD supercooling phenomena under confinement. A second decrease in rigid fraction value is detected at about 120 °C, compatible with T_g value of bulk pMMA. Lines are meant to guide the eye and error bars are within experimental points.

A compositional analysis of HD@pMMA NCs can be done by ATR-FTIR (Figure 5.7). In Figure 5.7 ATR-FTIR spectra of pure HD (red line), pure pMMA (green line) and HD@pMMA NCs (black line) are shown.

Pure pMMA spectrum and HD@pMMA NCs one exhibit the peaks typical of acrylates: the 1750 cm^{-1} peak and a very good overlap in the esters fingerprint region from 1600 cm^{-1} to 650 cm^{-1}.

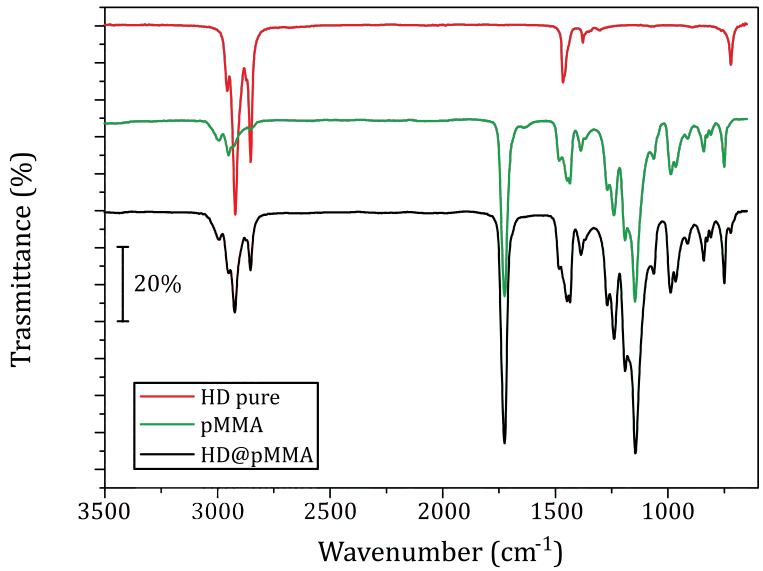

Figure 5.7: ATR-FTIR spectra of pure HD (red line), pure pMMA (green line) and HD@pMMA nanocapsules (black line). HD@pMMA NCs spectrum shows the main features of either pure pMMA spectrum and pure HD.

The main differences between the pure pMMA and the HD@pMMA spectra stand in an overexpression of the peaks in the region of aliphatic stretching (2800 cm^{-1} to 3000 cm^{-1}). By comparing these peaks with the HD ones (red line), it can be speculated that this difference can be ascribed to the presence of encapsulated HD. Moreover in the HD spectrum a peak around 722 cm^{-1} is detected: even if it does not appear in the pure pMMA spectrum (green line), it is clearly present in the fingerprint region of the HD@pMMA capsules one (black line).

In our opinion, all these evidences suggest that HD@pMMA nanocapsules were synthesized. Since the dry powder was obtained from an original purification procedure (section 2.2.1.4.1) consisting of four different centrifugation cycles (1 in methanol and 3 in hexane), we can strongly assume that from DSC, ^{1}H-TD-NMR and ATR-FTIR the HD is effectively sequestrated within the pMMA shell.

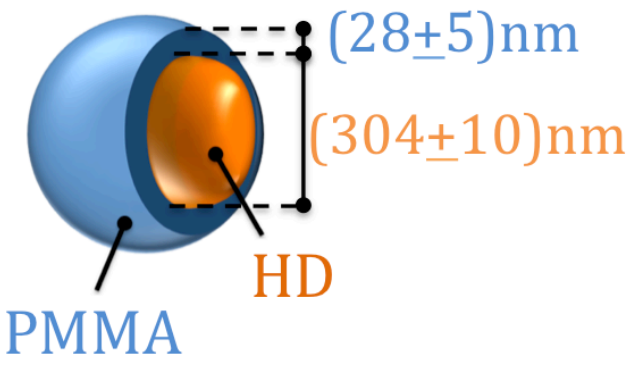

Figure 5.8: HD core diameter and PMMA shell thickness calculated assuming an homogeneous sphere with DLS average diameter and HD content measured with TGA and DSC. Bulk densities of PMMA (1.18 g/cm³) and of HD (0.77 g/cm³) were assumed for the calculations.

Since the HD content within the nanocapsules is known either from DSC and TGA and the average diameter of the nanocapsules was measured by DLS, an estimation of the PMMA shell thickness and of the HD core can be performed. Particularly, assuming a hollow sphere with the average DLS diameter of PMMA (bulk density 1.18 g/cm³) homogeneously filled by the 54% w/W of HD (bulk density 0.77 g/cm³), a PMMA shell thickness of (28±5) nm and a HD core of (304±10) nm were calculated.

5.1.2 TiO_2 Anatase nanocrystals encapsulation

Recent technological breakthroughs have been showing that many of the well-established materials (i.e. metals, ceramic and plastics) cannot fulfil all emerging specialized needs. Hybrid nanomaterials - consisting of inorganic and organic building blocks distributed at the nanoscale - have been showing for years their capability in exhibiting new synergic properties and behaviours[190]. Particularly, hybrid polymeric nanocomposites form a new class of materials with tuneable and superior properties[191]. Various strategies have been devised by both academic and industrial partners leading to an enhancement of their performances and subsequent extension of their possible range of applications[192]. Dispersion of oxide nanoparticles (like SiO_2, SnO_2 and TiO_2) into polymer matrix has proven itself as one of the most successful techniques to obtain materials with improved properties[193].

Specific applications - such as high refractive index devices, biomedical contrast enhanced imaging, colloidal crystals delivery - often require to exploit inorganic particles peculiar properties and integrate them into deliverable, bio-friendly and easy-to-handle nanocontainers[194]. Here we propose a single step emulsion polymerization (EP) for the in situ encapsulation of inorganic nanocrystals into liquid-core polymeric nanocapsules. As a case

study, we nanoencapsulate colloidal-synthesized oleic acid capped anatase TiO_2 nanocrystals into a biphasic (liquid-solid) *n*-hexadecane@poly(methyl methacrylate) (HD@PMMA) core@shell nanocapsule. In our opinion this nanoencapsulation strategy can be of real interest in the field of green hybrid nanomaterials chemistry, since it is possible to maximize the incorporation of the nano-oxide used in the process into the final product via an ambient pressure aqueous synthesis.

Besides, it has long been known that the quality of the nanoparticle dispersion into the polymer matrix dramatically drives the final properties of the nanocomposite. The phase stability of nanoparticle-polymer blends has attracted intense scrutiny and is challenging to predict because of computational difficulty in accessing the relevant length and time scales. Nanoparticles indeed have an insertion enthalpy that grows in proportion to the surface area of the nanoparticle ($\Delta H \approx 4\pi\chi r^2$, where χ is the Flory mixing parameter and r is the nanoparticle radius). Various strategies are therefore being proposed to enhance the dispersibility of several functional nanoparticles in polymer nanocomposites[195]. It is believed that a wetting nanoparticle-polymer interface[196] is required for homogeneous nanoparticle dispersion in bulk polymer nanocomposites. Indeed in recent years several techniques such as physicochemical processes, dispersion and suspension polymerization[197] have been developed to create hybrid compounds and integrated films with peculiar properties[198]. Several applications have taken advantages from the dispersion of nanoparticles into polymer matrix since optical, thermomechanical[192] and delivery properties can be enhanced and the compatibility between the filler and binder improved. Historically, emulsion polymerization has proven itself as an effective way to synthetize polymer/inorganic oxides containers[116] whose possible applications range from MRI spectroscopy for human beings to cosmetics, inks[199] and adhesives.

In this section a single step emulsion polymerization synthesis protocol for the in situ encapsulation of oleic acid capped TiO_2 nanocrystals (solvodynamic radius ≈ 4 nm, properties summary in Figure 5.9) into a deliverable nanocapsule of about 180 nm in radius consisting of a *n*-hexadecane (HD) core and a poly(methyl methacrylate) (PMMA) shell is shown. Firstly, TiO_2 nanocrystals (anatase, TiO_2 NC) capped with oleic acid were prepared via low temperature colloidal synthesis proposed by Cozzoli et al.[200], providing a big amount of highly crystalline anatase nanoparticles.

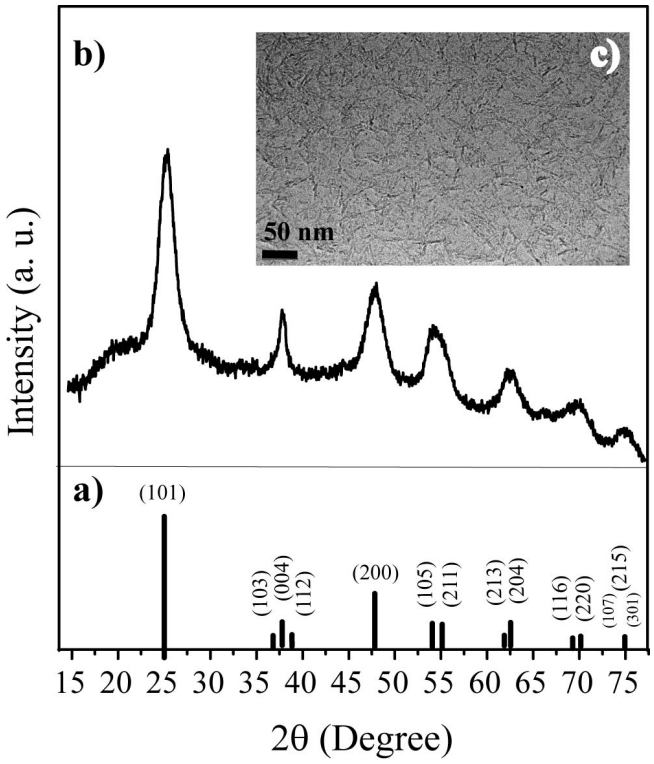

Figure 5.9: a) Anatase phase XRD pattern; b) TiO_2 nanocrystals XRD spectrum; c) TiO_2 nanocrystals TEM image. Courtesy of Dr. Annalisa Colombo synthetizing the TiO_2 nanocrystals. The synthesis was firstly proposed by P.D. Cozzoli et al., *J. Am. Chem. Soc.* 2003, *125*, 14539-14548.

Thanks to the nature of the capping agent (oleic acid – OA), TiO_2 nanocrystals are easily dispersible in HD in concentration up to ~30% in volume according to optical measurements. This dispersion is mixed with the proper amount of methyl methacrylate (MMA) and a radical initiator (AIBN), see section 2.2.1.4.2 for details. The resulting organic phase is emulsified in an aqueous solution of surfactants. The synthesis detail can be found in section 2.2.1.4.2.

MMA and HD are completely miscible, but shell growth occurs during the emulsion polymerization process due to the phase separation between HD and PMMA. The pristine emulsion is let thermalize at room temperature and characterized with DLS (Figure 5.10).

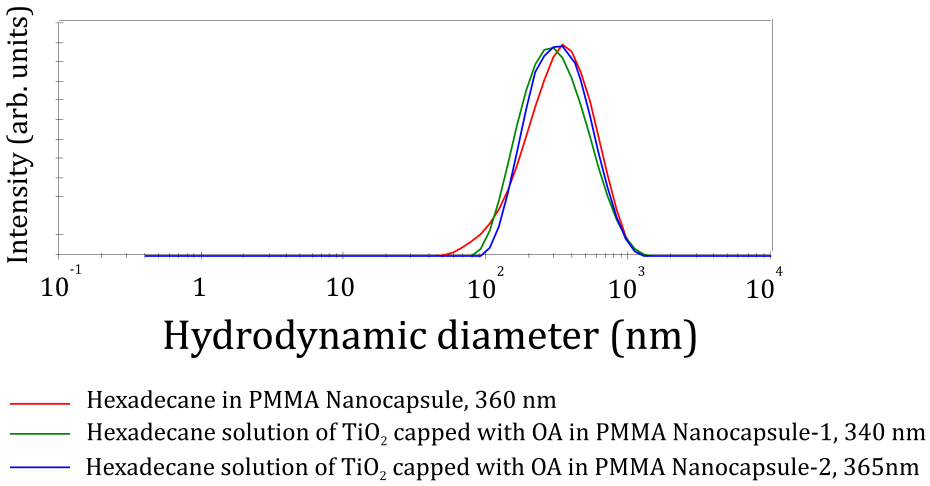

Figure 5.10: Comparison between HD@PMMA NCs (red line) and two different batches (green and blue line) of TiO_2@HD@pMMA particle size distribution in intensity. All samples shows a monomodal NCs size distribution.

In Figure 5.10 a comparison between particle size distributions in intensity of HD@PMMA empty nanocapsules (red line) and two different batches (green and blue line) of TiO_2-loaded HD@pMMA nanocapsules are shown. All the three samples have a monomodal nanocapsules size distribution. Moreover the presence of TiO_2 nanocrystals seems not to affect the final size distribution of the nanocapsules, since the three different distributions remain superimposable within the experimental error. Lastly, the encapsulation of TiO_2 nanocrystals was performed twice (green and blue line) and, even if the average hydrodynamic diameter value changes from 340 to 365 nm, the two overall particle distributions overlap within the experimental error. This suggests a good reliability of the proposed procedure.

In Figure 5.11 ATR-FTIR spectra of pure HD (red line), pure pMMA (green line), HD@pMMA nanocapsules (black line) and TiO_2@HD@pMMA nanocapsules (blue line) are compared. TiO_2@HD@pMMA spectrum shows the typical absorption shoulder starting at 1500 cm^{-1} due to the presence of TiO_2.

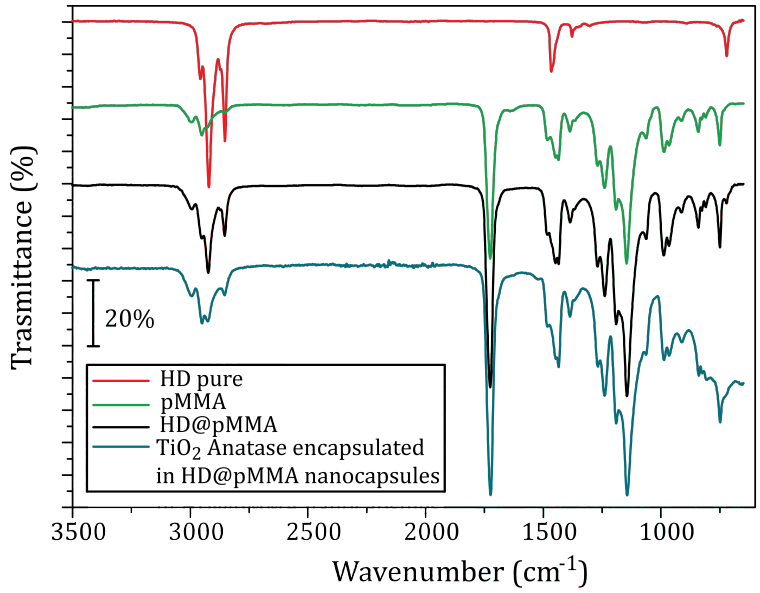

Figure 5.11: ATR-FTIR spectra of pure HD (red line), pure pMMA (green line), HD@pMMA nanocapsules (black line) and TiO_2@HD@pMMA nanocapsules (blue line). TiO_2@HD@pMMA spectrum shows the absorption shoulder due to the presence of TiO_2.

The presence of TiO_2 nanocrystals is also confirmed by TEM micrographics in Figure 5.12. Since the contrast in TEM images is mainly due to Z-number and density contrast, these black spots can be ascribed to the presence of TiO_2. Moreover, the morphology and shape of the spots is compatible with the one of the pristine TiO_2 nanocrystals in Figure 5.9.

TEM micrograph shows that, thanks to the presence of HD as a nanocrystals surrounding and wetting[196] medium, there is almost no coalescence among the TiO_2 nanoparticles within the capsule core.

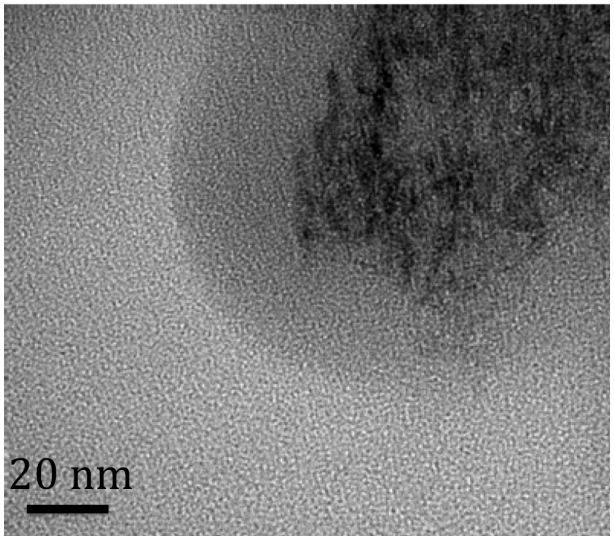

Figure 5.12: Representative TEM micrograph of an isolated TiO_2@HD@pMMA nanocapsule. Black spots are ascribed to the presence of TiO_2. Morphology and size of the dark spots are compatible with the one of the pristine TiO_2 nanocrystals in Figure 5.9. Black bar is 20 nm.

In TEM micrograph, the edge between HD and PMMA is not well defined, since their difference in Z-contrast and density contrast is too small to be detected in the imaging conditions.

TGA analysis gives a further evidences of the presence of TiO_2 embedded within the nanocapsules. Freshly prepared emulsion was indeed precipitated, purified and dried in vacuum (10^{-2} Torr) at room temperature prior to measurement. The dry powder was then analysed with TGA from 30°C to 800°C in air (10°C/min), detecting a 15 % w/W final solid residual (Figure 5.13). This value is far higher than the one recorded in the unloaded HD@pMMA nanocapsules.

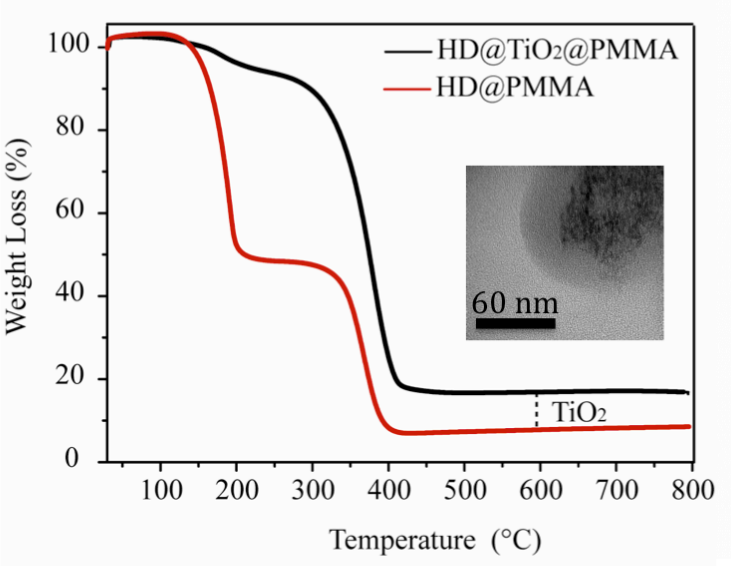

Figure 5.13: Comparison of the TGA traces of the TiO_2-loaded (black line) and unloaded (red-line) HD@PMMA nanocapsules. After the 30°C to 800°C heating in air (10°C/min), the residual solid content of the TiO_2-loaded (black line) is around the 15% w/W, far higher than the unloaded (red-line) one. Similarly, the HD content in TiO_2-loaded (black line) drops to some % w/W respect to the 53% w/W in the case of unloaded (red-line) nanocapsules. The inset shows a representative TEM micrograph of an isolated TiO_2@HD@pMMA nanocapsule.

Moreover, even if the presence of HD is still detectable from TGA, the HD content in TiO_2-loaded nanocapsules drops from more than 50% w/W in the unloaded nanocapsules to some % w/W. Accordingly with the TEM micrograph in the inset, this might suggest a huge TiO_2 crowding within the capsule HD core.

Another evidence of the fact that the presence of TiO_2 strongly affects the behaviour of HD within the nanocapsules is given from DSC analysis in Figure 5.14. In fact in Figure 5.14 a comparison of representative DSC traces of pure HD, HD@pMMA nanocapsules and TiO_2-

loaded HD@pMMA nanocapsules is reported. It is worth noticing that neither crystallization nor melting peaks due to the presence of HD are detected for TiO_2-loaded HD@pMMA NCs. This disagree either with the weight loss ascribed to HD in TGA traces and with the overexpression of the aliphatic vibrational modes in the 2800 cm^{-1} to 3000 cm^{-1} range of the ATR-FTIR spectrum (Figure 5.11).

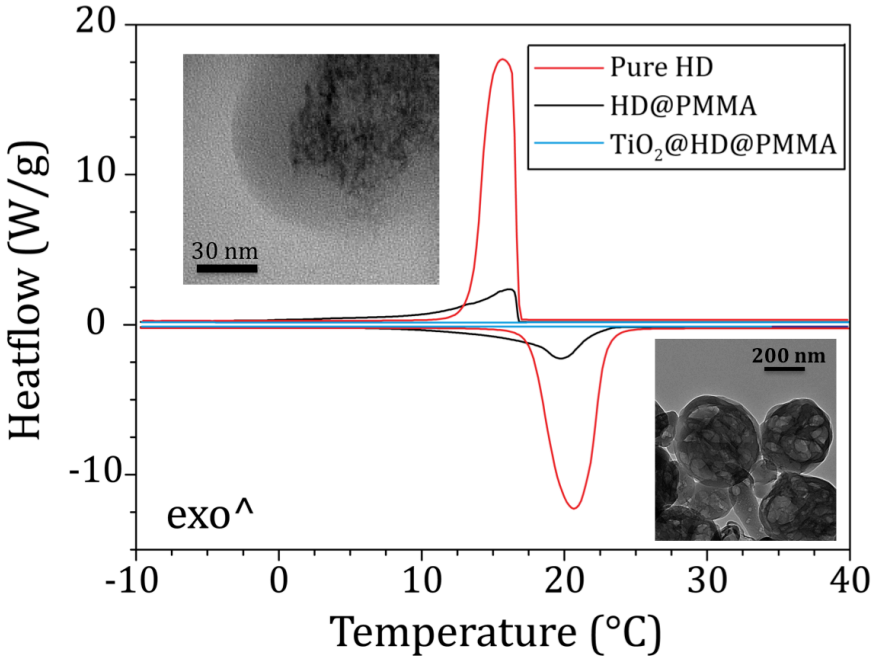

Figure 5.14: Comparison of representative DSC traces of pure HD, HD@pMMA NCs and TiO_2-loaded HD@pMMA NCs. Neither crystallization nor melting peaks due to the presence of HD are detected for TiO_2-loaded HD@pMMA NCs. Representative TEM of the TiO_2-loaded HD@pMMA NCs (up left) is presented together with a cryo-TEM image (bottom right) of the TiO_2-loaded HD@pMMA NCs, showing the beam damage on the HD phase.

However, M. Laus et al.[201] showed that thermal transition of polytetrafluoroethylene (PTFE) confined within PTFE-poly(methyl methacrylate) (PMMA) core@shell nanoparticles exhibits peculiar physic-chemical behaviour, associated to the high degree of PTFE compartmentalization. Namely, the dual crystallization of the PTFE was detected and ascribed to a fractionated crystallization mechanism[202] driven by the size of the PTFE droplets in the PMMA matrix. In our opinion, the HD crystallization within the TiO_2-loaded HD@pMMA nanocapsules is not detected in Figure 5.14 since the presence of inorganic nanocrystals inhibits heterogeneous crystallization, because of the TiO_2 crowding within the HD core. In other words, the TiO_2 within the cavity core is so high that the surface of the nanocrystals cannot act as a nucleation centre. This means that only homogeneous crystallization can take place. However the TiO_2 content within the core seems to be that high that no nucleation seed can be formed. In order to gather deeper insight about the behaviour of confined HD, a low temperature TEM image was detected on the TiO_2-loaded HD@pMMA nanocapsules.

For cryo-TEM examination a drop of diluted pristine emulsion dispersion was applied to a lacey carbon coated grid and excess sample liquid was blotted off with the edge of a filter paper. Immediately after the grid was plunged into liquid nitrogen. It is worth noticing that plunging into liquid ethane failed because the HD phase could be extracted from the nanocapsules and dissolved in this cryogene. Subsequently, the specimen was transferred to a Quorum K1250X cryo-preparation system to remove the water by sublimation at -50°C for 30 minutes at pressure lower than 10^{-4} mbar. After removal of the water by sublimation, the specimen was transferred to the TEM following the conventional cryo-transfer protocol for vitrified samples. Usually, cryo-TEM examinations were done at an as low as possible specimen temperature, so the examination at - 175°C was started. At this temperature, the hexadecane phase is crystalline. Beam damage immediately changes the morphology of the particles (Figure 5.15).

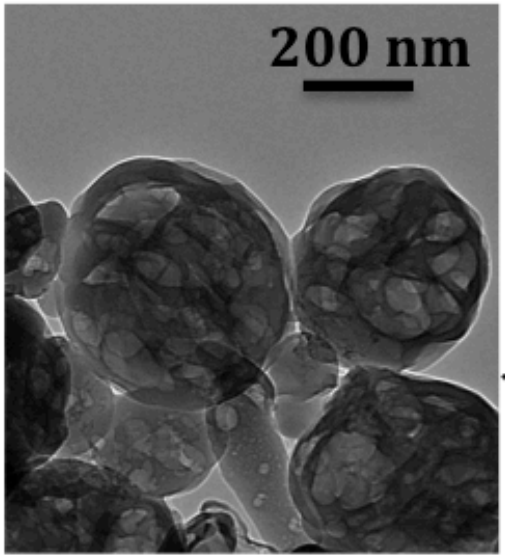

Figure 5.15: Representative cryo-TEM of the beam damage immediately changing the morphology of the TiO_2-loaded HD@pMMA particles. This could be ascribed to the presence of HD, strongly beam-sensitive.

Standing on these evidences, we can state that both HD and TiO_2 are present within the particle. It must be pointed out that there are several difficulties in calculating the real content either of HD and of TiO_2.

An direct proof that TiO_2 nanocrystals are present and embedded within the HD@PMMA capsule is given in Figure 5.16, showing the transmittance spectrum recorded between 300 nm and 1200 nm of dry TiO_2-loaded HD@pMMA nanocapsules powder redispersed in o-xylene. Prior to measurement, the freshly prepared emulsion of TiO_2@HD@pMMA nanocapsules was precipitated in methanol (centrifugation at 6000 rpm for 15 minutes) and

rinsed three times in hexane (three centrifugation steps at 6000 rpm for 15 minutes) in order to extract the HD and TiO_2 nanocrystals not included in the nanocapsule. The precipitate was then dried at room temperature in vacuum (10^{-2} Torr) overnight. The residual dry powder was redispersed in o-xylene and the spectrum in Fig. 5.16 was recorded.

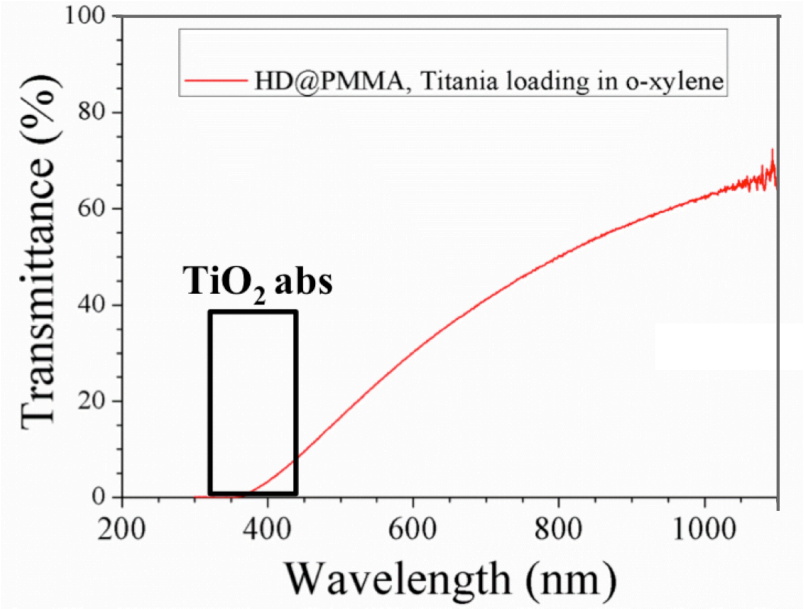

Figure 5.16: Transmittance spectrum recorded between 300 nm and 1200 nm of dry TiO_2-loaded HD@pMMA particles powder redispersed in o-xylene. The UV-Filter (λ<350nm) effect is due to the presence of TiO_2 nanocrystals.

Notwithstanding the hard precipitation an purification steps, the UV-filter effect due to the presence of TiO_2 nanocrystals is still present in the spectrum.

In our opinion all these evidences suggest the effective confinement of TiO_2 nanocrystals within the HD core of the HD@pMMA particles. Moreover the PMMA shell is able to survive on a 30 minutes timescale the action of aggressive solvent such as o-xylene, important parameter for post-processing and potential production.

5.2 TiO_2-loaded HD@PMMA nanocapsules as additives in bulk PMMA

Finally, 43 mg of purified TiO_2-loaded HD@pMMA nanocapsules dry powder were mixed with 1.3 ml of MMA and 0.93 mg of radical initiator (AIBN). The solution was added in a 4 ml screw-cap flask and homogenized till complete dissolution of the initiator. The solution was then put in an oven at 80°C for some days and annealed at 120°C overnight. The flask was

then let thermalized at room temperature. On the bottom of the flask, a several millimetre thick disk of transparent bulk PMMA was found (Figure 5.17, sample name B69).

Figure 5.17: Photograph of the disk of transparent bulk PMMA obtained by bulk polymerization of 1.3 ml of MMA and 0.93 mg of radical initiator (AIBN), mixed with 43 mg of purified TiO_2-loaded HD@pMMA nanocapsules dry powder (sample name B69). In the centre of the sample a refractive index of 1.50 was measured at 633 nm. Please note that the refractive index for pure PMMA is 1.48.

The disk was then characterized with DSC, in order to detect eventual traces of unreacted monomer or HD and to measure the glass transition temperature of the sample (Figure 5.18, sample name B69). In Figure 5.18 the first and third DSC scans are reported. Both of them show a T_g around 118°C, the typical glass transition temperature value for bulk PMMA.

Moreover, refractive index measurement were performed at the centre of the B69 sample by means of a METRICON 2010 prism-coupled refractometer equipped with a He-Ne 633nm laser. A refractive index value of 1.50 was measured, denoting an increase of 1.35% with respect of pure PMMA refractive index value of 1.48. In our opinion this underlines the presence of TiO_2 in the B69 samples.

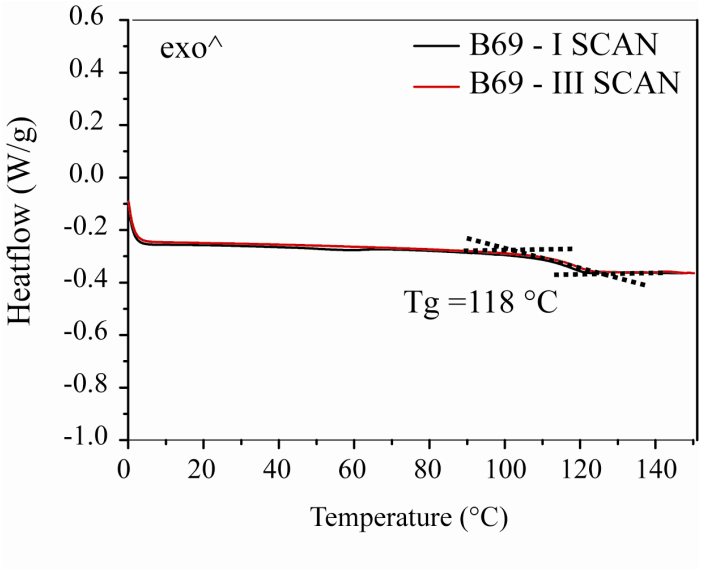

Figure 5.18: DSC curves of B69 obtained by bulk polymerization of 1.3 ml of MMA and 0.93 mg of radical initiator (AIBN), mixed with 43 mg of purified TiO_2-loaded HD@pMMA nanocapsules dry powder (sample name B69). No traces of unreacted monomer was detected and glass transition temperature measured in first

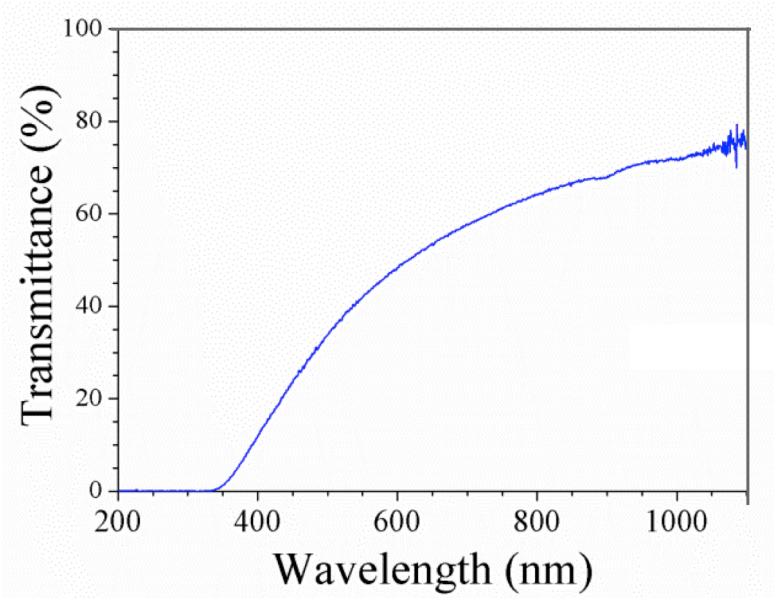

Figure 5.19: Transmittance spectrum recorded between 300 nm and 1200 nm on bulk B69 sample. The UV-Filter effect due to the presence of TiO_2 nanocrystals gives and indirect proof of the confinement of such nanocrystals within the sample.

The presence of TiO_2 nanocrystals within the bulk B69 sample was also confirmed by the UV-filter in the transmittance spectrum in Figure 5.19. Comparing the photograph in Figure 5.17 with the spectrum in Figure 5.19, it is possible to state that using TiO_2-loaded HD@pMMA nanocapsules dry powder as additive (3.3% w/W) during MMA bulk

polymerization can lead to PMMA bulk samples with improved refractive index and naked-eye transparency.

In conclusion, an effective protocol for the preparation of TiO_2-loaded HD@pMMA nanocapsules is presented together with the characterization of the structure. This system allows to handle inorganic 4 nm TiO_2 nanocrystals as a coarse dry powder, confining the inorganic nanocharge within the HD liquid core, maintaining the optical properties of the inorganic payload in organic bulk solutions and strongly limiting aggregation phenomena. Moreover, embedding the inorganic charge in an alkane droplet within a PMMA shell retains the optical properties of the inorganic without visible macroscopic aggregation even after strong external stress (i.e. bulk polymerization), making these nanocapsules particularly suitable for potentially handling other nanopowders as well.

5.3 HD@PMMA nanocapsules as Liquid-core SUC Nanoemitters

In this section the preparation of liquid-core SUC nanoemitters is presented. In section 4.5.14.5.1 we showed that the efficiency of SUC PBA@PS nanoemitters is strongly affected by the presence of O_2 and by the polymerization of the confined core. Here, in order either not to generate O_2-rich radicals passivizing the dyes involved in the sensitized up-conversion process nor to activate radical initiator directly within the oil phase, the oil soluble initiator was replaced with the water soluble 2,2'-Azobis(2-methylpropionamidine)dihydrochloride (AMPDC). Therefore, by triggering the decomposition of the radical initiator within the aqueous phase and by dissolving the SUC dyes in *n*-hexadecane (i.e. a saturated alkane hydrocarbon unreactive in presence of radicals), the probability that a free radical interacts and spoils the SUC dyes embedded in the core-forming medium is in principle minimized.

In particular, *n*-hexadecane (HD) was used as solvent for one of the most efficient donor/acceptor pair for green to blue SUC (Figure 5.20), namely platinum (II) octaetyl-porphyrin (PtOEP, 10^{-4} M) and 9,10-diphenylanthracene (DPA, 10^{-3} M). In solution, the chosen dyes ensure high optical density in the green (100% absorption at 532 nm with optical path *d* = 1 mm), almost complete donor-acceptor energy-transfer (>99%), and typical overall UCQY> 20% with excitation power densities of a few mW/cm^2 at 532 nm.[203]

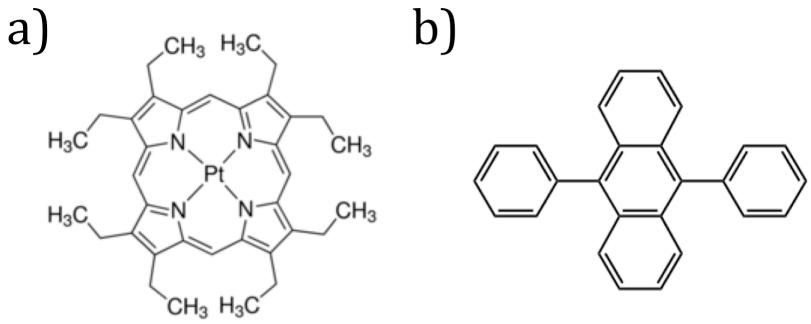

Figure 5.20: a) Structure formula of platinum (II) octaetyl-porphyrin (PtOEP), acting as donor in the SUC process. b) Structure formula of 9,10-diphenylanthracene (DPA), acting as acceptor in the SUC process.

5.3.1 Control experiments in solution

Prior to synthesis the effect of each components of the emulsion formulation on PtOEP time resolved photoluminescence (TRPL) was explored. Indeed, we already mentioned that porphyrins are renowned for their ability to form supramolecular aggregates in presence of surfactant such as sodium dodecyl benzene sulphate (SDS), with the so-called Surfactant Assisted Self-assembly (SAS)[204]. In fact, SAS has been recently reviewed by C. Zhang et al.[205] because of the ever increasing attention due to its excellent reproducibility, operational simplicity, strong capability for a hierarchical assembly, as well as good tune ability and controllability.

Three control experiments were performed. Firstly, the TRPL of PtOEP in degassed (via freeze pump and thaw) HD (10^{-4} M) was recorded under N_2 atmosphere (Figure 5.21-LEFT). A single component exponential decay was detected, with a characteristic lifetime of 83 μs.

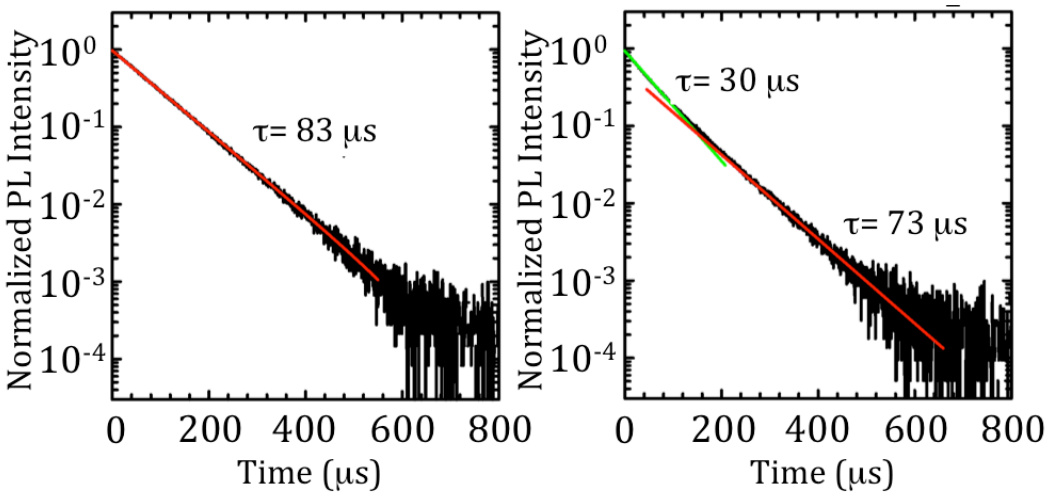

Figure 5.21: LEFT-TRPL Spectrum of PtOEP in HD solution (10^{-4} M) recorded in N_2 atmosphere (O_2<0.1 ppm). RIGHT-TRPL Spectrum of an aqueous emulsion prepared mixing 1.22 ml of PtOEP in HD solution (10^{-4} M) with 5 ml of SDS aqueous solution (3.75 g/L) recorded in N_2 atmosphere (O_2<0.1 ppm). Red and green lines represent the single component fittings.

Secondly, 1.22 ml of degassed PtOEP HD solution (10^{-4} M) was added to 5 ml of an aqueous solution of SDS (3.75 g/L), forming an oil in water emulsion. After homogenization at 1500 rpm under magnetic stirring for 30 minutes, the TRPL of the stable emulsion was recorded in order to understand the effect of the presence of water and SDS surfactant on PtOEP TRPL. Differently from the previous case, in Figure 5.21-RIGHT a two components exponential decay was detected. A fast characteristic lifetime of about 30 μs was detected and associated to a fraction of PtOEP molecules interacting with the surfactant. A slower lifetime of 73 μs comparable with the behaviour of PtOEP in pure HD was detected as well. It means that SDS is sequestrating part of PtOEP molecules, in agreement with SAS literature[204, 205].
A third control experiment was performed on a second aqueous emulsion prepared by adding an organic phase (0.33 ml of MMA monomer and 1.22 ml of degassed PtOEP HD solution (10^{-4} M)) to 5 ml of an aqueous solution of SDS (3.75 g/L), in order to mimic the prepolymerization conditions. After a 30 minutes homogenization under magnetic stirring at 1500 rpm the TRPL spectrum was recorded (Figure 5.22).

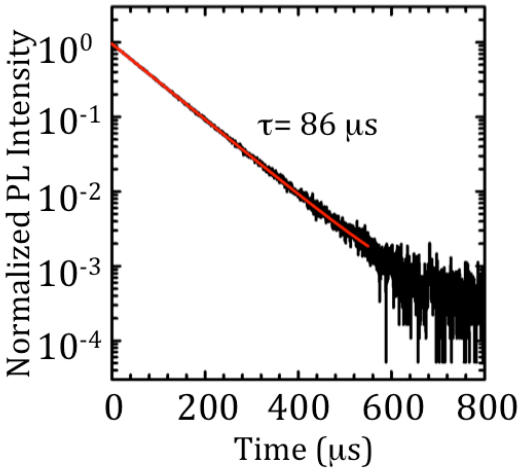

Figure 5.22: TRPL Spectrum of an aqueous emulsion prepared adding an organic phase (0.33 ml of MMA monomer and 1.22 ml of degassed PtOEP HD solution (10^{-4} M)) to 5 ml of SDS aqueous solution (3.75 g/L) recorded in N_2 atmosphere (O_2<0.1 ppm). Red line represent the single component fittings.

The TRPL spectrum in Figure 5.22 showed a single component exponential decay with a characteristic lifetime of 86 μs, in good agreement with the behaviour of PtOEP in pure HD solution. In our opinion the MMA –more polar than HD– added to the organic phase could shield the PtOEP from the columbic attraction towards SDS. This could be coherent with the fact that MMA is added in a 1:3.7 ratio in volume respect to the HD, thus leading to a change in polarity within the organic droplet. Such a polarity change, according to TRPL spectra, lowers the interaction between SDS and PtOEP. The emulsion formulation seems thus not to affect detrimentally the photophysics of PtOEP.

Standing on the results from control experiments, a TRPL spectrum of formed HD@PMMA nanocapsules enclosing PtOEP (10^{-4}M nominal concentration in the HD core) was recorded (Figure 5.23). The nanocapsules were synthesized by adding an organic phase (0.33 ml of MMA monomer and 1.22 ml of degassed PtOEP HD solution (10^{-4} M)) to 5 ml of SDS aqueous solution (3.75 g/L) containing $2.89 \cdot 10^{-2}$ mmol of the water-soluble radical initiator AMPDC. The solution was homogenized for 30 minutes at 1500 rpm at room temperature. The temperature was set at 80°C in order to activate the initiator and start the polymerization reaction under magnetic stirring at 700 rpm. The reaction was done under inert atmosphere (N_2, oxygen concentration < 0.1 ppm).

After 24 hours the emulsion was let thermalized at room temperature and the TRPL spectrum in Figure 5.23 was recorded. The TRPL spectrum of the PtOEP within the nanocapsules can be fitted with a single component exponential decay with characteristic lifetime of 73 μs, compatible with the one detected either in the pure HD control experiment.

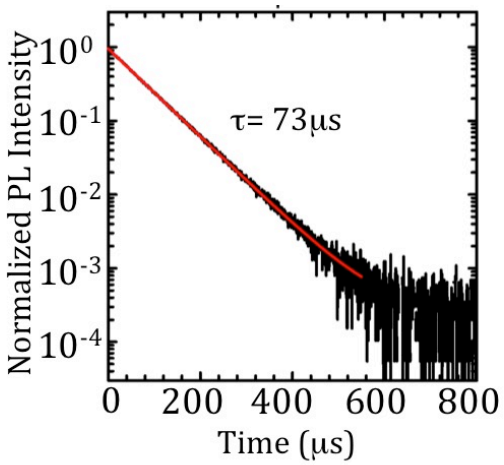

Figure 5.23: TRPL Spectrum of an aqueous nanocapsules emulsion recorded in N_2 atmosphere (O_2<0.1 ppm). The nanoparticles were prepared adding an organic phase (0.33 ml of MMA monomer and 1.22 ml of degassed PtOEP HD solution (10^{-4} M)) to 5 ml of SDS aqueous solution (3.75 g/L) containing $2.89 \cdot 10^{-2}$ mmol of AMPDC radical initiator. After 30 minutes of homogenization at 1500 rpm, the polymerization reaction lasted for 24 hours (stirring at 700 rpm) prior to TRPL spectrum recording. Red line represent the single component fittings.

Moreover no fast decay time (associated with PtOEP interacting with SDS) were detected at the end of the polymerization.

The freshly obtained nanocapsules emulsion was characterized by DLS (Figure 5.24). In this case the particle size distribution in number is shown, showing an average hydrodynamic diameter of 37 nm.

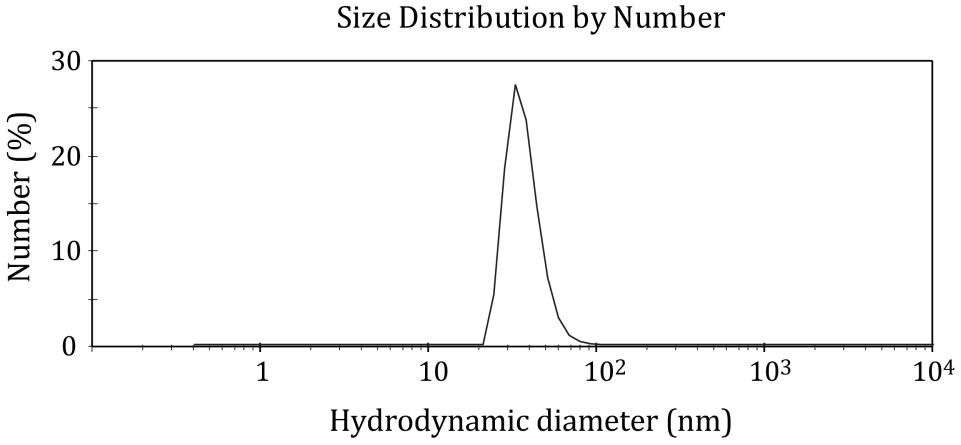

Figure 5.24: DLS particle size distribution in number of HD@pMMA nanocapsules loaded with PtOEP and DPA.

This value is coherent with the dimensions of the particles measured in the SEM micrograph in Figure 5.25, recorded on a drop of diluted emulsion casted on a silicon substrate. Prior to SEM micrograph recording, the deposited drop was let dry and sputtered with gold.

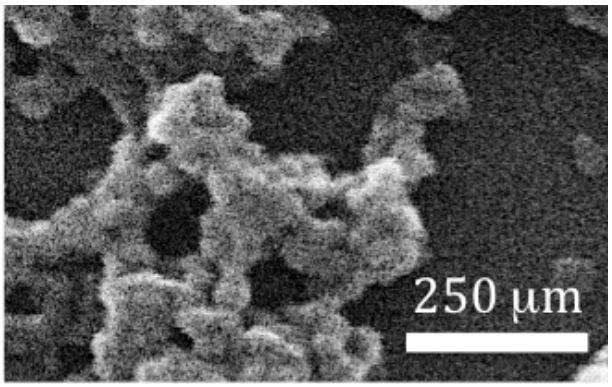

Figure 5.25: SEM micrograph of a drop obtained from diluted freshly prepared emulsion of HD@PMMA loaded with SUC dyes (PtOEP and DPA). Single nanocapsules dimension can still be detected notwithstanding their strong tendency to aggregation after water evaporation.

According to Figure 5.25, the characteristic dimensions of the nanocapsules are in the range of ~ 40 nm. It is worth noticing that, even if the particles show a strong tendency of aggregating upon capillary forces due to drying and adsorption on the silicon substrate, single particle edges are revealed coherently with the presence of a glassy PMMA shell. Notwithstanding the low resolution of the SEM used, still spherical shape of isolated NPs can be detected with dimensions compatible with the particle size distribution in number obtained by DLS (Figure 5.24).

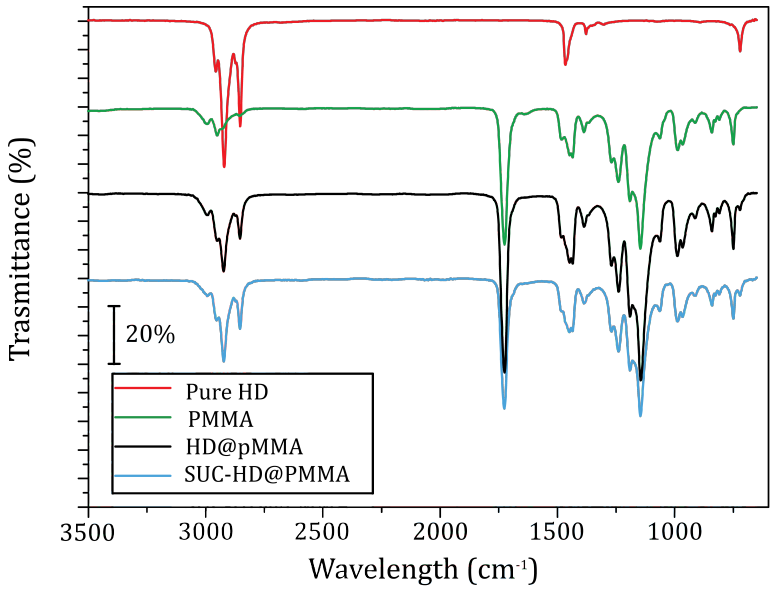

Figure 5.26: ATR-FTIR spectra of pure HD (red line), pure pMMA (green line), HD@pMMA nanocapsules (black line) and SUC-HD@pMMA nanocapsules (blue line). SUC-HD@pMMA spectrum is dominated either by the characteristic peaks of PMMA (1750 cm^{-1} and fingerprint region between 1000 cm^{-1} and 1300 cm^{-1}) and of the HD peaks (overexpression of the aliphatic modes in the 2800 cm^{-1} - 3000 cm^{-1} and characteristic 722 cm^{-1} peak in the fingerprint region).

Similarly to the procedure adopted in the former sections, dry powder of precipitated SUC-HD@PMMA nanocapsules was analysed with ATR-FTIR and compared to the blank references in Figure 5.26 (namely pure HD, pure PMMA and unloaded HD@PMMA nanocapsules). Prior to measurement, the freshly prepared emulsion of SUC-HD@pMMA nanocapsules was precipitated in methanol (centrifugation at 6000 rpm for 15 minutes) and rinsed three times in hexane (three centrifugation steps at 6000 rpm for 15 minutes) in order to extract the not included HD and SUC dyes. The precipitate was then dried at room temperature in vacuum (10^{-2} Torr) overnight. The residual dry powder was characterized with ATR-FTIR in Figure 5.26. Pure pMMA spectrum and HD@pMMA NCs one exhibit the peaks typical of acrylates: the 1750 cm^{-1} peak and a very good overlap in the esters fingerprint region from 1600 cm^{-1} to 650 cm^{-1}. The main differences between the pure pMMA and the HD@pMMA spectrum stand in an overexpression of the peak intensity in the region of aliphatic stretching (2800 cm^{-1} to 3000 cm^{-1}). By comparing these peaks with the HD ones, it can be speculated that this difference can be ascribed to the presence of encapsulated HD. Moreover in the HD@pMMA a peak around 722 cm^{-1} is detected: even if it does not appear in the pure pMMA spectrum, it is clearly present in the fingerprint region of the HD one.

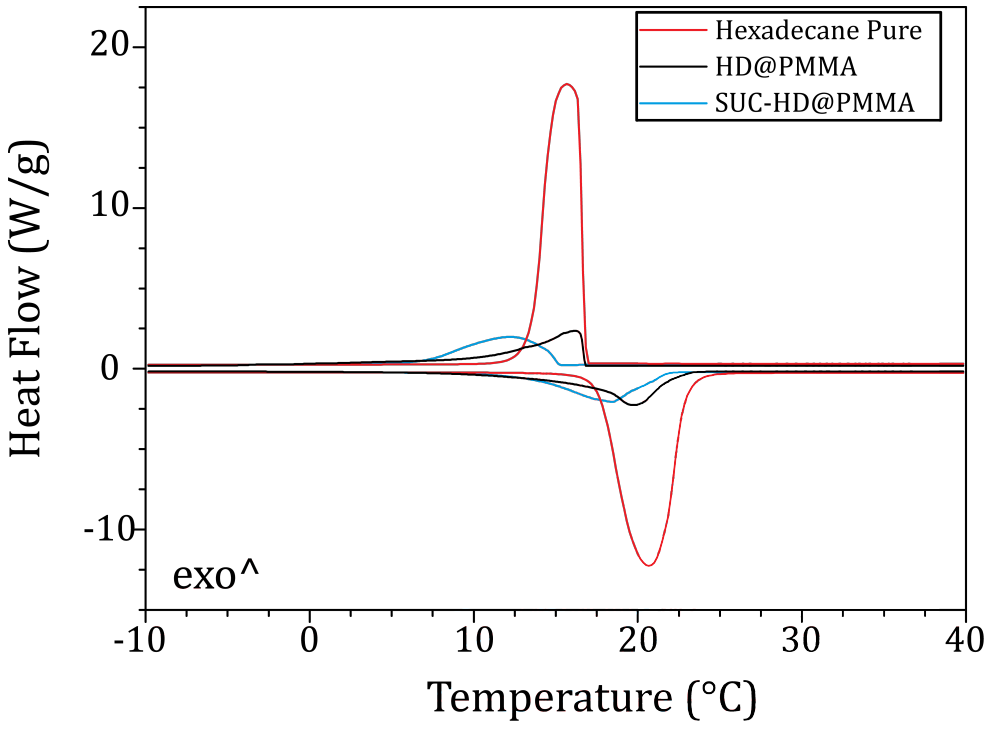

Figure 5.27: Comparison of representative DSC curves of pure HD (red line), HD@pMMA nanocapsules (black line) and SUC-loaded HD@pMMA nanocapsules (blue line). Assuming the peaks in SUC-HD@pMMA NCs are due only to the presence of HD, from the ration between the crystallization integrals of the HD@pMMA NCs and the pure HD, it is possible to estimate a ≈ 47% w/W HD content.

The powder of precipitated SUC-HD@PMMA nanocapsules was then characterized by DSC for detecting the presence of HD (Figure 5.27, blue line). The DSC traces (cooling and heating) were compared with the trace of blank HD@PMMA nanocapsules of 360 nm in average hydrodynamic diameter and with the trace of pure HD. As already mentioned, pure HD has a melting temperature of 17°C, with an enthalpy of melting of ≈ 255 Jg^{-1} (Figure 5.27). In Figure 5.27 one can see that the transition peaks in the pure HD get broader in the SUC-HD@pMMA sample, due to HD sequestration within a nanostructured shell. From the measured enthalpy of melting in SUC-HD@pMMA (≈123 Jg^{-1}) and by applying the literature procedure[41], the HD content can be estimated in 47% w/W. Moreover, comparing the SUC-loaded HD@PMMA nanocapsules of 37 nm in hydrodynamic diameter with the 360 nm blank HD@PMMA reported in Figure 5.27 (red line), the supercooling phenomena in the SUC-loaded ones are far higher accordingly with the smaller dimension and the higher surface/interface effects.

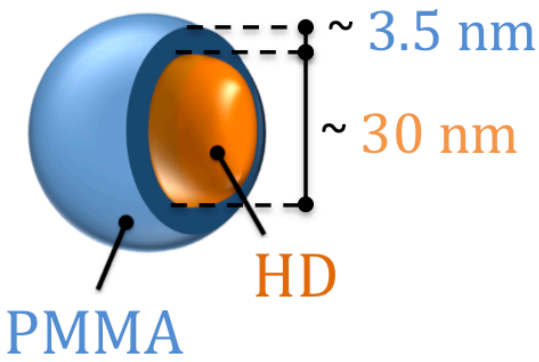

Figure 5.28: HD core diameter and PMMA shell thickness calculated assuming an homogeneous sphere with DLS average diameter and HD content measured with DSC.

Since the HD content within the nanocapsules is known from DSC and the average diameter of the capsule was measured by DLS, an estimation of the PMMA shell thickness and of the HD core can be performed. Particularly, assuming a hollow sphere with the average DLS diameter of PMMA (bulk density 1.18 g/cm^3) homogeneously filled by the 47% w/W of HD (bulk density 0.77 g/cm^3), a PMMA shell thickness of ~3.5 nm and a HD core of ~30 nm were calculated (Figure 5.28).

The freshly prepared SUC-HD@PMMA nanocapsules emulsion was then characterized in terms of photoluminescence. Firstly, the PL spectrum was recorded as a function of incident power (Figure 5.29). From Figure 5.29-LEFT one can see that the residual PL intensity at 650 nm of the PtOEP is always lower than the SUC signal between 400 nm and 530 nm (excitation at 532 nm). Indeed the SUC signal is barely always three times higher than the residual PtOEP

signal. With respect to the PBA@PS SUC nanoemitters, this is already a huge upgrade. In figure 5.29-RIGHT, the normalized PL intensity for each peak is reported as a function of the incident power (excitation wavelength 532 nm). Namely, for every single power value from 2 10^{-3} mW to 10 mW, the integral underneath the PtOEP peak (red circles) and underneath the SUC peak (blue triangles) was calculated and plotted in the graph.

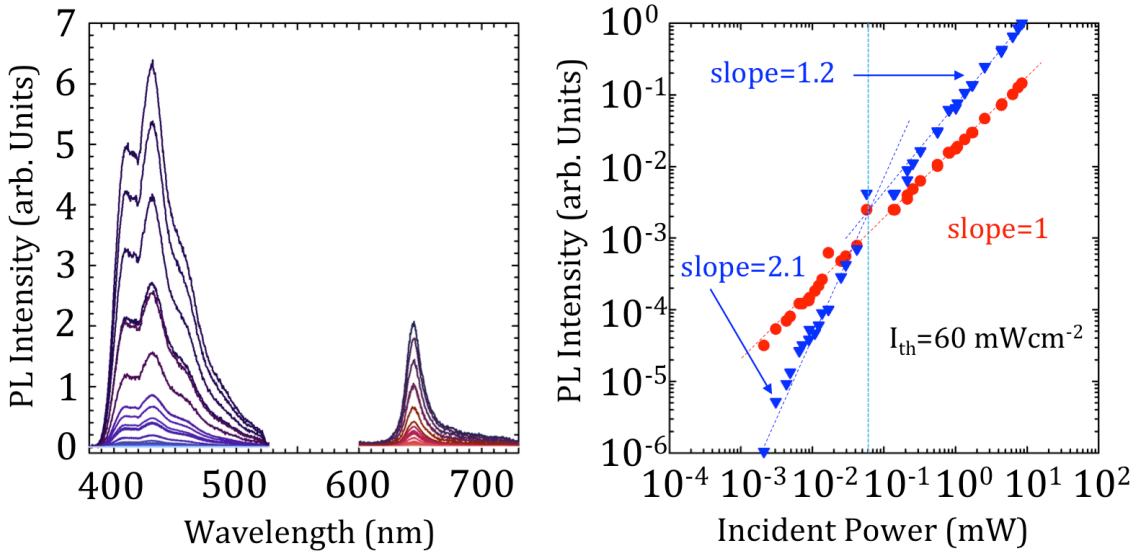

Figure 5.29: LEFT-PL intensity measured on the freshly prepared SUC-HD@PMMA nanocapsules excited at 532 nm as a function of wavelength an incident power (from 2 10^{-3} mW to 10 mW). Residual PtOEP is detected (at 650 nm) but always lower than the SUC signal (between 400 nm and 530 nm). Excitation wavelength 532 nm. RIGHT-Normalized PL intensity calculated as the integral underneath each peak as a function of incident power. Red dots takes into account the PtOEP behaviour, while blue triangles described the trend of the SUC signal. The SUC threshold is at 60 mWcm^{-2}.

The residual PtOEP PL peak (red circles) shows a linear dependence as a function of power: this is coherent with the fact that, in presence of DPA, PtOEP excited at 532 nm can whether transfers this energy leading to SUC (constant term) or emits if no DPA molecules are in its surroundings. Both this channels are proportional to the incident power in the range of the measurement. On the other hand, the SUC peak (blue triangles) exhibits a more complicate behaviour as a function of the incident power. Monguzzi et al.[206] already describes that, at different excitation powers, two regimes can be identified for the SUC signal depending on the main deactivation channel for the triplets: namely, the spontaneous decay and the bimolecular annihilation. In Figure 5.29-RIGHT, for low incident power values (i.e. < 60 mW) the SUC signal has a pseudo-quadratic (slope 2.1) dependence with the incident power. In fact, within this regime the main deactivation channel for the triplets is the spontaneous decay. For higher incident power values (> 60 mW) the SUC signal shows a slope of 1.2,

coherently with the fact that the main deactivation channel for the triplets is the bimolecular annihilation efficiently leading to SUC. The excitation power density at which triplet bimolecular annihilation becomes dominant is the threshold I_{th} to have efficient up conversion generation (in our case the value is 60 $mWcm^{-2}$).

The TRPL of PtOEP (Figure 5.30) was investigated in order to gather a deep understanding about the reason of the residual PtOEP emission detected in Figure 5.29. The TRPL spectrum in Figure 5.30 can be fitted with a two components exponential decay. Particularly, a fast decay time of 4 μs was detected and ascribed to the fraction of PtOEP molecules efficiently transferring with DPA molecules and triggering SUC. The second component shows a long decay time of 120 μs, suggesting the presence of *isolated* inactive PtOEP molecule embedded in a rigid (i.e. not liquid) environment. Actually, this fraction of "stuck" and inactive PtOEP is not surprising because it is already well known its affinity to surfactants (and SDS in particular) leading to the already mentioned SAS nanoarchitectures[204, 205]. Accordingly to the vast SAS literature, during the 24 hours synthesis probably a wide fraction of PtOEP is likely to go to the water/oil interface defined by the SDS surfactant. Moreover, this interface is the locus where the polymerization of PMMA takes place according to the sketch in Figure 5.2, causing the deactivation of part of the PtOEP in a bulk-like matrix.

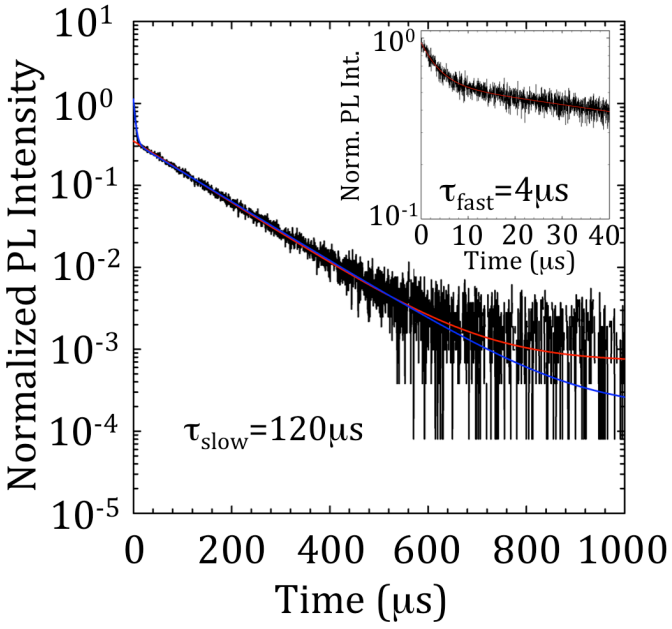

Figure 5.30: TRPL of the PtOEP within the SUC-HD@PMMA nanocapsules. The experimental decay curve can be fitted with two single exponentials decay, with characteristic decay times of 4 μs (PtOEP molecules participating to the SUC process, see inset) and 120 μs (isolated PtOEP molecules embedded in a rigid matrix not participating in the SUC process).

By calculating the integral underneath the slow decay (inactive PtOEP) and underneath the overall decay, the contribution of inactive isolated PtOEP molecules can be estimated as:

$$\frac{Area(slow)}{Area(tot)} = 93.25\%$$

It means that the 6.75 % of PtOEP present within the capsules participates to the SUC process. Nevertheless the overall efficiency of the liquid core nanocapsules is still higher than in the case of PBA@PS nanoparticles.

Considering that the 6.75% of PtOEP is effectively participating to the SUC process an energy transfer efficiency of the 99.4% can be calculated. This value is definitely higher than the 58% energy transfer yield recorded on PBA@PS nanoparticles and comparable with the behaviour of the SUC dyes in bulk liquids.

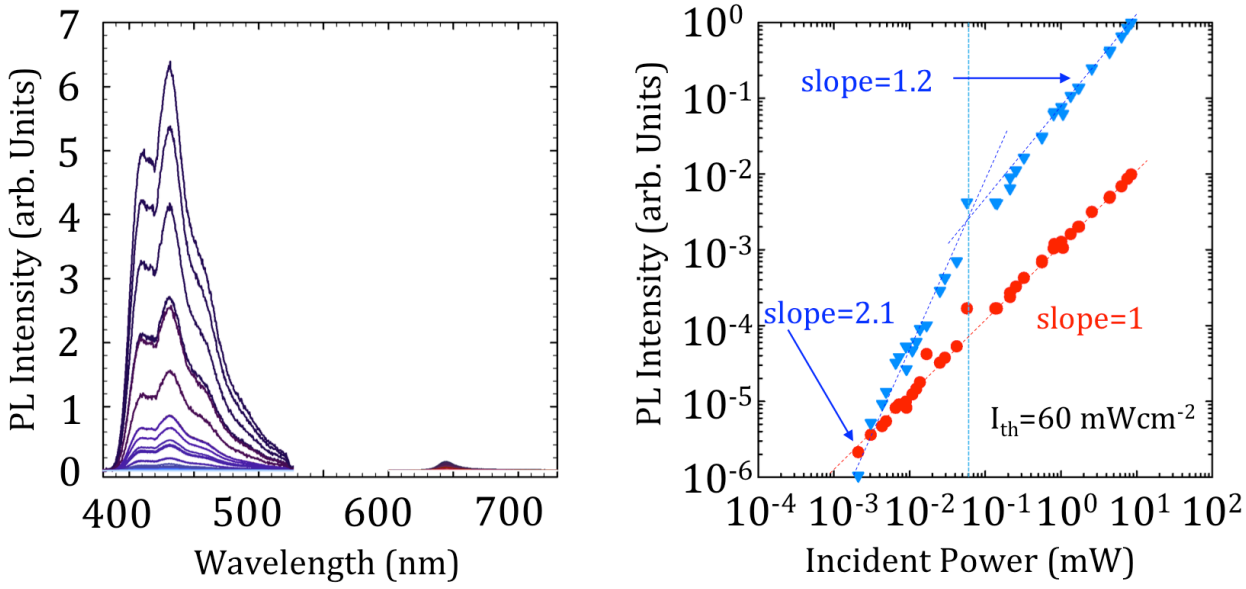

Figure 5.31: PL intensity measured on the freshly prepared SUC-HD@PMMA nanocapsules as a function of wavelength an incident power (from 2 10^{-3} mW to 10 mW) corrected with respect to the actual fraction of PtOEP molecules participating the SUC process (6.75% of the total). Residual PtOEP is detected (at 650 nm) but always lower than the SUC signal (between 400 nm and 530 nm). Wavelength for the excitation 532 nm.

Particularly, the spectrum in Figure 5.29-LEFT can be recalculated taking into account that the 93.25% of the PtOEP is not active. Therefore the 93.25% of the residual PtOEP peak in Figure 5.27 is ascribed to inactive PtOEP and the PL intensity profile can be corrected accordingly (i.e. multiplying the residual PtOEP PL at 650 nm by 0.0675) in Figure 5.31.

In our opinion the protocol presented in this section pops up new ideas for the design, characterization and understanding of liquid-core SUC nanoemitters, bypassing some issues due to the attitude of porphyrins to form SAS in presence of surfactants.

5.3.2 SUC-HD@PMMA nanocapsules in Poly(vinyl alcohol) bulk films

In the prior section we demonstrate that only the 6.75% of PtOEP actively participates to the SUC process (with an Energy Transfer yield of 99.4%) within the HD@PMMA nanocapsules. Here we will demonstrate that, notwithstanding the small fraction of PtOEP molecules contributing to SUC, this systems can be effectively used in proof-of-concept bulk Poly(Vinyl Alcohol) – PVA – systems. PVA is a water-soluble synthetic polymer (Figure 5.32) used in papermaking, textiles, and a variety of coatings[207].

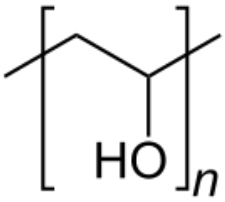

Figure 5.32: Simplified structure formula of poly(vinyl alcohol), PVA.

In this work commercial beads of PVA with degree of polymerization of 500 and degree of hydrolysation of 97.5-99.5 mol% provided by Fluka® were used. Firstly PVA beads were grinded in a miller, until a homogeneous fine powder was obtained. The PVA powder was dissolved in water (22% w/W) under stirring. 0.7 ml of PVA aqueous emulsion was then mixed with 1 ml of a 10 times diluted SUC-nanoemitters fresh emulsion. After homogenization with magnetic stirring, the obtained aqueous solution was drop-casted onto a freshly cleaned glass surface and dried at room temperature in order to evaporate the water.

Figure 5.33: a) Photograph of the PVA film loaded with nanoemitters, macroscopically transparent. b) Photograph of the PVA film showing its self-standing properties.

The dry PVA film can be shaped macroscopically in a controlled way, as shown in Figure 5.33. Moreover the obtained film is transparent (Figure 5.33-a) and self-standing (Figure 5.33-b).

The PVA film was then characterized by confocal microscope (Eclipse 80i Nikon) imaging at λ=532 nm in order to detect the presence either of PtOEP-rich domains (red) and SUC-active domains (blue). The image reported in Figure 5.34 was recorded using oil immersion objective in ambient condition (i.e. room temperature and presence of oxygen).

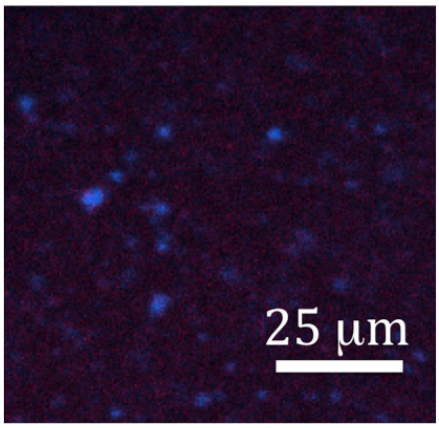

Figure 5.34: Optical image of the PVA film loaded withe SUC-HD@PMMA nanoemitters recorded with blue and red channel (λ_{exc}=532 nm). Small red spots representative of the inactive PtOEP domains are detected together with blue spots representative of SUC-active domains. The image was recorded in ambient conditions and presence of oxygen.

In Figure 5.34 both red and blue spots can be distinguished. The minoritarian red ones represent the inactive domain of isolated PtOEP molecules responsible for the long decay time (120 μs) in Figure 5.30. Bright blue spots associated with SUC domains can be detected as well. This confirms the fact that such SUC-HD@PMMA nanocapsules are able to shield the active dyes (PtOEP and DPA) from the detrimental effect due to the presence of atmospheric oxygen. It is worth noticing that the optical spot size (red and blue) in Figure 5.34 is not representative of the real size of the nanocontainers. In fact the confocal microscope used in this experiments has a typical lateral resolution of ~0.5 μm, far higher than the typical dimensions measured for such nanocapsules by SEM and DLS.

6 Monitoring the Kinetics of Polystyrene Nanoparticles Formation from Emulsion Droplets via Fluorescence Correlation Spectroscopy with Molecular Rotors tracers

6.1 Introduction

Since its first publication in 1977[208], the preparation of polymer nanoparticles with SEED was found to be one of the most effective approaches for nanoparticles preparation form preformed polymer. In detail, an organic solution of preformed polymer chains dissolved in a good organic solvent is mixed with an aqueous solution of surfactant. The obtained emulsion is formed by droplets of solvent where the polymer is dissolved. Polymer nanoparticles nucleate after the solvent evaporation of the organic solvent triggered by heating the solution. Still little is known for the details of particle formation during the transition from the initial liquid droplet emulsion to the final particle dispersion, especially in the case of particles with complex morphologies. A major reason is the lack of experimental techniques that can provide information on the internal morphology of very small nanodroplets and nanoparticles moving fast in a continuous liquid phase. In this respect, the sensitive and selective technique of fluorescence correlation spectroscopy (FCS, section 2.3.5) offers an interesting alternative and was already successfully used[209] to quantify several parameters such as the evolution of nanodroplet/nanoparticle size, the process of droplet coalescence, and the amount of encapsulated compounds. In this section, we will consider the use of the tailored molecular rotor ASB 158 as fluorescent nanodroplets/nanoparticles tracer in a FCS experiment as a method to obtain unique information on the kinetics of the nanoparticle formation during the SEED process. Molecular rotors are donor-acceptor organic molecules with peculiar photophysics due to their high degree of intramolecular rotational freedom. Particularly, their lifetime strongly depends on the local viscosity of the environment (see section 2.3.1.2 for details) and this capability has been already used to monitor processes such as block copolymer micelles formation[17] and bulk radical polymerization of methyl methacrylate[210]. We will demonstrate that combining FCS with molecular rotors potentially opens the possibility to monitor simultaneously the overall droplet/particle dynamics (in terms of diffusivity and size) and the inner morphology of the droplets/particles (i.e. remaining

solvent content or eventual phase separation), widening the range of parameters accessible in a single FCS experiment. In Figure 6.1 a sketch of the polymer nanoparticles formation during the SEED in presence of a molecular rotor tracer is shown.

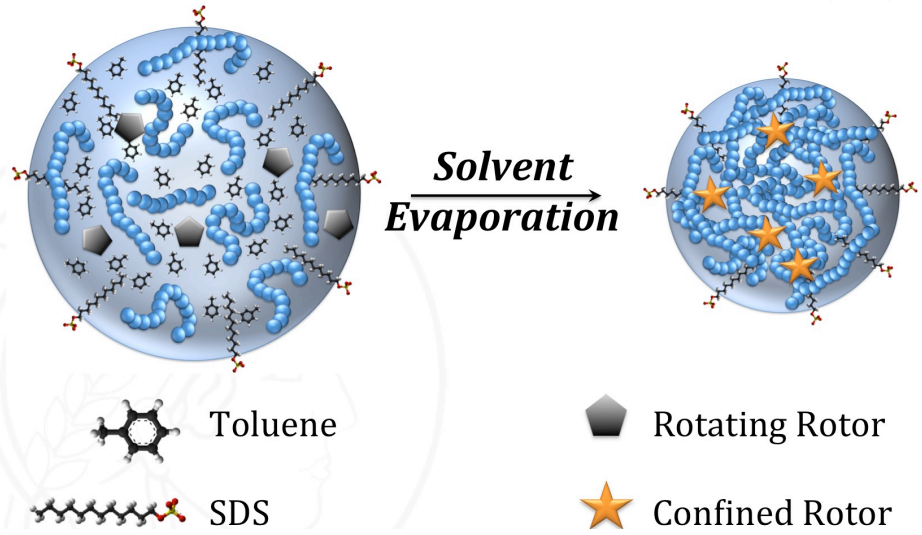

Figure 6.1: Sketch of the solvent evaporation kinetics monitored with FCS using a molecular rotor as tracer. Within the droplet we expect a slower rotor lifetime than in the final dried polymer nanoparticle, because the less solvent left in the droplet, the higher is the local viscosity. Moreover, assuming a homogeneous evaporation of the solvent without coalescence, the NPs final diameter is expected to be smaller than the droplet one.

Previous studies about the monitoring of the SEED process with FCS, underlined that coalescence is not playing a role in the polymer nanoparticle formation process[209b]. It is thus reasonable to assume that the average diameter of the droplet will decrease throughout the evaporation process, leading to the final polymer nanoparticle diameter. At the same time, using a hydrophobic molecular rotor as fluorescent tracer, we expect some changes in the lifetime. Particularly, we expect the measured lifetime to get longer as the solvent evaporation elapses. In fact the less solvent within the droplet, the high is the local viscosity probed by the rotor. As extensively reported in section 2.3.1.2, a higher viscosity triggers a slowdown of the measured lifetime.

6.2 *Coupling FCS with TRFS of the molecular rotor ASB158*

In Figure 6.2 the FCS correlation curves recorded on the initial droplet emulsion (circles for experimental points and red line for fitting) and on the final PS nanoparticles (triangles for experimental points and green line for fitting) are reported. The PS nanoparticles were obtained by heating the droplet emulsion 19.5 hours at 40°C. A decrease in the measured size from droplets (94±6) nm to nanoparticles (54±4) nm was detected. Accordingly with the sketch in Figure 6.1, this decrease in size is caused by toluene loss from the droplet and its evaporation through the continuous aqueous phase. Moreover no fast diffusing components - linked with small diffusing species such as individual rotor molecule or small rotor-labelled aggregates of polymer chains - were detected from the fitting.

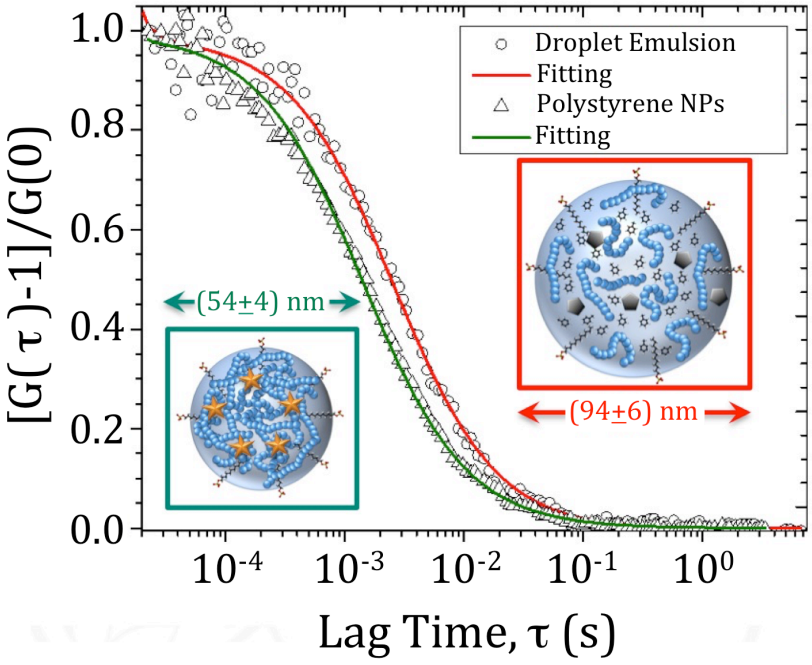

Figure 6.2: Normalized correlation curves (scattered symbols) and corresponding fits (lines). Scattered circles and red line represent the droplet situation, while the scattered triangles and green line represent the polymer nanoparticles situation.

In this way we underline that molecular rotors are dispersed only in the organic phase and can be effectively used as FCS tracers.

The time resolved fluorescence of the molecular rotor was measured at the same time on the same sample in the same probing volume during the same experiment. This is possible only by using a molecular rotor as fluorescent tracer (i.e. having a fluorescent molecule able to probe the properties of the surroundings as a function of lifetime change). In Figure 6.3 the rotor behaviour in pure toluene (black line), in the droplet emulsion (red line) and within the

polymer nanoparticles (green line) is reported. Accordingly with the increase in local viscosity moving from pure toluene to droplets emulsion to polymer nanoparticles, the lifetime of the molecular rotor increases from (4.8±0.1) ns in toluene to (5.6±0.1) ns in droplets emulsion and (6.2±0.1) ns in nanoparticles. The values were obtained fitting the experimental data with a single exponential decay.

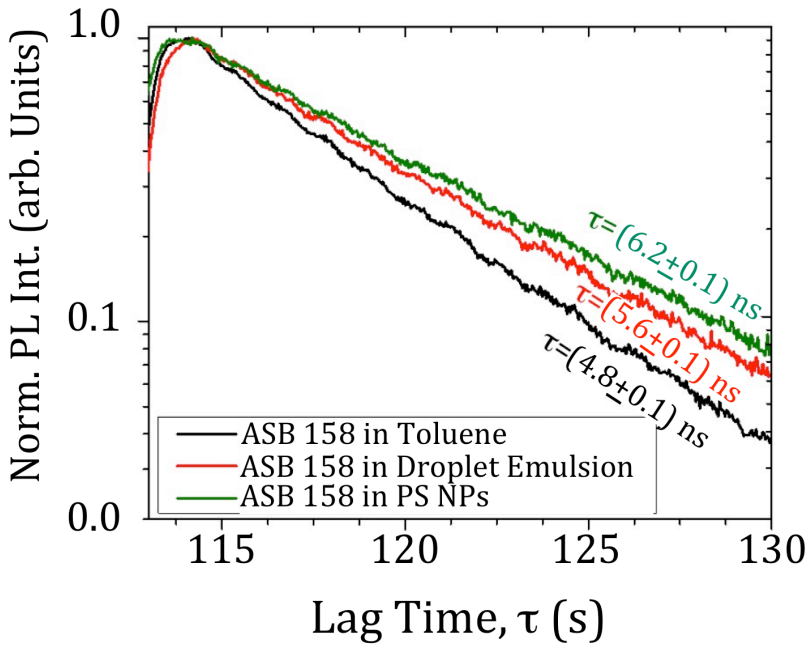

Figure 6.3: Time decay profile of the molecular rotor ASB158 acquired in a pure toluene solution without polymer (black line), in a droplet emulsion (4% polystyrene content, red line) and in the resulting aqueous emulsion of polystyrene nanoparticles obtained after toluene evaporation (40°C for 19.5 hours, green line).

From the fact that the rotor behaviour can be fitted with a single exponential decay in all three samples, we can speculate that the toluene evaporation occurs homogeneously throughout the nanoparticle formation process.

A further improvement in the data analysis would be correlating the measured lifetime with the toluene content within the droplets during the SEED process. In this regards we tried to build up a master curve (Figure 6.4).

The first issue to comment is the strong increase of the lifetime from pure toluene solution to emulsion droplets. Indeed within the droplets the nominal concentration of polystyrene is 4% w/W (see section 2.2.2.1). From the calibration line, the expected lifetime for a 4% w/W homogeneous solution of PS in toluene is (4.7±0.1) ns, comparable with the one in pure toluene (4.8±0.1) ns within error bars. This is not surprising, since it is known[62] that molecular rotors, even with a high dynamic response range, need a change in viscosity of 1 - 2 orders of magnitude for detecting measurable changes in lifetime (see Figure 2.6).

Accordingly, the 4% w/W PS concentration seams too low to confine the rotor and to cause an abrupt change in the measured lifetime.

However, in the freshly prepared droplet emulsion a lifetime of (5.6±0.1) ns was measured. This value is far higher than the expected value for a bulk solution of 4% w/W PS in toluene. Collateral lifetime measurements using toluene saturated with water were performed in order to understand the eventual effect of traces of water on the behaviour of the rotor. Notwithstanding no difference between the rotor lifetime behaviour in pure toluene and in water-saturated toluene were observed. The result suggests the increase in lifetime is not due either of the presence if water traces or to rotor amphiphilicity.

Lastly, the slight enhancement of the lifetime from the emulsion droplet to the dry polymer nanoparticle is coherent with the complete drying (i.e. toluene evaporation) of the droplet to form the polymer nanoparticle.

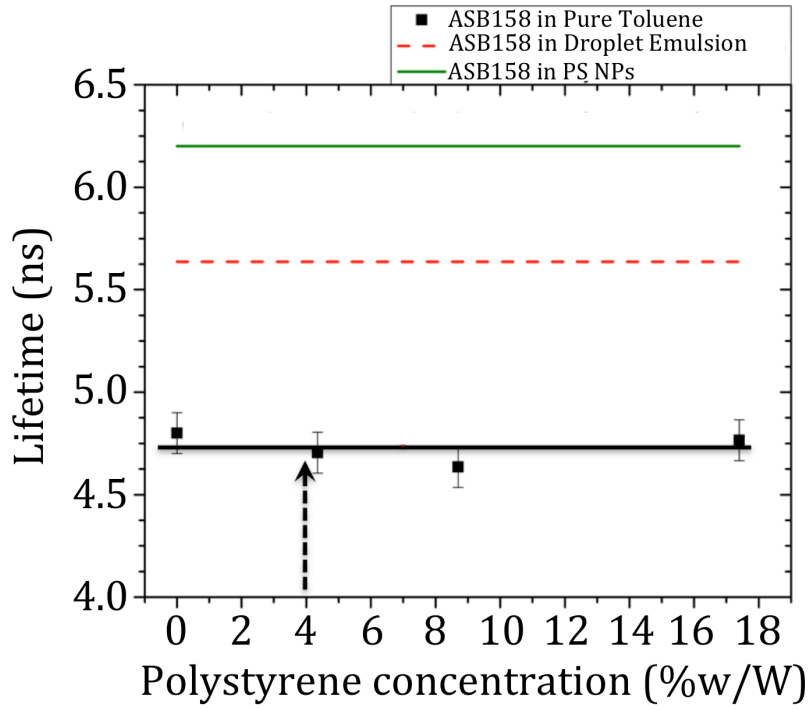

Figure 6.4: Calibration curve for the lifetime of the rotor ASB 158 as function of polystyrene concentration in toluene solution. Black squares are experimental points and black line is meant to guide the eye. Dashed red line is the measured lifetime in freshly prepared droplets (after stirring and ultrasonication). Solid green line is the measured lifetime in dry polymer nanoparticles.

In our opinion this abrupt change in lifetime within the droplet could be related to some processes happening during the preparation of the droplet emulsion, namely during the

homogenization steps (stirring and ultrasonication). As an indirect demonstration, a back on the envelope calculation is proposed. Starting from the measured droplet diameter of (94±6) nm and the final measured diameter of the dry polymer nanoparticles (54±4) nm, the loss in volume can be estimated assuming no coalescence (as demonstrated elsewhere[209b]) and ascribing the whole volume loss to toluene evaporation through the continuous phase. The volume loss during the SEED process can thus be estimated in $\sim 1.5 \cdot 10^{-16}$ ml per particle. Moreover, it is possible to estimate in $\sim 1.1 \cdot 10^{-16}$ g the mass of the final dry PS nanoparticle. Therefore the initial (i.e. after stirring and ultrasonication) PS concentration in the droplets is between 12% w/W and 35% w/W, far higher then the nominal 4% w/W. This could suggest that already after the homogenization step - necessary to prepare stable droplets - something is happening within the droplet emulsion. This kind of information is accessible (to our knowledge) only using molecular rotors as FCS tracers.

These enthusiastic preliminary results are stimulating further investigations about the use of molecular rotors with higher dynamic response as molecular tracers in FCS experiments, in order to gather new details about particle formation, especially in the case of particles with complex morphologies. Since the FCS focal volume is in the femtoliters range, adopting molecular rotors as FCS tracers could open new perspectives in the local definition of viscosity and, more generally, in the study of diffusivity at the nanoscale.

7 Conclusions

The main aim of this work was the preparation of functional polymer-based biphasic core@shell nanoparticles via emulsion polymerization, particularly in the fields of nanoadditive for extrinsic self-healing materials, encapsulation of bio-inspired lipophilic dyes and nanophotonic. Before going ahead with the preparation of the nanostructures, a method for the in-situ measurement of glass transition temperature based on the time-resolved fluorescence (TRFS) of AzeNaph1 molecular rotor at different temperatures was developed. This step was felt as necessary since it is known that glass transition temperature (T_g) of polymers confined to the nanoscale can deviate substantially from the bulk value, due to T_g-confinement effects. AzeNaph1 was found to be able to detect glass transition either in bulk polymer samples and in case-study polystyrene (PS) nanoparticles. Particularly, the T_g value detected in bulk polymer samples with TRFS agrees with the value detected via standard DSC. It was thus possible to demonstrate that AzeNaph1 TRFS can be used as a T_g-detector methodology even for the detection of glass transition directly in an emulsion of PS nanoparticles. Accordingly, nanoparticles as small as 30 nm in hydrodynamic radius were found to retain the bulk polystyrene T_g value (~100°C).

Moreover, another molecular rotor ASB158 has been used as a fluorescent tracer for Fluorescence Correlation Spectroscopy experiments. Taking into account the polymer viscosity/chain organization sensitivity of molecular rotors, the use of ASB158 as fluorescent tracer within nanodroplets/nanoparticles in a FCS experiment was found to be an effective way to obtain preliminary unique information on the kinetics of nanoparticles formation during the SEED process, thus widening the range of parameters accessible in a single FCS experiment.

Therefore, the observation that the T_g-related bulk polymer properties are conserved even in PS nanoparticles of 30 nm in radius was used as an important paradigm towards the preparation and application of biphasic polymer-based nanoparticles. With this regard, an optimized semicontinuous emulsion polymerization protocol for the preparation of poly (*n*-butyl acrylate)@polystyrene (PBA@PS) core@shell nanoparticles was developed. The main issue to overcome was the possibility to grow on a PBA core a PS shell. By controlling the dropping rate of both monomers and by using a branched sulfosuccinate sodium salt as surfactant, it was possible to obtain monodisperse biphasic nanoparticles with a precise core@shell morphology. The effective sequestration of the PBA core within the PS shell was demonstrated by several methods (DSC, ^{13}C-MAS-NMR, ^{1}H-TD-NMR, AFM, DLS). However

very few was known about the actual behaviour of a nanoembedded adhesive (such as PBA) within a plastomer shell (PS). In this regard, AFM force spectroscopy measurements (FS) were performed on a single PBA@PS nanoparticle. AFM-FS shows that PBA@PS nanoparticles are force-responsive nano-objects: pressed with forces in the order of some hundreds of nN, they can collapse and release a baroplastic glue. The applied force on the PBA@PS nanoparticles triggers the structural collapse of the nanoparticle, loosing its characteristic spherical shape towards a prolate and flattened fluid-like structure without any observable glassy residual. The ability of these nanoparticles formed by a glassy polymer (PS) and a soft polymer (PBA) to flow at room temperature as a melt-like blend, known as baroplasticty, is due to a pressure-enhanced miscibility between the two different nanodomains. To our knowledge we gave the first example of baroplasticity detected on a single particle scale. Beyond the basic research interest on the nanomorphology evolution under non-equilibrium stress, this result can be interesting in manufacturing a new class of sealing nanoadditives in the field of extrinsic self-healing materials.

We demonstrated that such PBA@PS can have even other applications. Namely, PBA@PS nanoemitters for sensitized up-conversion (SUC) deliverable as an optically active aqueous solution were prepared. $PdPh_4TBP$ and BPEA SUC dyes were added within the PBA core, known to have a very good permeability to SUC molecules and to be the reference matrix for solid-state SUC materials[153]. Notwithstanding an energy transfer efficiency of the 58% was measured in aqueous solution and a residual signal of inactive PdPh4TBP was detected. This result is in disagreement with the SUC behaviour of $PdPh_4TBP$ in the bulk control samples prepared as reference, showing an energy transfer efficiency higher than 95%. The efficiency drop from bulk polymerized PBA to PBA@PS core@shell is manifold. Firstly, emulsion polymerization is a template reaction where the polymerization locus is in the order of $\sim 10^2$ nm. It means that the core-formulation (i.e. radical initiator, monomer, SUC dyes and surfactant) is confined in droplets with typical volume in the order of $\sim 10^{-3}$ *f*L. Within such a small volume, the conjugated dyes in the monomer droplets are likely either to interact detrimentally with the initiator/surfactant molecules or to move towards the shell because of π–π interactions. This limit of PBA@PS nanoparticles was overcome by preparing a second family of core@shell nanoparticles: liquid-core nanocapsules, with a *n*-hexadecane (HD) core embedded in a plastomer poly(methyl methacrylate) (PMMA) shell. The SUC-dyes (PtOEP and DPA in this latter case) were directly added in the liquid HD and used to prepare the emulsion. The formation of the nanocapsules is driven by the phase separation occurring between PMMA and HD during the polymerization of MMA. The results show that the 6.75%

of PtOEP actively participates to the SUC process (with an Energy Transfer yield of 99.4%, comparable to the bulk liquid case) within the HD@PMMA nanocapsules. Even if a fraction of PtOEP molecules is stuck in a bulk-like environment according to TRPL experiments, this nanocapsules are able to behave as a bulk liquid solution. Moreover, such liquid-core nanoemitters were embedded in a bulk PVA film showing SUC in ambient conditions. In this way we demonstrated both the possibility of obtaining an aqueous emulsion of SUC nanoemitters to be dispersed in a bulk Proof-of-Concept self-standing bulk PVA sample. The bulk SUC film was found to be effective even in ambient conditions (i.e. in presence of oxygen), demonstrating the barrier-effect of the nanocapsules, protecting the SUC dyes and underlying the potentialities of this system for everyday-applications.

HD@PMMA nanocontainers were used for encapsulating TiO_2 anatase nanocrystals capped with oleic acid (dimensions ~ 4 nm) within the HD core. Anatase, with a refractive index ~ 2.5 higher than polymers, can be added to polymer matrices for the preparation of hybrid polymer materials with enhanced refractive index. Moreover, bulk PMMA is known to be transparent and to be shaped into self-standing slabs with large area (~ several tens of cm^2)[152, 177]. However TiO_2 anatase nanocrystals have a very high surface energy and can aggregate within bulk polymer matrix, leading to opaque materials almost irrelevant for real applications. Here we demonstrated that HD@PMMA nanocapsules can be loaded with TiO_2 anatase nanocrystals, without any aggregation. The TiO_2 crowding within the core is so high that it inhibits the crystallization of HD. More interestingly, these nanocapsules have been used as nanocarrier of TiO_2 during the bulk polymerization of PMMA, obtaining transparent bulk sample of PMMA with refractive index increased from 1.48 to 1.50.

Concluding, with this work we devise Proof-of-Concept examples about the applicability of polymer nanoparticles as functional ingredients within formulations for the preparation of hierarchical functional materials. Moreover, we strongly believe that emulsion polymerization can be of strategic interest in the contest of a more sustainable chemistry for materials science applications. Indeed, it can be performed in aqueous solution obtaining functional nanostructures that can encapsulate several active/hazardous molecules. On the long run, such nanostructures can be used either as an effective nano-additive for the preparation of functional materials or as a nano-carrier sequestrating hazardous chemicals, potentially limiting the risk for operators, consumers and users daily handling such reactants, goods and products all over the world.

8 Acknowledgements

Along these three years, I have learnt one very precious thing: Science is about People. People you meet, People you work with, People you know, People you like, People you dislike. My PhD work and personal growth would have been sterile, if I would not meet all these kinds of people.

I would like to thank my PhD supervisor Prof. Dr. Roberto Simonutti and my PhD dean Prof. Dr. Gianfranco Pacchioni for the financial, scientific and personal support all along these three years.

I have to thank all the people helping me in the development of the projects I was given:

Molecular Rotors: Dr. Gianfranco Vaccaro, Dr. Alberto Bianchi, Dr. Michele Mauri, Dr. Alessandro Sanguineti, Prof. Dr. Luca Beverina, Prof. Dr. Francesco Meinardi.
PBA@PS nanoparticles: Matteo Farina (PhD Student), Ivan Andreosso (M.Sc.) and Dr. Michael Kappl.
Carminic acid derivatives: Davide Origgi (M. Sc.), Prof. Dr. Laura Cipolla and Dr. Gianfranco Vaccaro.
SUC-Nanoemitters: Ivan Andreosso (M. Sc.), Riccardo Zagheno (M. Sc.), Jacopo Pedrini (PhD Student), Dr. Angelo Monguzzi and Prof. Dr. Francesco Meinardi.
TiO_2 encapsulation: Dr. Annalisa Colombo.
FCS coupling with Molecular Rotors: Dr. Kaloian Koynov, Andreas Best (Technician), Prof. Dr. Hans-Jürgen Butt, Li-Ping Lv (PhD Student), Dr. Daniel Crespy, Prof. Dr. Katharina Landfester.

I want to specially mention the M.Sc. students I had the opportunity to work with: Ivan Andreosso, Davide Origgi and Riccardo Zagheno. They teach me a lot about science, about team working, about myself (and that was the tough part).

I had the honour to work with Matteo Farina, who did the ^{1}H-TD-NMR you see in this work. I professionally owe him quite a lot: scientific discussions, experiments planning and scientific writing. Luckily, I had the possibility to share with him some deep personal moments. I have just to say thanks to Matteo as a scientist, as a man, as a friend (he knows the right order).

Among the awesome AK Butt crew I should thank quite some people for many different reason.
Dr. Kaloian Koynov: he took care about all the aspects of my stay in Mainz (housing, scientific projects, personal motivation). He really acted like a mentor during my half a year stay. The door of his office was always open, the coffee ready to drink and the chat easy to start.
I thank Michael Kappl (helping me with the AFM experiments you see here) because I think I am among the very few enjoying the AFM instrument dead time. And it is definitely thanks to the awesome discussions about travels, food, cities to visit,….and science, of course!

I have to thank the MPIP band (Dongsheng Wang, Dominik Pilat, Ilka Hermes, Sebastian Thomas and Zack Urbach) because we simply rocked at the MPIP Christmas Party!
Last but not least on the MPIP sight: thank you to the Office of Awesomeness (Jing, Jennifer, David, Franziska and Veronika). You can guess the motivation from the name.

I have to thank some of the MPIPers (Henning We, Dongsheng Wang –AGAIN!–, Zack Urbach and Thomas Nick) for invading my flat and visiting me as an old friend.

I thank my parents because they taught me that sometimes you have to sit down and listen to understand your role and to find your way. It took them quite some time and effort to teach me this. I hope now they can take some joy from the growth path I am walking on.

Lastly I would like to thank Anna. She keeps telling me: “You can do it!”, without shouting, without kidding, without betting. She seems to know it.
Well, now I know she was wrong.
I did not do it.
WE DID IT!

9 Publication List

In attached the detailed list of the scientific production during the PhD.

Posters:

L. Cipolla, L. Gabrielli, S. Bonetti, R. Simonutti, D. Origgi, "**STUDIES ON THE CHEMICAL DERIVATISATION OF CARMINIC ACID**" *XIV CSCC 2014 Carbohydrate Chemistry Interdipartimental Group* **June 22-25 2014**, Certosa di Pontignano (SI) – ITALY.

S. Bonetti, I. Andreosso, R. Simonutti, "**MINIEMULSION POLYMERIZATION: A TOP-DOWN APPROACH FOR FUNCTIONAL NANOCONTAINERS PREPARATION**" *XXI Convegno AIM 2014* **September 14-19 2014**, Torino – ITALY.

A. Bianchi, S. Bonetti, G. Vaccaro, L. Beverina, M. Mauri, F. Meinardi, R. Simonutti, "**AMPHIPHILIC BLOCK-COPOLYMERS AND REPTATION PHENOMENA: A PHOTOPHYSICS APPROACH BASED ON MOLECULAR ROTORS**" *XXI Convegno AIM 2014* **September 14-19 2014**, Torino – ITALY.

G. Vaccaro, A. Bianchi, S. Bonetti, M. Mauri, A. Sanguineti, F. Meinardi, L. Beverina, R. Simonutti, "**DIRECT MONITORING OF SELF-ASSEMBLY OF COPOLYMERIC MICELLES BY A LUMINESCENT MOLECULAR ROTOR**" *ECME* **September 3-7 2013**, London – UNITED KINGDOM.

S. Bonetti, M. Farina, M. Mauri, K. Koynov, H.-J. Butt, M. Kappl, R. Simonutti, "***IN-SITU* AFM MONITORING OF THE "POACHED-EGG" BREAKDOWN OF POLY(N-BUTYLACRYLATE)/POLYSTYRENE CORE-SHELL NANOPARTICLES AS POTENTIAL CAPSULE-BASED HEALING SYSTEM**" *E-MRS* **September 15-18**, Warsaw – POLAND.

Oral Presentations:

M. Mauri, A. Bianchi, S. Bonetti, G. Vaccaro, L. Beverina, F. Meinardi, R. Simonutti, "**MOLECULAR ROTORS: PROBE OF LOCAL POLYMER DYNAMICS**" *EPF 2013* **June 16-21 2013**, Pisa - ITALY.

M. Farina, S. Bonetti, M. Mauri, R. Simonutti, "**INTERFACES, INTERPHASE AND MORPHOLOGY OF POLY(N-BUTYLACRYLATE)/POLYSTYRENE NANOPARTICLES OBTAINED VIA MINIEMULSION POLYMERIZATION**" *8th ENCP Internation Conference on Nanostructured Polymer and Nanocomposites,* **September 16-19 2014**, Dresden - GERMANY.

S. Bonetti, A. Bianchi, M. Mauri, K. Koynov, M. Kappl, H.J. Butt, R. Simonutti, "**HIERARCHICAL SELF-ASSEMBLY OF POLY(N,N-DIMETHYLACRYLAMIDE)-BLOCK-POLYSTYRENE "CREW-CUT" AGGREGATES**" *EPF 2013* **June 16-21 2013**, Pisa - ITALY.

S. Bonetti, M. Farina, M. Mauri, I. Andreosso, R. Simonutti, "**EMERGING INTERPHASE IN POLY(*n*-BUTYLACRYLATE)/POLYSTYRENE CORE-SHELL NANOPARTICLES OBTAINED *VIA* SEMICONTINOUS MINIEMULSION POLYMERIZATION**" *ISPAC 2014* **June 16-18 2014**, Les Diablerets - SWITZERLAND.

S. Bonetti, M. Farina, A. Colombo, M. Kappl, I. Lieberwirth, M. Mauri, R. Simonutti, "**POLYMER NANOPARTICLES: FROM FUNDAMENTAL PROPERTIES TO POTENTIAL APPLICATIONS**" *250th ACS National Meeting* **August 16-20 2015**, Boston – Massachusetts USA.

S. Bonetti, J. Schultze, L.P. Lv, M. Mauri, L. Beverina, K. Landfester, H.-J. Butt, D. Crespy, R. Simonutti, K. Koynov, "**MONITORING THE KINETICS OF NANOPARTICLES FORMATION BY FLUORESCENCE**

CORRELATION SPECTROSCOPY WITH MOLECULAR ROTOR TRACERS" *2nd Workshop: FCS in Polymer Science* **September 24-25 2015**, Aachen – GERMANY. (***BEST PRESENTATION AWARD***)

Articles on peer-rewied journals:

G. Vaccaro, A. Bianchi, S. Bonetti, M. Mauri, A. Sanguineti, F. Meinardi, R. Simonutti, L. Beverina "**DIRECT MONITORING OF SELF-ASSEMBLY OF COPOLYMERIC MICELLES BY A LUMINESCENT MOLECULAR ROTOR**" *Chem. Commun*., **2013**, *49*, 8474-8476.

A. Bianchi, M. Mauri, S. Bonetti, K. Koynov, M. Kappl, I. Lieberwirth, H.-J. Butt, R. Simonutti, "**HIERARCHICAL SELF-ASSEMBLY OF PDMA-*b*-PS CHAINS INTO GRANULAR NANOPARTICLES",** *Macromol. Rapid. Commun.,* **2014**, *35*, 1994-1999.

S. Tavazzi, L. Ferraro, M. Fagnola, F. Cozza, S. Farris, S. Bonetti, R. Simonutti, A. Borghesi, "**MECHANICALLY TRIGGERED SOLUTE UPTAKE IN SOFT CONTACT LENSES",** *Colloids Surf., B,* **2015**, *130*, 16-22.

E. Mascheroni, R. Rampazzo, M.A. Ortenzi, G. Piva, S. Bonetti, L. Piergiovanni, **"COMPARISON OF CELLULOSE NANOCRYSTALS OBTAINED BY SULFURIC ACID HYDROLYSIS AND AMMONIUM PERSULFATE, TO BE USED AS COATING ON FLEXIBLE FOOD-PACKAGING MATERIALS"**, *Cellulose*, **2016**, *23*, 779-793.

S. Bonetti, M. Farina, M. Mauri, K. Koynov, H.-J. Butt, M. Kappl, R. Simonutti, **"CORE@SHELL POLY(*N*-BUTYL ACRYLATE)@POLYSTYRENE NANOPARTICLES: BAROPLASTIC FORCE-RESPONSIVENESS IN PRESENCE OF STRONG PHASE SEPARATION",** *Macromol. Rapid. Commun.* **2016**, DOI: 10.1002/marc.201500625.

APPENDIX

a. AFM, average diameter calculation

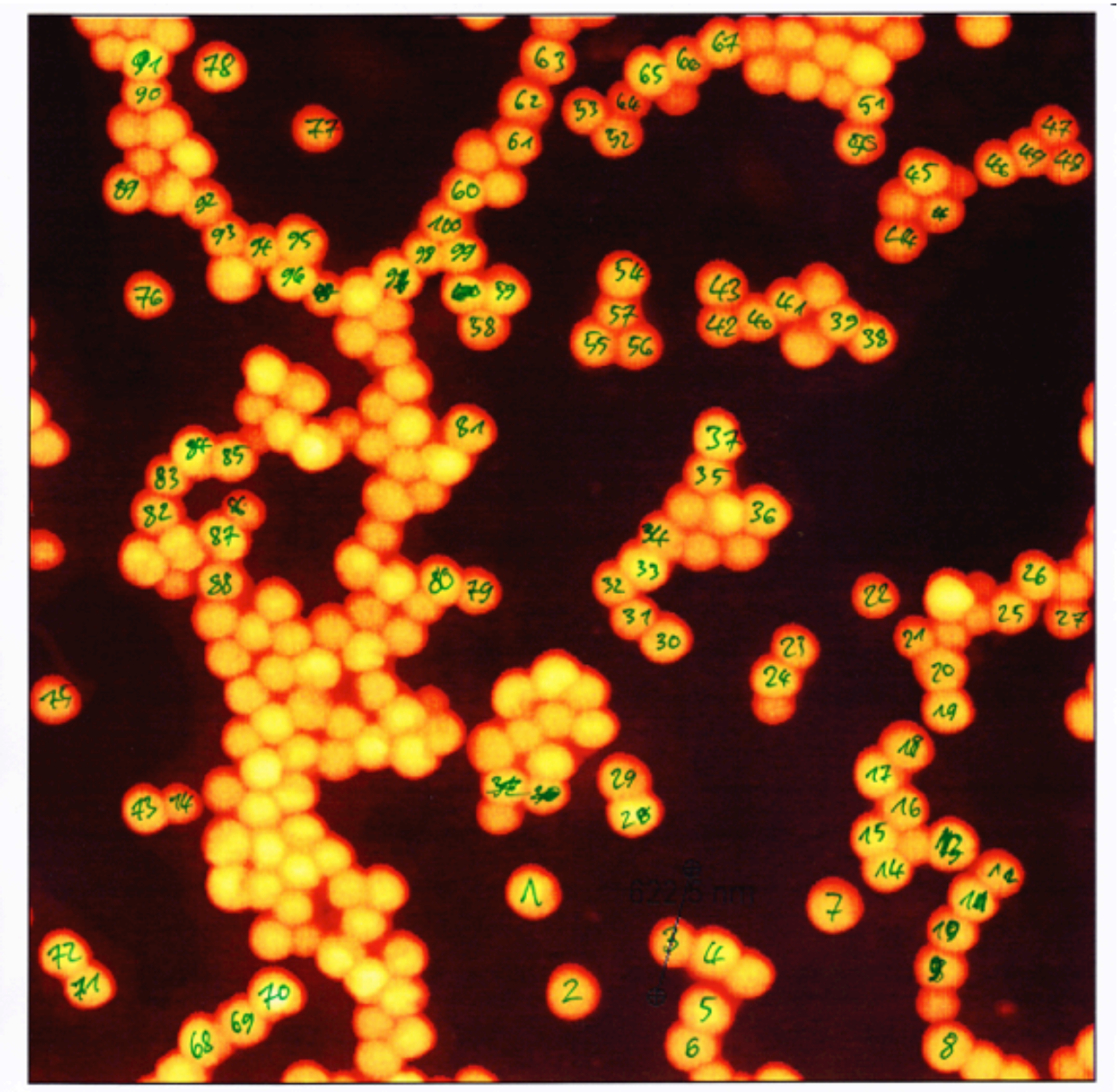

Figure a.1: AFM image used for the calculation of the average particle diameter. After S.Bonetti, M. Farina, M. Mauri, K. Koynov, H.-J. Butt, M. Kappl, R. Simonutti, *Macromol. Rapid Commun.* 2016, DOI: 10.1002/marc.201500625. © 2016 WILEY-VCH Verlag GmbH & Co. KGaA, Weinheim.

Particle Number	Measured size (nm)	***Particle Number***	Measured size (nm)	***Particle Number***	Measured size (nm)	***Particle Number***	Measured size (nm)	***Particle Number***	Measured size (nm)
1	178	***11***	172	***21***	150	***31***	160	***41***	160
2	167	***12***	159	***22***	164	***32***	164	***42***	150
3	160	***13***	162	***23***	156	***33***	187	***43***	157
4	177	***14***	172	***24***	166	***34***	157	***44***	146
5	177	***15***	182	***25***	163	***35***	163	***45***	171
6	167	***16***	160	***26***	162	***36***	173	***46***	162
7	165	***17***	187	***27***	150	***37***	182	***47***	158
8	154	***18***	166	***28***	185	***38***	168	***48***	140
9	153	***19***	167	***29***	167	***39***	151	***49***	152
10	159	***20***	155	***30***	159	***40***	153	***50***	167
51	170	***61***	160	***71***	163	***81***	164	***91***	190
52	150	***62***	176	***72***	176	***82***	153	***92***	157
53	163	***63***	169	***73***	167	***83***	155	***93***	150
54	167	***64***	139	***74***	152	***84***	177	***94***	149
55	163	***65***	165	***75***	166	***85***	157	***95***	165
56	152	***66***	165	***76***	152	***86***	150	***96***	170
57	151	***67***	170	***77***	177	***87***	159	***97***	160
58	159	***68***	183	***78***	177	***88***	160	***98***	161
59	178	***69***	162	***79***	156	***89***	172	***99***	168
60	174	***70***	191	***80***	171	***90***	165	***100***	153

Average Diameter = 164±11 nm, N=100.

b. SEM, Average NPs diameter calculation

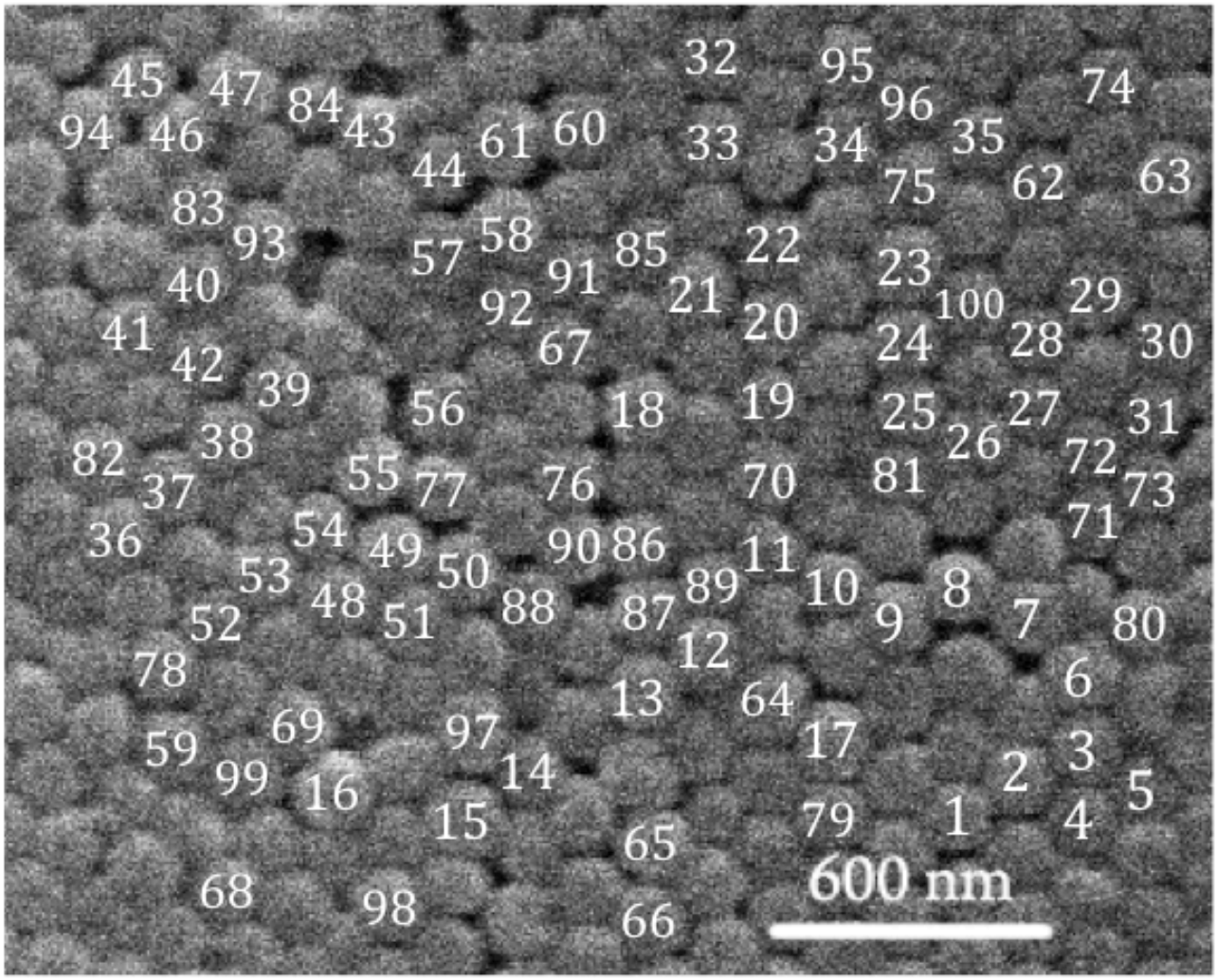

Figure a.2: AFM image used for the calculation of the average particle diameter. After S. Bonetti, M. Farina, M. Mauri, K. Koynov, H.-J. Butt, M. Kappl, R. Simonutti, *Macromol. Rapid Commun*. 2016, DOI: 10.1002/marc.201500625. © 2016 WILEY-VCH Verlag GmbH & Co. KGaA, Weinheim.

Particle Number	Measured size (nm)	***Particle Number***	Measured size (nm)	***Particle Number***	Measured size (nm)	***Particle Number***	Measured size (nm)	***Particle Number***	Measured size (nm)
1	171	***11***	149	***21***	177	***31***	166	***41***	177
2	143	***12***	171	***22***	183	***32***	177	***42***	171
3	171	***13***	177	***23***	177	***33***	160	***43***	174
4	166	***14***	151	***24***	171	***34***	174	***44***	171
5	174	***15***	171	***25***	166	***35***	180	***45***	166
6	194	***16***	177	***26***	177	***36***	177	***46***	163
7	171	***17***	154	***27***	149	***37***	166	***47***	177
8	157	***18***	166	***28***	149	***38***	174	***48***	174
9	143	***19***	143	***29***	177	***39***	177	***49***	171
10	166	***20***	154	***30***	171	***40***	180	***50***	180
51	174	***61***	174	***71***	169	***81***	171	***91***	174
52	154	***62***	174	***72***	171	***82***	174	***92***	171
53	166	***63***	171	***73***	169	***83***	169	***93***	171
54	143	***64***	177	***74***	171	***84***	149	***94***	160
55	149	***65***	171	***75***	174	***85***	149	***95***	149
56	154	***66***	166	***76***	183	***86***	146	***96***	177
57	171	***67***	174	***77***	177	***87***	174	***97***	171
58	166	***68***	166	***78***	171	***88***	180	***98***	171
59	177	***69***	171	***79***	169	***89***	146	***99***	183
60	180	***70***	174	***80***	166	***90***	171	***100***	171

Average Diameter = 168±11 nm, N=100.

REFERENCES

[1] J.P. Rao, K.E. Geckeler *Prog. Polym. Sci.* **2012**, *36*, 887

[2] M. Hosokawa, K. Nogi, M. Naito, T. Yokoyama "Nanoparticle technology handbook". Amsterdam, Netherlands: Elsevier; 2007.

[3] H. Fudouzi, Y. Xia, *Adv. Mater.* **2003**, *15*, 892–6.

[4] S. Brahim, D. Narinesingh, G.A. Elie, *Anal. Chim. Acta* **2001**, *448*, 27–36.

[5] Q. Zhang, K.T. Chuang, *Adv. Environ. Res.* **2001**, *5,* 251–8.

[6] J. Kreuter. "Nanoparticles". In: J. Kreuter, editor. Colloidal drug delivery systems, vol. 66. New York: Marcel Dekker; 1994. p. 219–342.

[7] C. Vauthier, P. Couvreur. "Development of nanoparticles made of polysaccharides as novel drug carrier systems". In: D.L. Wise, editor. Handbook of pharmaceutical controlled release technology. New York: Marcel Dekker; 2000. p. 13–429.

[8] P. Couvreur, C. Dubernet, F. Puisieux, *Eur. J. Pharm. Biopharm.* **1995**, *41*, 2–13.

[9] Isi web of Knowledge.

[10] Y. Zhao, R. Berger, K. Landfester, D. Crespy, Polym. Chem., 2014, 5, 365-371.

[11] http://www.agcs.allianz.com/sv-se/insights/expert-risk-articles/nanotechnology/

[12] *Cratylus* Paragraph Crat. 401 section d line 5.

[13] C. Zhang, Y. Guo, R.D. Priestley, *Macromolecules* **2011**, *44*, 4001-4006.

[14] a) G. Vignaud, M.S. Chebil, J.K. Bal, N. Delorme, T. Beuvier, Y. Grohens, A. Gibaud, *Langmuir* **2014**, *30*, 11599-11608. b) J.M. Torres, C.M. Stafford, D. Uhrig, B.D. Vogt, *J. Polym. Sci., Part B: Polym. Phys.* **2012**, *50*, 370-377. c) J.S. Sharp, J.H. Teichroeb, J.A. Forrest *Eur. Phys. J. E Soft Matter* **2004**, *15*, 473-487.

[15] M. Tress, E.U. Mapesa, W. Kossack, W.K. Kipnusu, M. Reiche, F. Kremer, *Science* **2013**, *341*, 1371.

[16] I. Bahar, B. Erman, F. Kremer, E. Fisher, *Macromolecules* **1992**, *25*, 816.

[17] G. Vaccaro, A. Bianchi, M. Mauri, S. Bonetti, F. Meinardi, A. Sanguineti, R. Simonutti, L. Beverina *Chem. Commun.* **2013**, *49*, 8474-8476.

[18] J.M. Nölle, C. Jüngst, A. Zumbusch, D. Wöll *Polymer Chem.* **2014**, *5*, 2700-2703.

[19] S.Bonetti, M. Farina, M. Mauri, K. Koynov, H.-J. Butt, M. Kappl, R. Simonutti, *Macromol. Rapid Commun.* **2016**, DOI: 10.1002/marc.201500625.

[20] a) K. Koynov, H.-J. Butt *Current Opinion in Colloid & Interface Science*, **2012**, *17*, 377-387.

[21] J.W. Vanderhoff, M.S. El Aasser, J. Ugelstad Polymer emulsification process. US Patent 4,177,177 (1979).

[22] C. Bindschaedler, R. Gurny, E. Doelker Process for preparing a powder of water-insoluble polymer which can be redispersed in a liquid phase, the resulting powder and utilization thereof. US Patent 4,968,350 (1990).

[23] H. Fessi, F. Puisieux, J.P. Devissaguet, N. Ammoury, S. Benita *Int. J. Pharm.* **1989,** *55*, R1–4.

[24] P. York *Pharm. Sci. Technol. Today* **1999**, *2*, 430–40.

[25] W.D. Harkins, *J. Am. Chem. Soc.* **1946**, *69*, 1428-1444.

[26] R.C. Dewald, L.H. Hart, W.F. Carroll, *J. Polym. Sci. Part A: Polym. Chem.* **1984**, *22*, 2923-2930.

[27] F. Candau, Y.S. Leong, R.M. Fitch *J. Polym. Sci. Part A: Polym. Chem.* **1985**, *23*, 193-214.

[28] R.A. Cox, M.C. Wilkinson, J.M. Creasey, A.R. Goodall, J. Hearn *J. Polym. Sci. Part A: Polym. Chem.* **1977**, *15*, 2311-2319.

[29] L. Danicher, Y. Frere, A.L. Calve *Macromol. Symp.* **2000**, *151*, 387–92.

[30] C.S. Chern, *Prog. Polym. Sci.* **2006**, *31*, 443-486.

[31] a) F.A. Bovey, I.M. Kolthoff, A.I. Medalia, E.J. Meehan. *Emulsion polymerization*. New York: Interscience Publishers; **1965**. b) D.C. Blakely. *Emulsion polymerization. Theory and practice.* London: Applied Science; **1975**. c) V.I. Eliseeva, S.S. Ivanchev, S.I. Kuchanov, A.V. Lebedev. *Emulsion polymerization and its applications in industry.* New York: Consultants Bureau; **1981**. d) J. Barton, I. Capek. *Radical polymerization in disperse systems.* New York: Ellis Horwood; **1994**. e) R.G. Gilbert. *Emulsion polymerization: a mechanistic approach*. London: Academic Press; **1995**. f) R.M. Fitch. *Polymer colloids: a comprehensive introduction*. London: Academic Press; **1997**.

[32] a) S.C. Thickett, R.G. Gilbert. *Polymer* **2007**, *48*, 6965–6991. b) J.M. Asua. *J. Polym. Sci. Part A Polym. Chem.* **2004**, *42*, 1025–1041.

[33] a) W.D. Harkins. *J. Chem. Phys.* **1945**, *13*, 381–382. b) W.D. Harkins. *J. Chem. Phys.* **1946**, *14*, 47–48. c) W.D. Harkins. *J. Am. Chem. Soc.* **1947**, *69*, 1428–1444.

[34] a) W.V. Smith, R.H. Ewart. *J. Chem. Phys.* **1948**, *16*, 592–599. b) V.W. Smith. *J. Am. Chem. Soc.* **1948**, *70*, 3695–3702. c) W.V. Smith. *J. Am. Chem. Soc.* **1949**, *71*, 4077–4082.

[35] a) J.L. Gardon. *J. Polym. Sci. A* **1968**, *6*, 623–41. b) J.L. Gardon. *J. Polym. Sci. A* **1968**, *6*, 643–664.

[36] Y. Luo, F.J. Schork. *J. Polym. Sci.: Part A: Polym. Chem.* **2002**, *40*, 3200–3211.

[37] F.K. Hansen, J. Ugelstad *J. Polym. Sci. Polym. Chem.* **1978**;*16*:1953–79.

[38] a) J. Barton, A. Karpatyova. *Makromol. Chem.* **1987**, *188*, 693–702. b) M. Nomura, K. Fujita, *Makromol. Chem. Rapid. Commun.* **1989**, *10*, 581–587.

[39] a) H. Edelhauser, J.W. Breitenbach, *J. Polym. Sci.* **1959**, *35*, 423– 428. b) J.W. Breitenbach, H. Edelhauser, *Makromol. Chem.* **1967**, *44*, 196 –211. c) P.J. Blythe, A. Klein, J.A. Philips, E.D. Dudol, M.S. El-Aasser. *J. Polym. Sci. Part A: Polym. Chem.* **1999**, *37*, 4449–4457. d) J.M. Asua, V.S. Rodrigues, E.D. Sudol, M.S. El-Aasser. *J. Polym. Sci. Part A: Polym. Chem.* **1989**, *27*, 3569–3587.

[40] P.J. Flory, Principles of Polymer Chemistry, Cornell University Press, Ithaca, NY, 1953, p. 136. ISBN 0-8014-0134-8

[41] A.R. Shirin-Abadi, A.R. Mahdavian and S. Khoee, *Macromolecules*, **2011**, *44*, 7405-7414.

[42] A. Bianchi, M. Mauri, S. Bonetti, K. Koynov, M. Kappl, I. Lieberwirth, H.-J. Butt, R. Simonutti, *Macromol. Rapid. Commun.* **2014**, *35*, 1944.

[43] a) D. Peer, J.M. Karp, S. Hong, O.C. FarokHzad, R. Margalit, R. Langer, *Nat. Nanotechnol.* **2007**, *2*, 751. b) R. Bodmeier, R.W. McGinty, *Pharm. Res.,* **1987**, *4*, 465.

[44] A.S. Arico, P. Bruce, B. Scrosati, J.M. Tarascon, W. Van Schalkwijk, *Nat. Mater.* **2005**, *4*, 366.

[45] T. Kietzke, D. Neher, K. Landfester, R. Montenegro, R. Guntner, U. Scherf, *Nat. Mater.* **2003**, *2*, 408.

[46] G.W. Burton, C.P. O'Farrel, *J. Elastomers Plastics* **1977**, *9*, 94.

[47] P.B. O'Donnell, J.W. McGinity, *Adv. Drug Delivery Rev.* **1997**, *28*, 25.

[48] R.H. Staff, M. Gallei, M. Mazurowski, M. Rehahn, R. Berger, K. Landfester, D. Crespy, *ACS Nano* **2012**, *6*, 9042.

[49] M. Antonietti, K. Landfester, *Prog. Polym. Sci.* **2002**, *27*, 689-757.

[50] D. Schäffel, R.H. Staff, H.-J. Butt, K. Landfester, D. Crespy, K. Koynov, *Nano Lett.* **2012**, *12*, 6012.

[51] F.M. Winnik, *Chem. Rev.* **1993**, *93*, 587. b) S. Nomula, S.L. Cooper, *Macromolecules* **2000**, *33*, 6402. c) A.V. Kabanov, I.R. Nazarova, I.V. Astafieva, E.V. Batrakova, V.Y. Alakhov, A.A. Yaroslavov, V.A. Kabanov, *Macromolecules* **1995**, *28*, 2303.

[52] K.Y. Law, *Chem. Phys. Lett.* **1980**, *75*, 545.

[53] N. Amdursky, Y. Erez, D. Huppert, *Acc. Chem. Res.* **2012**, *45*, 1548.

[54] a) M.A. Haidekker, E.A. Theodorakis, *J. Biol. Eng.* **2010**, *4*. b) Y. Shiraishi, T. Inoue, T. Hirai, *Langmuir* **2010**, *26*, 17505.

[55] a) R.O. Loufty, *Pure Appl. Chem.* **1986**, *58*, 1239. b) J.M. Nölle, C. Jüngst, A. Zumbusch, D. Wöll, *Polym. Chem.* **2014**, *5*, 2700.

[56] D.R. Rogers, *Am. J. Clin. Pathol.* **1965**, *44*, 59.

[57] M.A. Haidekker, M. Nipper, A. Mustafic, D. Lichlyter, M. Dakanali, E.A Theodorakis, *Advanced Fluorescence Reporters in Chemistry and Biology I: Fundamentals and molecular design,* Springer Ser Fluoresc (2010) 8: 267-308.

[58] a) V.I. Stsiapura, A.A. Masekevich, V.A. Kuzmitsky, K.K. Turoverov, I.M. Kuznetsova, *J. Phys. Chem. A* **2007**, *111*, 4829. b) Y. Erez, Y.H. Liu, N. Amdursky, D. Huppert, *J. Phys. Chem. A* **2011**, *115*, 8479. c) V.I. Stsiapura, A.A. Masekevich, S.A. Tikhomirov, O.V. Buganov, *J. Phys. Chem. A* **2010**, *114*, 8345.

[59] a) R.O. Loutfy, B.A. Arnold, *J. Phys. Chem.* **1982**, *86*, 4205-4211. b) M.A. Haidekker, T.P. Brady, D. Lichlyter, E.A. Theodorakis, *Bioorg. Chem.* **2005**, *33*, 415. c) F. Zhou, J. Shao, Y. Yang, J. Zhao, H. Guo, X. Li, S. Ji, Z. Zhang, *Eur. J. Org. Chem.* **2011**, 4773. DOI: 10.1002/ejoc.201100606.

[60] a) M.A. Haidekker, T.P. Brady, D. Lichlyter, E.A. Theodorakis, *J. Am. Chem. Soc.* **2006**, *128*, 398. b) M.A. Haidekker, A.G. Tsai, T. Brady, H.Y. Stevens, J.A. Frangos, E.A. Theodorakis, M. Intaglietta, *Am. J. Physiol. Heart Circ. Physiol.* **2002**, *282*, H1609.

[61] T. Förster, G. Hoffmann, *Z. Phys. Chem.* **1971**, *8*, 171.

[62] S. Raut, J. Kimball, R. Fudala, H. Doan, B. Maliwal, N. Sabnis, A. Lacko, I. Gryczynski, S.V. Dzyuba, Z. Gryczynski, *Phys. Chem. Chem. Phys.* **2014**, *16*, 27037.

[63] a) Berne, B.J.; Pecora R. Dynamic light scattering (Wiley-Interscience, New York, 1976); b) Schmitz K.S., An introduction to dynamic light scattering by macromolecules (Academic Press, INC.1990).

[64] Pecora R. J. Chem. Phys.1964, 40, 1604.

[65] A. Maus, C. Hertlein, K. Saalwächter, *Macromol. Chem. Phys.* **2006**, *207*, 1150-1158.

[66] a) H.-J. Butt, B. Cappella, M. Kappl, *Surf. Sci. Rep.* **2005**, *59*, 1-152. b) G. Binning, C.F. Quate, C. Gerger, *Phys. Rev. Lett.* **1986**, *56*, 930-933.

[67] H.G. Hansma, J. Vesenka, C. Siegerist, G. Kelderman, H. Morrett, S. Sinsheimer, V. Elings, C. Bustamante, P.K. Hansma, *Science* **1992**, *256*, 1180-1184.

[68] A.A. Deniz, S. Mukhopadhyay, E.A. Lemke, *J. R. Soc. Interface* **2008**, *5*, 15-45.

[69] M. Davies, A. Brindley, X. Chen, M. Marlow, S.W. Doughty, I. Shrubb, C.J. Roberts, *Pharm. Res.* **2005**, *22*, 1158-1166.

[70] H.S. Yang, Y.F. Wang, S.J. Lai, H.J. An, Y,F. Li, F.S. Chen, *J. Food Sci.* **2007**, *72*, R65-R75.

[71] C. Ton-That, A.G. Shard, D.O.H. Teare, R.H. Bradley *Polymer* **2001**, *42*, 1121-1129.

[72] a) G. Meyer, N.M. Amer, *Appl. Phys. Lett.* **1988**, *53*, 2400. b) S. Alexander, L. Hellemans, O. Marti, J. Schneir, V. Elings, P.K. Hansma, M. Longmire, J. Gurley, J. *Appl. Phys.* **1989**, *65*, 164.

[73] T.J. Senden, *Curr. Opin. Colloid Interf. Sci.* **2001**, *6*, 95.

[74] a) G. Gillies, C.A. Prestidge, P. Attard, Langmuir 17 (2001) 7955. b)

[75] a) D. Madge, E.L. E.lson, W.W. Webb, *Phys. Rev. Lett.* **1972**, *29*, 705. b) E.L. Elson, D. Madge, *Biopolymers* **1974**, *13*, 1. c) D. Madge, E.L. Elson, W.W. Webb, *Biopolymers* **1974**, *13*, 29.

[76] M. Ehrenberg, R. Riegler, *Chem. Phys.* **1974**, *4*, 390.

[77] P. Schwille, *Cell Biochem. Biophys.* **2001**, *34*, 383.

[78] a) R. Rigler, E. Elson, *Fluorescence correlation spectroscopy: theory and applications*; Springer: New York **2001**. b) E.L. Elson, *Biophys. J.* **2011**, *101*, 2855.

[79] a) S.X. Xie, J.K. Trautman, *Annu. Rev. Phys. Chem.* **1998**, *49*, 441. b) S. Nie, R.N. Zare, *Annu. Rev. Bioph. Biomol. Struct.* **1997**, *26*, 567.

[80] a) R. Rigler, J. Widengren, *Bioscience* **1990**, *3*, 180. b) R. Rigler, Ü. Mets, J. Widengren, P. Kask, *Eur. Biophys. J.* **1993**, *22*, 169.

[81] K. Koynov, H.-J. Butt, *AIP Conf. Proc.* **2013**, *1518*, 357.

[82] a) S.A. Kim, P. Schwille, *Curr. Opin. Neurobiol.* **2003**, *13*, 583. b) S.A. Sukhishvili, Y. Chen, J.D. Müller, E. Gratton, K.S. Schweizer, S. Granick, *Nature* **2000**, 146. c) T. Cherdhirankorn, A. Best, K. Koynov, K. Peneva, K. Müllen, G. Fytas, *J. Phys. Chem. B* **2009**, *113*, 3355. d) A. Michelman-Ribeiro, H. Boukari, R. Nossal, F. Horkay, *Macromolecules* **2004**, *37*, 10212. e) M. Doroshenko, M. Gonzales, A. Best, H.-J. Butt, K. Koynov, G. Floudas, *Macromol. Rapid Commun.* **2012**, *33*, 1568.

[83] R. Rilger, *Biochem. Biophys. Res. Commun.* **2010**, *396*, 170.

[84] a) R. Raccis, R. Roskamp, I. Hopp, B. Menges, K. Koynov, U. Jonas, W. Knoll, H.-J. Butt, G. Fytas, *Soft Matter* **2011**, *7*, 7042. b) D. Schäffel, S. Yordanov, R.H. Staff, A. Kreyes, Y. Zhao, M. Schmidt, K. Landfester, J. Hofkens, H.-J. Butt, D. Crespy, K. Koynov, *ACS Macro Lett.* **2015**, *4*, 171.

[85] K. Jaskiewicz, A. Larsen, I. Lieberwirth, K. Koynov, W. Meier, G. Fytas, A. Kroeger, K. Landfester, *Angew. Chem. Int. Ed.* **2012**, *51*, 4613.

[86] J. Zhao, S. Granick, *J. Am. Chem. Soc.* **2004**, *126*, 6242.

[87] a) J. Szymanski, M. Weiss, *Phys. Rev. Lett.* **2009**, *103*, 103. b) T. Kalwarczyk, N. Ziębacz, A. Bielejewska, K. Koynov, J. Szymaríski, A. Wilk, A. Patkowski, J. Gapinski, H.-J. Butt, R. Holyst, *Nano Lett.* **2011**, *11*, 2157.

[88] M. Giannelli, P.W. Beines, R.F. Roskamp, K. Koynov, G. Fytas, W. Knoll, *J. Phys. Chem. C* **2007**, *111*, 13205.

[89] T. Cherdhirankorn, V. Harmandaris, A. Juhari, P. Voudouris, G. Fytas, K. Kremer, K. Koynov, *Macromolecules* **2009**, *42*, 4858.

[90] T. Bonné, K. Lüdtke, R. Jordan, P. Štepanek, C. Papadakis, *Colloid Polym. Sci.* **2004**, *282*, 1425.

[91] D.C. Lamb, A. Schenk, C. Röcker, C. Scalfi-Happ, G.U. Nienhaus, *Biophys. J.* **2000**, *79*, 1129.

[92] a) J.R. Herman, T.R. Londo, N.A. Rahman, B.G. Barisas, *Rev. Sci. Instrum.* **1992**, *63*, 5454. b) E.B. Shera, N.K. Seitzinger, L.M. Davis, R.A. Keller, S.A. Soper, *Chem. Phys. Lett.* **1990**, *174*, 553. c) L.-Q. Li, L.M. Davis, *Appl. Opt.* **1995**, *34*, 3208. d) D.J. Creasey, P.A. Halford-Maw, D.E. Heard, J.E. Spence, B.J. Whitaker, *Rev. Sci. Instrum.* **1998**, *69*, 4068. e) X. Ming, P.R. Selvin, *Rev. Sci. Instrum.* **1999**, *70*, 3877.

[93] M. Böhmer, M. Wahl, H.-J. Rahn, R. Erdmann, J. Enderlein, *Chem. Phys. Lett.* **2002**, *353*, 439.

[94] Petrásek, Z.; Schwille, P. Biophys. J. 2008, 94, (4), 1437-1448.

[95] S. Kawana, R.A.L. Jones, *Phys. Rev. E* **2001**, *63*, 021501.

[96] a) J.L. Keddie, R.A.L. Jones, R.A. Cory *Europhys. Lett.* **1994**, *27*, 59. b) J.L. Keddie, R.A.L. Jones R.A. Cory *Faraday Discuss.* **1995**, *98*, 219. c) J.A. Forrest, K. Dalnoki-Veress, J.R. Dutcher *Phys. Rev. E* **1997**, *56*, 5705. d) K. Fukao and Y. Miyamoto *Europhys. Lett*. **1999**, *46*, 649.

[97] J.A. Forrest, K. Dalnoki-Veress, J.R. Stevens, J.R. Dutcher *Phys. Rev. Lett.* **1996**, *77*, 2002.

[98] a) C.L. Jackson, G.B. McKenna *J. Non-Cryst. Solids* **1991**, 131- 133, 221. b) M. Arndt, R. Stannarius, H. Groothues, E. Hempel, F. Kremer *Phys. Rev. Lett.* **1997**, *79*, 2077.

[99] a) K. Fukao, Y. Miyamoto *Phys. Rev. E* **2000**, *61*, 1743– 1754. b) K. Fukao, Y. Miyamoto *Phys. Rev. E* **2001**, 6401, 011803

[100] a) C.J. Ellison, J.M. Torkelson *Nature Mater.* **2003**, *2*, 695– 700

[101] P. Rittigstein, R.D. Priestley, L.J. Broadbelt, J.M. Torkelson *Nature Mater.* **2007**, *6*, 278– 282

[102] C.B. Roth, J.R. Dutcher *Eur. Phys. J. E* **2003**, *12*, S103– S107

[103] U.S. Patent 3, 263, 484.

[104] a) B. Wunderlich (**1990**) *Thermal analysis*. Academic Press, New York. b) W. Hemminger, G.W.H. Höhne (**1984**) *Calorimetry - fundamentals and practice*. VCH, Weinheim. c) M.J. Richardson (**1992**) *The application of differential scanning calorimetry to the measurement of specific heat*. In: K.D.Maglic, A. Cezairliyan, V.E. Pelewtsky (eds) Compendium of thermophysical property measurement methods, vol. 2. Plenum Press, New York. d) G.W.H. Höhne, W. Hemminger, H.J. Flammersheim (**1996**) *Differential scanning calorimetry - an introduction for*

practitioners. Springer, Berlin. e) M.E. Brown (**1998**) *Principles and practice*. In: P.K. Gallagher (ed) Handbook of thermal analysis and calorimetry, vol. 1. Elsevier, Amsterdam.

[105] a) V.B.F. Mathot (**1994**) *Calorimetry and thermal analysis of polymers*. Hanser Publishers, München. b) V.A. Bershtein, V.M. Egorov (**1994**) *Differential scanning calorimetry of polymers - physics, chemistry, analysis, technology*. In: T.J. Kemp (ed) Ellis Horwood series in polymer science and technology. Ellis Horwood Ltd, New York, London, Toronto, Sydney, Tokyo, Singapore. c) W.M. Groenewoud (**2001**) *Characterisation of polymers by thermal analysis*. Elsevier Science, Amsterdam. d) B. Wunderlich (**2005**) *Thermal analysis of polymeric materials*. Springer, Berlin.

[106] P.S. Gills, S.R. Sauerbrunn, M. Reading *J. Therm. Anal.* **1993**, *40*, 931-939.

[107] L.C. Thomas (**2005**) *Modulated DSC® Paper #1 Why Modulated DSC®? ; An Overview and Summaryof Advantages and Disadvantages Relative to Traditional DSC* TA Instruments, 109 Lukens Drive, New Castle, DE 19720, USA.

[108] F. Kremer, A. Schönhals, Eds., Broadband Dielectric Spectroscopy (Springer, Berlin, 2003).

[109] a) M. Wilhelm, C.L. Zhao, Y.C. Wang, R.L. Xu, M.A. Winnik, J.L. Mura, G. Riess, M.D. Croucher, *Macromolecules* **1991**, *24*, 1033. b) S.C. Lee, Y.K. Chang, J.S. Yoon, C.H. Kim, I.C. Kwon, Y.H. Kim, S.Y. Jeong *Macromolecules* **1992**, *32*, 1847. c) M.M. Mok, T.P. Lodge, J. *Polym. Sci, Part B: Polym. Phys.* **2012**, *50*, 500 (2012).

[110] a) M.A. Haidekker, E.A. Theodorakis, *J. Biol. Eng.* **2010**, *4.* b) K.Y. Law, *Chem. Phys. Lett.* **1980**, *75*, 545. c) Y. Shirashi, T. Inoue, T. Hirai, *Langmuir* **2010**, *26*, 17505.

[111] J.Y. Ye, T. Hattori, H. Nakatsuka, Y. Maruyama, M. Ishikawa, *Phys. Rev. B: Condens. Matter.* **1997**, *56*, 5286.

[112] a) X.J. Zhou, Y.Y. Zhou, J.J. Nie, Z.C. Ji, J.T. Xu, X.H. Zhang, B.Y. Du, *ACS Appl. Mater. Interfaces* **2014**, *6*, 6, 4498-4513; b)Y.J. Men, M. Drechler, J.Y. Yuan, *Macromol. Rapid. Commun.* **2013**, *34*, 21, 1721-1727; c) J.T. Zhang, S.W. Huang, Y.N. Xue, R.X. Zhou, *Macromol. Rapid. Commun.* **2006**, *26*, 16, 1346-1350.

[113] a) D. Yiamsawas, G. Baier, E. Thines, K. Landfester, F.R. Wurm, *RSC Adv*. **2014**, *4*, 11661-11663; b) K.Bley, N. Sinatra, N. Vogel, K. Landfester, C.K. Weiss, *Nanoscale* **2014**, *6*, 492-502; c) G. Mauthner, K. Landfester, A. Kock, H. Bruckl, M. Kast, C. Stepper, E.J.W. List, *Org. Electron.* **2008**, *9*, 2, 164-170.

[114] a) N. Manfredi, A. Bianchi, V. Causin, R. Ruffo, R. Simonutti, A. Abbotto, *J. Polym. Sci. A Polym. Chem.* **2014**, *52*, 719-727; b) M. Antonietti, S. Forster, *Adv. Mater.* **2003**, *15*, 16, 1323-1333; c) T. Kietzke, D. Neher, K. Landfester, R. Montenegro, R. Günter, U. Scherf, *Nat. Mater.* **2003**, *2*, 408-412.

[115] a) A.M. Van Herk, in *Hybrid latex particles, Preparation with (mini)emulsion polymerization*, (Eds: A.M. Van Herk, K. Landfester), Springer, **2010**, Ch.1; b) B. Charleux. F. D'Agosto, G. Delaittre, *Adv. Polym. Sci.* **2010**, 233.

[116] K. Landfester, *Angew. Chem. Int. Ed.* **2009**, *48*, 4488 – 4507.

[117] a) J. Nicolas, S. Murad, D. Brambilla, N. Mackiewicz, P. Couvreur, *Chem. Soc. Rev.* **2013**, *42*, 1147-1235; b) C. Wohnhaas, V. Mailander, M. Droege, M.A. Filatov, D. Busko, Y. Avlasevich, S. Baluschev, T. Miteva, K. Landfester, A. Turshato, *Macromol. Biosci.* **2013**, *13*, 1422-1430; c) T. Staudt, T.O. Machado, N. Vogel, C.K. Weiss, P.H.H Araujo, C. Sayer, K. Landfester, *Macromol. Chem. Phys.* **2013**, *214*, 2213-2222.

[118] a) L. Charoenmark, D. Polpanich, R. Thiramanas, P. Tangboriboonrat, *Macromol. Res.* **2012**, *20*, 590-596; b) S.W. Zhang, S.X. Zhou, Y.M. Weng, L.M. Wu, *Langmuir* **2005**, *21*, 2124-2148; c) N. Bechthold, F. Tiarks, M. Willert, K. Landfester, M. Antonietti, *Macromol. Symp.* **2000**, *151*, 549-555.

[119] D.C. Sundberg, Y.G. Durant, *Polym. React. Eng.* **2003**, *11*, 3, 379-432.

[120] a) R.A. Rmli, W.A. Laftah, S. Hashim, *RSC Adv.* **2013**, *3*, 36, 15543-15565. b) J. Stubbs, O. Karlsson, J.E. Jönsson, E. Sundberg, Y. Durant, D. Sundberg, *Colloids Surf.* **1999**, *153*, 255-270

[121] F. Mellinger, M. Wilhem, P. Belik, H. Schwind, H.W. Spiess, *Macromol. Chem. Phys.* **1999**, *200*, 2454-2460.

[122] L.A. Pérez-Carrillo, M. Puca, M. Rabelero, K.E. Meza, J.E. Puig, E. Mendizàbal, F. Lòpez-Serrano, R.G. Lòpez, *Polymer* **2007**, *48*, 1212-1218.

[123] Y.G. Durant, D.C. Sundberg, *Marcomolecules* **1996**, *29*, 26, 8466-8472.

[124] J. Push, A.M. Van Herk, *Macromolecules* **2005**, *38*, 16, 6909-6914.

[125] V. Dinnendahl, U. Fricke (2010) *Arzneistoff-Profile* (in German) 2 (23 ed.). Eschborn, Germany: GoviPharmazeutischerVerlag.

[126] a) J. Eastoe, B.H. Robinson, D.C. Steytler *J. Chem. Soc., Faraday Trans.* **1990**. b) M. Kotlarchyk, S.H. Chen, J.S. Huang, M.W. Kim *Phys. Rev. A* **1984**, *29*, 2054. c) S.H. Chen, S.L. Chang, R.J. Strey *J. Chem. Phys.* **1990**, *93*, 1907.

[127] a) J.E. Lundeen, Medicinal composition, useful for treating gastrointestinal disorder comprising fecal incontinence and fecal ur-gency, comprises varying amounts of capsaicin depending on strength of dosage, salt of imipramine, and docusate sodium. US Patent US2010159000-A1, June 24, 2010. b) S.A. Mueller-Lissner, A. Wald, *BMJ Clinical Evindence* **2010**, 2010: 0413.

[128] S. Nave, J. Eastoe, R.K. Heenan, D. Steytler, I. Grillo, *Langmuir* **2000**, *16*, 8741.

[129] a) I. Capek, T. Kocsisova, *Polymer Journal* **2011**, *43*, 700. b) S.M. Dong, S.Q. Cheng, P.B. Zetterlund, *Journal of Polymer Science, Part A Polym. Chem.* **2013**, *51*, 2104

[130] X. Gu, C.A. Michaels, D. Nguyen, Y.C. Jean, J.W. Martin, T. Nguyen, *Appl. Surf. Sci.* **2006**, *252*, 5168-5181.

[131] a) R.M. Silverstein, G.C. Bassler, T.C. Morrill, *Spectrometric Identification of Organic Compounds.* 4th ed. New York: John Wiley and Sons, **1981**. QD272.S6 S55. b) Nakanishi, Koji *Infrared Absorption Spectroscopy*. QD95.N383

[132] M. Mauri, M.K. Dibbanti, M. Calzavara, L. Mauri, R. Simonutti, V. Causin *Anal. Methods* **2013**, *5*, 4336-4344.

[133] P.G. De Gennes, *J. Chem. Phys.* **1971**, *55*, 572-579.

[134] M. Mauri, Y. Thomann, H. Schneider, K. Saalwächter *Solid State Nucl. Magn. Reson.* **2008**, *34*, 125-141.

[135] R. Simonutti, A. Comotti, S. Bracco, P. Sozzani *Chem. Mater.* **2001**, *13*, 771-777.

[136] R. Simonutti, A. Comotti, S. Bracco, P. Sozzani, F. Negroni *Chem. Mater.* **1999**, *11*, 822-828.

[137] A.J. Brandolini, D.D. Hills *NMR spectra of polymers and polymer additives* CRC Press: **2000**.

[138] a) P. Sozzani, S. Bracco, A. Comotti, R. Simonutti, P. Valsesia, Y. Sakamoto, O. Terasaki, *Nature Materials* **2006**, *5*, 545-551. b) J.A. Champion, Y.K. Katare, S. Mitragotri *Proceedings of the National Academy of Science of the United States of America* **2007**, *104*, 11901-11904.

[139] H.-J. Butt, B. Cappella, M. Kappl *Surf. Sci. Rep.* **2005**, *59*, 1-152.

[140] a) Q. Cheng, G.J. Vancso *Macromol. Rapid Commun.* **2011**, *32*, 1704-1709. b) Q. Cheng, H. Schonherr, G.J. Vancso *Soft Matter* **2009**, *5*, 4944-4950.

[141] A. Solmaz, T. Aytun, J.K. Deutsche, C.W. ow-Yang *Langmuir* **2012**, *28*, 10592-10596.

[142] D.A. Hajduk, P. Urayama, S.M. Gruner, S. Erramilli, R.A. Register, K. Brister, L.J. Fetters *Macromolecules* **1995**, *28*, 7148-7156.

[143] J.A. Gonzales-Leon, M.H. Acar, S.W. Ryu, A.V.G. Ruzette, A.M. Mayes *Nature* **2003**, *426*, 424-428.

[144] J.A. Gonzales-Leon, S.W. Ryu, S.A. Hewlett, S.H. Ibrahim, A.M. Mayes *Macromolecules* **2005**, *38*, 8036-8044.

[145] K.H. Lee, S.W. Ryu *Macromol. Res.* **2012**, *20*, 1294-1299.

[146] T.G. Fox, *Bull. Am. Chem. Phys. Soc.* **1956**, *1*, 123.

[147] a) A. Dazzi, A. Deniset-Besseau, P. Lasch, *Analyst* **2013**, *138*, 4191- 4201. b) M. Miljokovic, B. Bird, M. Diem, *Analyst* **2012**, *137*, 3954-3964.

[148] J. Nicolas, S. Murad, D. Brambilla, N. Mackiewicz, P. Couvreur, *Chem. Soc. Rev.* **2013**, *42*, 1147.

[149] a) C. Wohnaahs, V. Mailaender, M. Droege, M.A. Filatov, D. Busko, Y. Avlasevich, S. Baluschev, T. Miteva, K. Landfester, A. Turshato, *Macromol. Biosci.* **2013**, *13*, 1422. b) T. Staudt, T.O. Machado, N. Vogel, C.K. Weiss, P.H.H. Araujo, C. Sayer, K. Landfester, *Macromol. Chem. Phys.* **2013**, *214*, 2213.

[150]D.B. Hall, D.D. Deppe, K.E. Hamilton, A. Dhinojwala, J.M. Torkelson, *J. Non-Cryst. Solids* **1998**, *48*, 235.

[151] E. Penzel, *in Ullmann's Encycolpedia of Industrial Chemistry*, Wiley-VCH Verlaag GmbH&Co. KGaA, **2000**.

[152] F. Meinardi, A. Colombo, K.A. Velizhanin, R. Simonutti, M. Lorenzon, L. Beverina, R. Viswanatha, V.I. Klimov, S. Brovelli, *Nature Photonics* **2014**, *8*, 392.

[153] A. Monguzzi, F. Bianchi, A. Bianchi, M. Mauri, R. Simonutti, R. Ruffo, R. Tubino, F. Meinardi, *Adv. Energy Mater.* **2013**, *3*, 680.

[154] W. Zou, C. Visser, J.A. Maduro, M.S. Pshenichnikov, J.C. Hummelen, *Nature Photon.* **2012**, *6*, 560-564.

[155] A. Kudo, Y. MIseki, *Chem. Soc. Rev.* **2009**, *38*, 253.

[156] a) T.N. Singh-Rachford, F.N. Castellano, *Coord. Chem. Rev.* **2010**, *254*, 2560. b) A. Turshatov, D. Busko, Y. Avlasevich, T. Miteva, K. Landfester, S. Baluschev, *ChemPhysChem* **2012**, *13*, 3112. c) J. Zhao, S. Ji, H. Guo, *RSC Adv.* **2011**, *1*, 937.

[157] A. Monguzzi, R. Tubino, S. Hoseinkhani, M. Campione, F. Meinardi, *Phys. Chem. Chem. Phys.* **2012**, *14*, 4322.

[158] a) Y.Y. Cheng, B. Fuckel, T. Khoury, R. Clady, M.J.Y. Tayebjee, N.J. Ekins-Daukes, M.J. Crossley, T.W. Schmidt, *J. Phys. Chem. Lett.* **2010**, *1*, 1795. b) S. Balushev, V. Yakutkin, T. Miteva, Y. Avlasevich, S. Chernov, S. Aleshchenkov, G. Nelles, A. Cheprakov, A. Yasuda, K. Mullen, G. Wegner, *Angew. Chem.-Int. Ed.* **2007**, *46*, 7693. c) R.R. Islangulov, J. Lott, C. Weder, F.N. Castellano, *J. Am. Chem. Soc.* **2007**, *129*, 12652.

[159] D.Y. Kondakov, T.D. Pawlik, T.K. Hatwar, J.P. Spindler, *J. Appl. Phys.* **2009**, *106*, 124510.

[160] a) A. Monguzzi, M. Frigoli, C. Larpent, R. Tubino, F. Meinardi, *Adv. Funct. Mater.* **2012**, *22*, 139. b) V. Jankus, E.W. Snedden, D.W. Bright, V.L. Whittle, J.A.G. Williams, A. Monkman, *Adv. Funct. Mater.* **2012**, DOI:10.1002/adfm.201201284.

[161] L. Stryer, D.D. Thomas, C.F. Maeres, *Ann. Rev. Biophys. Bioeng.* **1982**, *11*, 203.

[162] a) P. Guo, P. Chen, W. Ma, M. Liu, *J. Mater. Chem.* **2012**, *22*, 20243-20249. b) Y. Qiu, P. Chen, M. Liu, *J. Am. Chem. Soc.* **2010**, *132*, 9644-9652. c) Y. Zhang, P. Chen, Y. Ma, S. He, M. Liu, *ACS Appl. Mater. Interfaces* **2009**, *1*, 2036-2043.

[163] a) P. Guo, G. Zhao, P. Chen, B. Lei, L. Jiang, H. Zhang, W. Hu, M. Liu, *ACS Nano* **2014**, *8*, 3402-3411. b) P. Guo, P. Chen, M. Liu, *Langmuir* **2012**, *28*, 15482-15490. c) J.-S. Hu, Y.-G. Guo, H.-P. Liang, L.-J. Wan, L. Jiang, *J. Am. Chem. Soc.* **2005**, *127*, 17090-17095. d) Y. Zhong, Z. Wang, R. Zhang, F. Bai, H. Wu, R. Haddad, H. Fan, *ACS Nano* **2014**, *8*, 827-833.

[164] D.C. Barber, R.A. Freitag, D.G. Whitten, *J. Phys. Chem.* **1991**, *95*, 4074-4086.

[165] J.H. van Esch, M.C. Feiters, A.M. Peters, R.J.M. Nolte, *J. Phys. Chem.* **1994**, *98*, 5541-5551.

[166] R.H. Schmehl, D.G. Whitten, *J. Phys. Chem.* **1981**, *85*, 3473-3480.

[167] a) R. Gautam, S.M.S. Chauhan, *Mater. Sci. Eng., C* **2014**, *43*, 447-457. b) P. Guo, P. Chen, W. Ma, M. Liu, *J. Mater. Chem.* **2012**, *22*, 20243-20249.

[168] K. Maiti, D. Mitra, R.N. Mitra, A.K. Panda, P.K. Das, A.K. Rakshit, S.P. Moulik, *J. Phys. Chem. B* **2013**, *114*, 7499-7508.

[169] H.-S. Bien, J. Stawitz, K. Wunderlich, "Anthraquinone Dyes and Intermediates", Ullmann's Encyclopedia of Industrial Chemistry, Wiley-VCH Verlag GmbH & Co. KGaA, **2000**.

[170] J.H.H. de Graaff "The colourful past: origins, chemistry and identification of natural dyestuff", London: Archetype Publications Ltd, **2004**.

[171] a) P. Chattopadhyay, S. Chatterjee, S.K. Sen, *African Journal of Biotechnology* **2008**, *7*, 2972. b) Y. Caro, L. Anamale, M. Fouillaud, P. Laurent, T. Petit, L. Dufosse, *Nat. Prod. Bioprospect* **2012**, *2*, 174-193.

[172] E. E. Langdon-Jones, S. J. A. Pope, *Coord. Chem. Rev.* **2014**, *269*, 32-53.

[173]W. Sangaroon, S. Laopha, P. Chaiamornnugool, S. Tontapha, S. Saekow, V. Amornkitbamrung, *J. Mol. Model* **2013**, *19*, 1407-1415.

[174] A. Ramirez-Cruz, C. Llanderal-Cazares, R. Racotta, *J. Insect. Sci.* **2008**, *8*, 5.

[175] Y. Kogo, H. Kikuchi, M. Matsuoka, T. Kitao, *Journal of the Society of Dyers and Colourists* **1980**, *96*, 475.

[176] a) Tanio N., *Polym. J.* **2002**, *34*, 466; b) Koike Y., Tanio N., Ohtsuka Y., *Macromolecules* **1989**, *22*, 1367.

[177] A. Colombo, F. Tassone, F. Santolini, N. Contiello, A. Gambirasio, R. Simonutti, *J. Mater. Chem. C* **2013**, *1*, 2927

[178] J.A. Kyle Material for protecting sheets, &c., in tinning. US Patent 1901; No. 679,972.

[179] A. Sharma, V. V. Tyagi, C. R. Chen and D. Buddhi, *Renewable Sustainable Energy Rev.* **2009**, *13*, 318–345.

[180] D.C. Hyun, N.S. Levinson, U. Jeong and Y. Xia, *Angew. Chem. Int. Ed.*, **2014**, *53*, 3780-3795.

[181] M.M. Kenisarin, *Renewable Sustainable Energy Rev.* **2010**, *14*, 955–970.

[182] A. Pasupathy, R. Velraj and R.V.Seeniraj, *Renewable Sustainable Energy Rev.* **2008**, *12*, 39-64.

[183] B.M. Diaconu, S. Varga and A.C. Oliveira, *Appl. Energy* **2010**, *87*, 620–628.

[184] P. Sánchez, M.V. Sánchez-Fernandez, A. Romero, J.F. Rodríguez and L. Sánchez-Silva, *Thermochim. Acta*, **2010**, *498*, 16–21.

[185] a) http://www.sofrigam.com; b) http://www.tcpreliable.com; c) http://www.pcm-solutions.com.

[186] a) S.W. Choi, Y. Zhang and Y. Xia, *Angew. Chem. Int. Ed.*, **2010**, *49*, 7904-7908; b)D. C. Hyun, P. Lu, S.-I. Choi, U. Jeong and Y. Xia *Angew. Chem. Int. Ed.* **2013**, *52*, 10468-10471; c) G. D. Moon, S. W. Choi, X. Cai, W. Li, E. C. Cho, U. Jeong, L. V. Wang and Y. Xia, *J. Am. Chem. Soc.* **2011**, *133*, 4762–4765; d) http://www.rubitherm.com.

[187] A. Castell, C. Solé, M. Medrano, J. Roca, L. F. Cabeza and D. García, *Appl. Therm. Eng.* **2008**, *28*, 1676–1686.

[188] a) A.R. Mahdavian, M. Ashjari and H.J. Salehi-Mobarakeh, *Appl. Polym.Sci.* **2008**, *110*, 1242–1249; b) G.H. Teo, Y.H. Ng, P.B. Zetterlund and S.C. Thickett, *Polymer* **2015**, *63*, 1-9. doi:10.1016/j.polymer.2015.02.035; c) F. Tiarks, K. Landfester and M. Antonietti, *Langmuir* **2001**, *17*, 908-918.

[189] a) R. Montengro, M. Antonietti, Y. Mastai, K. Landfester, *J. Phys Chem. B* **2003**, *107*, 5088-5094. b) D. Turnbull, R.L. Cormia, *J. Chem. Phys.* **1961**, *34*, 820-831.

[190] A.C. Balazs, T. Emrik, T.P. Russel, *Science* **2006**, *314*, 1107-1110.

[191] D.R. Paul, L.M. Robeson, *Polymer* **2008**, *49*, 3187-3204.

[192] S. Chandran, N. Begam, V. Padmanabhan, J.K. Basu, *Nat. Commun.* **2014**, *5*, 3697.

[193] S. Chandran, J.K. Basu, *Eur. Phys. J. E* **2011**, 34-99.

[194] E. Bourgeat-Lami, J. Lang, *J. Colloid Interface Sci.* **1999**, *210*, 281-289 (1999).

[195] M.E. Mackay, A. Tuteja, P.M. Duxbury, C.J. Hawker, B. Van Horn, Z. Guan, G. Chen5, R. S. Krishnan *Science* **2006**, *311*, 1740-1743.

[196] T. Araki, H. Tanaka, *Phys. Rev. B* **2006**, *73*, 061506.

[197] E. Bourgeat-Lami, J. Lang, *J. Colloid Interface Sci.* **1999**, *210*, 281-289.

[198] G.A. Sotiriou, C.O. Blattmann, S.E. Pratsinis, *Adv. Funct. Mater.* **2013**, *23*, 34-41.

[199] Ph. Viala, E. Bourgeat-Lamy, A. Guyot, P. Legrande, D. Lefebvre, *Macromol.Symp.* **2002** *187*, 651-661.

[200] P.D. Cozzoli, A. Kornowski, H. Weller, *J. Am. Chem. Soc.* **2003**, *1253*, 14539-14548.

[201] V. Kapeliouchko, G. Palamone, T. Poggio, G. Zuccheri, R. Passeri, K. Sparnacci, D. Antonioli, S. Deregibus, M. Laus, *J. Polym. Sci., Part A: Polym. Chem.* **2009**, *47*, 2928-2937.

[202] Y. Jin, A. Hiltner, E. Baer, *J Polym Sci Part B: Polym Phys* **2007**, *45*, 1138–1151.

[203] a) T. N. Singh-Rachford, F. N. Castellano, *Coord. Chem. Rev.* 2010, 254, 2560. b) J. Zhao, S. Ji, H. Guo, *RSC Adv.* 2011, 1, 937.

[204] a) P. Guo, G. Zhao, P. Chen, B. Lei, L. Jiang, H. Zhang, W. Hu, M. Liu, *ACS Nano* **2014**, *8*, 3402-3411. b) P. Guo, P. Chen, M. Liu, *Langmuir* **2012**, *28*, 15482-15490. c) J.-S. Hu, Y.-G. Guo, H.-P. Liang, L.-J. Wan, L. Jiang, *J. Am. Chem. Soc.* **2005**, *127*, 17090-17095. d) Y. Zhong, Z. Wang, R. Zhang, F. Bai, H. Wu, R. Haddad, H. Fan, *ACS Nano* **2014**, *8*, 827-833.

[205] C. Zhang, P. Chen, H. Dong, Y. Zhen, M. Liu, W. Hu, *Adv . Mater.* **2015**, *27*, 5379–5387.

[206] A. Monguzzi, J. Mezyk, F. Scotognella, R. Tubino, F. Meinardi, *Phys. Rev. B* **2008**, *78*, 195112-195116.

[207] M.L. Hallensleben "Polyvinyl Compounds, Others" in Ullmann's Encyclopedia of Industrial Chemistry, 2000, Wiley-VCH, Weinheim. doi:10.1002/14356007.a21_743

[208] G.W. Burton, C.P. O'Farrel, *Elastomer Plastics* **1977**, *9*, 94.

[209] a) K. Koynov, H.-J. Butt, *Current Opinion in Colloid & Interface Science* **2012**, *17*, 377-387. b) D. Schaeffel, R.-H. Staff, H.-J. Butt, K. Landfester, D. Crespy, K. Koynov *Nano Letters* **2012**, *12*, 6012-6017.

[210] J.M. Nölle, C. Jüngst, A. Zumbusch, D. Wöll *Polymer Chem.* **2014**, *5*, 2700-2703.